Current Distribution and Stability Criteria for Superconducting Cables in Transient Magnetic Fields

by

Matthew Anthony Ferri

B.S., Mechanical Engineering (1989)
Rice University

S.M., Nuclear Engineering (1994) and
S.M., Electrical Engineering and Computer Science (1994)
Massachusetts Institute of Technology

Submitted to the Department of Nuclear Engineering
in partial fulfillment of the requirements for the degree of

Doctor of Philosophy

at the

MASSACHUSETTS INSTITUTE OF TECHNOLOGY

June 1997

Author ....
Department of Nuclear Engineering
May 12, 1997

Certified by ....
Jeffrey P. Freidberg
Associate Director, Plasma Science and Fusion Center, Thesis Supervisor

Certified by ....
Joseph. V. Minervini
Head of PSFC Fusion Technology and Engineering Division, Thesis Supervisor

Certified by ....
Ali Shajii
Research Scientist, Plasma Science and Fusion Center, Thesis Reader

Accepted by ....
Jeffrey P. Freidberg
Chairman, Departmental Committee on Graduate Students

Current Distribution and Stability Criteria for Superconducting Cables in Transient Magnetic Fields

by

Matthew Anthony Ferri

Submitted to the Department of Nuclear Engineering
on May 12, 1997, in partial fulfillment of the
requirements for the degree of
Doctor of Philosophy

Abstract

A theoretical model of current distribution is developed to explain the performance limitations of superconducting cables in transient magnetic fields. The model self-consistently handles the coupled non-linear electromagnetic and thermal equations which govern the behavior of the cable during both normal operation and quench/recovery events. A two-strand cable is used as an analogy to clarify critical concepts which would be mathematically intractable for larger cable geometries.

The model emphasizes the role of "circulating currents" which are induced by ramping magnetic fields in the vicinity of the low resistance cable terminations. Unlike the fine-scale eddy currents which cause inter-strand coupling losses in cabled superconductors, circulating currents can cause significantly uneven distributions of the net transport current carried by the cable. Since circulating currents have not attracted much attention in the literature, the theoretical model offers unique insights into this important determinant of magnet performance.

Characteristic length scales have been identified which differentiate cable designs into one of nine classifications. Analytic formulae characterizing current distribution for each case are presented. Further, the stability criteria for cables in transient magnetic fields is shown to be heavily dependent on cable length. These results have important implications for researchers attempting to model full-scale magnets with lab-scale experiments.

The theoretical model is shown to explain some of the more confounding results from previously conducted experiments. The "Ramp-Rate Limitation" phenomenon first encountered in the United States Demonstration Poloidal Coil (US-DPC) experiment is shown to be a direct result of induced current imbalances within the conductor. The model would need further refinement, however, to accurately predict all features witnessed experimentally.

Finally, the findings of the theoretical analysis are used to propose suggestions for minimizing circulating currents in order to improve the performance of superconducting cables in transient magnetic fields. Directions for future investigations are also proposed.

Thesis Supervisor: Jeffrey P. Freidberg
Title: Associate Director, Plasma Science and Fusion Center

Thesis Supervisor: Joseph. V. Minervini
Title: Head of PSFC Fusion Technology and Engineering Division

Acknowledgments

My years at the Plasma Fusion Center have been a tremendous learning experience. I would like to thank everyone in the Technology and Engineering Division for their good will and camaraderie during this period. My special thanks go to Prof. Jeffrey Freidberg, Dr. Joseph Minervini, and Dr. Ali Shajii for the contributions they have made to my thesis research and the interest they have taken in my personal development.

My entire family has always encouraged me to follow my own path and accomplish whichever goals I set. I would not have made it this far without their unconditional support. They have my heartfelt and lifelong gratitude.

Since my wife, Yildiz, has contributed the most to my success, she gets the biggest THANK YOU. As hard as I have worked to earn a Ph.D., she is the true prize I will be taking away from my years at M.I.T.

Portions of this research were performed under appointment to the Magnetic Fusion Energy Technology Fellowship program administered by Oak Ridge Institute for Science and Education under contract number DE-AC05-76OR00033 between the U.S. Department of Energy and Oak Ridge Associated Universities.

Contents

List of Figures

List of Tables

Chapter 1

Introduction

Next generation fusion devices such as ITER[1] are relying on superconducting magnets consisting of Cable-In-Conduit Conductors (CICC) to provide the "magnetic bottle" needed for plasma confinement. In recent experiments however [1, 2, 3], CICC magnets have exhibited lower than expected limiting currents when operated in transient magnetic fields. While magnet designers are confident they can build robust magnets which will be immune from this so-called "Ramp-Rate Limitation," a thorough unerstanding of the physical mechanisms which cause this phenomenon could lead to better (i.e. less costly) designs.

The main goal of this thesis is to provide a solid foundation for the study of what is now believed to be the principal cause of ramp-rate limitation in CICC magnets, namely, uneven current distribution within the cable [4, 5, 6]. While the effects of current distribution have been studied before (see, for example, [7, 8, 9]), the theoretical analysis in this thesis for the first time begins with a self-consistent physical model which couples the electromagnetic and thermal equations which govern current distribution and stability in superconducting cables.

The thesis takes the philosophical approach of trying to explain the important physical insights in the simplest terms possible. For this reason, the geometrical complexity of actual multi-strand cables has been abandoned in favor of a two-strand

---

[1] ITER is the International Thermonuclear Experimental Reactor, a joint project of the American, Russian, Japanese and European fusion programs.

analogy which has the dual advantage of being mathematically tractable and physically intuitive. And despite its relative simplicity, the two-strand model contains all of the relevant physics needed to explain the detrimental effects of current distribution in larger cables.

1.1 Overview

The remainder of this chapter provides some general background on superconductors in general, and CICC applications in specific. A description of the relevant material properties and typical design configurations is followed by an introduction to the concept of stability in Section 1.2.1. At the end of the chapter, a brief review of the history of the ramp-rate limitation phenomenon is given.

Subsequent chapters focus on the modeling of current distribution and its effects for CICC. Chapter 2 provides an overview of the theoretical constructs used throughout the thesis and introduces the concept of circulating currents, the root cause of current imbalance within CICC. Despite their importance, circulating currents have previously been largely ignored in the literature; it is believed that this thesis provides the first comprehensive treatment of this topic.

In Chapter 3, the two-strand model which provides the theoretical framework used throughout the thesis is developed. In Chapters 4, 5 and 6, solutions to the two-strand model equations are found for differing operating scenarios. For the first time, important scaling laws are identified which allow the characterization of cables into classes which depend on length, joint design and transverse conductance. Important differences exist between the classes. One important finding is that "full-scale" cables are difficult to simulate with "lab-scale" experiments.

In Chapter 7, heuristic modifications to the two-strand model are made to allow a comparison of the theoretical analysis to experimental results. Despite the inherent limitations of the two-strand model, the theory qualitatively agrees with experiment for the two cases cited. While the theory would need to become more sophisticated in order to achieve a better correlation with the data, the results as presented are

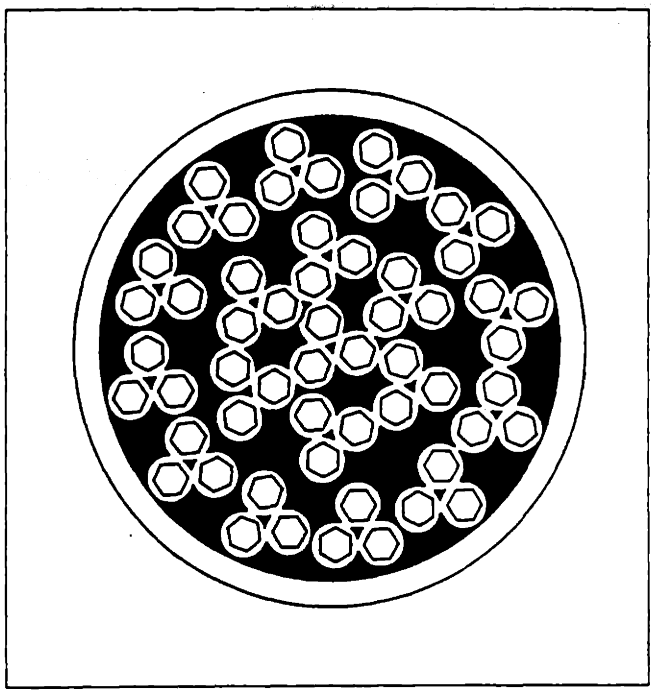

Figure 1-1: An example of a Cable-in-Conduit Conductor (CICC) shown in cross-section. Typically, the strands are twisted into triplets which are further twisted into bundles which are then twisted into sub-cables and so on until the entire cable is formed. Each strand consists of numerous superconducting filaments (not shown in this figure) [10].

sufficient to corroborate the hypothesis that circulating currents account for the ramp-rate limitation experienced in CICC magnets.

The thesis concludes with a summary of the major findings and suggestions for future work in Chapter 8.

1.2 Background

A CICC cable is composed of multiple strands of conductor, each of which is composed of numerous superconducting filaments embedded in a non-superconducting matrix, typically made of copper. The strands are twisted together and compacted within a structural conduit which provides a passage for a suprcritical helium coolant. A cross-section of a typical CICC is diagrammed in Fig. 1-1. This section reviews the relevant features of cable-in-conduit conductors (CICC's) and introduces the concept of Ramp Rate Limitation.

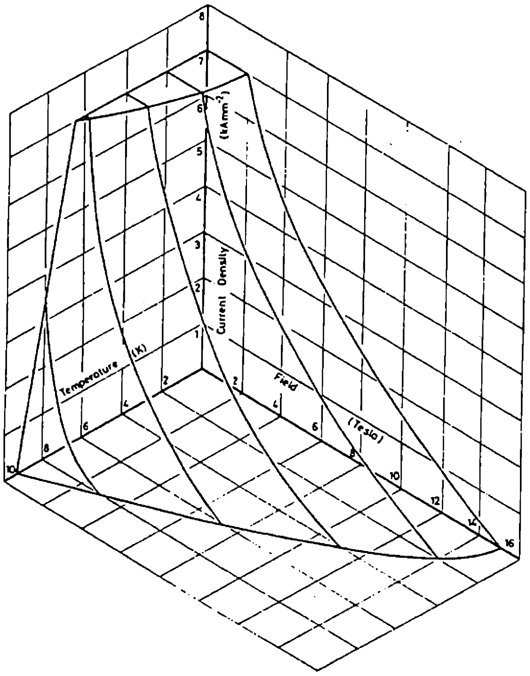

Figure 1-2: The critical surface plot for a commercially available Nb-Ti alloy. At operating points below the surface, the alloy is superconducting; above the surface, it is normal. *Source: reprinted with permission from Wilson,* Superconducting Magnets, *Copyright ©1983 by Oxford University Press.*

1.2.1 Basic Properties of Superconducting Materials

Superconducting materials exhibit their unique properties when operated within certain limits. Traditionally, these limits are defined as the critical temperature, T_c, the critical current density, J_c, and the critical magnetic field, B_c. These three quantities are interdependent and form a three dimensional "critical surface" in a phase space with coordinates of temperature, magnetic field, and current density. The critical surface defines the boundary between the superconducting state (below the surface) and the normal state (above the surface). The critical surface can be considered a material property of the superconductor although it is also affected by manufacturing techniques. The critical surface for a typical Nb-Ti alloy is shown in Fig. 1-2 as an example.

Any superconducting device must be designed so that the superconductor remains "comfortably" beneath its critical surface in the T, B, J–phase space. Any disturbance in temperature, field, or current density which moves the operating point above the critical surface will cause the superconductor to go normal. This process is commonly called "Quenching." The stability of the device against quenching is directly related to how close the nominal operating point is to the critical surface.

The properties of a material in the superconducting state are very different from its properties in the normal state. For stability analysis, the most important difference is the sudden change in the electrical resistivity. Surprisingly, most materials which possess a zero-resistivity superconducting state have relatively high resistivities in the normal state. At cryogenic temperatures, the normal state resistivity of practical superconductors is $10-100$ $\mu\Omega$-cm while, for comparison, the resistivity of copper is less than 0.1 $\mu\Omega$-cm [11]. For this reason, and since superconductors are usually operated at very high current densities (often greater than 10^9 A/m^2 [12]), any local transition to the normal state will be associated with tremendous Joule heating. Such local Joule heating would quickly and irrevocably drive the surrounding superconductor above the critical temperature and into the normal state.

To mitigate this "catastrophic" effect, superconducting wires are formed as a composite material: superconductor filaments embedded in a stabilizer. In the event of a local normal zone in the superconductor, the current can flow around the high resistivity region by traveling through the stabilizer (typically made of copper). The Joule heating associated with a normal zone is thus greatly reduced. In a good design, a coolant (typically suprcritical helium) will be able to absorb the heat generated and cool the strand back down to the operating temperature, where it will again be superconducting. This is known as "Quench Recovery."

A stability analysis of a superconducting system determines the size of disturbance which will cause a "Quench" and whether it will lead to a "Quench Recovery" or a full quench of the entire conductor. Traditional stability analyses usually study the stability of a conductor with respect to disturbances in temperature; the current density and magnetic field are assumed to be uniform and constant. Computer codes such as HESTAB [13] iteratively determine the minimum disturbance energy which would cause the wire to Joule heat to a point where the temperature remains above the critical temperature despite convective cooling provided by the suprcritical helium.

The applicability of such a stability analysis to the problem of ramp rate limitation will be briefly discussed at the end of this chapter in Section 1.2.3.

1.2.2 Cable-in-Conduit Conductors

Cable-in-Conduit Conductors (CICC's) were developed at MIT in the mid-1970's as the initial step in developing large superconducting magnets for fusion reactors and magneto-hydrodynamic (MHD) generators [10]. In the CICC design, multiple strands of superconducting wire are cabled together and enclosed in a conduit which provides structural support as well as a leak-tight passage for helium coolant. The principal advantage of this geometry is that the surface area to volume ratio is much higher than that of a "monolithic" design. The increased surface contact with the helium coolant provides improved stability with respect to perturbations in temperature. This and other advantages of CICC's for large scale applications are discussed in Hoenig [10].

The multiple strands of a CICC introduce new concerns for magnet applications. Unless completely insulated, the strands are in electrical contact with their neighbors and there are paths for currents to flow from strand to strand. If the strands are not twisted, induced loop voltages will be proportional to the field rate of change and to the dimensions of the cable (Faraday's Law). Since cables can be very long, significant induced voltages can occur even for small-diameter cables in slowly changing fields. These voltages will drive eddy currents which travel along the length of one superconducting strand and return down the length of a neighboring strand. The only resistance encountered is at the contact points where the current traverses strands. If this resistance is low, notable eddy currents can exist and the resulting Joule heating will significantly contribute to the AC losses in the cable. This loss must be compensated by additional cooling to maintain the conductor below the critical temperature [12].

AC loss is a particular concern for AC magnets, but is also of interest for DC magnets which must be brought from zero magnetic field to their operating magnetic field in a reasonable amount of time. Fortunately, twisting the strands together effectively reduces the magnetic coupling between strands, putting a handle on AC loss. Twisted strands in a changing external magnetic field experience an electric field which changes direction every half twist pitch length. The maximum induced voltages will thus be proportional to the twist pitch length rather than the length of the cable [12].

Another way to reduce the coupling between strands is to decrease the conductivity between them. The optimum choice of electrical conductivity between the strands balances the requirement of low AC loss (low conductivity) and adequate stability (high conductivity–to ease current transfer around local normal zones) [12]. For magnets that are designed to be ramped or cycled in time, AC loss is a primary concern and highly resistive oxide coatings are often used. Completely insulating the strands from each other is an option, but experience has shown that the performance of such magnets can be "surprisingly low" [14].

Although a simple twisting of all the strands, as diagrammed in Fig. 1-3, reduces eddy currents due to transverse magnetic fields, it does not help to reduce self-field effects. The self-field is the magnetic field of a wire generated by the transport current flowing through it. The self-field effect in multi-strand cables is similar to the "skin-effect" in homogeneous conductors–a diffusion process in which any change in current distribution begins at the surface and diffuses inward at a rate inversely proportional to the conductivity [15]. By analogy, any change in the current distribution in a simply twisted cable will first be felt by strands on the outside before diffusing inward. The superconducting nature of the strands would severely limit the rate at which the currents diffused. The resulting current imbalance would significantly reduce the overall performance of the cable.

A "fully transposed" cable, however, is one which eliminates the self-field effect by ensuring that no net self-field flux exists between the strands [12]. This is equivalent to saying that the self-inductance of every strand is the same and that the mutual-inductances between strands exactly balance. This can be achieved by a cabling pattern in which the strands traverse the cable cross-section in such a way that each spends an equal amount of time at each position in the cable space—i.e., the strands spiral radially inward then outward along the length of the cable.

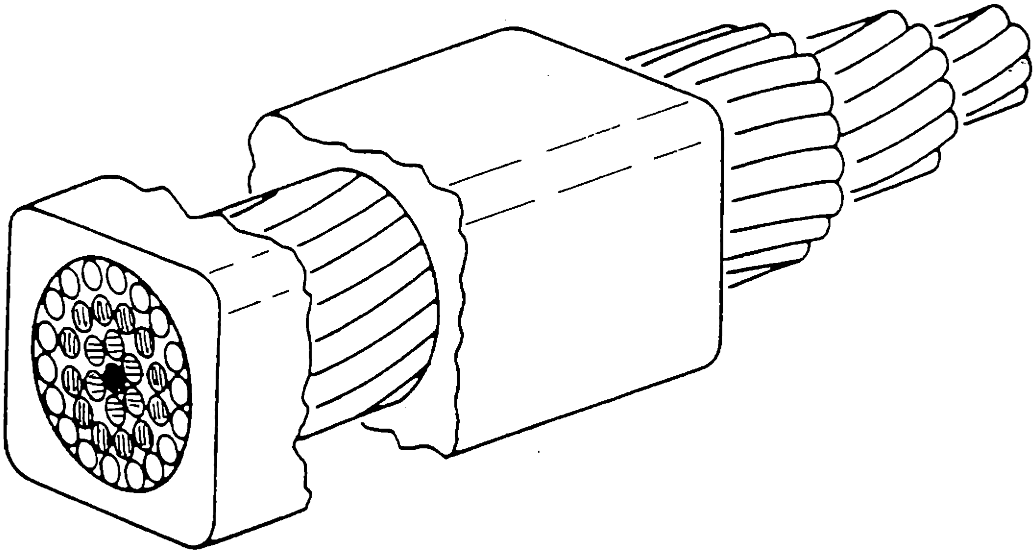

Figure 1-3: Sketch of a "simply twisted" cable. Strands on the outside remain on the outside over the length of the cable. Strands near the center stay near the center [16].

One such cabling pattern which achieves a fully transposed geometry is a derivative of the Litz wires often used for radio frequency work [12]. It begins by twisting a small number of wires into a "rope" with a tight twist pitch. Then several small ropes are twisted together with a somewhat looser twist pitch into a bundle. The process continues, twisting bundles into larger cables with looser twist pitches. An example of a cable made of five ropes of four strands each is shown in Fig. 1-4. The Cable-in-Conduit Conductors discussed later in this thesis are similarly comprised of multiply-twisted strands.

1.2.3 Ramp-Rate Limitation

To demonstrate the ability of CICC magnets to operate at the conditions required for a fusion device, the United States Demonstration Poloidal Coil (US-DPC) was designed and built by MIT and industrial partners. Tested in Japan in late 1990, the magnet performed well in DC tests but exhibited an unexpected ramp-rate limitation when ramped at high rate to high currents and fields. Figure 1-5 shows the measured

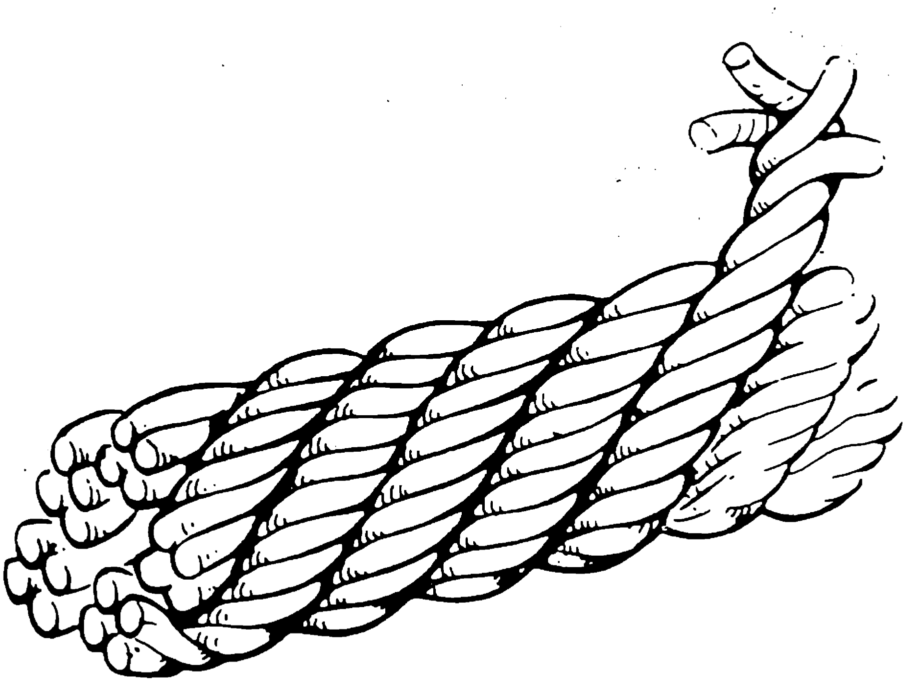

Figure 1-4: Sketch of a "fully transposed" cable in the form of a multiply twisted "rope." *Source: reprinted with permission from Wilson,* Superconducting Magnets, *Copyright ©1983 by Oxford University Press.*

limit for linear current ramping as a plot of maximum attainable current versus the ramp time taken to reach that current. It is evident from the figure that the design current of $\sim$ 30 kA could only be reached at slow ramp rates (i.e., longer ramp times) despite the fact it was designed to ramp to full current in approximately one second [1].

The results of the US-DPC experiment were extensively studied using the traditional stability analyses referred to in Section 1.2.1. As mentioned above, these analyses study the stability of a conductor to disturbances in temperature by determining if the cooling (heat transfer to helium) is enough to bring the conductor back down to its operating temperature after any foreseeable perturbation in temperature. Such perturbations would be caused by energy deposited in the strands from such causes as AC losses, nuclear heating, or frictional heating associated with wire motion. For this reason the measure of stability of a cable is often given as a "stability margin"—the volumetric energy perturbation which would marginally lead

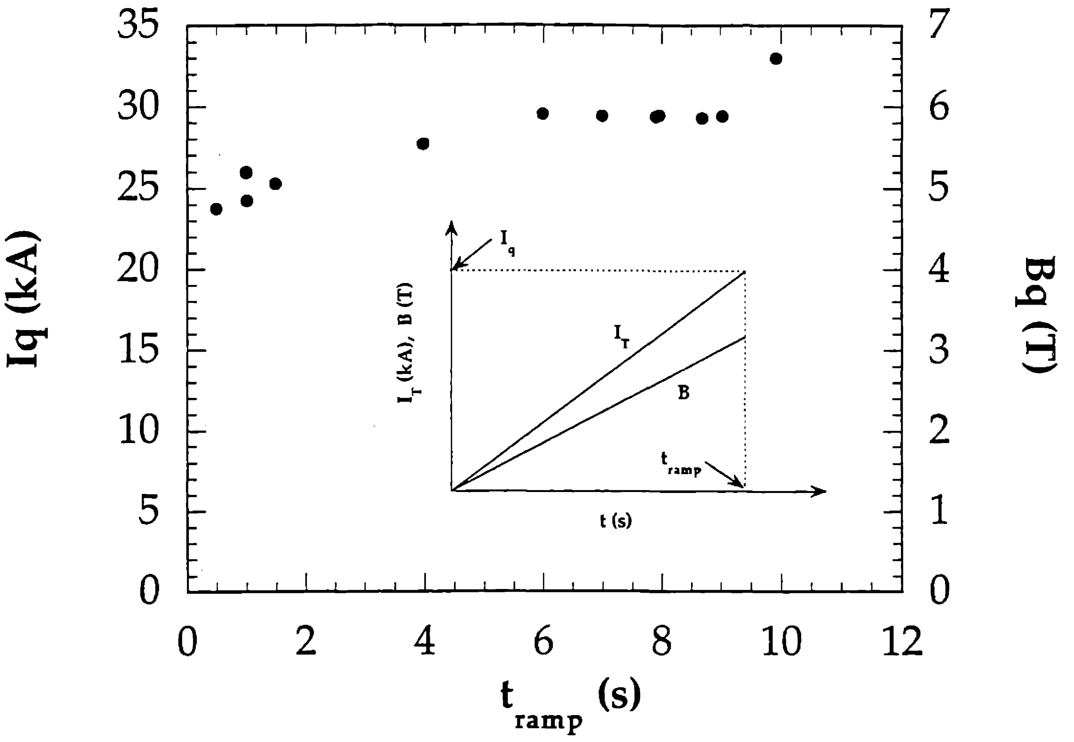

Figure 1-5: Quench current vs. ramp time for the US-DPC experiment. The time evolution of the transport current and magnetic field are also shown (inset). The degraded performance at faster ramp times is known as the "Ramp-Rate Limitation." [1]

to a non-recovering quench, typically measured in mJ/cc of wire [17].

In studies of the US-DPC coil, however, the stability margin was found to be on the order of 100 mJ/cc for operating scenarios at which premature quench was experienced [18]. This amount of energy is much larger than any foreseen energy deposition in the system, leaving the source of ramp-rate limitation a mystery [1].

What the traditional stability analyses fail to consider, however, is the possibility of non-uniform current distribution within the cable. The remainder of this thesis is devoted to modeling the current distribution to be expected in CICC cables and assessing the effects of this distribution on the stability of the magnet. By the end of the thesis, we reach the conclusion that non-uniform current distribution indeed accounts for the performance limitations encountered in the US-DPC as well as numerous follow-up experiments.

Chapter 2

Current Distribution in CICC

Cable-in-Conduit Conductors (CICC) have been used in numerous devices since they were first introduced in the mid-1970's [10]. Accordingly, the literature contains many reports of both experimental and theoretical studies of the performance of CICC's in varying conditions. Until recently, however, nearly all of these studies were predicated on the assumption that the current distribution among the cabled strands was nearly uniform. While this assumption is valid in many cases and leads to numerous useful results, its validity breaks down in the presence of pronounced transient fields.

This preliminary chapter offers a broad overview of the different sources of current distribution in CICC and defines certain concepts which will be used in later chapters. Unfortunately, the few researchers who have focused on non-uniform current distribution ([4, 7, 8, 9, 19], for example) have not yet reached a consensus on terminology. The terms chosen for this thesis are for the most part consistent with the literature but are defined below for further clarity.

The overall current distribution is a combination of the directly applied (transport) current and the induced currents. While it is convenient to distinguish between the different sources of current flow within a CICC, it must be remembered that the total current at a certain location is a superposition of the individual components.

2.1 Current Distribution within Composite Superconductors

In isolation, a single strand of composite superconductor looks like a complete cable unto itself. The strands are composed of tens to hundreds of superconducting filaments imbedded in a metallic matrix (usually copper). Although the filaments are not transposed, they are twisted in a helical manner to minimize the effects of transverse fields. The electrodynamic behavior of single strands in changing magnetic fields has occupied researchers since the fabrication technique was invented and still attracts as much or more attention than the study of CICC's or other cabled conductors. At this point, though, the physics of single strands is fairly well understood and several comprehensive references are available [12, 20, 21].

For the purposes of studying current distribution in cables, however, the individual strands can be treated in a macroscopic sense [22]. In other words, details of current distribution within each strand are not necessary.

2.2 Distribution of Transport Current

The transport current is defined as the net current passing through the cable and is generated by the magnet power supply. The cable is connected to the power supply through a low resitance joint at either end. Joint design is a topic within itself and much research is currently being done to optimize joints for cables in pulsed or ramping fields [23]. One goal of joint design is to insure each strand in the CICC is connected through the same resistance to the power supply leads. Such a joint would produce, in steady-state, a uniform transport current distribution throughout the cable.

For the purposes of this thesis, it is in fact assumed that the effects of unequal strand-to-joint resistances are minimal. Thus, the current distribution due solely to the transport current is considered uniform for each strand. As previously mentioned, though, the *overall* current distribution is *not* uniform because of the induced currents which will be discussed next.

2.3 Induced Currents

Transient magnetic fields cause induced current loops within CICC cables even though the strands are twisted to minimize such effects. In this thesis, the induced current is divided into two components: interstrand coupling currents and circulating currents. The interstrand coupling currents are the more familiar of the two but it is the circulating currents which are of primary interest in this thesis.

2.3.1 Interstrand Coupling Currents

Coupling currents are well-known to anyone who is familiar with composite superconductors. Just as transverse fields induce coupling currents in a single strand of a composite superconductor, they also induce interstrand coupling currents in a large cable of twisted strands.

The primary effect of these unwanted induced currents has long been known as "A.C. Loss," the Joule heating associated with eddy currents induced by changing transverse magnetic fields. This effect has been extensively studied for composite strands [20, 21] and cables [24] and can largely be understood without regard to how the cable is terminated.

As mentioned in Section 1.2.2, the characteristic length of the interstrand coupling currents is the twist-pitch length of the cable which determines the distance over which the coupling currents reverse direction. The maximum interstrand coupling current density in a strand is generally several orders of magnitude less than the transport current density and thus they do not noticeably contribute to imbalances in the overall current density of the cable. Section 4.2 goes into further detail about how interstrand coupling currents are nonetheless important in determining the boundary conditions which influence the circulating currents, which are discussed next.

2.3.2 Circulating Currents

Like interstrand coupling currents, circulating currents are induced by changes in the magnetic field. Circulating currents, however, have a characteristic length much longer than the longest twist-pitch length and can appreciably alter the overalll distribution of current density in the cable. In fusion magnets, circulating currents are mainly a result of the low resistance joints through which the cables are connected to the power supply. These low resistance paths can locally "undo" much of the benefit of subdividing the superconductor into twisted strands. In abstract terms, circulating currents can be thought of as the component of the total *induced* current distribution which passes through one or both joints.

In mathematical terms, circulating currents are driven by the end "boundary conditions." Depending on the properties of the cable, they can be isolated near the ends of the cable or they can join to form a "loop" current which changes the current distribution over the whole length of the cable. The concept of circulating currents is developed much more rigorously in Chapter 4.

2.4 Current Redistribution during Quench

The individual aspects of current distribution discussed so far—transport current, interstrand coupling current, circulating current—all presume the cable is operating in the superconducting state, as defined in Section 1.2.1. When all or a portion of the cable enters the normal state, the current distribution can change quickly and dramatically. For normal regions which occupy only a portion of the cable cross-section, current transfers from over-saturated strands to strands which are still superconducting. If the entire cross-section quenches over a long enough length, the higher resistance of each strand damps out the induced current effects described above and the current distribution becomes almost uniform.

In general, the redistribution of current due to quenching of the cable is non-linear in nature and requires a coupled solution of the time-dependent thermodynamic and electromagnetic behavior of the cable. This aspect of the stability analysis is dealt with in Chapter 5.

2.5 Summary

The overall distribution of current in a CICC is influenced by three distinct components: the transport current, the interstrand coupling current, and the circulating current. Of these three, the last is in many ways the least understood—it is certainly the least studied.

Circulating currents are induced by changes in the magnetic field but behave much differently than the eddy currents traditionally considered in AC loss analyses. In some situations, the uneven distribution of current caused by circulating currents can be appreciable and should be of concern to magnet designers. The remainder of this thesis is devoted to explaining these circulating currents and their effect on the stability of CICC magnets.

Chapter 3

The Two-Strand Model

This chapter focuses on the development of a two-strand model of current distribution in cables exposed to ramping magnetic fields. At first appearance, the model seems rather simple but the results derived from the two-strand example exhibit surprisingly complicated behavior. In later chapters, the model presented here will be shown to self-consistently explain much of the "anomalous" behavior witnessed in cables exposed to ramping magnetic fields.

This chapter begins with a discussion of the relative merits of the two-strand model over the more ambitious approach of solving the problem for an actual cable geometry. Next, a physical description of the two-strand cable is given and key attributes of the cable are identified. The cable is then analyzed on a differential scale from which the electromagnetic diffusion equations at the crux of the model are developed.

Although the temperature-dependent resistive elements in the model are included for completeness sake, the coupling of the circuit equations with the heat equations will not be presented until Chapter 5. The auxiliary equations needed to describe the strand resistance and the behavior of the critical current density are presented in that chapter, as well.

3.1 Simple vs. More Complicated Cables

The current distribution in a cable-in-conduit superconductor is difficult to analyze due to the complicated twisting geometry of the strands. For the purposes of analyzing stability and studying ramp-rate limitation, however, it is instructive to simplify the cable geometry as much as possible while still retaining the important physics of the problem. For this reason, it was decided to develop the foundation of the analysis using a two-strand model. This decision seems especially justified since the two-strand results developed in this thesis are already significantly more elaborate than those of previous studies [17, 25, 13]. The complexities of a fully-transposed multi-strand cable are best left for the next "iteration," should more detail be deemed necessary.

The advantages of first studying a two-strand model are strong ones. Most important, the mathematics of the two-strand model are relatively straight forward and do not cloud the underlying physics. In studying a full-sized CICC, it is necessary to use a continuum model and very sophisticated numerical techniques. Actually, in many circumstances, it is not even clear if such techniques exist. After studying the problem extensively, this author concluded that even if a solution were to be found, it would not be the best way to convey the important results which can be demonstrated with the simpler two-strand model.

The two-strand model offers a physically intuitive way to understand the sources of current distribution in superconducting cables. Although the model does not account for the full geometrical complexity of a full-scale cable, the results nonetheless shed light on many previously unappreciated aspects of current distribution and stability. Since the model can be studied analytically, it is possible to develop important figures-of-merit and scaling laws which can be used to classify the behavior of differing cable designs.

It is important to point out that the two-strand model is self-consistent; it does not rely on unknown or outside heat sources to initiate the quench and determine the stability of the cable. The only source of instability is the current re-distribution which is caused by a ramping magnetic field. If one were to actually construct a two-strand cable, the analysis presented in this thesis would accurately predict its behavior. The extension of the analysis to multi-strand cables is the subject of Chapter 7.

3.2 Two Strand Model Geometry and Properties

Before discussing the details of the two-strand model, it is necessary to give a brief physical description of the model in order to put the problem into context. The cables being considered in this thesis are typically wound into solenoidal coils. Rather than explicitly retaining the winding shape, however, the coil is considered to be straight and parallel to the x-axis. The effects of the winding are included through the spatial dependence of the magnetic field, (see Section 3.3.4).

The geometry of the two-strand model is diagrammed in Fig. 3-1. The individual elements of the model will be discussed thoroughly in the next section but the diagram and following description offer an overview. The two strands are twisted together in a double helix with characteristic twist-pitch length, ℓ_p, and distance between centers, w. In the figure, the strands are drawn as one-dimensional "filaments" even though they actually have a strand diameter, d. The total length of the cable is ℓ and the two strands are connected to the power supply at either end through low resistance joints with transverse resistance, $\Re_J$. The cable experiences a transverse magnetic field density, $B_\perp(x,t)$, that is in general a function of space and time. Along the length of the cable, the transverse electrical conductance-per-unit-length is $\sigma_\perp$. The value of $\sigma_\perp$ represents the conductivity of the medium which separates the two strands. This medium could be vacuum, for instance, or the other strands of a full cable, which we can treat as a medium with known properties.

To give an idea of the physical scale of the problem, the cables considered in this thesis will vary in length from $\ell=$ 1 to 100 m; the typical twist-pitch length will be of the order $\ell_p \sim$ 10 to 50 cm; and the cable width will vary from $w \sim \frac{1}{2}$to 5 cm. Further details of the electrical parameters are introduced in the next section. The details of the heat transfer parameters (not mentioned here) are left for Chapter 6.

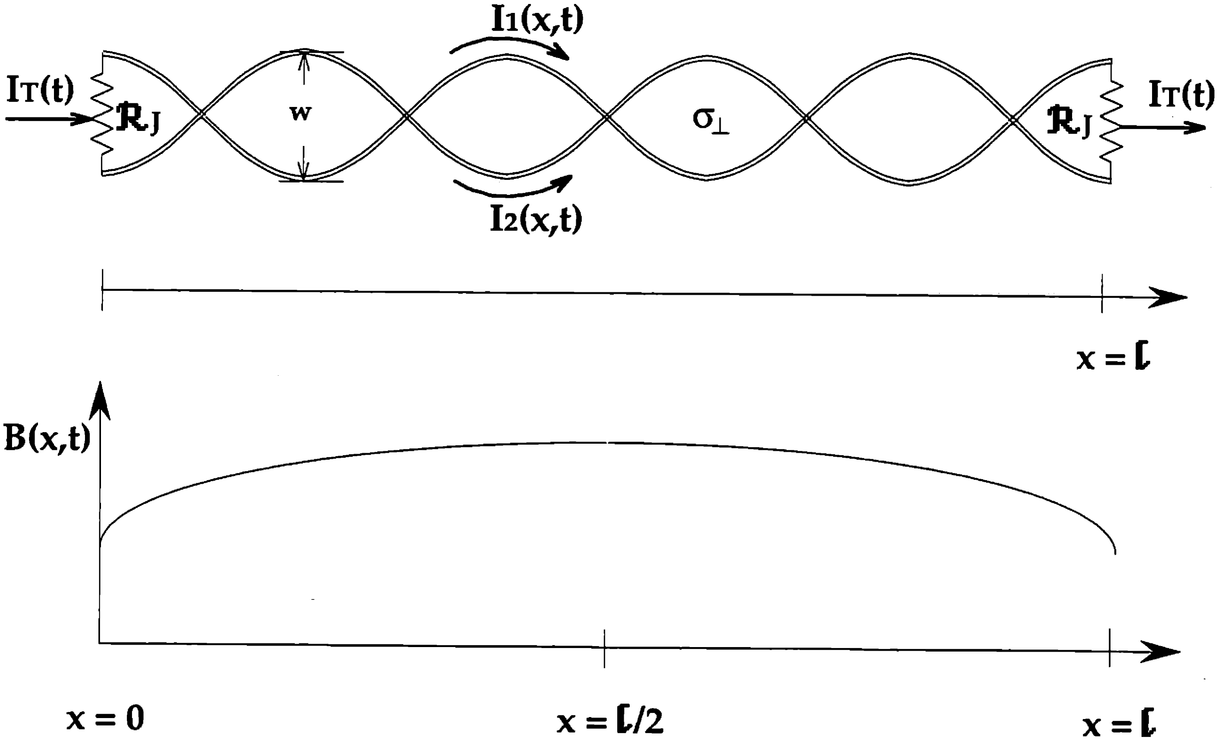

Figure 3-1: The two-strand model geometry. The two strands form a double-helix with a constant width w. Also shown is an example of the magnetic field profile, $B(x, t)$.

3.3 Notation and Parameters

At this point, we need to introduce the parameters and notation which will be used throughout the thesis. In later chapters, new notation will be defined as needed, but the definitions given here will hold true "globally."

3.3.1 Currents

The most important quantity in any discussion of current distribution is of course: current. As was discussed in Chapter 2, the total current in the cable can be thought to consist of several components. For the ease of mathematics and the ease of presentation, it will be useful to define separate notation for each component.

In general, the symbol I will be used to represent current in units of Amps. Since it is necessary to differentiate between the currents in each strand, the subscripts 1 and 2 will represent the first and second strand, respectively. Strand *one* will be defined to be the strand with the greater current—i.e. $I_1 \geq I_2$.[1] Because the strands are not insulated over their length, I_1 and I_2 are functions of axial location, x, and time, t.

Critical Current

Besides the strand currents, the study of current distribution and stability also involves another "current"— the critical current, I_c. The critical current is not actually a physical current but rather a definition of a limiting value for the current in the strands: when $I_1 \leq I_c$, strand *one* is "superconducting," all current flows through the superconducting filaments; when $I_1 > I_c$, strand *one* is "resistive," some or all of the current flows through the resistive matrix surrounding the superconducting filaments. It is this transition between superconducting and resistive states which makes the current distribution problem interesting. The value of I_c is a function of the magnetic field, $\mathbf{B}$, and temperature, T, and thus acts as a coupling term linking

---

[1] This relation remains unambiguous as long as field reversals are not considered.

together the current and heat equations which comprise the two-strand model. The role of the critical current is discussed extensively in Chapter 5.

A simple model of the critical current which is appropriate for a single wire of type II superconductor was proposed by Kim [26]:

$$I_c(T_b, B) = \xi / B \tag{3.1}$$

where ξ is a property of the strand (units AT) appropriate for a fixed temperature, T_b. The effects of temperature can usually be well approximated with a linear dependence (truncated at zero) [12], giving:

$$I_c(B,T) = \begin{cases} \frac{\xi}{B}(1 - \frac{T-T_b}{T_c-T_b}) & T < T_c(B) \\ 0 & T \geq T_c(B) \end{cases} \tag{3.2}$$

where the critical temperature, T_c, is a function of the magnetic field:

$$T_c(B) = \begin{cases} T_b + (T_{c0} - T_b)(1 - \frac{B}{B_{c0}}) & B < B_{c0} \\ T_b & B \geq B_{c0} \end{cases} \tag{3.3}$$

and T_{c0} and B_{c0} are characteristic properties of the superconductor which usually need to be determined experimentally.

This modified Kim's model, Equation (3.2), will be used in Chapters 5 and 6 to characterize typical Nb_3Sn conductors which have been used in numerous experiments [4, 5]. The appropriate values for the superconductor properties in this instance are:

$$\begin{aligned} \xi &= 1250 \text{ AT} \\ T_{c0} &= 18 \text{ K} \\ B_{c0} &= 19 \text{ T} \end{aligned}$$

The results developed in future chapters can be easily generalized to other superconductors which obey the modified Kim's model as well as superconductors with altogether different critical current characteristics.

Transport Current

When both strands are superconducting, it is useful to make the distinction between the induced current component and the transport current component of each of the strand currents. The transport current, $I_T(t)$, is defined as the total net current flowing through the cable: $I_T \equiv I_1 + I_2$. It is a known quantity which does not vary over the length of the cable (due to current conservation) but can be time dependent. In a coil generating its own magnetic field, $I_T(t)$ is directly proportional to the peak magnetic field, $B(\mathrm{t})$. For cables inserted into background field coils, however, $I_T(t)$ is independent of the magnetic field and can be an arbitrary function of time. For instance, we will later study cases for which the transport current is constant, $I_T(t) = I_T$, while the background field is ramped.

For the purposes of this thesis, the total transport current in the cable will be evenly divided between the two strands.[2] For the sake of convenience, then, the notation $I_{T/2}$ is used to designate one-half the transport current, i.e. $I_{T/2}(t) = \frac{1}{2}I_T(t)$. Thus, in the absence of magnetic fields (and in the case $I_1 < I_c$), the current in each strand would be: $I_1(x,t) = I_2(x,t) = I_{T/2}(t)$.

Induced Currents

With the introduction of a ramping magnetic field, however, induced currents must now be considered as well as transport currents. The induced currents in strands *one* and *two* are labeled $I_{\mathrm{B1}}(x,t)$ and $I_{\mathrm{B2}}(x,t)$, respectively. Notice that unlike the transport current components, the induced currents are functions of x as well as t. The total current in each strand is the combination of the transport current and the induced current:

$$\begin{aligned} I_1(x,t) &= I_{T/2}(t) + I_{\mathrm{B1}}(x,t) \\ I_2(x,t) &= I_{T/2}(t) + I_{\mathrm{B2}}(x,t) \end{aligned}$$

---

[2] The model could easily accommodate the more general case with the transport current not divided evenly between the two strands, but the maldistribution of transport current is not the focus of this thesis.

where, again, we are now only discussing the $I < I_c$ scenario. Adding these two equations and noting that $I_{T/2} = \frac{1}{2}I_T(t)$ and $I_T \equiv I_1 + I_2$ (by definition) yields the expected but important result:

$$I_{\mathrm{B1}}(x,t) + I_{\mathrm{B2}}(x,t) = 0 \tag{3.4}$$

This conservation law implies that any x-dependence of the induced current I_{B1}must be matched by the opposite dependence in I_{B2}. In other words, the current "exiting" strand *one* at location x flows across the cable and "enters" strand *two* at the same x location. Mathematically, this is stated as:

$$\frac{\partial I_{\mathrm{B1}}(x,t)}{\partial x} = -\frac{\partial I_{\mathrm{B2}}(x,t)}{\partial x}$$

Transverse Current-per-Unit-Length

The quantity $\frac{\partial}{\partial x}I_{\mathrm{B1}}(x,t)$ has the units [A·m^{-1}] and is the transverse current-per-unit-length flowing between the strands at location x. Since the medium between the strands is resistive (see 3.3.3), this transverse current produces Joule heating. The study of such interstrand coupling losses has been treated by several authors interested in AC losses [24] but does not play an important role in the stability model being developed here.

In cases where I_1 is no longer less than I_c, the distinction between transport current and induced currents is no longer useful and the transverse current-per-unit-length then includes the quench redistribution current (see Section 2.4) as well as the induced currents. Thus, to develop the general case, the more general notation $\frac{\partial}{\partial x}I_1(x,t)$ will be used throughout the remainder of this chapter.

Shorthand Notation for Currents

Since I_1 and I_2 are easily related, $I_1 + I_2 = I_T$, we often focus only on I_1 and drop the subscript: $I \equiv I_1$. The transverse current-per-unit-length is also shortened to $\frac{\partial}{\partial x}I$. Likewise, in the $I_1 < I_c$ regime, it is often convenient to use the notation I_B

and $\frac{\partial}{\partial x}I_B$ to replace $I_{\mathrm{B}1}$ and $\frac{\partial}{\partial x}I_{\mathrm{B}1}$.

3.3.2 Inductances

For the purposes of calculating inductances, the cables are considered to be straight, parallel cylinders. The necessary condition for this approximation to be valid is: $w/\ell_p \ll 1$ where w is the distance between centers and ℓ_p is the twist-pitch length. This criterion is easily met for the cables being considered here.

The mutual inductance-per-unit-length of two parallel cylinders is given by: [27]

$$\mathcal{M} = 0.2\left[\ln\left(\frac{\ell}{w} + \sqrt{1 + \frac{\ell^2}{w^2}}\right) - \sqrt{1 + \frac{w^2}{\ell^2}} + \frac{w}{\ell}\right]$$

where ℓ is the length and $\mathcal{M}$ is in units of [μH$\cdot$m^{-1}]. In the limit under consideration, $w/\ell \ll 1$, this reduces to:

$$\mathcal{M} = 0.2\left[\ln\frac{2\ell}{w} - 1\right]$$

The self-inductance-per-unit-length for a straight cylinder is: [27]

$$\mathcal{L}_s = 0.2\left[\ln\frac{2\ell}{r} - \frac{3}{4}\right]$$

where r is the radius of the cylinder and $\mathcal{L}_s$ is in units of [μH$\cdot$m^{-1}]. The quantity of interest for the model turns out to be the "effective" inductance, $\mathcal{L} = \mathcal{L}_s - \mathcal{M}$. From the above two relations we find:

$$\mathcal{L} = 0.2\left(\frac{1}{4} + \ln\frac{w}{r}\right)$$

This is the relation which will be used throughout the rest of the thesis.

3.3.3 Resistances

There are three "flavors" of resistance in the model: transverse joint resistance, transverse cable resistance, and strand resistance. Each plays a very distinct role in the behavior of a cable experiencing a ramping magnetic field.

Strand Resistance

The strand resistances, $\mathcal{R}_1$ and $\mathcal{R}_2$, are actually resistances-per-unit-length (Ω/m):

$$\mathcal{R} = \frac{\eta}{A_w}$$

where η is the resistivity and A_w is the cross-sectional area of the wire. Since the wires are composites of superconducting filaments within a conductive matrix, the value of η is a volume-weighted average of two resistive paths in parallel:

$$\eta = \left(\frac{\lambda}{\eta_{sc}} + \frac{(1-\lambda)}{\eta_m}\right)^{-1}$$

where λ is the volume fraction of superconductor in the wire, η_m is the resistivity of the matrix material, and η_{sc} is the resistivity of the superconductor.

The value of η_{sc} changes dramatically depending on whether the strand current is above or below the critical current:

$$\begin{aligned}
\eta_{sc} &\ll \eta_m \; ; 0 < I < I_c \\
\eta_{sc} &= \eta_{ff}; \; 0 < I_c < I \\
\eta_{sc} &\gg \eta_m \; ; 0 = I_c < I
\end{aligned}$$

where η_{ff} is the "flux flow resistivity" which will be discussed in Section 5.2.1. Thus, in general, η is a non-linear function: when I is less than I_c the strand is superconducting and $\eta = \eta_{sc}/\lambda$. When I is greater than I_c, η begins to increase dramatically, reaching the value $\eta = \eta_m/(1-\lambda)$ in the limit $I \gg I_c$.

In the first case, $I < I_c$, the value of the resistivity, η_{sc}, is known as the "dynamic resistivity"—the resistivity of a superconducting material experiencing a time-varying magnetic field [20, 21]. For typical cases considered here, $\eta_{sc} \sim 10^{-15}$–10^{-14} Ωm[24]. This translates into: $\mathcal{R}_{sc} \sim 10^{-9}$–$10^{-8}$ Ω/mfor typical strand dimensions.

Typical values for η_m are $\eta_m \sim 10^{-10}$–10^{-9} Ωm, resulting in $\mathcal{R}_m \sim 10^{-4}$–$10^{-3}$ Ω/m. Since the case for $I > I_c$ is not considered until Chapter 5, for now, $\mathcal{R}_1$ and $\mathcal{R}_2$ can be considered arbitrary functions of I and I_c.

Joint Resistance

As diagrammed in Fig. 3-1, the two strand cable is terminated at either end in a joint connecting the cable to the power supply. Although the joints have finite length, ℓ_T (where T stands for "termination"), the transverse joint resistance is treated as a concentrated resistance, $\Re_J$, in the initial presentation of the model. The effects of the finite length joint are discussed in Chapter 7. The distinctive typeface for $\Re_J$ was chosen to distinguish the concentrated joint resistance with units [Ω] from the strand resistance-per-unit-length, $\mathcal{R}$ (Ω/m). Although it is not required by the model, both joints are assumed to have the same resistance for the purpose of this presentation.

The model of the joint as a concentrated resistance is shown in Fig. 3-2. The transport current, I_T, enters the joint and is split between the two strands according to the relative resistances $\Re_J^{\uparrow}$ and $\Re_J^{\downarrow}$, as indicated in the figure. As mentioned in Section 3.3.1, the joint is designed in such a way that the transport current carried by each strand is considered to be equal—thus $\Re_J^{\uparrow} = \Re_J^{\downarrow}$. The overall transverse joint resistance is defined as $\Re_J \equiv \Re_J^{\uparrow} + \Re_J^{\downarrow}$. Fig. 3-2 will be referred to again when the boundary conditions are discussed. At that time, the transverse voltage across the joint, $\mathcal{V}_J$, as defined in the picture, will be used.

The value of $\Re_J$ will be one of the key parameters defining the current distribution behavior of the cable. It is important to note that the transverse joint resistance (referred to from here on simply as "joint resistance") is much larger than the characteristic joint resistance typically measured and reported experimentally. The difference arises from the different paths through the joint followed by the induced currents as opposed to the transport current. A discussion of this distinction is given in Chapter 7. Since joints can be made in a variety of ways, the typical resistances can vary greatly and thus a large range of values, $\Re_J = 10^{-8}$–10^{-6} Ω, is considered in the results to be presented.

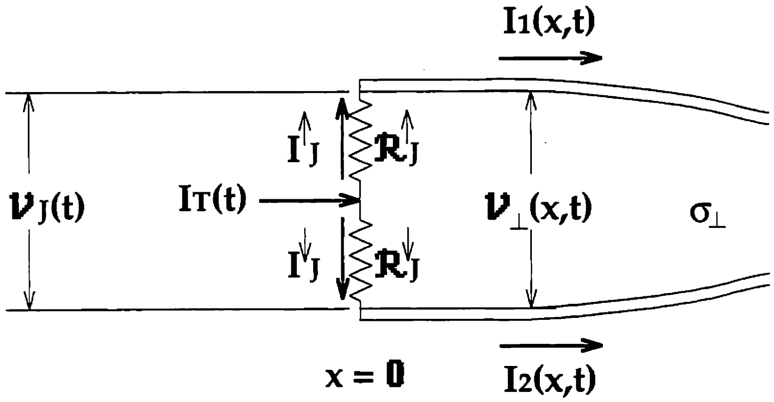

Figure 3-2: Idealized model of cable termination. Each Joint is treated as a "lumped parameter" resistance, $\Re_J \equiv \Re_J^{\uparrow} + \Re_J^{\downarrow}$.

Transverse Conductivity

The transverse cable resistance (referred to from here on as "transverse resistivity") can also cover a large range of values, depending on cable design. The transverse resistance is not necessarily a material property since it can be strongly affected by the cable manufacturing process. The surface condition of the strands also plays an important role since the transverse resistance is dominated by contact resistance between the strands. Also, strands are often deliberately coated with oxide layers to further reduce the transverse resistance.

Since the transverse resistance is distributed over the length of the cable, it is easier to define in terms of its inverse, $\sigma_\perp$, the transverse conductance-per-unit-length. In the two-strand model, $\sigma_\perp$ is equivalent to the local conductance-per-unit-length ($\Omega^{-1}\text{m}^{-1}$) between the two strands.

Although, in principal, $\sigma_\perp$ could vary over length, it is considered to be a uniform property in this model. This simplification can be justified by noting that the current profiles of interest have length scales much longer than the twist-pitch length, the scale over which $\sigma_\perp$would tend to vary. While the spatial distribution of $\sigma_\perp$could be very important in AC loss calculations which focus on fine-scale current distributions, a uniform $\sigma_\perp$ is the appropriate limit for the problem being considered here.

The value of $\sigma_\perp$ is notoriously difficult to estimate. Similar cables measured in different ways can lead to results which vary by orders of magnitude [14, 28, 29]. For this reason, $\sigma_\perp$ is left as an unspecified parameter in the model. Nonetheless, it is one of the most important parameters in the model as its value will figure into all of the scaling relations developed in the next two chapters. To give an idea of the range over which $\sigma_\perp$ can vary, values ranging from 10–1000 $\Omega^{-1}\mathrm{m}^{-1}$are considered in this thesis.

3.3.4 The Magnetic Field

The magnetic fields considered in this model are generated by solenoidal magnets. The field experienced by the cable is either the self-field of the coiled cable (for larger windings) or the solenoidal field produced by a background field magnet (for smaller windings). Of course, combinations of the two are possible. In any case, the field at a given point along the cable is a known function of the operating conditions. This specification of the field as a function of space and time, $\mathbf{B}(x,t)$, is what allows us to "unwind" the magnet into a straight length. For small scale coils placed inside larger magnets, the field can often be considered spatially uniform, i.e. $\mathbf{B}(x,t) = \mathbf{B}(t)$.

Because of the symmetry of the double-helix cable winding, there are only two principle directions in the cable: axial and transverse. It is the transverse component, $\mathbf{B}_\perp$, of the magnetic field which produces the flux linkages which drive the induced currents studied in this thesis. Furthermore, because of the symmetrical geometry of solenoidal coils, the magnetic field is everywhere orthogonal to the axis of the cable and thus the magnitude of the transverse component, $B_\perp$, is equal to the total magnitude of the field:

$$B_\perp(x,t) = |\mathbf{B}(x,t)|$$

The cable is twisted, of course, to minimize the effects of changes in the transverse field. As can be seen in the Fig. 3-1, the twisting effectively reduces the net flux linked by the cable since the induced voltages on strand *one* change sign at every multiple of the twist-pitch length. But as discussed in Chapter 2, no cable is perfectly twisted and, as we shall see, even a seemingly minor net flux linkage can cause large induced currents.

Although the model can handle magnetic fields with arbitrary time-dependencies, only cases $B_\perp(x,t) = \dot{B}_\perp(x)t$ will be considered in order to simplify the analysis. Since the linearly ramped magnetic field is of primary practical importance and there is ample experimental data for this case, this is not a severe limitation. The numerical solutions of Chapters 5 and 6 could easily be extended to handle the more general case, but doing so does not add much insight into the problem.

In cases where the field is a function of x, the model requires that the axial gradients of $B_\perp$ are more gradual than the twist-pitch of the cable:

$$\frac{1}{B_\perp}\frac{\partial B_\perp}{\partial x} \ll \frac{1}{\ell_p} \tag{3.5}$$

This condition will be valid when the cable rests within an external field or when the inner circumference of the solenoid is longer than the twist-pitch length of the cable, ℓ_p. The importance of this condition will become apparent in Chapter 4.

It should be noted that the magnitude of $B_\perp$ is always much greater than the correction term, $\tilde{\mathbf{B}}$, generated by the self-field of the induced currents in the cable. Thus the statement in the first paragraph of this section, "$B_\perp$(x,t) is a known function" is true for all cases. This can most easily be verified when the actual induced currents are calculated in Chapter 4.

3.4 Derivation of the Two-Strand Model Equation

Now that the important parameters have been introduced, we will start to develop the model equations. The first step will be to transform the magnetic field in such a way that the strands can be considered "untwisted." This straight-forward transformation simplifies the description of the problem and helps in the derivation of the equations.

The "untwisted" cable is then analyzed on a differential length scale to determine the differential equations which govern the current distribution in the cable. Special care is taken to derive the proper boundary conditions at each joint. Using Faraday's

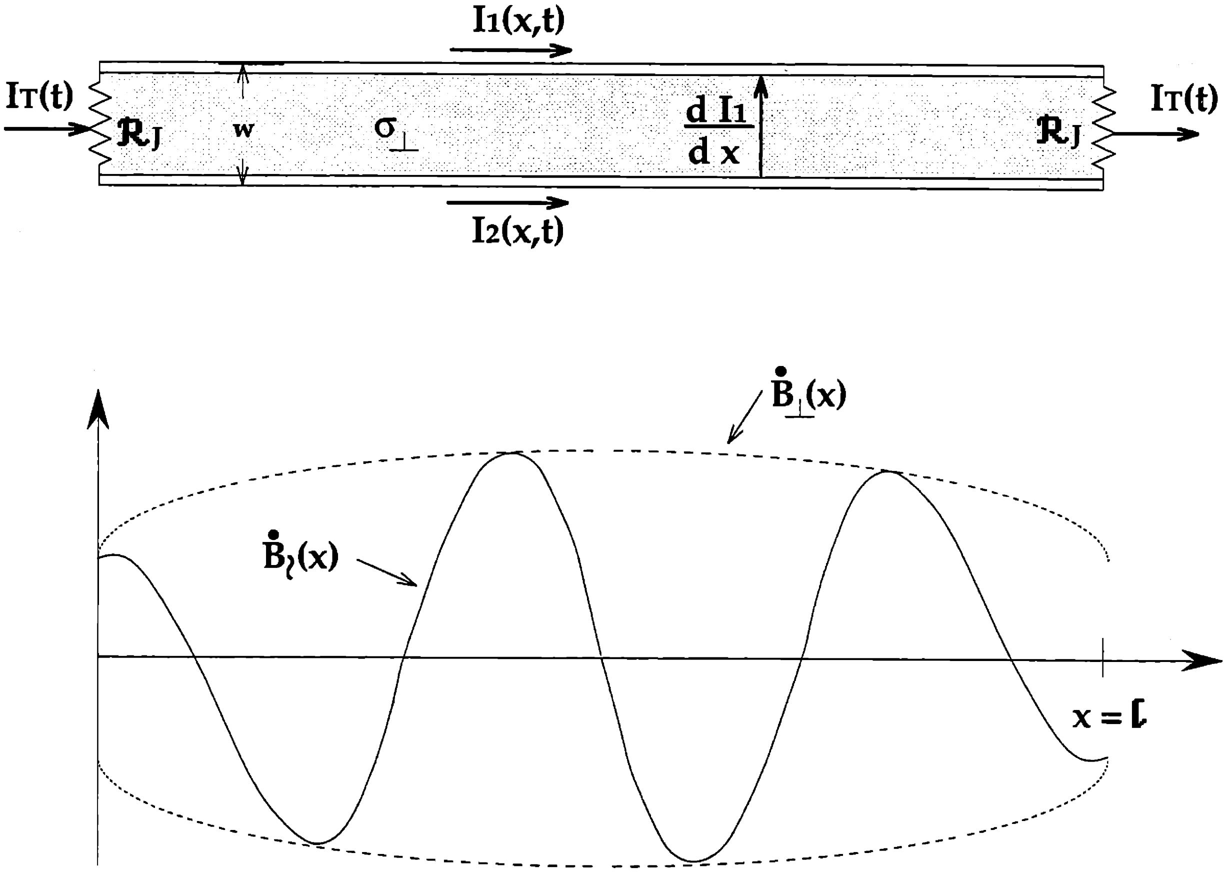

Figure 3-3: The "untwisted" two-strand model geometry and the corresponding transformation of the magnetic field.

law and its associated continuity conditions at the boundaries ($x = 0, \ell$), we show that the initial differential equations are reduced to the desired theoretical model.

3.4.1 The Untwisting Transformation

Rather than dealing with the twisted geometry of the double-helix, it proves convenient to study the problem from the reference frame of the two strands. The distance between the two strands, w, is constant over the length of the cable and thus there is a reference frame in which the two strands form a rectangular region, as diagrammed in Fig. 3-3. In order to make this geometric transformation, however, the magnetic field must be transformed as well.

It is easy to see from the physical geometry, Fig. 3-1, that the small amount of magnetic flux, $d\Phi$, enclosed by the two strands over an infinitesimal length, dx, is:

$$d\Phi = B_\perp(x,t)w \cdot dx \cos\left(\frac{2\pi x}{\ell_p} + \theta\right)$$

where θ is an arbitrary offset angle (i.e., the flux is not necessarily at an extremum at $x = 0$). The $\cos\left(\frac{2\pi x}{\ell_p} + \theta\right)$ term enters due to the twisting of the strands. In the untwisted reference frame, a similar calculation produces the result:

$$d\Phi = B_\wr(x,t)w \cdot dx$$

where $B_\wr$ is the transformed magnetic field. Since the true Φ is independent of the reference frame, the necessary transformation is obviously:

$$B_\wr(x,t) \mapsto B_\perp(x,t)\cos\left(\frac{2\pi x}{\ell_p} + \theta\right) \tag{3.6}$$

By "untwisting" the strands, we have in effect "twisted" the magnetic field.

Since none of the other parameters are affected by this change in reference frames, we are now prepared to derive the final model. As will be evident in the next section, the untwisting of the cable makes the problem much easier to conceptualize.

3.4.2 The Two-Strand Model Differential Equation

Using the untwisted geometry, the next step is to look at the model on the differential level. Fig. 3-4 shows a schematic of the two strands over an infinitesimal length, dx, centered at an arbitrary location $0 < x < \ell$. The goal is to use the integral form of Faraday's law over a closed path and find the limit as $dx \to 0$. The chosen path of integration is shown in Fig. 3-5.

$$\oint_C \mathbf{E} \cdot d\mathbf{s} = -\frac{d}{dt}\int_S \mathbf{B} \cdot d\mathbf{a} \tag{3.7}$$

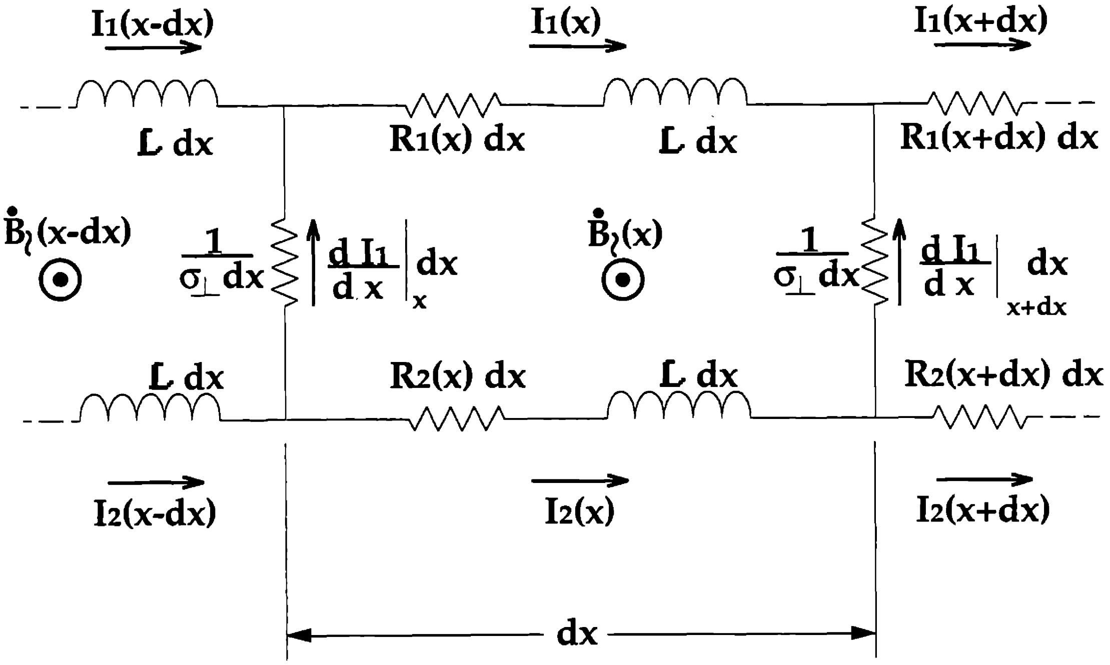

Figure 3-4: Schematic of differential section of the two-strand model geometry

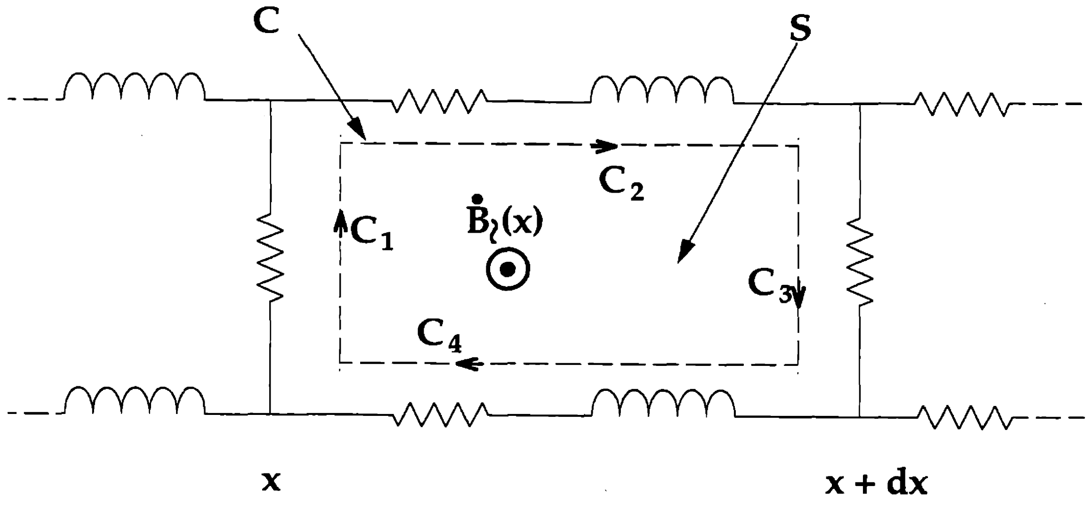

Figure 3-5: Path of integration used to develop two-strand model equation from differential model.

The rectangular path of integration, C, starts at location x on strand *two*, crosses the cable along C_1, follows strand *one* from x to $x + dx$ along C_2, re-crosses the cable along C_3, and then follows strand *two* from $x + dx$ to x along C_4. As drawn, the direction of the unit vector, $d\mathbf{a}$, (which is normal to the surface S bounded by C) is into the page.

The voltages along the first and third legs of the path, C_1 and C_3, are related to the transverse current-per-unit-length between the strands, $\frac{\partial}{\partial x}I$, at locations x and $x+dx$, respectively. Since the transverse conductivity-per-unit-length is uniform, the partial path integrals are simply:

$$\int_{C_1} \mathbf{E} \cdot d\mathbf{s} = \frac{1}{\sigma_\perp} \frac{\partial I_1}{\partial x}\bigg|_x \tag{3.8}$$

$$\int_{C_3} \mathbf{E} \cdot d\mathbf{s} = -\frac{1}{\sigma_\perp} \frac{\partial I_1}{\partial x}\bigg|_{x+dx} \tag{3.9}$$

where $\frac{1}{\sigma_\perp}\frac{\partial}{\partial x}I_1(x)$ is the transverse voltage from strand *two* to strand *one* at location x. (The path length of integration, w, is implicitly contained in the definition of $\sigma_\perp$.)

The voltages along the second and fourth legs of the path, C_2 and C_4, have resistive and inductive components. In Fig. 3-4, $\mathcal{L}$ represents the *effective* inductance-per-unit-length, as discussed in Section 3.3.2. The resistive elements, as mentioned above, are non-linear functions of strand current and temperature. The coefficients $\mathcal{R}_1$ and $\mathcal{R}_2$ are thus the only non-constant coefficients in the integral equation. The partial path integrals are:

$$\int_{C_2} \mathbf{E} \cdot d\mathbf{s} = \int_x^{x+dx} \left(\mathcal{L}\frac{\partial I_1}{\partial t} + \mathcal{R}_1 I_1\right) dx'$$

$$\int_{C_4} \mathbf{E} \cdot d\mathbf{s} = -\int_{x+dx}^{x} \left(\mathcal{L}\frac{\partial I_2}{\partial t} + \mathcal{R}_2 I_2\right) dx'$$

For sufficiently small dx, $I_1$and I_2 are approximately constant over the length $dx$and the integrals on the RHS reduce to:

$$\int_{C_2} \mathbf{E} \cdot d\mathbf{s} = dx \left(\mathcal{L}\frac{\partial I_1}{\partial t} + \mathcal{R}_1 I_1\right) \tag{3.10}$$

$$\int_{C_4} \mathbf{E} \cdot ds \;=\; -dx\left(\mathcal{L}\frac{\partial I_2}{\partial t} + \mathcal{R}_2 I_2\right) \tag{3.11}$$

The signs of the voltages are consistent with the chosen path of integration.

The complete closed path integral over C is the summation of the individual parts calculated in Eqs. (3.8)–(3.11):

$$\oint_C \mathbf{E}\cdot ds = dx\left(\mathcal{L}\frac{\partial I_1}{\partial t} + \mathcal{R}_1 I_1\right) - dx\left(\mathcal{L}\frac{\partial I_2}{\partial t} + \mathcal{R}_2 I_2\right) - \frac{1}{\sigma_\perp}\left(\left.\frac{\partial I_1}{\partial x}\right|_{x+dx} - \left.\frac{\partial I_1}{\partial x}\right|_{x}\right) \tag{3.12}$$

Using the definition of the transport current ($I_T \equiv I_1 + I_2$) and the shorthand notation introduced earlier (e.g. $I \equiv I_1$), Eq. (3.12) can be written as:

$$\oint_C \mathbf{E}\cdot ds = dx\left[-\frac{1}{\sigma_\perp}\left(\frac{\left.\frac{\partial I}{\partial x}\right|_{x+dx} - \left.\frac{\partial I}{\partial x}\right|_{x}}{dx}\right) + 2\mathcal{L}\frac{\partial I}{\partial t} + (\mathcal{R}_1 + \mathcal{R}_2)I - \left(\mathcal{L}\frac{\partial I_T}{\partial t} + \mathcal{R}_2 I_T\right)\right]$$

In the limit $dx \rightarrow 0$, the first term on the RHS reduces to a second derivative:

$$\lim_{dx\rightarrow 0}\oint_C \mathbf{E}\cdot ds = dx\left[-\frac{1}{\sigma_\perp}\frac{\partial^2 I}{\partial x^2} + 2\mathcal{L}\frac{\partial I}{\partial t} + (\mathcal{R}_1 + \mathcal{R}_2)I - \left(\mathcal{L}\frac{\partial I_T}{\partial t} + \mathcal{R}_2 I_T\right)\right] \tag{3.13}$$

The area integral on the RHS of Eq. (3.7) is relatively easy to calculate. In the untwisted reference frame the transformed magnetic field is $\mathbf{B} \mapsto B_\wr$ (see Eq. (3.6)). For sufficiently small dx, $B_\wr$ is constant over the area, S, and the area integral is thus given by:

$$\begin{aligned} -\frac{d}{dt}\int_S \mathbf{B}\cdot d\mathbf{a} &= -\frac{d}{dt}\int_S B_\wr \cdot d\mathbf{a} \\ &= -\frac{d}{dt}\left(-B_\wr w \cdot dx\right) \\ &= dx\left[\frac{\partial B_\perp(x,t)}{\partial t} w \cos\left(\frac{2\pi x}{\ell_p} + \theta\right)\right] \end{aligned} \tag{3.14}$$

where the signs are in accordance with $d\mathbf{a}$pointing into the page and the direction of $B_\wr$ chosen to be out of the page, as drawn in Fig. 3-5.

Combining Eqs. (3.13) and (3.14), we achieve the final equation for the current distribution in the two-strand model:

$$\frac{1}{\sigma_\perp}\frac{\partial^2 I}{\partial x^2} - 2\mathcal{L}\frac{\partial I}{\partial t} - (\mathcal{R}_1 + \mathcal{R}_2)I = -\frac{\partial B_\perp}{\partial t} w \cos\left(\frac{2\pi x}{\ell_p} + \theta\right) - \mathcal{L}\frac{\partial I_T}{\partial t} - \mathcal{R}_2 I_T \quad (3.15)$$

Equation (3.15) is a non-linear diffusion equation for I, the current in strand *one.* The current in strand *two* is related to this value through the definition of the transport current. The field, $B_\perp(x,t)$, and the transport current, $I_T(t)$, are assumed to be known functions. The equation is non-linear because the coefficients $\mathcal{R}_1$ and $\mathcal{R}_2$ are non-linear functions of I and T, the temperature of the strands. Since it is second order in space and first order in time, the Eq. (3.15) requires two boundary conditions and one initial condition.

3.4.3 Boundary Conditions

The boundary conditions on Eq. (3.15) are derived from the continuity of transverse electric field and the continuity of current at the ends of the cable. The cable is terminated at either end in low resistance joints connected to the power supply. As mentioned in Section 3.3.3, the joints will initially be approximated as resistors at $x = 0$ and $x = \ell$. The effects of including the finite length of the joints is studied in Chapter 7.

Continuity at the Joints

Referring back to Fig. 3-2, the voltage across the joint resistor at $x = 0$ measured from strand *two* to *one* is:

$$\mathcal{V}_J = -\Re_J^{\downarrow} I_J^{\downarrow} + \Re_J^{\uparrow} I_J^{\uparrow}$$

At other locations, the voltage across the cable, $\mathcal{V}_\perp(x)$ is (see Eq. (3.8)):

$$\mathcal{V}_\perp(x) = \frac{1}{\sigma_\perp}\left.\frac{\partial I_1}{\partial x}\right|_x$$

In order to satisfy Faraday's continuity condition, the transverse electric field must be continuous everywhere. Thus, at the boundary of the cable, $\mathcal{V}_J = \mathcal{V}_\perp(x = 0)$, or:

$$\Re_J^{\uparrow} I_J^{\uparrow} - \Re_J^{\downarrow} I_J^{\downarrow} = \lim_{x \to 0} \frac{1}{\sigma_\perp} \left. \frac{\partial I_1}{\partial x} \right|_x \tag{3.16}$$

Using continuity of current, it is easy to see from Fig. 3-2 that the currents flowing through each half of the joint are merely the strand currents evaluated at $x = 0$. Thus:

$$I_J^{\uparrow} = \left. I_1 \right|_{x=0} \tag{3.17}$$

$$I_J^{\downarrow} = \left. I_2 \right|_{x=0} \tag{3.18}$$

Combining Eqs. (3.16)–(3.18) and once again using the definition of the transport current to eliminate I_2, the desired boundary condition is achieved:

$$x = 0; \qquad \Re_J I - \frac{1}{\sigma_\perp} \frac{\partial I}{\partial x} = \frac{1}{2} \Re_J I_T \tag{3.19}$$

where $I \equiv I_1$ and $\Re_J \equiv \Re_J^{\uparrow} + \Re_J^{\downarrow}$. The boundary condition at $x = \ell$ is found in the same manner. Later in the analysis, it becomes useful to identify the natural length scales in the problem; one of them enters through the joint condition:

$$\ell_J \equiv \frac{1}{\sigma_\perp \Re_J}$$

The boundary length scale, ℓ_J, is discussed further in Section 4.2.3. Using this notation, the necessary boundary conditions are:

$$x = 0; \qquad I - \ell_J \frac{\partial I}{\partial x} = I_{T/2} \tag{3.20}$$

$$x = \ell; \qquad I + \ell_J \frac{\partial I}{\partial x} = I_{T/2} \tag{3.21}$$

where the notation introduced previously, $I_{T/2} \equiv \frac{1}{2} I_T$ is used. These boundary conditions are in general true for all operating conditions. Together with Eq. (3.15) and an initial condition, they completely specify the problem at hand.

Initial Conditions

Although the general model is valid for all initial conditions, the current profile in strand one is usually considered to be uniform in space at time $t = 0$, i.e. $I(x)|_{t=0} = I|_{t=0}$. In cases where the coiled cable produces its own field, the initial current is typically considered to be $I|_{t=0} = 0$. For cases where a background magnetic field is ramped but the transport current is constant, $I|_{t=0} = I_{T/2} = \frac{1}{2}I_T$. There are no induced currents in the cable at time $t = 0$.

3.5 Summary

At the beginning of this chapter, the decision was made to study the effect of current distribution in cabled superconductors using a two-strand model. The two-strand model offers a physically intuitive way to understand how ramping magnetic fields induce circulating currents in cables terminated in low-resistance joints. Despite its simplicity, the model can be used to reach surprising results which will be presented in later chapters.

The notation and parameters used throughout the thesis were introduced in Section 3.3. Of primary interest were the definitions of the different components of the strand current and the distinction between induced currents and transport current. Notation emphasizing this distinction will not be used until Chapter 4 but was introduced in Section 3.3 for the sake of completeness. The remainder of Section 3.3 discussed the inductive and resistive elements of the model and the transverse component of the magnetic field.

Finally the two-strand model equations were derived in Section 3.4. An "untwisting" transformation was used to simplify the derivation of the equations in the differential limit. Equation (3.15) with its associated boundary conditions, Eqs. (3.20) and (3.21), is the equation for the current in strand *one* in its most general form. It is repeated here and will be referred to often in the coming chapters.

The two-strand current distribution equation:

$$\frac{1}{\sigma_\perp}\frac{\partial^2 I}{\partial x^2} - 2\mathcal{L}\frac{\partial I}{\partial t} - (\mathcal{R}_1 + \mathcal{R}_2)I = -\frac{\partial B_\perp}{\partial t} w \cos\left(\frac{2\pi x}{\ell_p} + \theta\right) - \mathcal{L}\frac{\partial I_T}{\partial t} - \mathcal{R}_2 I_T \quad (3.22)$$

$$x = 0; \qquad I - \ell_J \frac{\partial I}{\partial x} = I_{T/2} \quad (3.23)$$

$$x = \ell; \qquad I + \ell_J \frac{\partial I}{\partial x} = I_{T/2} \quad (3.24)$$

$$t = 0; \qquad I(x) = I|_{t=0} \quad (3.25)$$

Equations (3.22)–(3.25) hold true for all ranges of $\mathcal{R}$ and any $B_\perp(x,t)$. To solve Eq. (3.22) in its general form, however, requires a numerical solution since the equation is non-linear and coupled to the heat equation (through the coefficients $\mathcal{R}_1$ and $\mathcal{R}_2$, the resistances of the two strands). The introduction of the heat equation and the numerics involved are presented in Chapter 5. When the resistance terms are small (as is true when the strands are superconducting), though, the model can be solved analytically. Solutions for this scenario are developed in Chapter 4. And even when the non-linear terms are important, a linear approximation to the problem yields analytic results (primarily for shorter cables) which provide new insight. These approximate linear solutions are developed in Chapter 6.

Chapter 4

Current Distribution in the Superconducting Domain

The differential equation developed in Chapter 3, Eq. (3.22), describes the distribution of current in a two-strand cable for a given transport current, I_T, and a prescribed transverse magnetic field, $B_\perp$. As presented, however, this current distribution equation is not complete since the functional dependencies of the strand resistances, $\mathcal{R}_1$ and $\mathcal{R}_2$ have not yet been defined.

In this chapter, a range of operating conditions to be known as the "Superconducting Domain" is defined under which the simple limit $\mathcal{R}_1 = \mathcal{R}_2 = 0$ becomes appropriate, thus completing the model equations. The complentary domain, the "Resistive Domain," is discussed in Chapter 5. This chapter begins by defining the conditions which must be true in order for the simplifying assumptions of the Superconducting Domain to be valid.

The chapter continues with a derivation of the solution of the current distribution equations in the Superconducting Domain. One of the important findings is the existence of three distinct solution regimes corresponding to the overall length of the cable: short, finite or infinite. Within each of these length regimes, the solutions further reduce to different asymptotic limits depending on the nature of the joint resistance: short-circuit, resistive, or open-circuit. Results are presented illustrating the differing behavior of the solutions in each case. Analytic formulae defining the boundaries of these regimes and there subcases are emphasized.

Having achieved the solution for the currents in each strand as a function of time and space, it is possible to determine at what point the Superconducting Domain is no longer valid, i.e. when $I_1 = I_c$. Thus, the results of this chapter will serve to provide the initial conditions for the fully coupled electrical and thermal equations of the Resistive Domain, the subject of the next chapter.

4.1 The Superconducting Domain

We start this chapter where we left off in Chapter 3 with the general model for current distribution in the two strand cable Eqs. (3.22)–(3.24) (repeated here):

$$\frac{1}{\sigma_\perp}\frac{\partial^2 I}{\partial x^2} - 2\mathcal{L}\frac{\partial I}{\partial t} - (\mathcal{R}_1 + \mathcal{R}_2)I = -\frac{\partial B_\perp}{\partial t} w \cos\left(\frac{2\pi x}{\ell_p} + \theta\right) - \mathcal{L}\frac{\partial I_T}{\partial t} - \mathcal{R}_2 I_T \qquad (4.1)$$

$$x = 0; \qquad I - \ell_J \frac{\partial I}{\partial x} = I_{T/2} \qquad (4.2)$$

$$x = \ell; \qquad I + \ell_J \frac{\partial I}{\partial x} = I_{T/2} \qquad (4.3)$$

where $I_{T/2} = I_T/2$.

The goals of this chapter are to define conditions for which the resistive terms, $(\mathcal{R}_1 + \mathcal{R}_2)I$ and $\mathcal{R}_2 I_T$, are negligible and then find the corresponding solutions to Eq. (4.1).

Scaling the resistive terms relative to the first two terms on the LHS of Eq. (4.1) reveals that the resistive terms can be neglected when the following two conditions are valid:

$$\mathcal{R}\sigma_\perp \ell^2 \ll 1 \qquad (4.4)$$

$$\frac{\mathcal{R}t}{2\mathcal{L}} \sim \frac{\mathcal{R}B_{\max}}{2\mathcal{L}\dot{B}} \ll 1 \qquad (4.5)$$

where t is time and the other variables are defined in Section 3.3. For typical $\sigma_\perp \sim$ 100—1000 $\Omega^{-1}\mathrm{m}^{-1}$, these conditions will *always* be true (except for the longest cables, i.e. $\ell > 1$ km) when the strands are in their superconducting state, $\mathcal{R} \sim \mathcal{R}_{sc} \sim 10^{-8}$ Ω/m, and will *never* be true when the strands are resistive, $\mathcal{R} \sim \mathcal{R}_m \sim 10^{-4}$ Ω/m.

We define the domain of operations when both conditions, Eqs. (4.4) and (4.5), are true to be the Superconducting Domain. Simply put, the Superconducting Domain is valid for all cables of interest as long as the strand *one* current is less than the critical current, i.e. $I < I_c$. In this domain, the resistive terms in Eq. (4.1) can be neglected resulting in the reduced equation for current distribution:

$$\frac{1}{\sigma_\perp}\frac{\partial^2 I}{\partial x^2} - 2\mathcal{L}\frac{\partial I}{\partial t} = -\frac{\partial B_\perp}{\partial t} w \cos\left(\frac{2\pi x}{\ell_p} + \theta\right) - \mathcal{L}\frac{\partial I_T}{\partial t} \tag{4.6}$$

It is this equation which will be used as the basis for the further results presented in this chapter.

When $I = I_c$, Eqs. (4.4) and (4.5), break down and the resistive terms in Eq. (4.1) must be kept. This case will be handled in Chapter 5. For the rest of this chapter, it is tacitly assumed that $I < I_c$.

4.2 Equations for the Induced Currents in the Superconducting Domain

Equation (4.6) is a inhomogenous diffusion equation with a diffusivity, $\alpha^2 = (2\sigma_\perp\mathcal{L})^{-1}$. Rewriting it in standard form:

$$\alpha^2\frac{\partial^2 I}{\partial x^2} - \frac{\partial I}{\partial t} = -\frac{\dot{B}_\perp w}{2\mathcal{L}} \cos\left(\frac{2\pi x}{\ell_p} + \theta\right) - \frac{\partial I_{T/2}}{\partial t} \tag{4.7}$$

where the "dot" notation, $\dot{B}_\perp$, refers to the partial time derivative, $\frac{\partial}{\partial t}B_\perp$. Since only the case of linear ramping fields will be considered, $\dot{B}_\perp$ is a constant.

Equation (4.7) will be solved using a multiple length scale expansion which separates the induced current into its two components, circulating currents and interstrand coupling currents. As discussed in Chapter 2, the circulating currents are characterized by length scales on the order of the cable lenfgth, ℓ, while the inter-strand coupling currents are characterized by the length scale of the twist-pitch, ℓ_p. The multiple length scale expansion allows each of the two components to be solved independently as long as they are properly matched at the boundaries.

The asymptotic length limits of "infinite" and "short" cables will be addressed before tackling the more general problem for the "finite" cable. Also, the joints will be classified as either "open-circuit", "resistive", or "short-circuit" depending on the joint resistance, $\Re_J$. In each case, the boundary conditions will need to be handled differently in order to reach an analytic solution.

4.2.1 Superposition of Transport Current

The first step in solving Eq. (4.7) is to exploit the distinction between transport current and induced current introduced in Section 3.3.1. If we define:[1]

$$I = I_{T/2}(t) + I_B(x,t)$$

we see that the particular solution $I_{T/2}$ matches the last term on the RHS of Eq. (4.7) and also homogenizes the boundary conditions, Eqs. (4.2) and (4.3). Thus, we are left with the following equations and boundary conditions for the induced current I_B:

$$\alpha^2 \frac{\partial^2 I_B}{\partial x^2} - \frac{\partial I_B}{\partial t} = -\frac{\dot{B}_\perp w}{2\mathcal{L}} \cos\left(\frac{2\pi x}{\ell_p} + \theta\right) \tag{4.8}$$

$$\begin{aligned} x = 0; \qquad I_B - \ell_J \frac{\partial I_B}{\partial x} &= 0 && (4.9) \\ x = \ell; \qquad I_B + \ell_J \frac{\partial I_B}{\partial x} &= 0 && (4.10) \end{aligned}$$

Thus, in the Superconducting Domain, the induced currents are entirely decoupled from the transport current. The final solution for the total strand current will be a

---

[1] Most of the notation in this chapter was introduced in Section 3.3.

simple superposition of the the transport current plus the induced current.

Although we will now focus exclusively on the induced current, it is the total current $I = I_{T/2} + I_B$ which must remain less than the critical current in order for the Superconducting Domain to be valid.

4.2.2 Multiple Length Scale Expansion

The length scale of the source term in the current diffusion equation above, Eq. (4.8), is the twist-pitch length, ℓ_p. The other geometric length scale in the problem is the length of the cable, ℓ. Since $\ell \gg \ell_p$, a multiple length scale expansion helps to obtain the analytic solution for the induced I_B.

The multiple length scale expansion is defined for the arbitrary operator, U as $U(x) = \langle U \rangle (x) + \tilde{U}(x)$ where $\langle\rangle$indicates a local averaging over the length ℓ_p:

$$\langle U \rangle = \begin{cases} \frac{1}{x} \int_0^x U dx & 0 \leq x \leq \ell_p \\ \frac{1}{\ell_p} \int_x^{x+\ell_p} U dx & \ell_p \leq x \leq \ell - \ell_p \\ \frac{1}{\ell - x} \int_x^{\ell} U dx & \ell - \ell_p \leq x \leq \ell \end{cases} \tag{4.11}$$

From the discussion in Chapter 2 it is clear that the local average of the induced current, $\langle I_B \rangle$, is the term that has been identified as the circulating current. The remaining term $\tilde{I}_B = I_B - \langle I_B \rangle$ is the component of the induced current typically referred to as the interstrand coupling current.

Since the circulating currents are of principle interest in this thesis, the goal of the multiple length scale expansion will be to solve for $\langle I_B \rangle$. In the process, the solution for $\tilde{I}_B$ will be needed to provide "closure" and resolve the boundary conditions.[2]

---

[2] The notation used here, $\langle I_B \rangle$ and $\tilde{I}_B$, is typical for multiple length scale expansions. In this case, however, the selection of the accent mark $\sim$ offers the advantage of reminding us that the $\tilde{I}_B$ term balances the sinusoidal source term.

Local Averaging, $\langle I_B \rangle$

Taking the local average of Eq. (4.8) produces the result:

$$\alpha^2 \left\langle \frac{\partial^2 I_B}{\partial x^2} \right\rangle - \frac{\partial \langle I_B \rangle}{\partial t} = -\frac{w}{2\mathcal{L}} \left\langle \dot{B}_\perp \cos\left(\frac{2\pi x}{\ell_p} + \theta\right) \right\rangle \tag{4.12}$$

The first term on the LHS can be simplified. For ease of understanding, we consider only the middle branch of the averaging operator (i.e. $\ell_p \leq x \leq \ell - \ell_p$) but the other branches are analogous.

$$\begin{aligned} \left\langle \frac{\partial^2 I_B}{\partial x^2} \right\rangle &= \frac{1}{\ell_p} \left(\left.\frac{\partial I_B}{\partial x}\right|_{x+\ell_p} - \left.\frac{\partial I_B}{\partial x}\right|_{x} \right) \\ &= \frac{1}{\ell_p} \left.\frac{\partial \langle I_B \rangle}{\partial x}\right|_{x}^{x+\ell_p} + \frac{1}{\ell_p} \left.\frac{\partial \tilde{I}_B}{\partial x}\right|_{x}^{x+\ell_p} \\ &\equiv \frac{\partial^2 \langle I_B \rangle}{\partial \bar{x}^2} + \frac{1}{\ell_p} \left.\frac{\partial \tilde{I}_B}{\partial x}\right|_{x}^{x+\ell_p} \end{aligned}$$

where $\bar{x}$is used instead of x to indicate that the features of the locally averaged current, $\langle I_B \rangle$, vary on a length scale $\bar{x} \gg \ell_p$. Thus, the limit $\ell_p/\bar{x} \longrightarrow \epsilon$ is used to define the partial second order partial differential, $\frac{\partial^2}{\partial \bar{x}^2} \langle I_B \rangle$.

For cases of interest, the scaling $\tilde{I}_B \ll \langle I_B \rangle$ will be valid. This intuition must be verified, of course, after the actual values of $\tilde{I}_B$ and $\langle I_B \rangle$ have been calculated. In the meantime, the following limit is assumed:

$$\left\langle \frac{\partial^2 I_B}{\partial x^2} \right\rangle \approx \frac{\partial^2 \langle I_B \rangle}{\partial \bar{x}^2} \tag{4.13}$$

The RHS term of Eq. (4.12) also needs to be studied. To simplify the mathematics, the model is limited to cases where field gradients are gradual, as defined by the criterion:

$$\frac{1}{B_\perp} \frac{\partial B_\perp}{\partial x} \ll \frac{1}{\ell_p} \tag{4.14}$$

This assumption means the value of the magnetic field, $B_\perp$, is approximately constant over the length scale of the averaging function. For the solenoidal coils being considered here, this criterion is rarely a limitation—see Section 3.3.4.[3] The local averaging of the source term in Eq. (4.12) thus simplifies to:

$$\left\langle \dot{B}_\perp \cos\left(\frac{2\pi x}{\ell_p}+\theta\right)\right\rangle \approx$$
$$\dot{B}_\perp \begin{cases} \frac{\ell_p}{2\pi x}\left[\sin\left(\frac{2\pi x}{\ell_p}+\theta\right)-\sin\theta\right] & 0\le x\le \ell_p \\ 0 & \ell_p \le x \le \ell-\ell_p \\ \frac{\ell_p}{2\pi(\ell-x)}\left[\sin\left(\frac{2\pi \ell}{\ell_p}+\theta\right)-\sin\left(\frac{2\pi x}{\ell_p}+\theta\right)\right] & \ell-\ell_p\le x\le \ell \end{cases} \tag{4.15}$$

Since the first and last branches, $0 \le x \le \ell_p$ and $\ell - \ell_p \le x \le \ell$, of Eq. (4.15) correspond to the limits $\bar{x} \mapsto 0$ and $\bar{x} \mapsto \ell$, the RHS vanishes for all three branches and the desired result is:

$$\left\langle \dot{B}_\perp \cos\left(\frac{2\pi x}{\ell_p}+\theta\right)\right\rangle = 0 \tag{4.16}$$

Substituting Eqs. (4.13) and (4.16) into Eq. (4.12) produces the homogenous equation for the locally averaged induced current in strand *one*:

$$\alpha^2 \frac{\partial^2 \langle I_B\rangle}{\partial \bar{x}^2} - \frac{\partial \langle I_B\rangle}{\partial t} = 0 \tag{4.17}$$

The multiple length scale analysis has allowed us to derive an equation for the longer scale induced current, $\langle I_B\rangle$ (the quantity in which we are interested) that is independent of the magnetic field distribution and the twist-pitch length of the cable. These factors have not gone away, of course; they now enter the equation through the boundary conditions.

The Difference Term, $\tilde{I}_B$

At $x = 0$ and $x = \ell$, the boundary conditions (Eqs. (4.9) and (4.10)) are defined for the quantity I_B, not $\langle I_B\rangle$. Thus, it is still necessary to solve for the difference term, $\tilde{I}_B$, in order to generate the necessary boundary conditions for Eq. (4.17). Also, we need to calculate $\tilde{I}_B$ to verify the assumption $\tilde{I}_B \ll \langle I_B\rangle$ which was used to simplify

---

[3] The more general case of arbitrary $B_\perp(x)$ can also be handled but the mathematics become more cumbersome.

Eq. (4.13).

The equation for $\tilde{I}_B$ is obtained by subtracting the locally averaged Eq. (4.17) from the point equation, Eq. (4.8). The result yields:

$$\alpha^2 \frac{\partial^2 \tilde{I}_B}{\partial x^2} - \frac{\partial \tilde{I}_B}{\partial t} = -\frac{\dot{B}_\perp w}{2\mathcal{L}} \cos\left(\frac{2\pi x}{\ell_p} + \theta\right) \tag{4.18}$$

Since any larger scale features have been averaged out, the length scale over which the difference term $\tilde{I}_B$ varies is $\sim \ell_p$. Using this scale length, the characteristic time constant of Eq. (4.18) can be defined as: $\tau_p \equiv \ell_p^2/\alpha^2 = 2\sigma_\perp \mathcal{L} \ell_p^2$. Using the typical values introduced in Section 3.3 ($\sigma_\perp \sim 10^3\ \Omega^{-1}\text{m}^{-1}$, $\mathcal{L} \sim 10^{-6}\ \mu\text{H}$, $\ell_p \sim 1$ m) the value of the interstrand time constant is $\tau_p \sim 1$ msec. If we limit ourselves to studying times, $t \gg \tau_p$ (which will certainly be the case for any practical ramp time), Eq. (4.18) will have reached steady state and the equation simplifies to:

$$\alpha^2 \frac{\partial^2 \tilde{I}_B}{\partial x^2} = -\frac{\dot{B}_\perp w}{2\mathcal{L}} \cos\left(\frac{2\pi x}{\ell_p} + \theta\right) \tag{4.19}$$

Again using the no sharp gradients assumption from Eq. (4.14), the steady state solution for the difference term is thus:

$$\begin{aligned} \tilde{I}_B &= \frac{\dot{B}_\perp w \ell_p^2}{8\pi^2 \mathcal{L} \alpha^2} \cos\left(\frac{2\pi x}{\ell_p} + \theta\right) \\ &= \frac{\dot{B}_\perp w \ell_p^2 \sigma_\perp}{4\pi^2} \cos\left(\frac{2\pi x}{\ell_p} + \theta\right) \end{aligned} \tag{4.20}$$

Notice there are no linear or constant terms because they are included in the $\langle I_B \rangle$ term by definition of the local averaging operator, Eq. (4.11).

The difference term, $\tilde{I}_B$, is the component of the induced current associated with the interstrand coupling current. The interstrand coupling current is often defined as the current-per-unit-length flowing between the strands, or $\frac{\partial}{\partial x}\tilde{I}_B$, where

$$\frac{\partial \tilde{I}_B}{\partial x} = -\frac{\dot{B}_\perp w \ell_p \sigma_\perp}{2\pi} \sin\left(\frac{2\pi x}{\ell_p} + \theta\right) \tag{4.21}$$

This interstrand coupling current is interesting because it generates a heat load which is measured as AC loss. In fact, as discussed in Chapter 2, most previous studies of induced currents in twisted cables have the calculation of the interstrand coupling current and its associated losses as their final goal (albeit in far more detail). For the purposes of this thesis, however, the interstrand coupling current is an intermediate step needed to specify the boundary conditions for the larger scale induced current, $\langle I_B \rangle$.

Since the value of $\tilde{I}_B$ and the scaled derivative $\ell_J \frac{\partial}{\partial x} \tilde{I}_B$ become components of the boundary conditions, it is useful to introduce the following notation which will be used in later sections:

$$\begin{aligned} b_0 = \tilde{I}_B \Big|_{x=0} &= \frac{\dot{B}_\perp w \ell_p^2 \sigma_\perp}{4\pi^2} \cos\theta_0 && (4.22) \\ b_0' = \frac{\partial \tilde{I}_B}{\partial x} \bigg|_{x=0} &= -\frac{\dot{B}_\perp w \ell_p \sigma_\perp}{2\pi} \sin\theta_0 && (4.23) \\ b_1 = \tilde{I}_B \Big|_{x=\ell} &= \frac{\dot{B}_\perp w \ell_p^2 \sigma_\perp}{4\pi^2} \cos\theta_1 && (4.24) \\ b_1' = \frac{\partial \tilde{I}_B}{\partial x} \bigg|_{x=l} &= -\frac{\dot{B}_\perp w \ell_p \sigma_\perp}{2\pi} \sin\theta_1 && (4.25) \end{aligned}$$

where $\theta_0 \equiv \theta$ and $\theta_1 \equiv \left(\frac{2\pi\ell}{\ell_p} + \theta\right)$.

It is interesting to note that only the value of the magnetic field at the joints, $\dot{B}_\perp(x{=}0{,}\ell)$, enters into the boundary equations. This is only partially due to the limitation of studying transverse magnetic fields with gradual gradients. In numerical solutions for arbitrary field profiles, the field at the joint dominates the size of the constants, b_0, b_1, b_0', and b_1', even when the field profile possessed sharp gradients.

One of the implications of this result is that when modeling large scale coils in the lab, it is necessary to match not only the peak field conditions (which affect the stability of the cable) but also the field conditions at the joints (which affect the magnitude of the induced currents). A well designed small-scale simulation will also have to match the larger coil in other aspects, as will be described in the next section.

4.2.3 Derived Length Scales

So far, three natural scale lengths have arisen in the problem: the length of the cable, ℓ, the twist-pitch length, ℓ_p, and the length scale which enters the problem through the boundary conditions, ℓ_J. A fourth length scale, the "diffusion length", ℓ_D, can be derived from the diffusion equation for the circulating current, Eq. (4.17). In order to continue with the solution, it is first useful to define different operating regimes based on the relative ordering of these four lengths. Since the lengths ℓ_J and ℓ_D have not yet been discussed, they will be defined before the necessary criteria are developed.

The Diffusion Length, ℓ_D

The diffusion length is derived from scaling the two terms of the homogenous diffusion equation, Eq. (4.17). At a given time, t, the second derivative in space must be of the same order as the time derivative. The resulting length scale of the spatial gradient is ℓ_D, i.e.:

$$\alpha^2 \frac{\langle I_B \rangle}{\ell_D^2} \sim \frac{\langle I_B \rangle}{t} \longrightarrow \ell_D \equiv \alpha\sqrt{t}$$

where α is the diffusivity defined as $\alpha \equiv (2\sigma_\perp \mathcal{L})^{-\frac{1}{2}}$.

Since the diffusion length is time-dependent, the regimes of operation which will next be developed are also time-dependent. The most logical time to use is the ramp time, $t_{ramp} = B_{\max}/\dot{B}$, the time it takes to linearly ramp the magnetic field from zero to its final value. Thus, unless otherwise noted:

$$\ell_D \equiv \alpha\sqrt{t_{ramp}} = \sqrt{\frac{t_{ramp}}{2\sigma_\perp \mathcal{L}}} = \sqrt{\frac{B_{\max}}{2\sigma_\perp \mathcal{L}\dot{B}}} \tag{4.26}$$

The Boundary Scale Length, ℓ_J

The remaining length scale, ℓ_J, is derived from the ratio of the transverse cable resistance, $\sigma_\perp^{-1}$, to the joint resistance, $\Re_J$:

$$\ell_J \equiv \frac{1}{\sigma_\perp \Re_J}$$

The length ℓ_J only enters the problem through the boundary conditions, (see Eq. (4.9)) and thus will be called the "boundary scale" length . It is a measure of the distance from the joint at which the boundary conditions will still strongly affect the solution if a steady state condition were to be reached.

To understand this last statement it is useful to think of how a two-strand cable would react to an external voltage being applied across the cable at its mid-section, $x = \ell/2$. Current would flow from strand *two* to strand *one* at location $x = \ell/2$ and then would have to find the path of least resistance to close the circuit. The two available paths are to cross through the transverse conductance, $\sigma_\perp$, over the two half-lengths of the cable or to cross at the joints at either end of the cable. In steady state, inductance is not a factor. The resistance of the first path is $1/(\sigma_\perp \ell)$ and the resistance of the second path is $1/\Re_J$. If the length of the cable is longer than ℓ_J, the first path is the least resistive and the majority of the current does not pass through the joint. On the other hand, if $\ell < \ell_J$, the path through the joints is the least resistive and thus the boundary conditions strongly affect the solution even at the center of the cable.

4.2.4 Cable Length Classification

The induced currents (and thus the current distribution) in a cable depends a great deal on the length scales just defined. In this section, criteria will be developed to differentiate cables into one of three length regimes. In each case, the behavior of the induced currents is sufficiently distinct as to warrant a separate treatment of the problem. The three categories are: the asymptotic limits of "short" and "infinite" cables and the intermediate case of the "finite" cable. It is necessary to consider all three cases since practical cables span this entire range.

The length classifications short, finite, and infinite relate the physical cable length, ℓ, to the diffusion length, ℓ_D, defined in Section 4.2.3. The cutoff criteria are listed in Table 4.1. The physical interpretation of these criteria is that for "short" cables, the induced currents are fully diffused across the cable length while for "infinite" cables, the currents induced at either end have not diffused far enough to reach the opposite

ordering	*length classification*
$\ell \ll \ell_D$	short
$\ell \sim \ell_D$	finite
$\ell \gg \ell_D$	infinite

Table 4.1: Definition of Cable Length Classifications ($\ell_D \equiv \sqrt{t_{ramp}}/\sqrt{\sigma_\perp \mathcal{L}}$)

end. In the "finite" cable, the currents induced at each boundary reach the other end of the cable, but are not fully diffused.

Since the transverse conductivity, $\sigma_\perp$, can vary over a large range, two cables of the same physical length can easily fall into different length classifications. Similarly, a cable that is infinitely long for fast ramps can be merely finite for slow ramps. Nonetheless, a rough idea of the lengths being discussed can be estimated using typical values of the parameters involved. Using: $\sigma_\perp = 1000\ \Omega^{-1}\text{m}^{-1}$, $\mathcal{L} = 5 \cdot 10^{-7}$ H, and $t_{ramp} = 5$ sec, the calculated diffusion length is $\ell_D = 100$ m. Thus, using these parameters, a large-scale model coil (e.g. US-DPC, $\ell \sim 70$ m) would be finite, most lab-scale cables ($\ell \sim 5$ m) would be short, and proposed fusion reactor coils (e.g. ITER, $\ell \sim 1$ km) would be infinite.

It is especially important to keep these scalings in mind when trying to simulate coils with a long physical length with lab-scale cables of a much shorter length. It is likely that the two coils could fall into different length classifications and thus exhibit different induced current behavior.

For short and infinite cables, we will be able to achieve closed form analytic solutions. For the finite case, an analytic solution is found but the resulting infinite series does not converge on a known function. Before proceeding to these solutions, however, another set of classifications proves useful: the characterization of the joints.

4.2.5 Joint Classification

The joints are equally as important as the cable length in determining the behavior of current distribution in cables exposed to ramping magnetic firelds. In this section,

ordering	*joint classification*
$\ell \gg \ell_J$	open-circuit
$\ell \sim \ell_J$	resistive
$\ell_J \gg \ell$	short-circuit

Table 4.2: Definition of Joint Classifications ($\ell_J \equiv (\sigma_\perp \Re_J)^{-1}$)

criteria will be developed to classify the joints into one of three regimes: open-circuit, resistive or short-circuit. In each case, the boundary conditions on the current diffusion equation are sufficiently distinct so as to warrant a separate treatment for each.

The joints are characterized by the ratio of the boundary scale length, ℓ_J, to the cable length, ℓ. The three possible orderings are listed in Table 4.2 along with the corresponding joint classifications. In all cases, both ℓ and $\ell_J \gg \ell_p$, the twist-pitch length of the cable.[4]

It should be noted that the terms short-circuit, resistive and open-circuit in no way refer to the inductive/resistive time-constant of the cable. For instance, the induced currents in a short-circuited cable are not necessarily "inductance limited" as the term sometimes implies. In the sense in which it is used here, the short-circuit classification only means the induced currents flow predominantly through the joints—the transverse current over the cable length is negligible. In this case the L/R time constant, $\tau_{LR} = \ell\mathcal{L}/\Re_J$, can be greater than or less than the ramp time, t_{ramp}.

Although the term "joint classification" has been used in Table 4.2, the same joint on a different cable would not necessarily fall into the same classification. The transverse conductivity, $\sigma_\perp$, is equally as important as $\Re_J$ in determining the joint classification. If the parameters of the cable have been specified, though, the selection of joint design alone can determine the behavior of the cable in ramping magnetic fields.

---

[4] The case $\ell_J \sim \ell_p$ implies the transverse resistance of the joint is on the same order as the transverse resistance of the cable over one twist-pitch length—i.e., the effects of the joint are negligible. This would represent a very poorly designed joint and is thus not of much interest here.

The classification of cables into one of the three joint categories is an important step in comparing the behavior of two different cable designs. Specifically, in designing small-scale experiments to model the effects of induced currents in large coil designs, it is critical to design the joint in such a way that the two cables fall into the same joint classification.

The 3 x 3 World of $\langle I_B \rangle$

Together with the three cable length classifications defined in Section 4.2.4, the three joint classifications emphasized in the previous section provide a 3 x 3 matrix of operating regimes in which the solutions to Eq. (4.8) behave differently. For all cases in which circulating currents exist, a given cable (characterized by ℓ, $\ell_J$and ℓ_D) falls into one of the three joint classifications: open-circuit, resistive, or short-circuit, as well as one of the three length regimes: short, finite or infinite.

The purpose of characterizing the cable using this 3 x 3 matrix is to better understand how the boundary conditions produce the circulating currents which are the focus of this chapter. For each case, a slightly different solution technique is needed to acquire a closed form analytic answer. In the finite length case, however, closed form solutions cannot be found but an infinite series solution is obtained instead.

4.2.6 Boundary Conditions

Having characterized the different operating regimes, it is now time to complete the task of calculating $\langle I_B \rangle$. The first step is to separate the boundary conditions, Eqs. (4.9) and (4.10), into their locally averaged and difference term components using the definition $I_B = \langle I_B \rangle + \tilde{I}_B$:

$$x = 0; \qquad \langle I_B \rangle - \ell_J \frac{\partial \langle I_B \rangle}{\partial x} = -\tilde{I}_B + \ell_J \frac{\partial \tilde{I}_B}{\partial x} \tag{4.27}$$

$$x = \ell; \qquad \langle I_B \rangle + \ell_J \frac{\partial \langle I_B \rangle}{\partial x} = -\tilde{I}_B - \ell_J \frac{\partial \tilde{I}_B}{\partial x} \tag{4.28}$$

where the solutions for $\tilde{I}_B$ and $\frac{\partial}{\partial x}\tilde{I}_B$, evaluated at $x = 0$ and $x = \ell$, are given in Eqs. (4.22)–(4.25).

Since it has been shown that$\frac{\partial}{\partial x}\langle I_B\rangle \sim \langle I_B\rangle/\ell$ while $\frac{\partial}{\partial x}\tilde{I}_B \sim \tilde{I}_B/\ell_p$ the relative scaling of the terms in the boundary conditions depends on the ordering of the lengths ℓ, ℓ_p, and ℓ_J. Since we have stated that we are interested in cables with $\ell \gg \ell_p$, the first term on the RHS of Eqs. (4.27) and (4.28) is negligible. The different possible orderings of ℓ and ℓ_J were defined in Table 4.2; in each case, different terms on the LHS of Eqs. (4.27) and (4.28), dominate. The possibilities are thus:

$$\text{open-circuit} \quad (\ell \gg \ell_J): \quad \begin{cases} x = 0; & \langle I_B\rangle = \ell_J \left.\frac{\partial \tilde{I}_B}{\partial x}\right|_{x=0} \\ x = l; & \langle I_B\rangle = -\ell_J \left.\frac{\partial \tilde{I}_B}{\partial x}\right|_{x=\ell} \end{cases} \tag{4.29}$$

$$\text{resistive} \quad (\ell \sim \ell_J): \quad \begin{cases} x = 0; & \langle I_B\rangle - \ell_J\frac{\partial}{\partial x}\langle I_B\rangle = \ell_J \left.\frac{\partial \tilde{I}_B}{\partial x}\right|_{x=0} \\ x = l; & \langle I_B\rangle + \ell_J\frac{\partial}{\partial x}\langle I_B\rangle = -\ell_J \left.\frac{\partial \tilde{I}_B}{\partial x}\right|_{x=\ell} \end{cases} \tag{4.30}$$

$$\text{short circuit} \quad (\ell_J \gg \ell): \quad \begin{cases} x = 0; & \frac{\partial\langle I_B\rangle}{\partial x} = -\left.\frac{\partial \tilde{I}_B}{\partial x}\right|_{x=0} \\ x = l; & \frac{\partial\langle I_B\rangle}{\partial x} = -\left.\frac{\partial \tilde{I}_B}{\partial x}\right|_{x=\ell} \end{cases} \tag{4.31}$$

Note that in each case $\tilde{I}_B/\langle I_B\rangle \ll 1$, as assumed. In particulat, for the open- and resistice circuit cases, $\tilde{I}_B/\langle I_B\rangle \sim \ell_p/\ell_J \ll 1$, while in the short-circuit case, $\tilde{I}_B/\langle I_B\rangle \sim \ell_p/\ell \ll 1$.

Eqs. (4.29)–(4.31) provide the necessary boundary conditions for Eq. (4.17), the diffusion equation which defines the behavior of the circulating currents in the two strand model. In each case, the RHS of the boundary condition is a known value, as specified in Eqs. (4.22)–(4.25).

4.3 Solutions to the Induced Current Equations

The results of Section 4.2 were the homogenous diffusion equation for the locally averaged induced current (i.e., the circulating current) and the associated boundary conditions, simplified for each possible joint classification. In addition, three cable length regimes were identified: short, finite, an infinite.

In this section, each of the three length regimes is examined separately in order to emphasize the asymptotic limits of the short and infinite cases. The infinite regime will be discussed first, followed by the short regime. In each case the ordering of the length scales, ℓ, ℓ_D, and ℓ_J, implies an asymptotic limit which allows the solution to be found in closed form. The more general case of the finite cable is studied last.

For each length regime, the problem is further divided into the three joint classifications: open-circuit, resistive, or short-circuit. These distinctions are not only helpful in describing the behavior of the cable but also help in solving the equations since the appropriate boundary conditions, Eqs. (4.29)–(4.31), are different in each case.

4.3.1 The Infinitely Long Cable, $\ell \gg \ell_D$

Referring to Table 4.1, a cable can be considered infinitely long when $\ell \gg \ell_D$, where $\ell_D = \sqrt{t_{ramp}}/\sqrt{\sigma_\perp \mathcal{L}}$. When this condition is true, the effects of the circulating currents induced at one joint never reach the opposite end of the cable. Thus, each joint can be considered separately and the two solutions later superposed. This section focuses on the joint located at $x = 0$ but the results are equally valid for the joint at $x = \ell$.

As a result of the infinitely long condition, the boundary condition at $x = \ell$ can be replaced with the much simpler condition: $\langle I_B \rangle \to 0$ as $x \to \infty$. This substitution alone greatly simplifies the solutions and thus justifies the separate treatment of the infinite case. The resulting equation, with general boundary conditions, for the infinite case is thus (referring to Eqs. (4.17) and (4.27)) :

$$\alpha^2 \frac{\partial^2 \langle I_B \rangle}{\partial x^2} - \frac{\partial \langle I_B \rangle}{\partial t} = 0 \qquad (4.32)$$

$$\begin{aligned} x = 0; \qquad \langle I_B \rangle - \ell_J \tfrac{\partial \langle I_B \rangle}{\partial x} &= -b_0 + \ell_J b_0' && (4.33) \\ x \to \infty; \qquad \langle I_B \rangle &\to 0 && (4.34) \end{aligned}$$

ℓ	1000	m
ℓ_p	$2 \cdot 10^{-1}$	m
w	10^{-2}	m
θ	$-\pi/2$	
$\sigma_\perp$	100	$\Omega^{-1}\mathrm{m}^{-1}$
$\mathcal{L}$	0.7	μH
$\dot{B}_\perp(0)$	2	T/s
t_{ramp}	5	s
ℓ_D	~ 200	m
b_0'	$\sim 6 \cdot 10^{-2}$	Amps m^{-1}

Table 4.3: Cable parameters used in examples for Infinite Cable Length Regime.

where the definitions of b_0 and b_0' are given in Eqs. (4.22) and (4.23).

Exploiting the different joint regimes which have been identified in Section 4.2.5, the boundary conditions at $x = 0$ can be simplified using the reductions given in Eqs. (4.29)–(4.31). The distinct solution for each joint regime is developed separately in the following paragraphs.

A standard format will be introduced in which the validity regime and reduced boundary conditions for each scenario are stated before solving the diffusion equation, Eq. (4.32). In each case the solution is evaluated for typical cable parameters and the results presented graphically.

For the infinite length regime, the typical cable parameters are given in Table 4.3. The last two quantities in the table are derived from the other parameters according to the definitions in Eqs. (4.23) and (4.26). The other length scale of interest, ℓ_J, will be determined by the choice of $\Re_J$ which will be different for each case.

In general, the final solutions will be directly proportional to a trigonemetric function (or combination of functions) of θ. The value of θ therefore plays an important role in determining the magnitude of induced currents in the two-strand model. A statistical study of the effects of the arbitariness of θ is considered in Chapter 7 but, for now, the value of θ is chosen arbitrarily.

Infinite Length, Open-Circuit Joints

validity regime:

- $\ell \gg \ell_D$
- $\ell \gg \ell_J$

boundary conditions:

- $x = 0; \quad \langle I_B \rangle = \ell_J b_0'$
- $x \rightarrow \infty; \quad \langle I_B \rangle \rightarrow \infty$

The Laplace transform is used to solve the diffusion equation for the given boundary conditions in the semi-infinite domain $0 \leq x < \infty$. The Laplace transform of $\langle I_B \rangle$ will be defined as $Z(p)$ where p is the transform variable. The transform of Eq. (4.32) and its boundary conditions thus produces:

$$\alpha^2 \frac{\partial^2 Z}{\partial x^2} - pZ = 0 \tag{4.35}$$

$$\begin{array}{lrcl} x = 0; & Z & = & p^{-1} \ell_J b_0' \qquad (4.36) \\ x \rightarrow \infty; & Z & \rightarrow & 0 \qquad (4.37) \end{array}$$

where the initial condition is $\langle I_B \rangle_{(t=0)} = 0$. The value of Z is found using standard solution techniques for ordinary differential equations. And, with a thorough table of Laplace transforms [30], the inverse transform can be found directly:

$$\begin{array}{rcl} Z & = & \ell_J b_0' p^{-1} \exp^{-p^{\frac{1}{2}} x/\alpha} \\ \Updownarrow & & \\ \langle I_B \rangle & = & \ell_J b_0' \mathrm{Erfc}\left(\dfrac{x}{2\alpha\sqrt{t}} \right) \end{array} \tag{4.38}$$

where Erfc(x) is the complement to the error function, $\mathrm{Erfc}\,(x) \equiv 1 - \mathrm{Erf}\,(x)$. Reducing this result to the "primary" parameters listed in Table 4.3 helps to show how

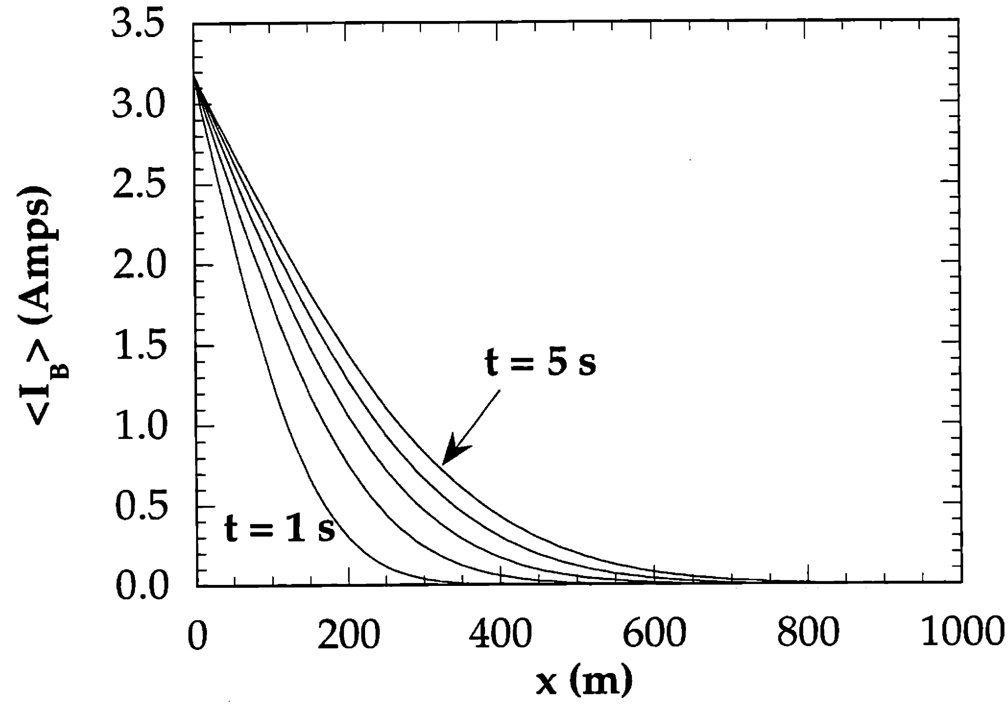

Figure 4-1: Example of circulating current in the Infinite Length, Open-Circuit Joints Regime.

$\langle I_B \rangle$ scales:

$$\langle I_B \rangle = -\frac{\dot{B}_\perp w \ell_p \sin(\theta)}{2\pi \Re_J} \text{Erfc}\left(\frac{x\sqrt{\sigma_\perp \mathcal{L}}}{\sqrt{2t}}\right) \tag{4.39}$$

To give a sense of how the circulating current behaves it is useful to present the solution graphically. Using the parameters given in Table 4.3, the choice of $\Re_J = 2 \cdot 10^{-4}\ \Omega$ gives $\ell_J/\ell \ll 1$ and thus satisfies the validity conditions for this regime. For these values, Eq. (4.39) is plotted for several values of t in Fig. 4-1.

Since the open-circuit, infinitely long regime produces the smallest $\langle I_B \rangle$, this is a good time to check the assumption used in the multiple length scale expansion, namely $\langle I_B \rangle \gg \tilde{I}_B$. Comparing the solution for $\langle I_B \rangle$, Eq. (4.39), to the solution for $\tilde{I}_B$, Eq. (4.20), it can be seen that this criterion is always true for $\ell_J \gg \ell_p$, consistent with the validity regime for this and all other regimes considered in this thesis.

Infinite Length, Resistive Joints

validity regime:

- $\ell \gg \ell_D$
- $\ell \sim \ell_J$

boundary conditions:

- $x = 0; \quad \langle I_B \rangle - \ell_J \frac{\partial \langle I_B \rangle}{\partial x} = \ell_J b_0'$
- $x \to \infty; \quad \langle I_B \rangle \to 0$

The Laplace transform is again employed to simplify the partial differential diffusion equation into an ordinary differential equation:

$$\alpha^2 \frac{\partial^2 Z}{\partial x^2} - pZ = 0 \tag{4.40}$$

$$\begin{aligned} x = 0; \qquad & Z - \ell_J \tfrac{\partial Z}{\partial x} &=& \; p^{-1} \ell_J b_0' && (4.41) \\ x \to \infty; \qquad & Z &\to& \; 0 && (4.42) \end{aligned}$$

where the appropriate boundary equation for resistive joints was found in Eq. (4.30).

The value of Z is found using standard solution techniques. With a thorough table of Laplace transforms [30] the inverse transform can be found directly:

$$\begin{aligned} Z &= \ell_J b_0' \frac{\alpha}{\ell_J} p^{-1} \left(p^{\frac{1}{2}} + \frac{\alpha}{\ell_J} \right)^{-1} \exp^{-p^{\frac{1}{2}} x/\alpha} \\ &\Updownarrow \\ \langle I_B \rangle &= \ell_J b_0' \left[\operatorname{Erfc}\left(\frac{x}{2\alpha\sqrt{t}} \right) - \exp\left(\frac{x}{\ell_J} + \frac{\alpha^2}{\ell_J^2} t \right) \operatorname{Erfc}\left(\frac{x}{2\alpha\sqrt{t}} + \frac{\alpha\sqrt{t}}{\ell_J} \right) \right] \end{aligned} \tag{4.43}$$

The advantage of solving the infinite length regime separately can now be appreciated as it would be difficult to extract the asymptotic limit represented by Eq. (4.43) from the infinite series solution for the finite cable regime which will be developed later.

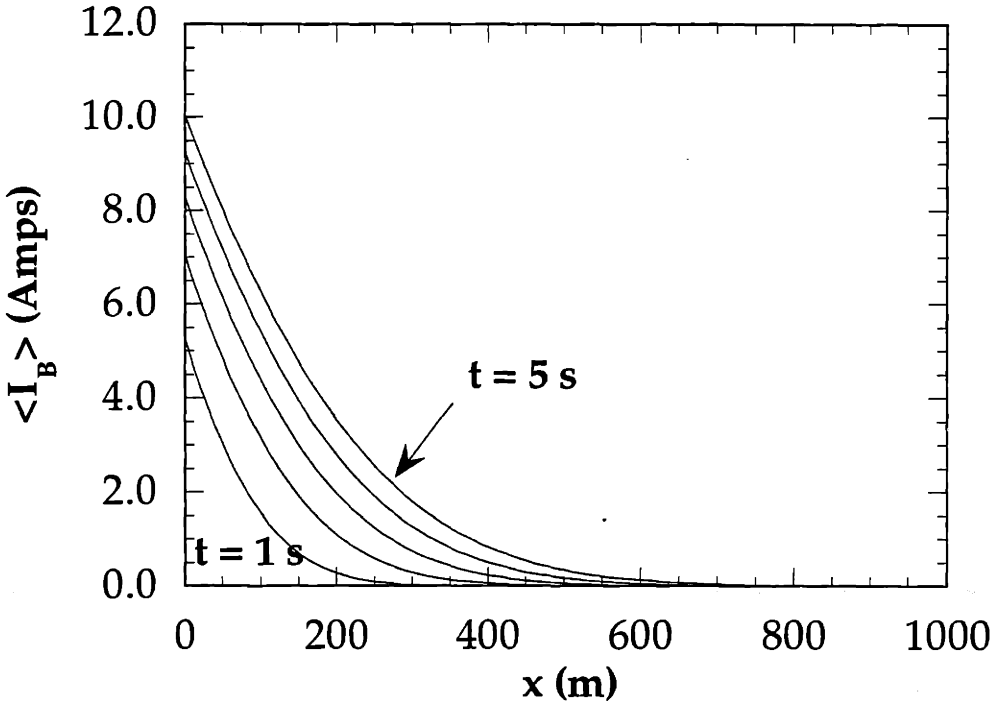

Figure 4-2: Example of circulating current in the Infinite Length, Resistive Joints Regime.

To better appreciate how $\langle I_B \rangle$ scales with the engineering parameters, Eq. (4.43) can be rewritten:

$$\langle I_B \rangle = -\frac{\dot{B}_\perp w \ell_p \sin(\theta)}{2\pi \Re_J} \left[\begin{array}{l} \mathrm{Erfc}\left(\frac{x\sqrt{\sigma_\perp \mathcal{L}}}{\sqrt{2t}}\right) \\ -\exp\left(\sigma_\perp \Re_J \ell \left[\frac{x}{\ell} + \frac{\Re_J t}{2\mathcal{L}\ell}\right]\right) \mathrm{Erfc}\left(\frac{x\sqrt{\sigma_\perp \mathcal{L}}}{\sqrt{2t}} + \frac{\Re_J \sqrt{\sigma_\perp t}}{\sqrt{2\mathcal{L}}}\right) \end{array} \right] \tag{4.44}$$

To give a sense of how the circulating current behaves it is useful to present the solution graphically. Using the parameters given in Table 4.3, the choice of $\Re_J = 2 \cdot 10^{-5}\ \Omega$ gives $\ell_J/\ell \sim 1$ and thus satisfies the validity conditions for this regime. For these values, Eq. (4.44) is plotted for several values of t in Fig. 4-2.

Infinite Length, Short-Circuit Joints

validity regime:

- $\ell \gg \ell_D$
- $\ell_J \gg \ell$

boundary conditions:

- $x = 0; \quad \frac{\partial \langle I_B \rangle}{\partial x} = -b'_0$
- $x \rightarrow \infty; \quad \langle I_B \rangle \rightarrow 0$

The equation and boundary condition in the transform domain are:

$$\alpha^2 \frac{\partial^2 Z}{\partial x^2} - pZ = 0 \tag{4.45}$$

$$\begin{array}{lrcl} x = 0; & \frac{\partial Z}{\partial x} & = & -p^{-1} b'_0 \quad (4.46) \\ x \rightarrow \infty; & Z & \rightarrow & 0 \quad (4.47) \end{array}$$

The value of Z is found using standard solution techniques. Using a thorough table of Laplace transforms [30] the inverse transform can be found directly:

$$\begin{aligned} Z &= \alpha b'_0 p^{-\frac{3}{2}} \exp^{-p^{\frac{1}{2}} x/\alpha} \\ &\Updownarrow \\ \langle I_B \rangle &= \alpha b'_0 \left[2\pi^{-\frac{1}{2}} t^{\frac{1}{2}} \exp\left(\frac{-x^2}{4\alpha^2 t} \right) - \frac{x}{\alpha} \mathrm{Erfc}\left(\frac{x}{2\alpha\sqrt{t}} \right) \right] \end{aligned} \tag{4.48}$$

To better demonstrate the scaling of $\langle I_B \rangle$ in the infinite length, short-circuit joint regime, the result can be rewritten in terms of the engineering parameters:

$$\langle I_B \rangle = -\frac{\dot{B}_\perp w \ell_p \sqrt{\sigma_\perp t} \sin(\theta)}{\pi^{3/2} \sqrt{2\mathcal{L}}} \left[\exp\left(\frac{-sig\mathcal{L} x^2}{2t} \right) - \frac{\pi \sigma_\perp \mathcal{L}}{4t} x \mathrm{Erfc}\left(\frac{x\sqrt{\sigma_\perp \mathcal{L}}}{\sqrt{2t}} \right) \right] \tag{4.49}$$

As might be expected, the magnitude of $\langle I_B \rangle$ no longer depends on $\Re_J$.

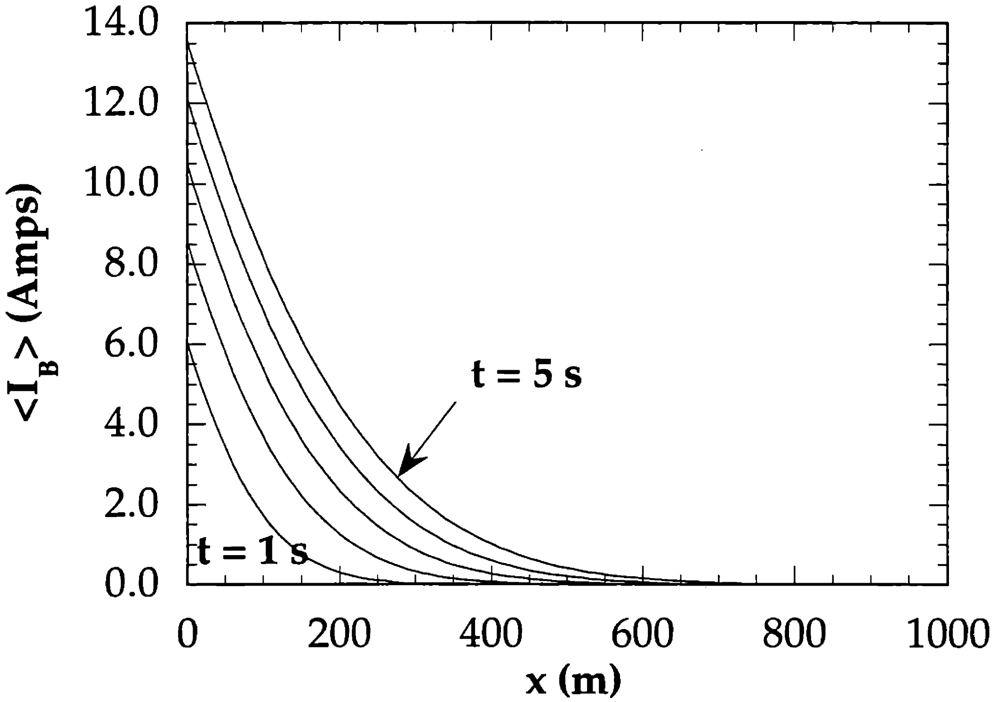

Figure 4-3: Example of circulating current in the Infinite Length, Short-Circuit Joints Regime.

To give a sense of how the circulating current behaves it is useful to present the solution graphically. Using the parameters given in Table 4.3, the choice of $\Re_J = 1 \cdot 10^{-6}\ \Omega$ gives $\ell_J/\ell \gg 1$ and thus satisfies the validity conditions for this regime. For these values, Eq. (4.49) is plotted for several values of t in Fig. 4-3.

Summary of Infinitely Long Cable Results

The solutions developed above for the cases of infinitely long cables with open-circuit, resistive, or short-circuit joints only dealt with the end of the cable at $x = 0$. The solutions for the currents induced at the opposite nd, $x = \ell$, are exactly analogous and can be linearly superposed with the solutions presented here.

Since the time it takes for the circulating currents to diffuse into the center of an infinite cable is by definition longer than the ramp-time, t_{ramp}, infinite cables suffer the least from the effects of current distribution. This is good news for the design of large scale magnet systems but highlights the difficulties of modeling large magnets with lab-scale experiments.

4.3.2 The Short Cable, $\ell \ll \ell_D$

When the length of the cable is much shorter than the diffusion length for ramp-times of interest, the cable falls in the short cable regime. In this asymptotic limit, the circulating current is fully diffused across the cable and both joints play a dominant role in determining the overall current at all points along the cable at all times of interest.

Whereas the Laplace transform proved to be an effective tool for solving $\langle I_B \rangle$ in the infinite regime, the addition of the second boundary condition makes this method more difficult to employ. Instead, a perturbation analysis is used to solve the diffusion equations.

Again, the different joint regimes identified in Section 4.2.5 will be used to allow asymptotic solutions to be reached directly, where appropriate. The solution for each joint classification is developed separately using the format introduced in the last section. A specific example for each case will be given based on the typical cable described in Table 4.4.[5] First though, the perturbative method which will be used is explained for the general case.

---

[5] The cable parameters are the same as were used for the infinite case except for the length and the addition of θ_1.

ℓ	10	m
ℓ_p	$2 \cdot 10^{-1}$	m
w	10^{-2}	m
θ_0	$-\pi/2$	
θ_1	$\pi/4$	
$\sigma_\perp$	100	$\Omega^{-1}\text{m}^{-1}$
$\mathcal{L}$	0.7	μH
$\dot{B}_\perp(0)$	2	T/s
t_{ramp}	5	s
ℓ_D	~ 200	m
b'_0	$\sim 6 \cdot 10^{-2}$	Amps m^{-1}
b'_1	$\sim -4 \cdot 10^{-2}$	Amps m^{-1}

Table 4.4: Cable parameters used in examples for Short Cable Length Regime.

Short Length – Perturbative Solution Method

In the short cable regime, it is useful to exploit the scaling $\ell \ll \ell_D$ to allow a perturbation solution of the current diffusion equation. In doing so, it is convenient to begin by introducing the dimensionless variables, $\hat{x} \equiv x/\ell$ and $\hat{t} \equiv t/t_{ramp}$. Substituting these terms into Eq. (4.17) gives:

$$\frac{\partial^2 \langle I_B \rangle}{\partial \hat{x}^2} - \epsilon^2 \frac{\partial \langle I_B \rangle}{\partial \hat{t}} = 0 \tag{4.50}$$

while the boundary conditions, Eqs. (4.27) and (4.28) become (in general):

$$\begin{aligned} \hat{x} = 0; \qquad \langle I_B \rangle - \frac{\ell_J}{\ell} \frac{\partial \langle I_B \rangle}{\partial \hat{x}} &= -b_0 + \ell_J b'_0 && (4.51) \\ \hat{x} = 1; \qquad \langle I_B \rangle + \frac{\ell_J}{\ell} \frac{\partial \langle I_B \rangle}{\partial \hat{x}} &= -b_0 - \ell_J b'_0 && (4.52) \end{aligned}$$

where $\epsilon^2 \equiv \ell^2/(\alpha^2 t_{ramp}) = (\ell/\ell_D)^2$ is a very small number for the short cable regime. The other dimensionless parameter which appears is ℓ_J/ℓ. Depending on the joint classification (open-circuit, resistive or short-circuit), ℓ_J/ℓ will be $\sim \epsilon$, ~ 1, or $\sim 1/\epsilon$, respectively. Each case will lead to a different solution, presented individually in the three sections which follow this general discussion.

To take advantage of the small parameter, ϵ, the induced current can be expanded in a perturbation series:

$$\langle I_B \rangle (\hat{x}, \hat{t}) = \langle I_B \rangle_0 (\hat{x}, \hat{t}) + \langle I_B \rangle_2 (\hat{x}, \hat{t}) + \ldots \tag{4.53}$$

where $\langle I_B \rangle_2 / \langle I_B \rangle_0 \sim \epsilon^2$. The next step is to substitute this expansion into Eq. (4.50) and then group terms of similar order. Collecting terms of the order ϵ^0 produces the result:

$$\frac{\partial^2 \langle I_B \rangle_0}{\partial \hat{x}^2} = 0 \tag{4.54}$$

while the collecting terms of the order ϵ^2 produces the equation:

$$\frac{\partial^2 \langle I_B \rangle_2}{\partial \hat{x}^2} - \epsilon^2 \frac{\partial \langle I_B \rangle_0}{\partial \hat{t}} = 0 \tag{4.55}$$

The way in which these two equations will be solved depends on the boundary conditions. In general, we are only interested in the zero-th order term and will only obtain $\langle I_B \rangle_2$ if it is a necessary step in solving for $\langle I_B \rangle_0$.

At this point, the ordering of terms in the boundary conditions cannot be identified since we have not yet specified which joint regime is applicable. In each of the sections below, the scaling of the boundary conditions changes, thus producing results with different behavior. At the start of each section, the ϵ^0 order boundary conditions are listed, in accordance with Eqs. (4.29)–(4.31)

Short Length, Open-Circuit Joints

validity regime:

- $\ell \ll \ell_D$
- $\ell \gg \ell_J$

boundary conditions (order ϵ^0):

- $\hat{x} = 0; \quad \langle I_B \rangle_0 = \ell_J b_0'$
- $\hat{x} = 1; \quad \langle I_B \rangle_0 = -\ell_J b_1'$

For this regime, we can solve the current diffusion equation for $\langle I_B \rangle_0$ directly. Equation (4.54) is integrated twice to produce the result:

$$\langle I_B \rangle_0 = C_1(\hat{t})\hat{x} + C_2(\hat{t}) \tag{4.56}$$

where C_1 and C_2 are unknown functions of $\hat{t}$ which, in general, need to be solved using the ϵ^0 order boundary conditions as well as the higher order equations.

In this case, however, C_1 and C_2 can be found directly from the order ϵ^0 boundary conditions (listed above) and the higher order terms are never needed. The solution is:

$$C_1 = -\ell_J(b_0' + b_1') \tag{4.57}$$

$$C_2 = \ell_J b_0' \tag{4.58}$$

For time-scales of interest, the induced current is steady-state with a linear profile:

$$\langle I_B \rangle \approx \langle I_B \rangle_0 = -\ell_J(b_0' + b_1')\hat{x} + \ell_J b_0' \tag{4.59}$$

Rewriting this equation in terms of the primary variables produces:

$$\langle I_B \rangle = \frac{\dot{B}_\perp w \ell_p}{2\pi \Re_J}\left[\sin(\theta_1) - (1 - \frac{x}{\ell})\sin(\theta_0)\right] \tag{4.60}$$

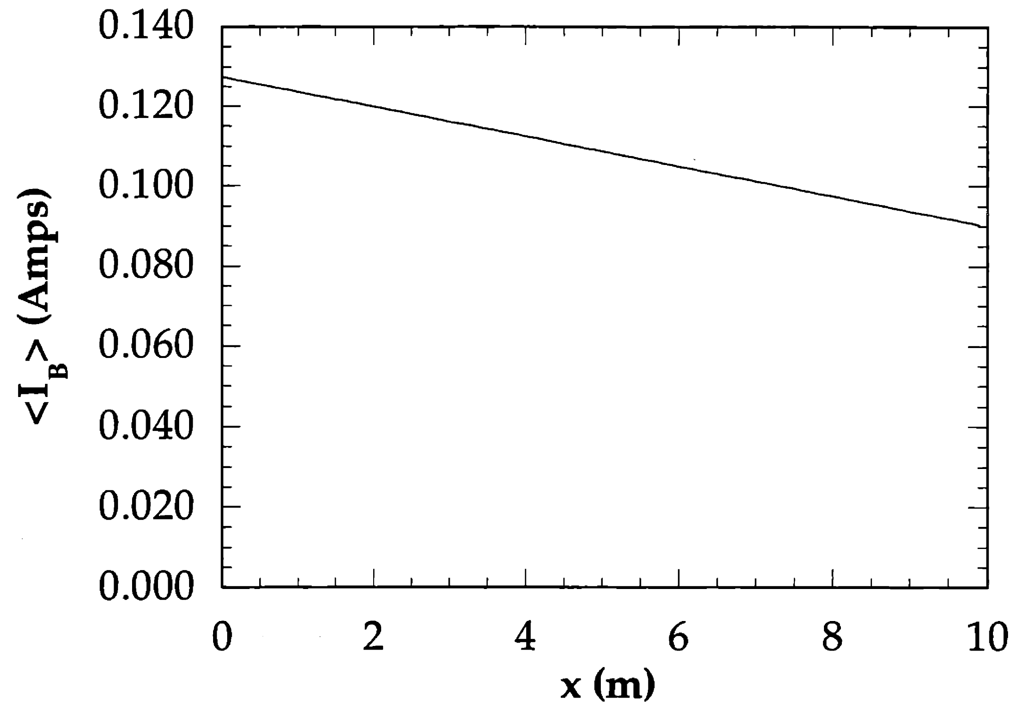

Figure 4-4: Example of circulating current in the Short Length, Open-Circuit Joints Regime.

For the typical cable parameters given in Table 4.4, a joint resistance of $\Re_J = 5 \cdot 10^{-3}\ \Omega$ gives $\ell_J/\ell \ll 1$ thus satisfying the validity criteria for this regime. Evaluating Eq. (4.60) for these values produces the steady-state current profile depicted in Fig. 4-4. Notice that in order to obtain $\ell_J \ll \ell$ the necessary joint resistance, $\Re_J$, is much larger than values which will be considered practical in the thesis. Nonetheless the details of the Short Length, Open-Circuit Joints Regime have been included for the sake of completeness.

Short Length, Resistive Joints

validity regime:

- $\ell \ll \ell_D$
- $\ell \sim \ell_J$

boundary conditions (ϵ^0 order):

- $\hat{x} = 0; \quad \langle I_B \rangle_0 - \frac{\ell_J}{\ell} \frac{\partial \langle I_B \rangle_0}{\partial \hat{x}} = \ell_J b_0'$
- $\hat{x} = 1; \quad \langle I_B \rangle_0 + \frac{\ell_J}{\ell} \frac{\partial \langle I_B \rangle_0}{\partial \hat{x}} = -\ell_J b_1'$

Again, for this regime, we can solve the current diffusion equation for $\langle I_B \rangle_0$ directly. Equation (4.54) is integrated twice to produce the result:

$$\langle I_B \rangle_0 = C_1(\hat{t})\hat{x} + C_2(\hat{t}) \tag{4.61}$$

where C_1 and C_2 can be found directly from the zero-th order boundary conditions (listed above). The solution is:

$$C_1 = \frac{-\ell \ell_J (b_0' + b_1')}{\ell + 2\ell_J} \tag{4.62}$$

$$C_2 = \frac{\ell_J(\ell + \ell_J) b_0' - \ell_J^2 b_1'}{\ell + 2\ell_J} \tag{4.63}$$

For time-scales of interest, the induced current is again steady-state with linear profile, but with more complicated coefficients. Rewriting this equation in terms of the primary variables and dimensional units produces:

$$\langle I_B \rangle = \frac{\dot{B}_\perp w \ell_p}{2\pi \Re_J} \left[\frac{(1 + \sigma_\perp \Re_J x)\sin(\theta_1) - (1 + \sigma_\perp \Re_J (\ell - x))\sin(\theta_0)}{2 + \sigma_\perp \Re_J \ell} \right] \tag{4.64}$$

For the typical cable parameters given in Table 4.4, a joint resistance of $\Re_J = 5 \cdot 10^{-4}\ \Omega$ gives $\ell_J/\ell \sim 1$ thus satisfying the validity criteria for this regime. Evaluating Eq. (4.64) for these values produces the steady-state current profile depicted in Fig. 4-5. Again, the relatively high value of $\Re_J$ needed to match the validity regime

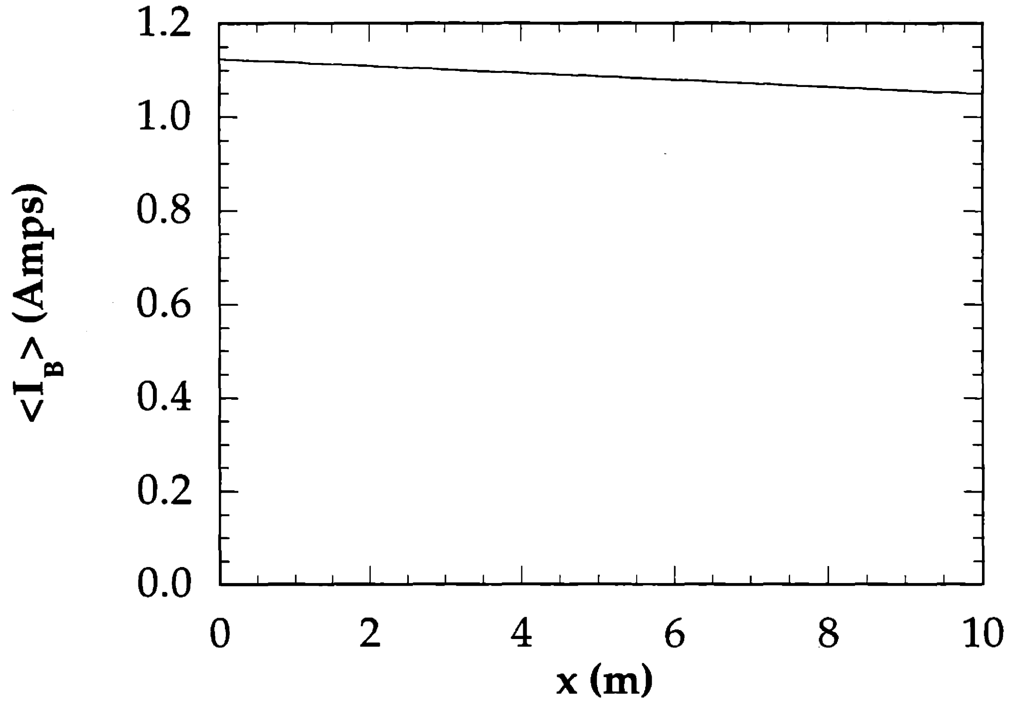

Figure 4-5: Example of circulating current in the Short Length, Resistive Joints Regime.

indicates that this will not be a regime of principal interest when considering actual cable design.

Short Length, Short-Circuit joints

validity regime:

- $\ell \ll \ell_D$
- $\ell_J \gg \ell$

boundary conditions (order $1/\epsilon$):

- $\hat{x} = 0; \quad \frac{\partial \langle I_B \rangle_0}{\partial \hat{x}} = 0$
- $\hat{x} = 1; \quad \frac{\partial \langle I_B \rangle_0}{\partial \hat{x}} = 0$

boundary conditions (orderϵ^0):

- $\hat{x} = 0; \quad \langle I_B \rangle_0 - \frac{\ell_J}{\ell} \frac{\partial \langle I_B \rangle_2}{\partial \hat{x}} = \ell_J b_0'$
- $\hat{x} = 1; \quad \langle I_B \rangle_0 + \frac{\ell_J}{\ell} \frac{\partial \langle I_B \rangle_2}{\partial \hat{x}} = -\ell_J b_1'$

In the short-circuit regime, the large parameter $\ell_J/\ell \sim 1/\epsilon$ elevates the derivative terms of the boundary conditions to $1/\epsilon$ order and thus the derivatives $\langle I_B \rangle_0$ must disappear at $\hat{x} = 0$ and $\hat{x} = 1$.

For this case, we will need to use the second-order equations in order to solve the current diffusion equation for the zero-th order term. Again, the first step is to integrate Eq. (4.54) to produce the result:

$$\langle I_B \rangle_0 = C_1(\hat{t})\hat{x} + C_2(\hat{t}) \tag{4.65}$$

In this instance, however, the $1/\epsilon$ order boundary conditions above are no longer sufficient to entirely specify C_1 and C_2. Both conditions specify $C_1 = 0$ but leave C_2 an unknown function of time, $\hat{t}$. Thus we only learn that $\langle I_B \rangle_0$ has no $\hat{x}$ dependence,

$$\langle I_B \rangle_0 = \langle I_B \rangle_0 (t)$$

To solve for $\langle I_B \rangle_0$, it is necessary to invoke Eq. (4.55) where the terms of order ϵ^2

are balanced. Integrating Eq. (4.55) over the length of the cable, we arrive at

$$\frac{1}{\ell}\left(\left.\frac{\partial\langle I_B\rangle_2}{\partial\hat{x}}\right|_{\hat{x}=1}-\left.\frac{\partial\langle I_B\rangle_2}{\partial\hat{x}}\right|_{\hat{x}=0}\right)-\epsilon^2\frac{\partial\langle I_B\rangle_0}{\partial\hat{t}}=0 \tag{4.66}$$

From the boundary condition for the order-ϵ^2 terms, above,

$$\left.\frac{1}{\ell}\frac{\partial\langle I_B\rangle_2}{\partial\hat{x}}\right|_{\hat{x}=0} = \frac{1}{\ell_J}\langle I_B\rangle_0 - b_0' \tag{4.67}$$

$$\left.\frac{1}{\ell}\frac{\partial\langle I_B\rangle_2}{\partial\hat{x}}\right|_{\hat{x}=1} = -\frac{1}{\ell_J}\langle I_B\rangle_0 - b_1' \tag{4.68}$$

Substituting these results into Eq. (4.66) provides the closure necessary to solve for $\langle I_B\rangle_0$. The resulting ordinary differential equation in time can be solved (with initial condition $\langle I_B\rangle_0$(t=0) = 0) to yield:

$$\langle I_B\rangle_0=\frac{\ell_J}{2}(b_0'-b_1')\left(1-e^{-\hat{t}/\hat{\tau}_J}\right) \tag{4.69}$$

where $\hat{\tau}_J \equiv \tau_J/t_{ramp}$ and $\tau_J \equiv \ell\mathcal{L}/\Re_J$ is the L/R time-constant of a cable with insulated strands. Although we have determined that for this regime the joints are short-circuits compared to the alternate reistive path, $1/(\sigma_\perp\ell)$, the term short-circuit does not imply $\hat{t} \ll \hat{\tau}_J$.

Rewriting Eq. (4.69) in terms of the primary variables produces:

$$\langle I_B\rangle=\frac{\dot{B}_\perp w\ell_p}{4\pi\Re_J}\left(\sin(\theta_1)-\sin(\theta_0)\right)\left(1-e^{-t/\tau_J}\right) \tag{4.70}$$

For the typical cable parameters given in Table 4.4, a joint resistance of $\Re_J = 5\cdot10^{-6}\ \Omega$ gives $\ell_J/\ell \gg 1$ thus satisfying the validity criteria for this regime. Evaluating Eq. (4.70) for these values produces the current profiles depicted in Fig. 4-6 for several values of time, t. The characteristic time-constant for this example is $\tau_J = 1.4$ s. Since the circulating current does not vary over the length of the cable, it makes sense to plot $\langle I_B\rangle$ vs. time, as shown in Fig. 4-7

The value of $\Re_J$ chosen for this example can be considered typical for lab-scale cables. Thus, the solution for the Short Length, Short-Circuit Regime just developed

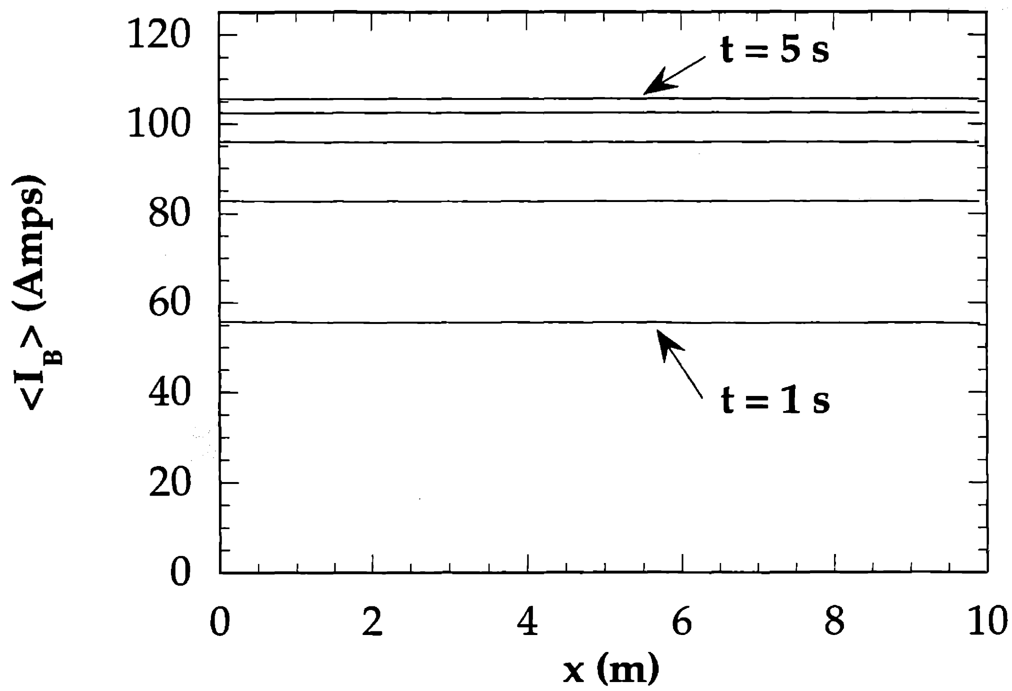

Figure 4-6: Example of circulating current in the Short Length, Short-Circuit Joints Regime.

will be used again in later sections of this thesis when short cables are analyzed.

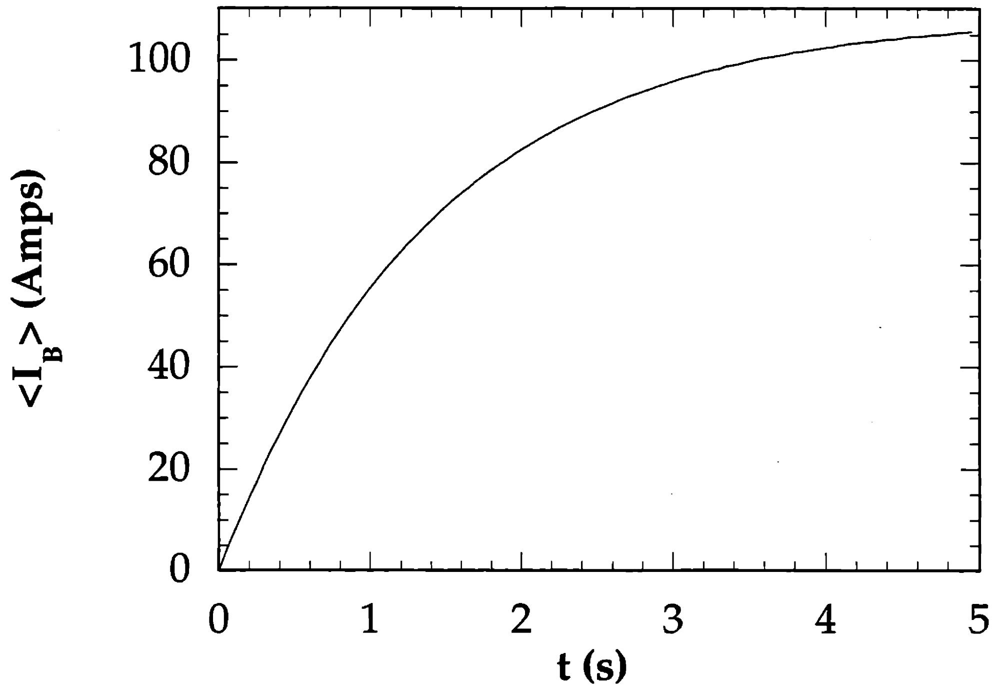

Figure 4-7: Example of circulating current vs. time in the Short Length, Short-Circuit Joints Regime.

Short Cables, Summary

While solutions were found for Short Cables with joints ranging from open-circuit to short-circuit, it was shown that for typical values of joint resistance, $\Re_J$, only the short-circuit regime will be of practical interest for the cables considered in the remainder of this thesis. Focusing then on only the asymptotic limit of short-circuit joints, Eq. (4.70) revealed that the induced currents are uniform in space and exponentially approach a steady-state in time. The characteristic time-constant, $\tau_J = \ell\mathcal{L}/\Re_J$ will be an important factor in the consideration of Ramp-Rate Limitation in short cables, as discussed in Chapter 6.

4.3.3 Finite Length cables, $\ell \sim \ell_D$

When the cable length, ℓ, is of the same order as the diffusion length, ℓ_D, the solutions for the induced currents are more difficult since asymptotic expansions are not possible. Although they can be found, the solutions take the form of infinite series; no closed form exists. Even so, it is still useful to consider the three distinct joint regimes separately as the solutions for open-circuit and short-circuit joints can be found more simply than the general solution for resistive joints.

Since the perturbative expansion used for short cables no longer helps for finite cables, we once again turn to Laplace transform methods. Unfortunately, the inverse transforms no longer converge on closed form solutions. For the cases of open-circuit and short-circuit joints, the inverse transforms correspond to integrals of theta functions, a type of elliptic function which can be represented by rapidly converging series [31]. In the more general case of resistive joints, the solution in transform space has to be inverted by integrating over the complex plane using residue theory. The solution for each case is developed separately below using the now familiar format developed above.

For the finite case, it proves useful to shift the origin of the reference frame to the center of the cable. Thus, the domain $-\frac{\ell}{2} \leq x \leq \frac{\ell}{2}$ will be used in the following sections. The results can easily be shifted back to the original scale when necessary

ℓ	100	m
ℓ_p	$2 \cdot 10^{-1}$	m
w	10^{-2}	m
θ_0	$-\pi/2$	
θ_1	$\pi/4$	
$\sigma_\perp$	100	$\Omega^{-1}\mathrm{m}^{-1}$
$\mathcal{L}$	0.7	μH
$\dot{B}_\perp(0)$	2	T/s
t_{ramp}	5	s
ℓ_D	~ 200	m
b_0'	$\sim 6 \cdot 10^{-2}$	Amps m^{-1}
b_1'	$\sim -4 \cdot 10^{-2}$	Amps m^{-1}

Table 4.5: Cable parameters used in examples for Finite Cable Length Regime.

(i.e., when plotting solutions). A specific example for each solution will be given based on the typical cable described in Table 4.5.[6]

---

[6] The cable parameters are the same as were used for the short case except for the length, ℓ.

Finite Length, Open-Circuit Joints

validity regime:

- $\ell \sim \ell_D$
- $\ell \gg \ell_J$

boundary conditions:

- $x = -\frac{\ell}{2}; \quad \langle I_B \rangle = \ell_J b_0'$
- $x = \frac{\ell}{2}; \quad \langle I_B \rangle = -\ell_J b_1'$

Taking the Laplace transfrom of the current diffusion equation and the appropriate boundary conditions listed above yields:

$$\alpha^2 \frac{\partial^2 Z}{\partial x^2} - pZ = 0 \tag{4.71}$$

$$\begin{aligned} x = -\tfrac{\ell}{2}; \qquad & Z = p^{-1}\ell_J b_0' && (4.72) \\ x = \tfrac{\ell}{2}; \qquad & Z = -p^{-1}\ell_J b_1' && (4.73) \end{aligned}$$

where Z is the transform of $\langle I_B \rangle$ and p is the transform variable. The initial condition is assumed to be $\langle I_B \rangle (t = 0) = 0$. The value of Z is found using standard solution techniques for ordinary differential equations:

$$Z = \frac{\ell_J}{2}\left(b_0' - b_1'\right)\frac{\cosh\left(\frac{\sqrt{p}x}{\alpha}\right)}{p\cosh\left(\frac{\sqrt{p}\ell}{2\alpha}\right)} - \frac{\ell_J}{2}\left(b_0' + b_1'\right)\frac{\sinh\left(\frac{\sqrt{p}x}{\alpha}\right)}{p\sinh\left(\frac{\sqrt{p}\ell}{2\alpha}\right)} \tag{4.74}$$

Using a thorough table of Laplace transforms, the inverse of the first and second terms on the RHS (designated below with the subscripts a and b, respectively) are found to be

$$\begin{aligned} \langle I_B \rangle_a &= -\frac{\ell_J}{\ell}\alpha^2\left(b_0' - b_1'\right)\frac{\partial}{\partial x}\int_0^t \Theta_1\left(\frac{x}{\ell}\middle|\frac{i4\pi\alpha^2 t}{\ell^2}\right)dt && (4.75) \\ \langle I_B \rangle_b &= -\frac{\ell_J}{\ell}\alpha^2\left(b_0' + b_1'\right)\frac{\partial}{\partial x}\int_0^t \Theta_4\left(\frac{x}{\ell}\middle|\frac{i4\pi\alpha^2 t}{\ell^2}\right)dt && (4.76) \end{aligned}$$

where the theta function of the first kind, Θ_1, and the theta function of the fourth kind, Θ_4, are defined as: [31]

$$\begin{aligned} \Theta_1(\nu|\,\tau) &\equiv i\sum_{n=-\infty}^{\infty}(-1)^n e^{i\pi(n-1/2)^2\tau}e^{i\pi(2n-1)\nu} \qquad (4.77)\\ \Theta_4(\nu|\,\tau) &\equiv \sum_{n=-\infty}^{\infty}(-1)^n e^{i\pi n^2\tau}e^{i\pi 2n\nu} \qquad (4.78)\end{aligned}$$

Using these definitions, $\langle I_B\rangle_a$ and $\langle I_B\rangle_b$ can be reduced to:

$$\begin{aligned} \langle I_B\rangle_a &= \frac{-2\ell_J}{\pi}(b_0'-b_1')\sum_{n=1}^{\infty}\frac{(-1)^n}{2n-1}\left(1-e^{-(2n-1)^2\pi^2\alpha^2t/\ell^2}\right)\cos\left(\frac{(2n-1)\pi x}{\ell}\right) \qquad (4.79)\\ \langle I_B\rangle_b &= \frac{2\ell_J}{\pi}(b_0'+b_1')\sum_{n=1}^{\infty}\frac{(-1)^n}{2n}\left(1-e^{-4n^2\pi^2\alpha^2t/\ell^2}\right)\sin\left(\frac{2n\pi x}{\ell}\right) \qquad (4.80)\end{aligned}$$

Rewriting this result in terms of the primary variables gives a better sense of how the circulating currents scale for this case:

$$\langle I_B\rangle = \frac{\dot{B}_\perp w\ell_p}{\pi^2\Re_J}\left\{\begin{array}{c} (\sin\theta_1-\sin\theta_0)\sum_{n=1}^{\infty}\frac{(-1)^n}{2n-1}\left(1-e^{-t/\tau_{a_n}}\right)\cos\left(\frac{(2n-1)\pi x}{\ell}\right)\\ +(\sin\theta_1+\sin\theta_0)\sum_{n=1}^{\infty}\frac{(-1)^n}{2n}\left(1-e^{-t/\tau_{b_n}}\right)\sin\left(\frac{(2n)\pi x}{\ell}\right)\end{array}\right\} \qquad (4.81)$$

where the time constants are defined using the notation

$$\begin{aligned} \tau_\perp &\equiv 2\sigma_\perp\mathcal{L}\ell^2 \qquad (4.82)\\ \tau_{a_n} &\equiv \tau_\perp/(2n\pi-\pi)^2 \qquad (4.83)\\ \tau_{b_n} &\equiv \tau_\perp/(2n\pi)^2 \qquad (4.84)\end{aligned}$$

For Eq. (4.81), x ranges from $-\ell/2 \leq x \leq \ell/2$.

To give a graphical example, the joint resistance $\Re_J = 5\cdot 10^{-4}\ \Omega$ is used. The resulting ratio of the boundary scale to the cable length is, $\ell_J/\ell \ll 1$ thus satisfying the validity regime for this regime. The corresponding results are plotted in Fig. 4-8. In the figure, the x-axis has been re-shifted to the range $0 \leq x \leq \ell$ in order to be consistent with the other figures in this chapter. The solution is plotted for the first 100 terms of the infinite series but in this case more terms would be needed to

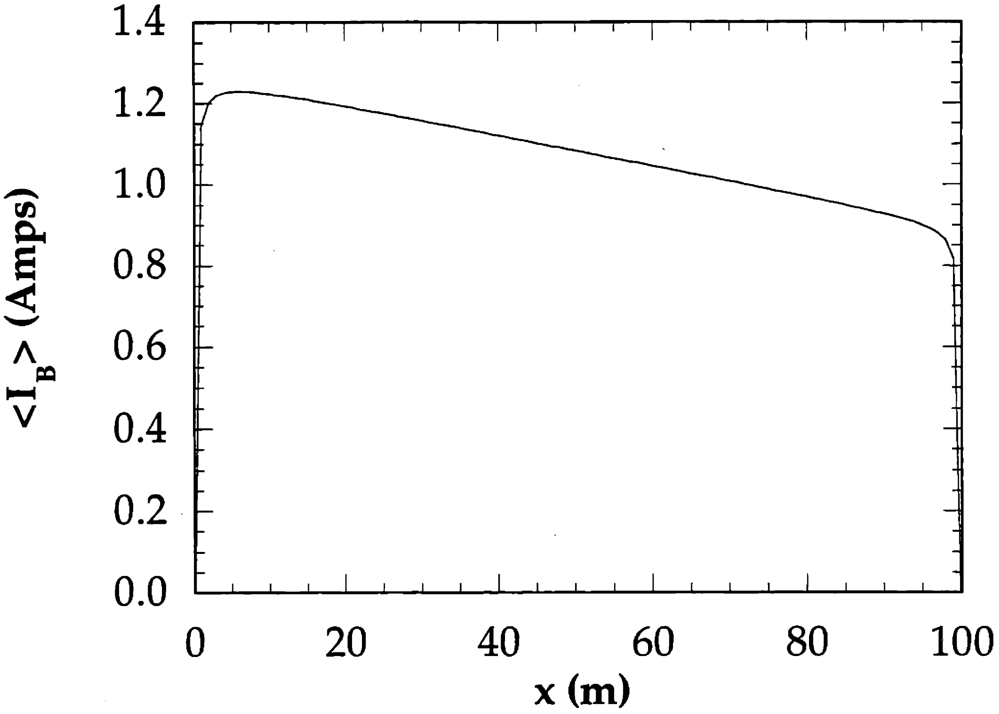

Figure 4-8: Example of circulating current in the Finite Length, Open-Circuit Joints Regime.

achieve better matching at the ends—the solution should be linear in x. Luckily, this limitation will not affect future work as the open-circuit joint regime is not of particular interest for the studies of current distribution.

Finite Length, Short-Circuit Joints

validity regime:

- $\ell \sim \ell_D$
- $\ell_J \gg \ell$

boundary conditions:

- $x = -\frac{\ell}{2}$; $\quad \frac{\partial \langle I_B \rangle}{\partial x} = -b_0'$
- $x = \frac{\ell}{2}$; $\quad \frac{\partial \langle I_B \rangle}{\partial x} = -b_1'$

Taking the Laplace transfrom of the current diffusion equation and the appropriate boundary conditions listed above yields:

$$\alpha^2 \frac{\partial^2 Z}{\partial x^2} - pZ = 0 \tag{4.85}$$

$$\begin{aligned} x = -\tfrac{\ell}{2}; &\qquad \tfrac{\partial Z}{\partial x} &= -p^{-1} b_0' \qquad (4.86) \\ x = \tfrac{\ell}{2}; &\qquad \tfrac{\partial Z}{\partial x} &= -p^{-1} b_1' \qquad (4.87) \end{aligned}$$

where the initial condition is assumed to be $\langle I_B \rangle (t = 0) = 0$. The value of Z is found using standard solution techniques for ordinary differential equations:

$$Z = \frac{\alpha}{2} (b_0' - b_1') \frac{\cosh\left(\frac{\sqrt{p}x}{\alpha}\right)}{p^{3/2} \sinh\left(\frac{\sqrt{p}\ell}{2\alpha}\right)} - \frac{\alpha}{2} (b_0' + b_1') \frac{\sinh\left(\frac{\sqrt{p}x}{\alpha}\right)}{p^{3/2} \cosh\left(\frac{\sqrt{p}\ell}{2\alpha}\right)} \tag{4.88}$$

Using a thorough table of Laplace transforms, the inverse of the first and second terms on the RHS (designated below with the subscripts a and b, respectively) are found to be

$$\begin{aligned} \langle I_B \rangle_a &= \frac{\alpha^2}{\ell} (b_0' - b_1') \int_0^t \Theta_4 \left(\frac{x}{\ell} \middle| \frac{i4\pi\alpha^2 t}{\ell^2} \right) dt \qquad (4.89) \\ \langle I_B \rangle_b &= \frac{\alpha^2}{\ell} (b_0' + b_1') \int_0^t \Theta_1 \left(\frac{x}{\ell} \middle| \frac{i4\pi\alpha^2 t}{\ell^2} \right) dt \qquad (4.90) \end{aligned}$$

where the theta function of the first kind, Θ_1, and the theta function of the fourth kind, Θ_4, are defined in Eqs. (4.77) and (4.78). Using those definitions, $\langle I_B \rangle_a$ and $\langle I_B \rangle_b$ can be reduced to:

$$\begin{aligned} \langle I_B \rangle_a &= \frac{2\ell}{\pi^2}\left(b_0' - b_1'\right)\left[\frac{\pi^2\alpha^2 t}{2\ell^2} + \sum_{n=1}^{\infty}\frac{(-1)^n}{4n^2}\left(1 - e^{-4n^2\pi^2\alpha^2 t/\ell^2}\right)\cos\left(\frac{2n\pi x}{\ell}\right)\right] \quad (4.91) \\ \langle I_B \rangle_b &= \frac{2\ell}{\pi^2}\left(b_0' + b_1'\right)\sum_{n=1}^{\infty}\frac{(-1)^n}{(2n-1)^2}\left(1 - e^{-(2n-1)^2\pi^2\alpha^2 t/\ell^2}\right)\sin\left(\frac{(2n-1)\pi x}{\ell}\right) \quad (4.92) \end{aligned}$$

Writing this result in terms of the primary variables gives a better sense of how the circulating currents scale for this case:

$$\langle I_B \rangle = \frac{\dot{B}_\perp w \ell_p \sigma_\perp \ell}{2\pi}\left\{\begin{array}{l} (\sin\theta_1 - \sin\theta_0)\left[\frac{t}{\tau_\perp} + \frac{2}{\pi^2}\sum_{n=1}^{\infty}\frac{(-1)^n}{(2n)^2}\left(1 - e^{-t/\tau_{b_n}}\right)\cos\left(\frac{2n\pi x}{\ell}\right)\right] \\ -\,(\sin\theta_1 + \sin\theta_0)\frac{2}{\pi^2}\sum_{n=1}^{\infty}\frac{(-1)^n}{(2n-1)^2}\left(1 - e^{-t/\tau_{a_n}}\right)\sin\left(\frac{(2n-1)\pi x}{\ell}\right) \end{array}\right\} \quad (4.93)$$

where the definitions of τ_{a_n}, τ_{b_n} and $\tau_\perp$ were given in Eqs. (4.82) and (4.83). For Eq. (4.93), x ranges from $-\ell/2 \leq x \leq \ell/2$.

To give a graphical example, the joint resistance $\Re_J = 10^{-6}\ \Omega$ is used. The resulting ratio of the boundary scale to the cable length is, $\ell_J/\ell \gg 1$ thus satisfying the validity regime for this regime. The corresponding results are plotted in Fig. 4-9. In the figure, the x-axis has been re-shifted to the range $0 \leq x \leq \ell$ in order to be consistent with the other figures in this chapter.

The behavior of this regime is characteristized by the linear (in time) growth term. For times such that $t \gg \tau_\perp$ the exponential terms will be saturated and the "shape" of the profile will be fixed while its "offset" grows in time. Of course this behavior is limited to the validity regime of this region; for long enough times, the criterion $\ell \sim \ell_D$ is no longer valid.

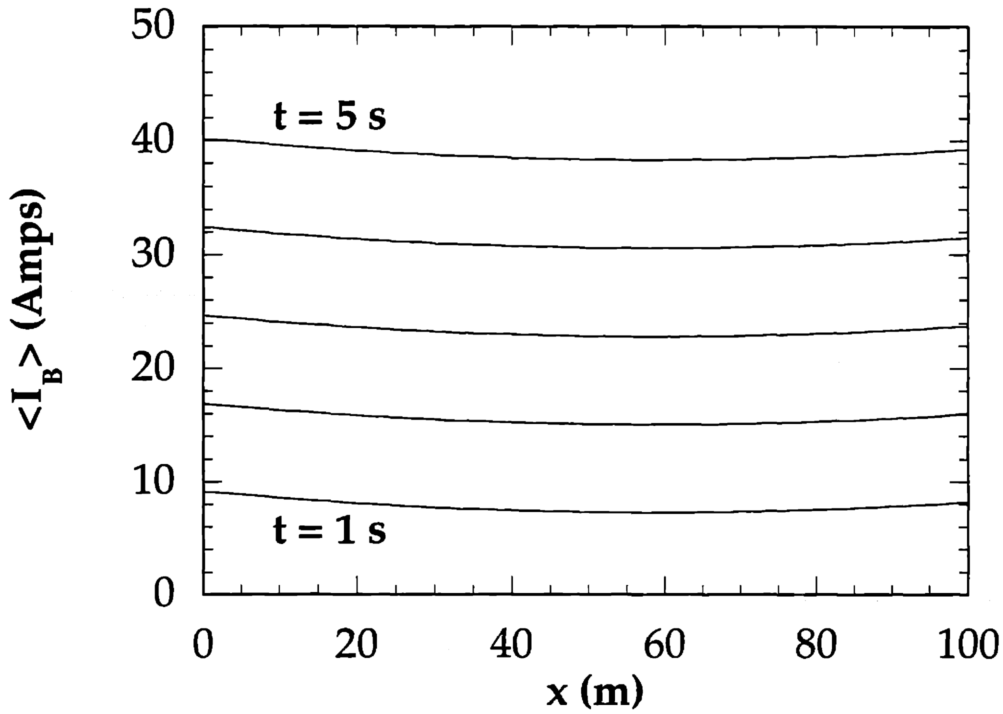

Figure 4-9: Example of circulating current in the Finite Length, Short-Circuit Joints Regime.

Finite Length, Resistive Joints

validity regime:

- $\ell \sim \ell_D$
- $\ell_J \sim \ell$

boundary conditions:

- $x = -\frac{\ell}{2}$; $\langle I_B \rangle - \ell_J \frac{\partial \langle I_B \rangle}{\partial x} = \ell_J b_0'$
- $x = \frac{\ell}{2}$; $\langle I_B \rangle + \ell_J \frac{\partial \langle I_B \rangle}{\partial x} = -\ell_J b_1'$

Taking the Laplace transfrom of the current diffusion equation and the appropriate boundary conditions listed above yields:

$$\alpha^2 \frac{\partial^2 Z}{\partial x^2} - pZ = 0 \tag{4.94}$$

$$\begin{aligned} x = -\tfrac{\ell}{2}; \qquad & Z - \ell_J \tfrac{\partial Z}{\partial x} &= \ p^{-1} \ell_J b_0' \qquad (4.95) \\ x = \tfrac{\ell}{2}; \qquad & Z + \ell_J \tfrac{\partial Z}{\partial x} &= \ -p^{-1} \ell_J b_1' \qquad (4.96) \end{aligned}$$

where the initial condition is assumed to be $\langle I_B \rangle (t = 0) = 0$. The value of $Z$is found using standard solution techniques for ordinary differential equations:

$$\begin{aligned} Z \ = \ & \frac{\ell_J}{2} (b_0' - b_1') \frac{\cosh\left(\frac{\sqrt{p}x}{\alpha}\right)}{p\left[\cosh\left(\frac{\sqrt{p}\ell}{2\alpha}\right) + \frac{\sqrt{p}\ell_J}{\alpha} \sinh\left(\frac{\sqrt{p}\ell}{2\alpha}\right)\right]} \\ & - \frac{\ell_J}{2} (b_0' + b_1') \frac{\sinh\left(\frac{\sqrt{p}x}{\alpha}\right)}{p\left[\sinh\left(\frac{\sqrt{p}\ell}{2\alpha}\right) + \frac{\sqrt{p}\ell_J}{\alpha} \cosh\left(\frac{\sqrt{p}\ell}{2\alpha}\right)\right]} \end{aligned} \tag{4.97}$$

Unfortunately, our trusty thorough table of Laplace transforms will not have the inverse of the the above function, even in series form. In this case, the inverse can be found using contour integration and residue calculus. Since the mathematics become quite involved, the details are presented in Appendix A. The resulting series is:

$$\begin{aligned}\langle I_B\rangle = & \\ & \frac{\ell_J}{2}\left(b_0'-b_1'\right)\left[1+\sum_{n=1}^{\infty}\left(\frac{e^{-4\hat{k}_n^2\alpha^2 t/\ell^2}\cos\left(\hat{k}_n\frac{x}{\ell}\right)}{\cos\left(\hat{k}_n\right)-\left(\frac{1}{2}+3\frac{\ell_J}{\ell}\right)\hat{k}_n\sin\left(\hat{k}_n\right)-\frac{\ell_J}{\ell}\hat{k}_n^2\cos\left(\hat{k}_n\right)}\right)\right] \\ & -\frac{\ell_J}{2}\left(b_0'+b_1'\right)\left[\frac{x}{\ell_J+\frac{\ell}{2}}+\sum_{n=1}^{\infty}\left(\frac{e^{-4\check{k}_n^2\alpha^2 t/\ell^2}\sin\left(\check{k}_n\frac{x}{\ell}\right)}{\sin\left(\check{k}_n\right)+\left(\frac{1}{2}+3\frac{\ell_J}{\ell}\right)\check{k}_n\cos\left(\check{k}_n\right)-\frac{\ell_J}{\ell}\check{k}_n^2\sin\left(\check{k}_n\right)}\right)\right]\end{aligned} \tag{4.98}$$

where $\hat{k}_n$ and $\check{k}_n$ are the n-th positive solutions to the transcendental equations:

$$\hat{k}_n\tan\left(\hat{k}_n\right) = \frac{\ell}{2\ell_J}\,; \qquad n>0 \tag{4.99}$$

$$\check{k}_n\cot\left(\check{k}_n\right) = -\frac{\ell}{2\ell_J}\,; \qquad n>0 \tag{4.100}$$

for $n = 1,2,3\ldots\infty$.

Writing the final result in terms of the primary variables is more difficult due to the non-explicit nature of the $\hat{k}_n$ and $\check{k}_n$ terms, but reducing the remaining terms gives a better sense of how the circulating currents scale for this case:

$$\langle I_B\rangle = \frac{\dot{B}_\perp w\ell_p\sigma_\perp\ell}{2\pi\Re_J}\left\{\begin{array}{l}\left(\sin\theta_1-\sin\theta_0\right)\left[1+\sum_{n=1}^{\infty}\hat{C}_n e^{-t/\hat{\tau}_n}\cos\left(\frac{\hat{k}_n x}{\ell}\right)\right] \\ \quad+\left(\sin\theta_1+\sin\theta_0\right)\left[\frac{2\sigma_\perp\Re_J x}{2+\sigma_\perp\Re_J\ell}\sum_{n=1}^{\infty}\check{C}_n e^{-t/\check{\tau}_n}\sin\left(\frac{\check{k}_n x}{\ell}\right)\right]\end{array}\right\} \tag{4.101}$$

where the definitions of the time-constants $\hat{\tau}_n$ and $\check{\tau}_n$ as well as the coefficients $\hat{C}_n$ and $\check{C}_n$ are related to the eigenvalues $\hat{k}_n$ and $\check{k}_n$:

$$\hat{\tau}_n = 2\sigma_\perp\mathcal{L}\ell^2\left(2\hat{k}_n\right)^2 \tag{4.102}$$

$$\check{\tau}_n = 2\sigma_\perp\mathcal{L}\ell^2\left(2\check{k}_n\right)^2 \tag{4.103}$$

$$\hat{C}_n = \left[\cos\left(\hat{k}_n\right)-\left(\frac{1}{2}+\frac{3}{\sigma_\perp\Re_J\ell}\right)\hat{k}_n\sin\left(\hat{k}_n\right)-\frac{1}{\sigma_\perp\Re_J\ell}\hat{k}_n^2\cos\left(\hat{k}_n\right)\right]^{-1} \tag{4.104}$$

$$\check{C}_n = \left[\sin\left(\check{k}_n\right)+\left(\frac{1}{2}+\frac{3}{\sigma_\perp\Re_J\ell}\right)\check{k}_n\cos\left(\check{k}_n\right)-\frac{1}{\sigma_\perp\Re_J\ell}\check{k}_n^2\sin\left(\check{k}_n\right)\right]^{-1} \tag{4.105}$$

where $n = 1,2,3\ldots\infty$. For Eq. (4.101), x ranges from $-\ell/2 \le x \le \ell/2$.

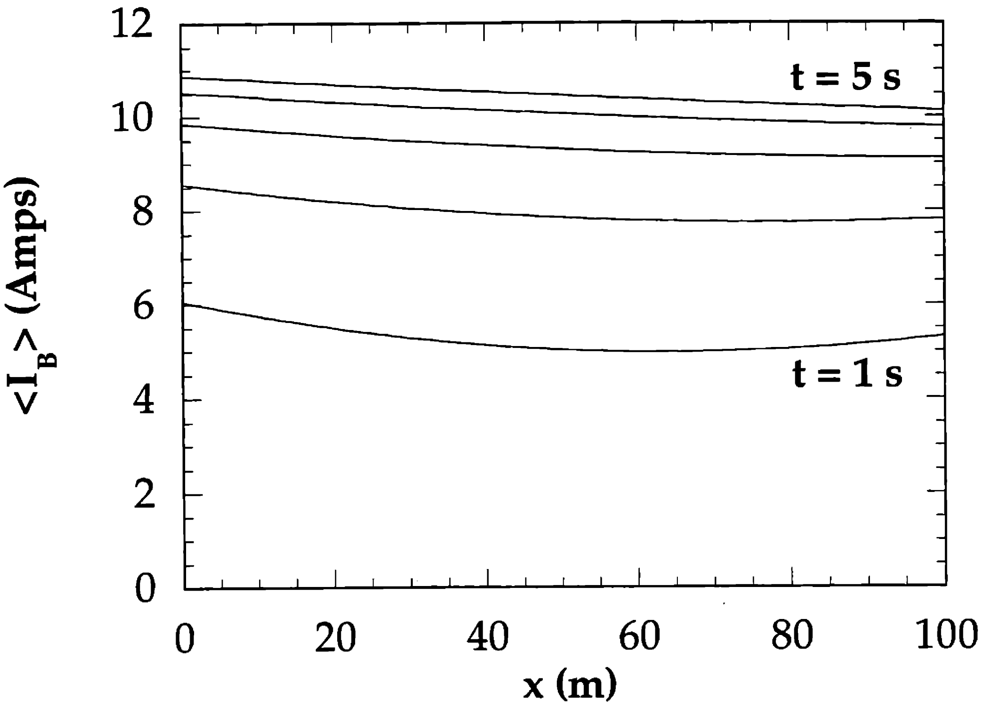

Figure 4-10: Example of circulating current in the Finite Length, Resistive Joints Regime.

To give a graphical example, the joint resistance $\Re_J = 5 \cdot 10^{-5}\ \Omega$ is used. The resulting ratio of the boundary scale to the cable length is, $\ell_J/\ell \sim 1$ thus satisfying the validity conditions for this regime. The corresponding results are plotted in Fig. 4-10. In the figure, the x-axis has been re-shifted to the range $0 \leq x \leq \ell$ in order to be consistent with the other figures in this chapter.

Although we have limited the validity region of this regime to cables in which $\ell \sim \ell_J \sim \ell_D$, this result, Eq. (4.101), is actually valid globally. It is only in this regime, however, when no asymptotic limits can be taken that this full solution is necessary. Since Eq. (4.101) cannot be written explicitly (i.e. $\hat{k}_n$ and $\check{k}_n$ are roots of a transcendental equation), it is very useful to have independent, explicit solutions for the other regimes.

Finite Cables, Summary

The solutions for the circulating currents in finite cables were found for the range of joint regimes from open-circuit to short-circuit. In each case, the solution was given in the form of an infinite series. While the series solution for the open-circuit case did not converge well at the endpoints $x = 0$ and $x = \ell$, the solutions for the resistive and short-circuit cases exhibited rapid convergence.

For the short-circuit and open-circuit joint regimes, the characteristic time-constants and scaling factors could be calculated explicitly. For resistive joints, however, the time–constants and scaling factors have to be found through solving transcendental equations. For this reason, the Finite-Resistive solution is reserved for the case when no other solution is applicable even though it can actually be used for all cases.

4.4 Conclusion

In this chapter, the domain of operation known as the Superconducting Domain was identified. Basically, the Superconducting Domain is defined by the criterion: $I < I_c$. In this domain, the resistance of the strands is negligible and the current diffusion equation can be solved analytically. Since the governing equation (in this domain) is linear, the induced current, I_B, and transport current, I_T, can be solved separately and later superposed. The goal of this chapter was thus to solve for the induced currents in the Superconducting Domain.

As shown in Chapter 3, the simplicity of the two strand model allows us to focus exclusively on the current in strand *one*, which for convenience is referred to simply as I. The current in strand *two* is related to I through the equation: $I_2 = I_T - I$.

A multiple length scale analysis further divided the induced currents into two components: the circulating current, $\langle I_B \rangle$, and the interstrand coupling current, $\tilde{I}_B$. The circulating currents have been identified as important determinants of current distribution and Ramp-Rate Limitation. While the interstrand coupling currents are interesting in there own right from the point of view of AC losses, they are needed here only to resolve the boundary conditions on the circulating current equation.

The multiple length scale expansion resulted in a homogenous diffusion equation for the circulating current:

$$\alpha^2 \frac{\partial^2 \langle I_B \rangle}{\partial \bar{x}^2} - \frac{\partial \langle I_B \rangle}{\partial t} = 0 \tag{4.106}$$

The difficulty in solving this equation arose from the need to satisfy boundary conditions of mixed-type at either end of the cable:

$$x = 0; \qquad \langle I_B \rangle - \ell_J \frac{\partial \langle I_B \rangle}{\partial x} = \ell_J \frac{\partial \tilde{I}_B}{\partial x} \tag{4.107}$$

$$x = \ell; \qquad \langle I_B \rangle + \ell_J \frac{\partial \langle I_B \rangle}{\partial x} = -\ell_J \frac{\partial \tilde{I}_B}{\partial x} \tag{4.108}$$

where the spatial derivative of the interstrand coupling current, $\frac{\partial}{\partial x}\tilde{I}_B$ is a known value.

Although a general solution to Eqs. (4.106)–(4.108) was eventually developed, it suffered from two drawbacks: the solution could only be expresed as an infinite series and the coefficients were not explicit—they were roots of transcendental equations. To avoid these difficulties, it proved useful to find closed form analytic solutions for different regimes of operation wherever possible.

To identify asymptotic limits in which closed form analytic solutions were available, two characteristic length scales were introduced: the diffusion length, $\ell_D = \sqrt{t_{ramp}}/\sqrt{2\sigma_\perp \mathcal{L}}$, and the boundary scale, $\ell_J = (\sigma_\perp \Re_J)^{-1}$. The different possible relative orderings of ℓ_D, ℓ_J and the cable length, ℓ, resulted in a 3 x 3 matrix which described the different operating regimes. A graphical depiction of these regimes and their boundaries is given in Fig. 4-11.

For each of the three cable length regimes (infinite, finite, short) a separate solution technique was needed to find an analytic solution to the current diffusion equation, Eq. (4.106). Additionally, for each of the three joint regimes (open-circuit, resistive, short-circuit), different asymptotic limits of the boundary coditions, Eqs. (4.107) and (4.108), was needed. Solutions for the circulating current, $\langle I_B \rangle$, in each of the nine resulting possibilities were discussed individually in Section 4.3. Rather than tabulat-

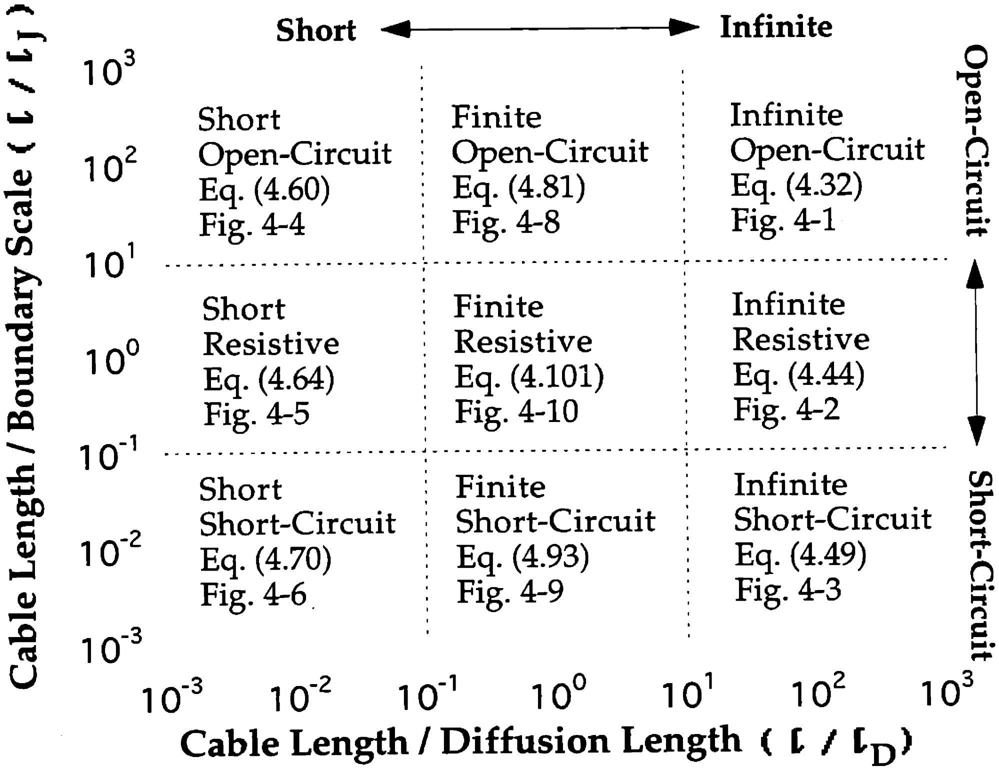

Figure 4-11: The 3 x 3 matrix of operating regimes. ($\ell_D = \sqrt{t_{ramp}}/\sqrt{2\sigma_\perp \mathcal{L}}$, $\ell_J = (\sigma_\perp \Re_J)^{-1}$)

ing the nine results here, reference is made to the appropriate equations in Fig. 4-11. The same figure also refers to plots of the solution in each regime for representative cable parameters. The equations and figures do not include the transport current for each strand, $I_{T/2}$; the total strand *one* current would be $I = I_{T/2} + \langle I_B \rangle$ where $I_{T/2}$ is an independently determined quantity.

Each solution is dependent in some way on the arbitrary angle, θ. In order to present the solutions as simply as possible, the values of θ used in the examples were chosen to highlight the different features of the model. A thorough discussion of the importance of θ and how it might best be characterized is reserved for Chapter 7.

In the examples presented for the nine different operating regimes, the magnitude of the circulating current varied over a large range. In some cases, the induced current was negligible compared to expected values of the transport current per strand ($I_{T/2} \sim 100$ Amps). In other cases, the induced current is large enough to actually affect the stability of the cable. Naturally, we will tend to focus on the cases in which $\langle I_B \rangle$ is large enough to cause concern.

From this point of view, one regime of particular interest was identified as the Short Cable/Short-Circuit Joint regime which was valid for lab-scale cables with a wide range of joint resistances. In this regime, the circulating currents can be of the same order of magnitude as the transport current per strand. This case is studied extensively in Chapter 6.

The Finite Length/Resistive Joint and Finite Length/Short-Circuit Joint regimes are also of interest since the induced currents can range from approximately 5% to 20% of the transport current for typical cable parameters. The Finite Length Regime will be treated in Chapter 5.

The Infinite regimes proved less interesting because the induced currents were generally small and did not diffuse to the central, high-field region of the cable. This may suggest that short test cables used to model the behavior of large magnet systems will be much more susceptible to Ramp-Rate Limitation and cause unnecessary worry for magnet designers.

The current distribution in the Superconducting Domain (as calculated using the analytic results of this chapter) will serve as the initial conditions for the Resistive Domain considered in the next chapter. With a simple model of the critical current as a function of magnetic field, the analytic solutions for the current, I, can be solved for the transition point $I(x,t) = I_c(x,t)$ for the earliest possible time, t. At this point, the strand resistance is no longer negligible and the analytic solutions are no longer valid.

Of course, it is possible for the ramping field and current to reach "flat-top" at time $t = t_{ramp}$ before the onset of the Resistive Domain. After flat-top, $\dot{B}_{\perp} = 0$ and thus the induced currents start to decay. Thus, if I is not greater than I_c at some point during the ramp, the cable never enters the Resistive Domain.

Even without considering the non-linear Resistive Domain, the results of this chapter already point to several important conclusions. First, the magnitude of the circulating currents, and thus the imbalance in current distribution, depends only on the transverse magnetic field at the joints, $\dot{B}_{\perp}(x = 0)$ and $\dot{B}_{\perp}(x = \ell)$. While the peak field (usually at the center of the cable, $x = \ell/2$), is important for calculating the critical current, it does not directly affect current distribution in the Superconducting Domain. One implication of this finding is that when modeling large magnet systems using smaller scale experiments, it is important to consider both the peak field as well as the field at the joints.

Another important conclusion was the definition of the 3 x 3 matrix of operating regimes. Again, experimental comparisons of the effects of current distribution in differing magnet designs need to take account of the possibly different regimes of operation for each cable.

Chapter 5

Current Distribution and Stability Analysis in the Resistive Domain for Full-Scale Magnets

In this chapter, the current distribution in a two-strand cable will be studied for the case when one or both strands become resistive. Unlike Chapter 4 where analytical solutions were found for the Superconducting Domain, this chapter will focus on the numerical solutions of the coupled electrical and thermal equations which define the two-strand model in the Resistive Domain. Special attention will be paid to the notion of stability in full-scale magnets while lab-scale cables will be studied extensively in the next chapter.

The Resistive Domain is defined simply as the complement of the Superconducting Domain; if either strand is resistive over any portion of its length, the Superconducting Domain is no longer valid and the cable is said to be in the Resistive Domain. This chapter begins with a description of the transition from the Superconducting Domain to the Resistive Domain and then develops the electrical and thermal equations necessary to fully characterize the cable's behavior when the strands become resistive. The validity regime of the Resistive Domain is limited to a brief period of time in order to take advantage of the incompressibile helium assumption which applies only during the initial phases of heating. As such, the Resistive Domain model is adequate for studying stability but is inadequate for studying the full quench evolution.

Since the Resistive Domain equations form a non-linear set of second-order partial differential equations, numerical techniques must be employed to solve the model. The details of the numerics are developed in Section 5.3.

In Section 5.4, an example scenario is presented to highlight the general features of the behavior of full-scale magnets in the Resistive Domain. The numerical results are presented graphically and lead to the conclusion that full-scale magnets are unconditionally unstable in the Resistive Domain. The discussion of lab-scale magnets, which behave very differently, is postponed until Chapter 6.

5.1 Onset of the Resistive Domain

The solutions derived for the Superconducting Domain in Chapter 4 are valid for $t \leq t_\star$ where $t_\star$ is the time at which the current in strand *one* first reaches the critical current at any point along the cable. In other words, $t_\star$ is found by solving the equation:

$$\min[I_c(x,t_\star) - I_{SCdomain}(x,t_\star)] = 0 \tag{5.1}$$

where I_c is a specified function of magnetic field and temperature and $I_{SCdomain}$, is the total current in strand *one*, expressed analytically using the results of Chapter 4. The min operator works by scanning the range $0 \leq x \leq \ell$ to find which x minimizes the value of its argument. While both I_c and $I_{SCdomain}$ are expressed analytically, it is in general impossible to solve Eq. (5.1) explicitly. Even so, standard root finding techniques can be used to quickly converge on $t_\star$. The functional dependence of I_c was defined in Eq. (3.2) and is repeated here for ease of reference:

$$I_c(B,T) = \begin{cases} \frac{\xi}{B}(1 - \frac{T-T_b}{T_c-T_b}) & T < T_c(B) \\ 0 & T \geq T_c(B) \end{cases} \tag{5.2}$$

where:

$$T_c(B) = \begin{cases} T_b + (T_{c0} - T_b)(1 - \frac{B}{B_{c0}}) & B < B_{c0} \\ T_b & B \geq B_{c0} \end{cases} \tag{5.3}$$

and ξ, T_{c0}, and B_{c0} are characteristic properties of the superconductor, as explained in Section 3.3.1. Typical values are: $\xi = 1250$ AT, $T_{c0} = 18$ K, $B_{c0} = 19$ T.

For $t < t_\star$ the strands are in the Superconducting Domain and the current distribution can be calculated analytically. For $t > t_\star$ the strands are in the Resistive Domain and the current distribution is now coupled to the thermal equations. The new system of equations needs to be solved numerically, starting from the analytically calculated initial condition $I(x, t_\star) = I_{SCdomain}(x, t_\star)$.

5.2 Resistive Domain Model Equations

The electrical equations for the two-strand model were developed for the general case in Chapter 3. At the time, however, the temperature dependent strand resistances, $\mathcal{R}_1$ and $\mathcal{R}_2$, were left as arbitrary functions of the strand temperatures, T_1 and T_2, respectively. At this point, then, it becomes necessary to specify the definition of strand resistance and introduce the thermal equations which only become important in the Resistive Domain.

5.2.1 Electrical Equation in the Resistive Domain

The general equation for current distribution and the appropriate boundary conditions were developed in Eq. (3.22) and are repeated here:

$$\frac{1}{\sigma_\perp}\frac{\partial^2 I}{\partial x^2} - 2\mathcal{L}\frac{\partial I}{\partial t} - (\mathcal{R}_1 + \mathcal{R}_2)I = -\frac{\partial B_\perp}{\partial t} w \cos\left(\frac{2\pi x}{\ell_p} + \theta\right) - \mathcal{L}\frac{\partial I_T}{\partial t} - \mathcal{R}_2 I_T \tag{5.4}$$

$$\begin{aligned} x = 0; \qquad I - \ell_J \frac{\partial I}{\partial x} &= I_{T/2} & (5.5) \\ x = \ell; \qquad I + \ell_J \frac{\partial I}{\partial x} &= I_{T/2} & (5.6) \end{aligned}$$

where $I = I_1$, the current in strand *one*.

In Chapter 4, a local averaging technique was used in the Superconducting Domain to isolate the interstrand coupling currents, which are characterized by the length scale ℓ_p, from the longer length scale components of the current distribution. Without repeating the details, (refer to Section 4.2.2), this procedure can again be used in the Resistive Domain—this time keeping the resistive terms $\mathcal{R}_1$ and $\mathcal{R}_2$. The resulting equation is: [1]

$$\alpha^2 \frac{\partial^2 I}{\partial x^2} - \frac{\partial I}{\partial t} - \frac{1}{2\mathcal{L}} \left(\mathcal{R}_1 + \mathcal{R}_2 \right) I = -\frac{1}{\mathcal{L}} \mathcal{R}_2 I_{T/2} - \frac{\partial I_{T/2}}{\partial t} \tag{5.7}$$

$$\begin{aligned} x = 0; \qquad I - \ell_J \frac{\partial I}{\partial x} &= -\ell_J \frac{\dot{B}_\perp w \ell_p \sigma_\perp}{2\pi} \sin\theta_0 + I_{T/2} && (5.8) \\ x = \ell; \qquad I + \ell_J \frac{\partial I}{\partial x} &= \ell_J \frac{\dot{B}_\perp w \ell_p \sigma_\perp}{2\pi} \sin\theta_1 + I_{T/2} && (5.9) \end{aligned}$$

where I represents the total current in strand *one* (transport current plus induced current) locally averaged over the twist-pitch length, ℓ_p. As defined previously: $I_{T/2} = I_T/2$, $\ell_J = (\sigma_\perp \Re_J)^{-1}$, $\alpha^2 = (2\sigma_\perp \mathcal{L})^{-1}$ and θ_0 and θ_1 represent the orientation of the joints with respect to the direction of the magnetic field at $x = 0$ and $x = \ell$, respectively.

Non-linear Strand Resistance

The strand resistances, $\mathcal{R}_1$ and $\mathcal{R}_2$, will now be defined. In general, $\mathcal{R}$ is a function of the strand current, I, and the temperature and field dependent critical current, I_c:

$$\begin{aligned} \mathcal{R}(x,t) &= \mathcal{R}\left(I(x,t), I_c(x,t)\right) \\ I_c(x,t) &= I_c\left(B(x,t), T(x,t)\right) \end{aligned}$$

Since the strand is a composite, the overall electrical resistance of a single strand is equivalent to the resistance of two parallel paths: one path through the superconducting filaments and the other through the matrix. In Chapter 4 we ascertained that the resistance of the superconducting path is negligible when the strand current

---

[1] For ease of presentation, the notation $\langle I \rangle$ introduced in Chapter 4 is shortened to I for the purposes of this chapter.

is less than the critical current. Thus, $\mathcal{R} = 0$ when $I < I_c$.

When the current in the strand is greater than the critical value, however, the superconducting filaments develop a "flux-flow" resistance and the current begins to be resistively shared between the superconductor and the matrix [12, 32]. Because the flux-flow resistivity is much greater than the resistivity of the matrix, the superconductor in effect carries only an amount of current equal to the critical current, I_c. The remainder, $I - I_c$, travels through the matrix. The resistive voltage per length in this case is $I\mathcal{R} = \mathcal{R}_m(I - I_c)$. Thus the non-linear resistance can be defined as:

$$\mathcal{R} = \begin{cases} 0 & I \le I_c(B,T) \\ \mathcal{R}_m(I - I_c)/I & I > I_c(B,T) \end{cases} \tag{5.10}$$

where $\mathcal{R}_m$ is the resistance per unit length of the matrix material defined as

$$\mathcal{R}_m = \frac{\eta_m}{(1-\lambda)A_s}$$

where λ is the volume fraction of superconductor in the strand, η_m is the resistivity of the matrix and A_s is the cross-sectional area of a strand. $\mathcal{R}$ as a function of I/I_c is depicted in Fig. 5-1

Since the current and temperature of strands *one* and *two* are distinct, correctly calculating $\mathcal{R}_1$ and $\mathcal{R}_2$ from Eq. (5.10) involves a little book-keeping:

$$\mathcal{R}_1 = \mathcal{R}(I_1, I_{c_1}) \tag{5.11}$$

$$\mathcal{R}_2 = \mathcal{R}(I_2, I_{c_2}) \tag{5.12}$$

where $I_1 = I$, $I_2 = I_T - I$, $I_{c_1} = I_c(B, T_1)$, and $I_{c_2} = I_c(B, T_2)$. The fact that I_c depends on the temperature is what couples the electrical equation to the thermal equation within the Resistive Domain.

The resistance relations defined in Eqs. (5.11) and (5.12) complete the electrical model given in Eq. (5.7). That equation is valid only in the Resistive Domain, $t > t_\star$, where the initial condition at $t = t_\star$ is found from the analytic solutions to the

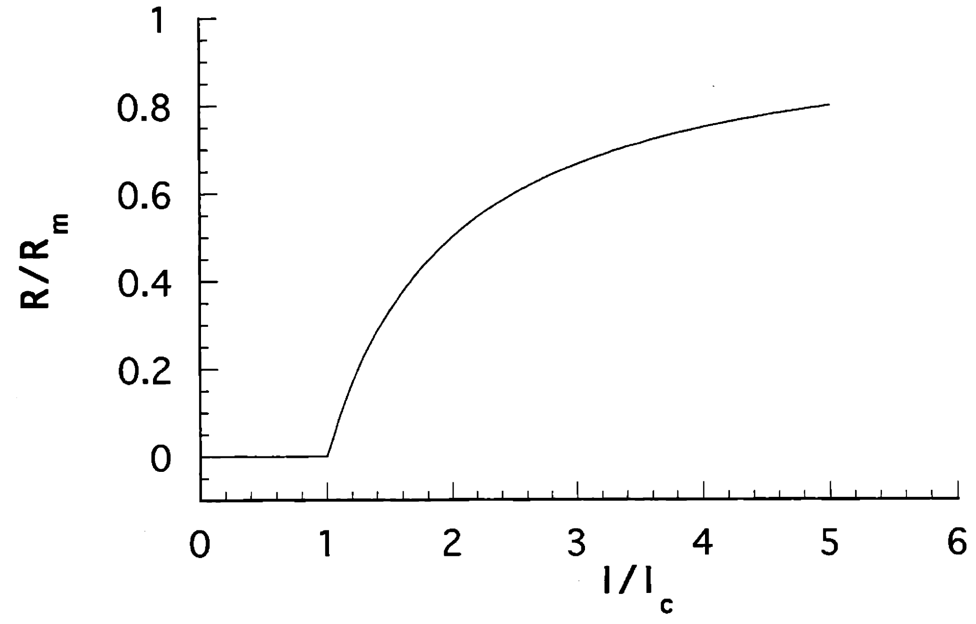

Figure 5-1: Non-linear strand resistance, $\mathcal{R}$, per length.

Superconducting Domain equations.

5.2.2 Temperature Equations in the Resistive Domain

Once the model enters the Resistive Domain, Joule heating occurs and the strand temperatures begin to rise. As shown in the previous section, the rising temperatures change the resistances of the strands, thus coupling the thermal equations to the electrical equation. The thermal portion of the two-strand model is now introduced.

The thermal portion of the model is similar to the one-dimensional model used in the Quencher code developed by A. Shajii, [33]. The Quencher model was designed to simulate quench propagation within cable-in-conduit conductors as the result of externally applied heat loads. In that model, the current distribution was considered uniform across the cross-section of the cable and the transport current was a known function of time. As a result, the thermal equations themselves formed a closed system and there was no coupling to an electrical model.

The Quencher model is derived from the general 3-D mass, momentum, and energy equations for the conductor and the helium coolant. The 3-D equations are then reduced to a 1-D model appropriate for cables in a cryogenic environment. It is this 1-D model which will be used as the basis of the thermal model presented here. The Quencher model goes on to take further limits of the 1-D model which are appropriate for analyzing the development of quenches induced by external heat sources. These limits, however, are not the appropriate limits for the study of quench/recovery events caused by uneven current distribution in the cable. The final two-strand thermal model is therefore significantly different than the existing Quencher model.

The 1-D thermal equations as derived in [33] are given here for ease of reference.

Cable Energy Equation:

$$\rho_c C_c A_c \frac{\partial T_c}{\partial t} = A_c \frac{\partial}{\partial x} \kappa_c \frac{\partial T_c}{\partial x} + Q - hp(T_c - T_h) \tag{5.13}$$

Conduit Wall Energy Equation:

$$\rho_w C_w A_w \frac{\partial T_w}{\partial t} = A_w \frac{\partial}{\partial x} \kappa_w \frac{\partial T_w}{\partial x} - hp(T_w - T_h) \tag{5.14}$$

Helium Mass, Momentum, Energy and State Equations:

$$\begin{aligned}
\frac{\partial \rho_h}{\partial t} + \frac{\partial}{\partial x}(\rho_h v_h) &= 0 & (5.15)\\
\rho_h \frac{\partial v_h}{\partial t} + \rho_h v_h \frac{\partial v_h}{\partial x} &= -\frac{\partial P_h}{\partial x} - \frac{f \rho_h |v_h| v_h}{2 d_h} & (5.16)\\
\rho_h C_h A_h \left(\frac{\partial T_h}{\partial t} + v_h \frac{\partial T_h}{\partial x} \right) + \rho_h C_\beta A_h T_h \frac{\partial v_h}{\partial x} &= hp(T_c - T_h) + hp(T_w - T_h) \\
&\quad + \frac{f \rho_h A_h |v_h| v_h^2}{2 d_h} & (5.17)\\
P_h &= P_h(\rho_h, T) & (5.18)
\end{aligned}$$

where the subscripts "c", "w", and "h" stand for cable, wall and helium, respectively. Standard notation is used for the material properties and flow parameters while the quantity Q represents the Joule heating in the cable. The notation will be introduced formally as each equation is discussed in detail below. The geometry of the problem

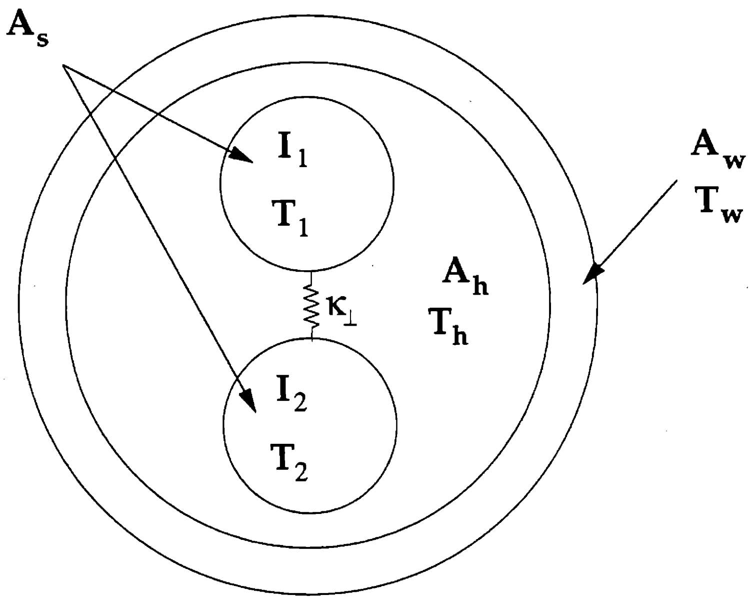

Figure 5-2: Cross-section of two-strand model geometry

under consideration is diagrammed in cross-section in Fig. 5-2.

We will now make the necessary modifications and limiting assumptions to obtain the final 1-D thermal model to be used throughout the rest of this thesis.

The Strand Equations

In the present model, the non-uniform current distribution results in differing amounts of Joule heating in the two strands and thus requires different temperature equations for each. Dividing the energy equation for the whole cable, Eq. (5.13), into two produces:

$$\rho_s C_s A_s \frac{\partial T_1}{\partial t} =$$

$$A_s \frac{\partial}{\partial x} \kappa_s \frac{\partial T_1}{\partial x} - \kappa_\perp (T_1 - T_2) - hp(T_1 - T_h) + \mathcal{R}_1(I_1, I_{c_1}) I_1^2 + \frac{1}{2\sigma_\perp} \left(\frac{\partial I_1}{\partial x} \right)^2 \tag{5.19}$$

$$\rho_s C_s A_s \frac{\partial T_2}{\partial t} =$$

$$A_s \frac{\partial}{\partial x} \kappa_s \frac{\partial T_2}{\partial x} - \kappa_\perp (T_2 - T_1) - hp(T_2 - T_h) + \mathcal{R}_2(I_2, I_{c_2}) I_2^2 + \frac{1}{2\sigma_\perp} \left(\frac{\partial I_1}{\partial x} \right)^2 \tag{5.20}$$

where the subscript "s" stands for an individual strand. The two parameters which do not require much discussion are T_1 and T_2, the temperatures of strands *one* and *two*; T_h, the bulk helium temperature; A_s, the cross-sectional area of the strand; and p, the perimeter of the strand. The other parameters are discussed in the next paragraphs.

The material properties of the composite strand combine the properties of both the superconductor and the matrix. The quantity $\rho_s C_s$ is the volume averaged specific heat of the composite conductor and κ_s is the volume averaged thermal conductivity:

$$\rho_s C_s = \lambda \rho_{sc} C_{sc} + (1-\lambda)\rho_m C_m \tag{5.21}$$

$$\kappa_s = \lambda \kappa_{sc} + (1-\lambda)\kappa_m \tag{5.22}$$

where the subscripts "m" and "sc" stand for the matrix material (copper) and the superconductor, respectively. C is the specific heat, ρ is the density, κ is the thermal conductivity, and λ is the volume fraction of superconductor in the strand. The necessary properties as a function of temperature are found using computer subroutines developed for the numerical studies of quench propagation, [34].

The first term on the RHS in each of Eqs. (5.19) and (5.20) is the axial heat conduction along the strands. The second term, involving $\kappa_\perp$, represents the transverse conduction and is new to this analysis since there were no transverse temperature gradients in the Quencher model. The quantity $\kappa_\perp$ represents the transverse thermal conductance per length, W/m-K, and is thus analogous to $\sigma_\perp$, the transverse electrical conductance per length. The value of $\kappa_\perp$ can vary over a wide range depending on a number of factors (strand compaction, surface coatings, etc.) but it turns out the exact value is not critical to the stability analysis of the cable. In general, it is sufficient to study the two extremes: $\kappa_\perp \to 0$ and $\kappa_\perp \to \infty$.

The parameter h is the heat transfer coefficient derived from Newton's law of cooling [33, 35]. For a given cable and given flow conditions, this value needs to be determined experimentally for most practical cases. In the work presented here, a typical value of $h = 500$ W/m^2-K will be used.

The $\mathcal{R}(I, I_c)I^2$ terms in Eqs. (5.19) and (5.20) represent the Joule heating per-unit-length caused by current flowing *through* the strands. The term:

$$\frac{1}{2\sigma_\perp}(\frac{\partial}{\partial x}I)^2 = \lim_{dx\to 0}\frac{1}{2}\frac{1}{dx}\frac{1}{\sigma_\perp dx}(\frac{\partial I}{\partial x}dx)^2$$

represents the Joule heating per-unit-length caused by current flowing *between* the strands (refer to Fig. 3-4). This transverse Joule heating is deposited evenly in both strands, thus accounting for the factor of 1/2. The transverse Joule heating is much smaller than the "parallel" Joule heating but is included in the model for the sake of completeness.

The Joule heating terms further couple the thermal equations to the electrical equations. They also make the model non-linear—a much more difficult problem than the coupling. Because of these terms, the two-strand model cannot be solved analytically in the Resistive Domain. Approximate solutions which linearize the Joule heating term are appropriate for a limited subset of cables and will be discussed in Chapter 6. Other than that, though, the Resistive Domain will have to be treated using numerical techniques.

The Wall Equation

While the conduit wall temperature plays an important role in quench development, it has little effect on the stability of the cable. In order to better concentrate on the important factors in the analysis, the conduit wall is not considered in the two-strand model. Formally, the limit $A_w \to 0$ is used, where A_w is the cross-sectional area of the conduit. In this limit, Eq. (5.14) reduces to: $T_w = T_h$.

The Helium Equations

Because the supercritical helium typically used to cool CICC's is compressible, it is necessary to solve the mass, momentum, energy and state equations simultaneously in order to ascertain the temperature of the helium. The one-dimensional set of these equations was given in Eqs. (5.15)–(5.17). Those equations are repeated here with the modifications consistent with separate strand temperatures and the negligible wall approximation, $T_w = T_h$:

$$\begin{aligned}
\frac{\partial \rho_h}{\partial t} + \frac{\partial}{\partial x}(\rho_h v_h) &= 0 && (5.23)\\
\rho_h \frac{\partial v_h}{\partial t} + \rho_h v_h \frac{\partial v_h}{\partial x} &= -\frac{\partial P_h}{\partial x} - \frac{f \rho_h |v_h| v_h}{2 d_h} && (5.24)\\
\rho_h C_h A_h \left(\frac{\partial T_h}{\partial t} + v_h \frac{\partial T_h}{\partial x} \right) + \rho_h C_\beta A_h T_h \frac{\partial v_h}{\partial x} &= hp(T_1 - T_h) + hp(T_2 - T_h) \\
&\quad + \frac{f \rho_h A_h |v_h| v_h^2}{2 d_h} && (5.25)\\
P_h &= P_h(\rho_h, T) && (5.26)
\end{aligned}$$

where ρ_h is density, v_h is the velocity of the helium, P_h is the pressure, f is the friction factor, d_h is the hydraulic diameter, C_h is the specific heat of helium at constant volume and $C_\beta \equiv (1/\rho_h)\partial p/\partial T_h$. The two terms on the RHS of the momentum equation, Eq. (5.24), are the pressure gradient and the frictional resistance. The terms on the LHS of the energy equation,Eq. (5.25), represent, in order, latent heating, convection, and compressibility. Notice that there is no conduction term in the helium energy equation as it is shown to be negligible for cryogenic purposes, [33]. The last term on the RHS of Eq. (5.25) is the viscous dissipation while the remaining two terms on the RHS represent heat transfer at the strand boundaries. The equation of state, Eq. (5.26), relates the pressure to the density and temperature and is necessary to close the system.

These equations can be simplified significantly if we limit ourselves to a regime in which the helium can be considered incompressible, i.e. $\frac{\partial}{\partial t}\rho_h \approx 0$. For sufficiently short times, Δt, this condition will always be true. To determine the limiting Δt, it is useful to study the relative scaling of the terms in the mass equation, Eq. (5.23). The incompressible approximation is valid when the ratio of the first term to the second is $\gg 1$. The length scale of the spatial derivative is the length of the normal zone,

ℓ_{nz}.[2] Thus, the criterion becomes:

$$\frac{\Delta t v_h}{\ell_{nz}} \ll 1$$

For typical helium velocities on the order of $v_h = 1$ m/s and normal zone lengths on the order of $\ell_{nz} = 1$ m, the incompressible approximation is valid for $\Delta t \ll 1$ s.

Since the purpose of this thesis is to study stability rather than quench, it is advantageous to place a limit on the maximum "quench evolution" time for which the model will be valid. For this purpose, we define τ_s to be the "stability time scale" where $\tau_s \sim 100$ ms is small enough to ensure that the incompressible approximation is valid. For times $t - t_\star < \tau_s$, then, the helium energy equation is decoupled from the mass, momentum, and state equations, simplifying to:

$$\rho_h C_h A_h \frac{\partial T_h}{\partial t} = hp(T_1 - T_h) + hp(T_2 - T_h) \tag{5.27}$$

This is the necessary helium temperature equation for the two-strand model. The equation is valid for $t - t_\star < \tau_s \sim 100$ ms during which time both the convection and compressibility terms in Eq. (5.25) are negligible.

Thermal Boundary and Initial Conditions

The temperature equations for the strands, Eqs. (5.19) and (5.20) require boundary conditions at $x = 0$ and $x = \ell$. In the Quencher model, [33], the choice of proper boundary conditions was of significant importance. In this model however the restriction to a validity regime of $t - t_\star < \tau_s$ greatly reduces the role of the boundary conditions.

We can consider two cases: $\ell_{nz} < \ell$ and $\ell_{nz} = \ell$. In the former case, the restriction to $t - t_\star < \tau_s$ ensures the thermal propagation does not reach the ends of the cable. Thus, the cable can be considered an infinite domain for the purposes of determining the thermal boundary conditions.. The latter case, $\ell_{nz} = \ell$, ensures that the heating is

---

[2] The normal zone is defined as the region of the cable experiencing Joule heating.

uniform over the length of the cable and thus there are no axial temperature gradients. In either case, the following boundary conditions are appropriate:

$$x = 0; \qquad \frac{\partial T_1}{\partial x} = \frac{\partial T_2}{\partial x} = 0 \tag{5.28}$$

$$x = \ell; \qquad \frac{\partial T_1}{\partial x} = \frac{\partial T_2}{\partial x} = 0 \tag{5.29}$$

The helium temperature equation does not need boundary conditions because the conduction, axial convection, and compressible terms are all negligible.

The initial conditions are straightforward—at the onset of the Resistive Domain, all temperatures are equal to the background helium temperature, T_b:

$$t = t_\star; \qquad T_1(x) = T_2(x) = T_h(x) = T_b \tag{5.30}$$

5.2.3 Summary of the Resistive Domain Equations

Combining the electrical equation, Eq. (5.7), with the thermal equations developed for the stability time-scale provides the final model equations for the two-strand model in the Resistive Domain. The model is not valid for studying quench development since the validity regime breaks down for $t - t_\star > \tau_s$. However, the model is able to determine whether the cable will eventually quench or recover, and thus provides the tool necessary to study how current distribution affects the stability of the cable.

For ease of reference, the two-strand model equations in the Resistive Domain are collected here together with their boundary conditions and auxiliary equations:

The Two-Strand Model Equations for the Resistive Domain:

$$\frac{\partial I}{\partial t} = \alpha^2 \frac{\partial^2 I}{\partial x^2} - \frac{1}{2\mathcal{L}} \left(\mathcal{R}_1 + \mathcal{R}_2\right) I + \frac{1}{\mathcal{L}} \mathcal{R}_2 I_{T/2} + \frac{\partial I_{T/2}}{\partial t} \tag{5.31}$$

$$\begin{aligned} \rho_s C_s A_s \frac{\partial T_1}{\partial t} &= A_s \frac{\partial}{\partial x} \kappa_s \frac{\partial T_1}{\partial x} - \kappa_\perp (T_1 - T_2) - hp(T_1 - T_h) \\ &\quad + \mathcal{R}_1 I^2 + \frac{1}{2} \frac{1}{\sigma_\perp} \left(\frac{\partial I}{\partial x}\right)^2 \end{aligned} \tag{5.32}$$

$$\begin{aligned} \rho_s C_s A_s \frac{\partial T_2}{\partial t} &= A_s \frac{\partial}{\partial x} \kappa_s \frac{\partial T_2}{\partial x} - \kappa_\perp (T_2 - T_1) - hp(T_2 - T_h) \\ &\quad + \mathcal{R}_2 (I_T - I)^2 + \frac{1}{2} \frac{1}{\sigma_\perp} \left(\frac{\partial I}{\partial x}\right)^2 \end{aligned} \tag{5.33}$$

$$\rho_h C_h A_h \frac{\partial T_h}{\partial t} = hp(T_1 - T_h) + hp(T_2 - T_h) \tag{5.34}$$

Auxiliary Equations:

$$\mathcal{R}_1 = \begin{cases} 0 & I \leq I_c(B, T_1) \\ \mathcal{R}_m (I - I_c(B, T_1))/I & I > I_c(B, T_1) \end{cases} \tag{5.35}$$

$$\mathcal{R}_2 = \begin{cases} 0 & I_T - I \leq I_c(B, T_2) \\ \mathcal{R}_m (I_T - I - I_c(B, T_2))/(I_T - I) & I_T - I > I_c(B, T_2) \end{cases} \tag{5.36}$$

$$I_c(B, T) = \begin{cases} \frac{\xi}{B}\left(1 - \frac{T - T_b}{T_c - T_b}\right) & T < T_c(B) \\ 0 & T \geq T_c(B) \end{cases} \tag{5.37}$$

$$T_c(B) = \begin{cases} T_b + (T_{c0} - T_b)\left(1 - \frac{B}{B_{c0}}\right) & B < B_{c0} \\ T_b & B \geq B_{c0} \end{cases} \tag{5.38}$$

Boundary and Initial Conditions:

$$x = 0\ ; \qquad I - \ell_J \frac{\partial I}{\partial x} = -\ell_J \frac{\dot{B}_\perp w \ell_p \sigma_\perp}{2\pi} \sin\theta_0 + I_{T/2} \tag{5.39}$$

$$\frac{\partial T_1}{\partial x} = \frac{\partial T_2}{\partial x} = 0 \tag{5.40}$$

$$x = \ell\ ; \qquad I + \ell_J \frac{\partial I}{\partial x} = \ell_J \frac{\dot{B}_\perp w \ell_p \sigma_\perp}{2\pi} \sin\theta_1 + I_{T/2} \tag{5.41}$$

$$\frac{\partial T_1}{\partial x} = \frac{\partial T_2}{\partial x} = 0 \tag{5.42}$$

$$t = t_\star\ ; \qquad I(x) = I_{SCdomain}(x, t_\star) \tag{5.43}$$

$$T_1 = T_2 = T_b \tag{5.44}$$

5.3 Numerical Procedure

Following the success of the numerical approach used in the Quencher model, it was decided that a similar global collocation procedure with adaptive meshing [36] would be the best choice for the two-strand Resistive Domain model. The details of the numerical procedure parallels that of reference [33]. Using a second-order fully implicit time-advance algorithm reduces Eqs. (5.31)–(5.34) to a set of six ordinary differential equations which are solved using the Colsys package developed by Ascher, [37].

5.3.1 Time Advance Algorithm

The second-order accurate approximation to the time derivative will be defined by a standard finite difference operator L_2 where:

$$\left.\frac{\partial U}{\partial t}\right|_{t+dt} \approx L_2 U \equiv \frac{1}{2dt}\left[3\, U|_{t+dt} - 4\, U|_t + U|_{t-dt}\right] \tag{5.45}$$

where U is an arbitrary quantity and dt is the timestep size. The value of U is known at times t and $t - dt$. This method is fully implicit.

5.3.2 Reduction of the Helium Temperature Equation

The first step in reducing the model to a system of ODE's is to solve for the helium temperature in terms of the two strand temperatures. To do so, Eq. (5.34) is discretized as follows:

$$\rho_h C_h A_h \left.\frac{\partial T_h}{\partial t}\right|_{t+dt} \approx \rho_h C_h A_h L_2 T_h = hp\left(T_1 + T_2 - 2T_h\right)\big|_{t+dt} \tag{5.46}$$

where the RHS is evaluated at $t+dt$. Because we have limited the model to time-scales which ensure the incompressibility of the helium, $\rho_h C_h A_h$ is approximately constant and thus this routine is fully implicit. Using the definition of the operator L_2, given in Eq. (5.45), the helium temperature can be stated as:

$$T_h\big|_{t+dt} = \frac{T_1\big|_{t+dt} + T_2\big|_{t+dt} + \epsilon\left(4\,T_h\big|_t - T_h\big|_{t-dt}\right)}{2+3\epsilon} \tag{5.47}$$

where $\epsilon = (\rho_h C_h A_h)/(hp2dt)$.

Since the helium temperature enters the strand temperature equations through the heat transfer term, it is useful to introduce a shorthand notation which can be used in future equations:

$$\begin{aligned} S_{h_1} &\equiv hp(T_1 - T_h)\big|_{t+dt} \\ &= \frac{hp}{2+3\epsilon}\left\{(T_1 - T_2)\big|_{t+dt} + \epsilon\left(3\,T_1\big|_{t+dt} - 4\,T_h\big|_t + T_h\big|_{t-dt}\right)\right\} \qquad (5.48) \\ S_{h_2} &\equiv hp(T_2 - T_h)\big|_{t+dt} \\ &= \frac{hp}{2+3\epsilon}\left\{(T_2 - T_1)\big|_{t+dt} + \epsilon\left(3\,T_2\big|_{t+dt} - 4\,T_h\big|_t + + T_h\big|_{t-dt}\right)\right\} \qquad (5.49) \end{aligned}$$

where S_{h_1} and S_{h_2} will be called the helium coupling terms. These definitions will allow the temperature equations for stands *one* and *two* to be expressed without reference to $T_h|_{t+dt}$.

5.3.3 The Reduced Set of ODE's

Having dealt with the helium temperature equation, the next step is to reduce the remaining model equations into first-order ODE's. To do so, it is useful to introduce three variables:

$$\iota \equiv \frac{\partial I}{\partial x} \tag{5.50}$$

$$q_1 = -\kappa_s \frac{\partial T_1}{\partial x} \tag{5.51}$$

$$q_2 = -\kappa_s \frac{\partial T_2}{\partial x} \tag{5.52}$$

Using these new variables, we can rewrite the three second-order equations, Eqs. (5.31)–(5.33), as a first order vector equation:

$$\frac{\partial \mathbf{v}}{\partial x} = \mathbf{F}(x, \mathbf{v}) \tag{5.53}$$

where the vector $\mathbf{v}$ is:

$$\mathbf{v} = \begin{bmatrix} I \\ \iota \\ T_1 \\ q_1 \\ T_2 \\ q_2 \end{bmatrix} \tag{5.54}$$

and the vector $\mathbf{F} = [F_1, F_2, F_3, F_4, F_5, F_6]'$ (where $'$ indicates "transpose") has components:

$$\begin{aligned}
F_1 &= \iota & (5.55)\\
F_2 &= \alpha^{-2}\left[L_2 I + \frac{\mathcal{R}_1 + \mathcal{R}_2}{2\mathcal{L}} I - \frac{\mathcal{R}_2}{\mathcal{L}} I_{T/2} - \frac{\partial I_{T/2}}{\partial t}\right] & (5.56)\\
F_3 &= -q_1/\kappa_s & (5.57)\\
F_4 &= -\rho_s C_s L_2 T_1 + A_s^{-1}\left[\mathcal{R}_1 I^2 + \frac{1}{2}\frac{1}{\sigma_\perp}\iota^2 - S_{h_1} - \kappa_\perp (T_1 - T_2)\right] & (5.58)\\
F_5 &= -q_2/\kappa_s & (5.59)
\end{aligned}$$

$$F_6 = -\rho_s C_s L_2 T_2 + A_s^{-1}\left[\mathcal{R}_2(I_T - I)^2 + \frac{1}{2}\frac{1}{\sigma_\perp}\iota^2 - S_{h_2} - \kappa_\perp(T_2 - T_1)\right] \quad (5.60)$$

The terms S_{h_1} and S_{h_2} are defined in Eqs. (5.48) and (5.49). Equation (5.53) represents the full two-strand model in the Resistive Domain. It needs to be solved at each time-step of the time evolution.

The necessary boundary conditions were given in Eqs. (5.39)–(5.42) and can be directly translated into vector notation:

$$x = 0\ ; \qquad v_1 - \ell_J v_2 = -\ell_J \frac{\dot{B}_\perp w \ell_p \sigma_\perp}{2\pi} \sin\theta_0 + I_{T/2} \quad (5.61)$$

$$v_4 = v_6 = 0 \quad (5.62)$$

$$x = \ell\ ; \qquad v_1 + \ell_J v_2 = \ell_J \frac{\dot{B}_\perp w \ell_p \sigma_\perp}{2\pi} \sin\theta_1 + I_{T/2} \quad (5.63)$$

$$v_4 = v_6 = 0 \quad (5.64)$$

where the individual components of $\mathbf{v}$ are defined in Eq. (5.54).

The initial conditions, Eqs. (5.43) and (5.44) translate into:

$$t = t_\star\ ; \qquad v_1(x) = I_{SCdomain}(x, t_\star) \quad (5.65)$$

$$v_2(x) = \frac{\partial}{\partial x} I_{SCdomain}(x, t_\star) \quad (5.66)$$

$$v_3(x) = v_5(x) = T_b \quad (5.67)$$

$$v_4(x) = v_6(x) = 0 \quad (5.68)$$

thus completing the numerical model.

Equation (5.53) together with its boundary and initial conditions can be solved using a collocation scheme provided by the Colsys package of software [37]. At each time step, each component of the vector $\mathbf{v}$ is resolved to within a user-specified tolerance. The package is called repeatedly as the time is advanced from $t = t_\star$, the onset of the Resistive Domain, to $t = t_\star + \tau_s$, the end of the stability event. At $t = t_\star + \tau_s$, the cable is either well on its way to quenching or has recovered. For the purpose of studying stability, no information beyond $t = t_\star + \tau_s$ is necessary.

The application of Colsys to quench propagation was studied extensively in [33] where convergence limits as well as CPU requirements were analyzed. The ability of Colsys to re-mesh the domain at each time-step allowed the routine to efficiently but robustly track the sharp quench boundaries at the edge of the normal zone. The same behavior has been observed in solving the two-strand model. New convergence studies have not been conducted because the results of the model indicated they were not needed. This will be discussed in Section 5.4.2.

5.4 Numerical Solutions in the Resistive Domain

The two-strand numerical model has been run numerous times for varying parameters. The end objective was to better understand how current distribution affected the stability of the cable. Since the model cannot be solved analytically, the effects of varying each of the operational parameters was studied independently. Some of these results will be presented shortly.

The overall result, however, was easier to quantify than the need to run numerous trials might suggest. After an exhaustive search, it has been determined that if the cable enters the Resistive Domain, the only factor which affects stability (for "realistic" design parameters) is the cable length, ℓ. A short enough cable can recover while a cable longer than a certain length will always quench once it enters the Resistive Domain.

The important implication of the above statement is that, for longer cables, the analysis presented in Chapter 4 for the Superconducting Domain is sufficient to derive a robust stability criterion. For stable operation in a ramped magnetic field, the ramp time, t_{ramp}, must be less than the transition time to the Resistive Domain, $t_{\star}$. Since $t_{\star}$ can be calculated from analytic formulae, the stability analysis of longer cables is greatly simplified.

Before jumping ahead, however, the temperature evolution and current redistribution in the Resistive Domain will be demonstrated using a numerical example. The conclusion that longer cables are inherently unstable once they enter the Resistive Domain will be shown convincingly although only a representative sample of the many runs which lead to this conclusion will be discussed. The study of "short" strands in the Resistive Domain is in a sense more interesting because their behavior is more varied—both recovery and quench are possible outcomes. The presentation of this interesting behavior is delayed until Chapter 6 where it will be studied both numerically and analytically.

5.4.1 Definition of "Full-Scale" and "Lab-Scale Cables"

For the purposes of the following discussion, "long" cables can be equated with full-scale solenoidal magnets which generate their own field and thus experience a spatially varied magnetic field, $B(x,t)$. "Short" cables will be classified as lab-scale cables which are tested inside the bore of larger background field magnets and thus reside in an approximately uniform magnetic field, $B(t)$.

A more rigorous criterion can be applied, though, which requires the introduction of a new concept, the characteristic current transfer length. We will stipulate that a long cable is one with a length longer than the characteristic current transfer length, ℓ_X. The characteristic transfer length of the cable is derived from the steady state limit of Eq. (5.7) with strand *one* fully quenched (i.e. $I_{c_1} = 0$):

$$\alpha^2 \frac{\partial^2 I}{\partial x^2} - \frac{\mathcal{R}_m}{2\mathcal{L}} I = 0 \tag{5.69}$$

Using scaling arguments to balance the LHS terms provides the desired definition of ℓ_X:

$$\ell_X = \sqrt{\frac{2\alpha^2 \mathcal{L}}{\mathcal{R}_m}} = \sqrt{\frac{1}{\sigma_\perp \mathcal{R}_m}}$$

For the range of $\sigma_\perp$and $\mathcal{R}_m$ considered in this thesis, (see Section 3.3), ℓ_X ranges from ~ 1 m to ~ 10 m. The cable length, ℓ, must be greater than this value of ℓ_X in order to be considered long. In practice, this criterion coincides with the previously mentioned distinction between full-scale and lab-scale magnets.

5.4.2 Specification of Full-Scale Magnets

Full-scale magnets are large enough to provide their own magnetic field. Thus, the field at any location is directly proportional to the transport current: $B(x,t) \propto I_T(t)$. In this thesis, we primarily consider only solenoidal magnets. For a given solenoid, the transverse magnetic field is most easily calculated as a function of the position vector, $\mathbf{r}$, measured from the midpoint of center-line of the magnet. Knowing how the cable is wound, however, allows a simple mapping $\mathbf{B}(\mathbf{r}) \mapsto \mathbf{B}(x)$, where x is the distance from the leftmost joint.

In general, the field profile, $B(x,t)$, will be at a maximum at the center, $x = \ell/2$ and will fall off toward the ends, $x = 0$ and $x = \ell$.[3] The constant of proportionality between the transport current and the peak field at the center of the cable is known as the "load-line", Λ, where:

$$I_T(t) = \Lambda B_\perp(x = \ell/2, t) = \Lambda \dot{B}_{\mathrm{max}} t \tag{5.70}$$

for the linear field ramps considered here.

For the purposes of demonstrating the behavior of full-scale coils in the Resistive Domain, a triangular field profile will be used although an actual field profile would be a more complicated function of x. The results will prove, however, that the only aspects of the field profile which affect stability are the three local values of the field: $B_\perp(x = 0, t)$, $B_\perp(x = \ell/2, t)$ and $B_\perp(x = \ell, t)$. A triangular profile is sufficient to match these three conditions for an arbitrary field profile.

To demonstrate the effects of current distribution on the stability of a full-scale magnet, a two-strand cable "reminiscent" of the US-DPC experiment will be used.[4] The properties of this hypothetical cable are given in Table 5.1. The effects of varying the parameters listed in the table will be studied as well.

---

[3] This x-dependence is typical of "double-pancake" windings, see [1].

[4] A more rigorous attempt to explain the actual Ramp-Rate Limitation experienced in the US-DPC will be presented in Chapter 8. For now, we just borrow certain geometrical properties from that experiment: strand size and composition, cable length, twist-pitch length, load-line, etc.

cable length	ℓ	75 m
twist-pitch length	ℓ_p	30 cm
cable width	w	1.5 cm
effective inductance per length	$\mathcal{L}$	1 μH
transverse electrical conductivity	$\sigma_\perp$	100 Ω^{-1}m^{-1}
transverse joint resistance	$\Re_J$	1 $\mu\Omega$
joint orientation at $x = 0$	θ_0	$-\pi/2$
joint orientation at $x = \ell$	θ_1	$\pi/2$
helium background temperature	T_b	4.5 K
helium pressure	P_h	5 atm.
helium cross-sectional area	A_h	0.64 mm^2
strand (one) cross-sectional area	A_s	0.48 mm^2
volume fraction superconductor	λ	0.45
matrix resistance per length	$\mathcal{R}_m$	1 mΩ-m^{-1}
heat transfer coefficient	h	500 W/m^2-K
transverse thermal conductivity	$\kappa_\perp$	0 W/m-K
peak field ramp-rate	$\dot{B}_{\text{max}}$	1 T/s
field ramp-rate at joints	$\dot{B}_{\text{min}}$	0.5 T/s
load-line	Λ	47 A/T

Table 5.1: The Hypothetical Full-Scale Cable Properties.

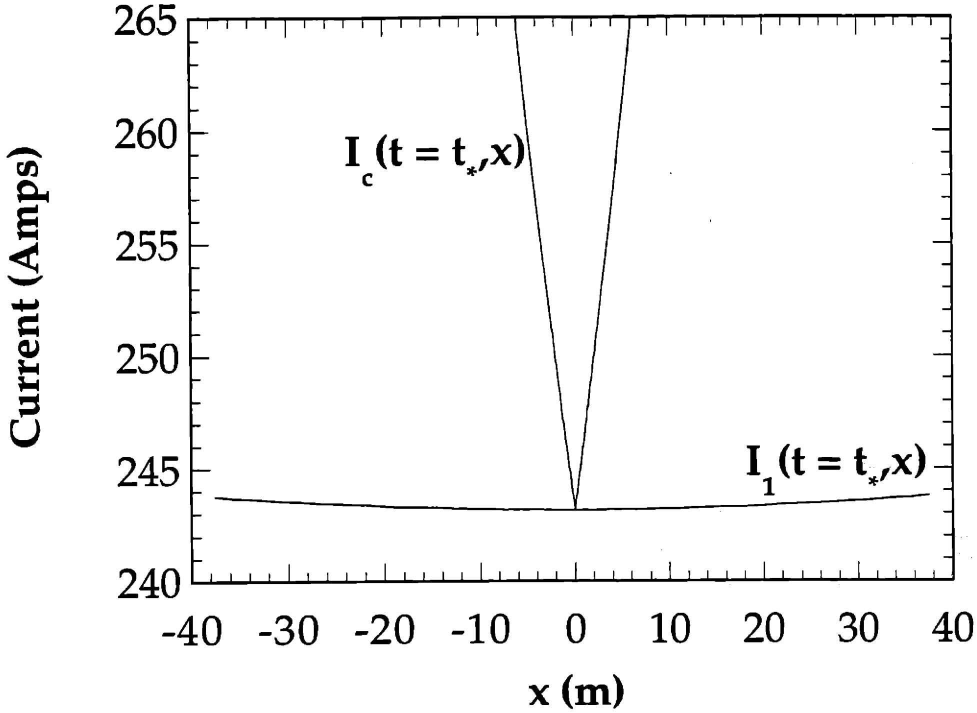

Figure 5-3: The onset of the Resistive Domain occurs when the strand current profile intercepts the critical current profile at $t = t_\star$.

Beginning of the Stability Event

The Resistive Domain begins when the current in strand *one* reaches the critical current. The cable described in Table 5.1 falls within the Finite Length/Short-Circuit Joint Regime described in Section 4.3.3 and the analytic solution for the total strand current for this regime was given in Eq. (4.93). Using this result and Eq. (5.2) which describes the behavior of the critical current, the onset of the Resistive Domain is found to occur at $t_\star = 8.57$ s. A plot of the resulting initial condition showing $I_{1_{SCdomain}}(x, t_\star)$ and $I_c(x, t_\star)$ is shown in Fig. 5-3.

Notice from Fig. 5-3 that the triangular shape of the magnetic field profile produces an inverted triangular profile for the critical current. The fact that the critical current is at a minimum at $x = \ell/2$ guarantees that the normal zone is initiated at the center of the cable. For this reason, it is interesting to look at the time evolution of the current and the critical current at $x = \ell/2$, as shown in Fig. 5-4. The figure graphically shows how $t_\star$ is determined. The associated value $I_\star$ is indicated as well.

Figure 5-4 also shows the time evolution of the average current carried by each

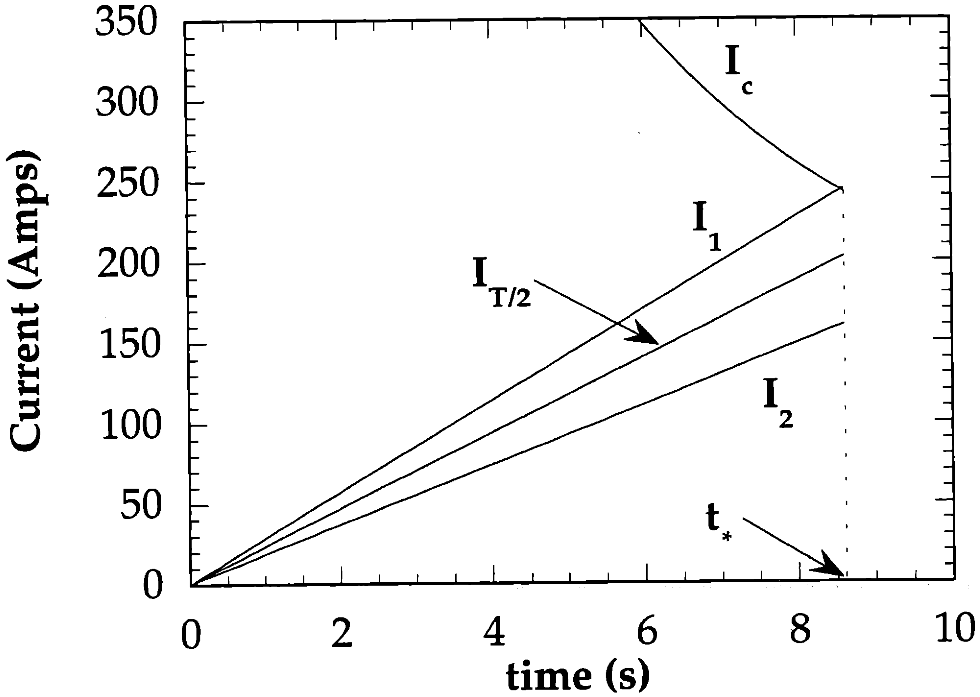

Figure 5-4: Time evolution of $I_1(x = \ell/2, t)$, $I_2(x = \ell/2, t)$, $I_c(x = \ell/2, t)$, and $I_{T/2}(t)$ in the Superconducting Domain. The Resistive Domain begins at $t = t_*$.

strand, $I_{T/2}$. The difference between the intercepts $I_1 = I_c$ (at $t = t_* = 8.57$ s) and $I_{T/2} = I_c$ (at $t = 9.41$ s) demonstrates the effects of circulating currents on the onset of the Resistive Domain. For this example, the cable first becomes resistive approximately 9% earlier than would have been anticipated had the circulating currents not been considered.

The results of the numerical model developed in Section 5.3 above will determine whether this earlier-than-anticipated resistance actually leads to a premature quench.

Numerical Results

Once the problem enters the Resistive Domain, the numerical methods developed in Section 5.3 are used to solve the ensuing development of current and temperature profiles. For the example case cited here, the results are presented graphically in Figs. 5-5 through 5-11. Although the figures and discussion refer to one specific case, it has been found that all cables longer than the transfer length, ℓ_X, exhibit the same qualitative behavior.

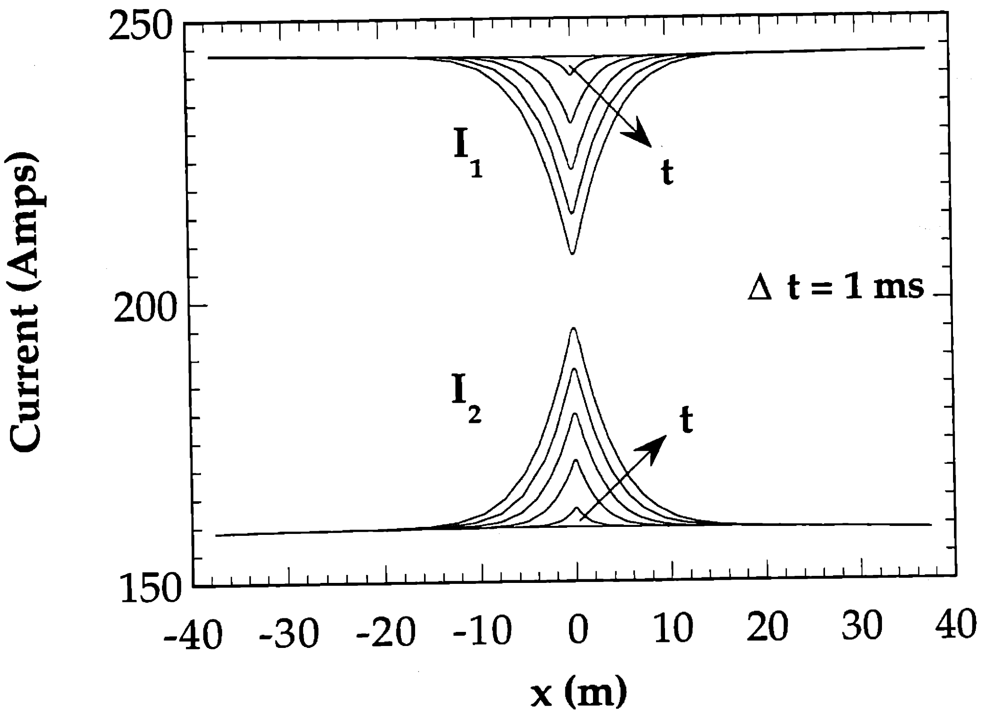

Figure 5-5: Current profiles for strands *one* and *two* during the first 5 ms of the Resistive Domain.

Figure 5-5 shows profiles of the current in strands *one* and *two* at a series of times after the onset of the Resistive Domain at $t = t_\star$. The last profile plotted is for $t = t_\star + 5$ ms and the time between profiles is 1 ms. The figure shows that the resistive zone which develops in strand *one* causes current to transfer from strand *one* to strand *two* through the transconductance, $\sigma_\perp$. The length of the transfer region grows but is characterized by the steady state transfer length, ℓ_X. For longer cables, the joints are far enough removed from the disturbance region that they play no role in the current redistribution—this is an important distinction between the behavior of full-scale and lab-scale magnets.

Before discussing the current distribution further, the temperature profile and critical current profile for strand *one* are plotted in Figs. 5-6 through 5-7 to complete the picture of what is happening during the first milli-seconds of the resistive regime. Figure 5-6 shows the temperature of strand *one*, T_1, in the immediate vicinity of the resistive region (note the change of scale for the x-axis) for the first 5 ms of the Resistive Domain. The temperature dependent strand *one* critical-current profile,

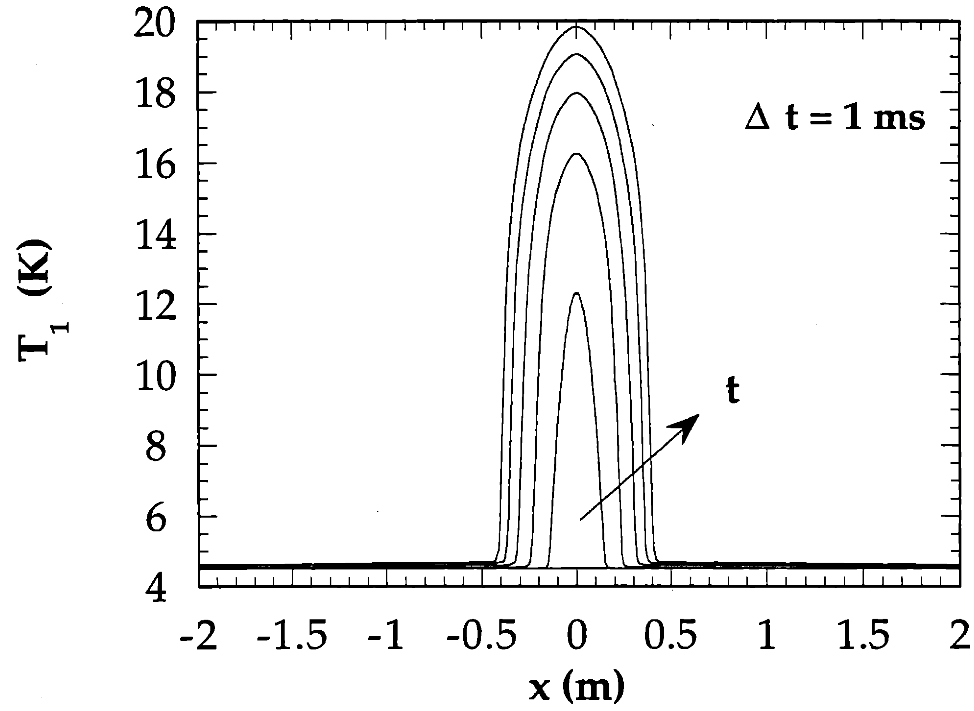

Figure 5-6: Temperature profiles for strand *one* during the first 5 ms of the Resistive Domain.

I_{c_1}, is plotted for the same range of x and t in Fig. 5-7. The sharp gradients in each plot result from the dominance of the Joule heating term over the conductance term in Eq. (5.32).

Since most of the interesting behavior occurs near the center of the cable, it is easier to visualize the stability event by focusing on the evolution of the local temperature and current at the single location, $x = \ell/2$. Figure 5-8 shows the temperatures of the two strands and of the helium at the center of the normal region vs. time. Figure 5-9 shows the current in strand *one* I_1, and the temperature dependent critical current, $I_{c_1}(B,T_1)$, at $x = \ell/2$ as a function of time. Figure 5-10 is similar, but shows the strand *two* values, I_2 and $I_{c_2}(B,T_2)$. In Fig. 5-11, the local combined Joule heating of both strands at $x = \ell/2$ is plotted vs. time. The features of each of these plots are described in the following paragraphs.

Together, the time-evolution of the strand currents and temperatures at the center of the normal zone paint a clear picture of what happens when induced circulating currents cause one strand of the two-strand cable to prematurely reach critical current

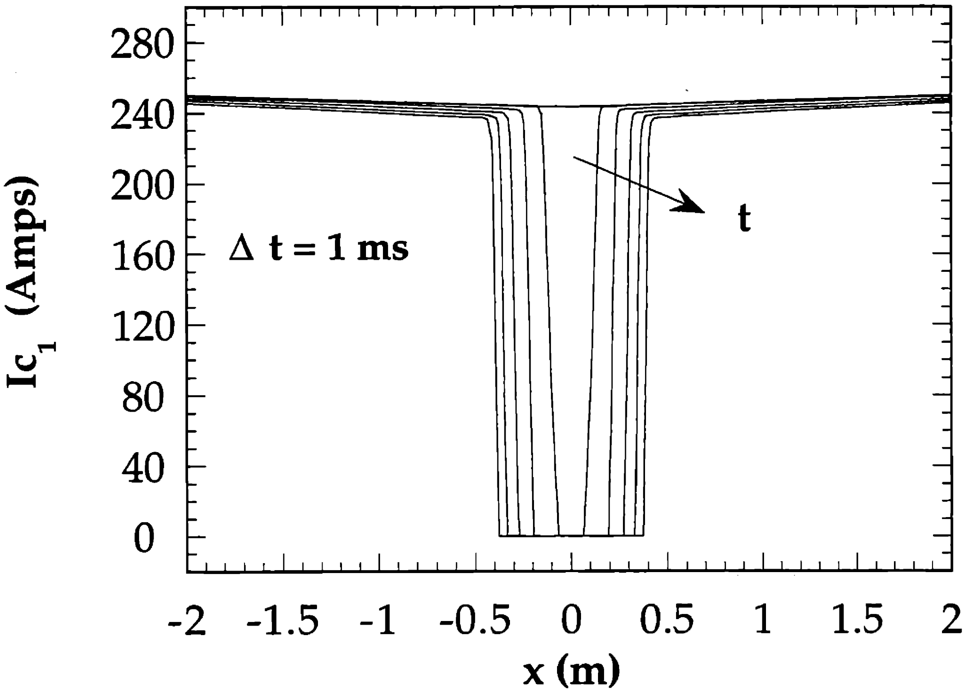

Figure 5-7: Critical current profiles for strand *one* during the first 5 ms of the Resistive Domain.

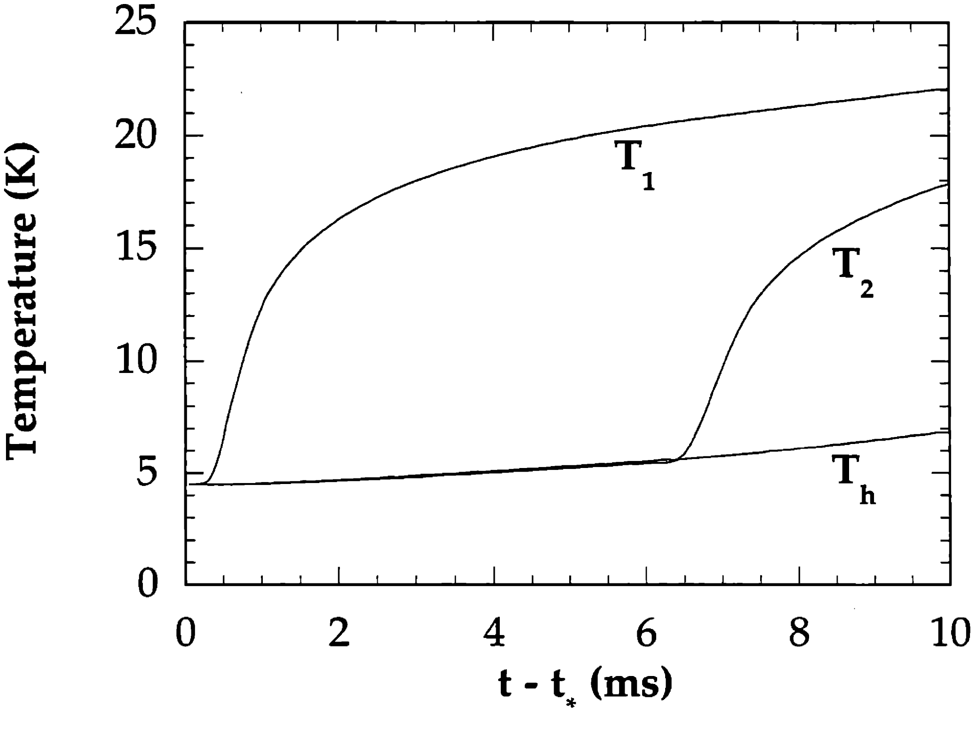

Figure 5-8: Time evolution of the temperatures, T_1, T_2, T_h at $x = \ell/2$.

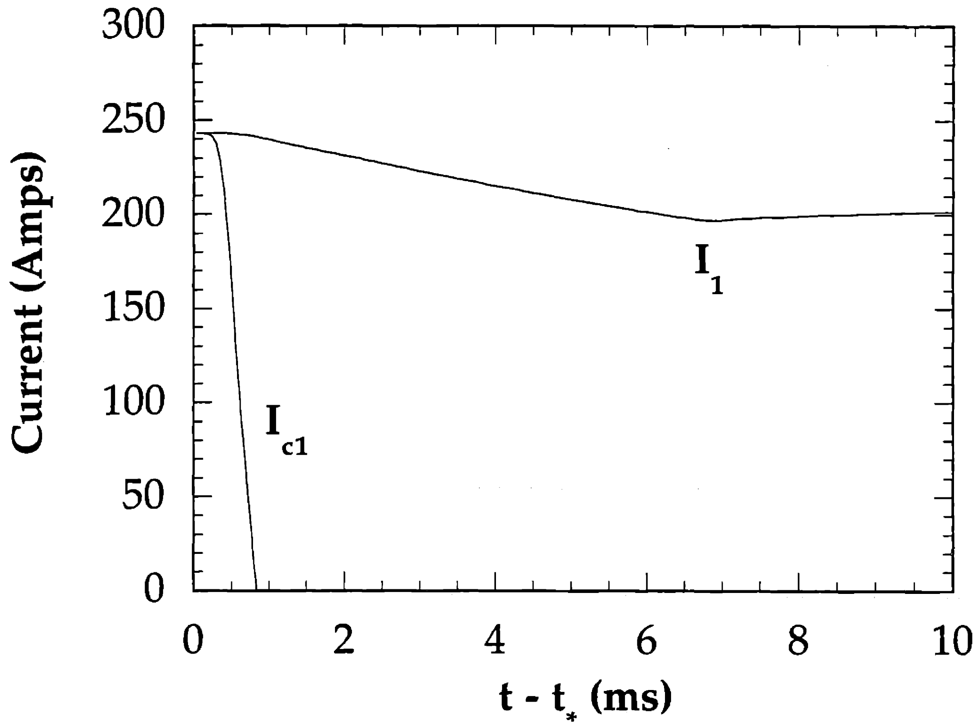

Figure 5-9: Time evolution of the strand *one* current, I_1, and critical current, I_{c_1}, at $x = \ell/2$.

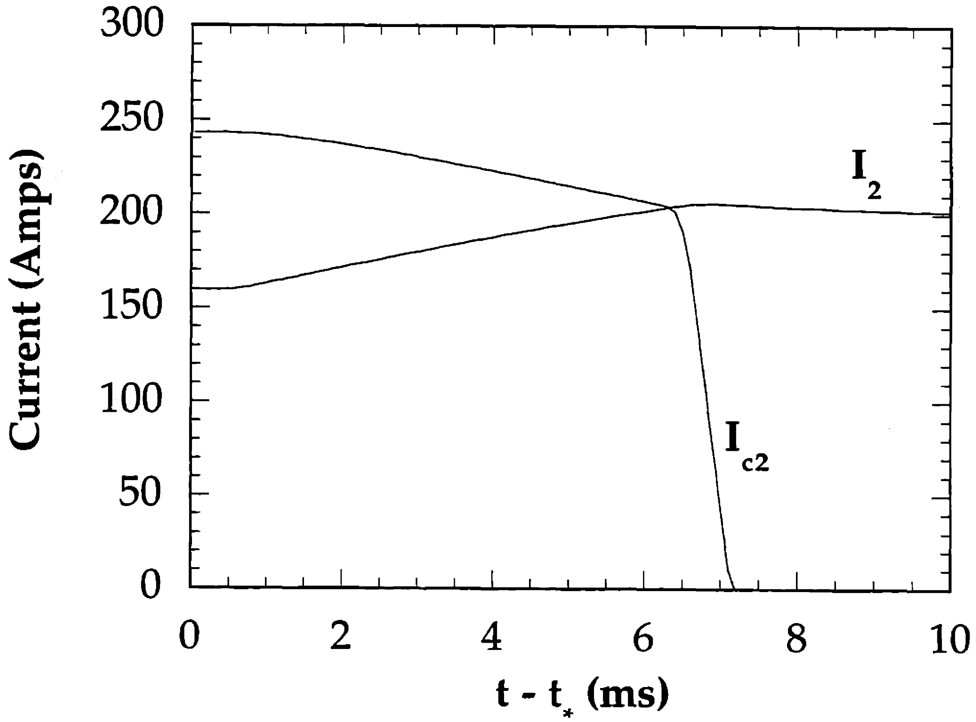

Figure 5-10: Time evolution of the strand *two* current, I_2, and critical current, I_{c_2}, at $x = \ell/2$.

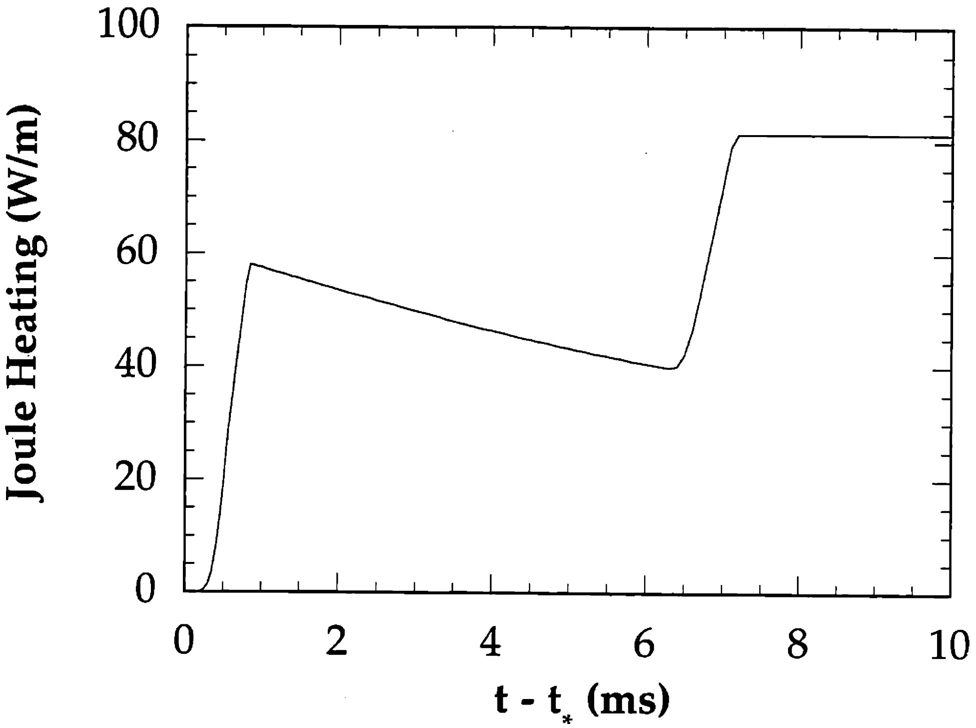

Figure 5-11: Time evolution of the combined local Joule heating in strands *one* and *two* (i.e. $\mathcal{R}_1 I_1^2 + \mathcal{R}_2 I_2^2$) at $x = \ell/2$.

in the peak-field region. Initially the small heat capacity of the strand at cryogenic helium temperatures results in a rapid temperature rise in strand *one*, as seen in the first few milli-seconds of Fig. 5-8. The critical current in strand *one* quickly declines due to the elevated temperatures, as shown in Fig. 5-9. Current in strand *one* locally transfers to strand *two* to avoid the resistive normal zone, but the rate of this transfer is limited by the strand inductances. This current transfer takes place over a length of the cable on the order of the characteristic transfer length, ℓ_X—see Fig. 5-5. Over the first 1 ms, the transfer length and amount of current transferred grow, but the critical current drops much more quickly than does the strand *one* current (see Fig. 5-9) resulting in even more Joule heating, as shown in the first 1 ms of Fig. 5-11.

Eventually, the higher strand *one* temperature translates into increased heat capacitance and slower rate of temperature rise (see Fig. 5-8, 1–5 ms). Also, once the critical current reaches zero, the Joule heating actually diminishes since the strand *one* current continues to fall (shown in Fig. 5-11 from 1–6 ms). The situation "worsens" however, when the rising strand *two* current (absorbing the current transferred out of *one*) intercepts the declining strand *two* critical current (see Fig. 5-10 at $t = 6$ ms). At this point, both strands begin Joule heating and both T_1 and T_2 monotonically rise. The cable is irrevocably quenched.

An extensive survey of the entire parameter space has determined that this same scenario occurs for every cable longer than the characteristic transfer length, $\ell > \ell_X$. Cases were run to study the effects of varying: $\dot{B}_\perp$, h, $\kappa_\perp$, $\sigma_\perp$, and $\mathcal{R}_m$. Although the quantitative features of each case (e.g. time at which strand *two* quenches, characteristic transfer length, etc.) vary, there was no case for which the cable proved to be stable.

Numerical Conclusions for Full-Scale Magnets

The results of the numerical model for full-scale magnets were quite conclusive: a single strand driven to its critical current by a combination of transport and induced currents will lead to a non-recovering quench. The inability of the current in a quenching strand to transfer quickly to its neighbor limits the ability of the unsaturated strand to act as a "protection circuit" on the stability time-scale.

It is interesting to compare stability (or in this case, instability) in the Resistive Domain to a different type of stability analysis which is prevalent in the literature [12, 17]. The "energy margin" of a cable is defined as the amount of energy a cable can absorb quasi-instantaneously and still recover. This traditional measure of stability was discussed in Chapter 2. Under normal operating conditions, a full-scale magnet is designed to be stable with respect to even fairly large energy disturbances. If so, why does the present analysis result in unconditionally unstable cables?

To answer this last question, it is necessary to identify the different initial conditions assumed for stability in the Resistive Domain versus the energy margin analysis. The energy margin analysis assumes that the transport current is evenly distributed amongst the cabled strands, thus each strand begins with $I < I_c$. If the initial energy deposition plus subsequent Joule heating can be dissipated quickly enough, the cable can return to the state $I < I_c$ *without* any current transfer.

The Resistive Domain, on the other hand, by definition assumes the current in strand *one* has reached I_c—even before any heat has been added to the system. Unless the strand *one* current can transfer to the other strand more quickly than the critical current declines (due to Joule heating), the cable in the Resistive Domain will experience continuous Joule heating and eventually quench. The fact that in the Resistive Domain stability depends on the rate of current transfer is what dooms longer cables to unconditional instability.

It is possible to combine the energy margin approach with the effects of current distribution. Before the Resistive Domain is reached, a given cable with an analytically calculated current distribution could be subjected to an energy perturbation. In this instance, there would be some amount of energy for which the cable would be marginally stable. The attraction of focusing solely on the current distribution as the source of instability, however, is that the results can self-consistently predict the stability of an actual cable. There is no need to postulate a mysterious disturbance to explain the onset of quench.[5]

Although the conclusion that all full-scale cables are unstable in the Resistive Domain is disappointing in the sense that the numerical model incessantly produces only one answer, we are in fact now able to clearly state a stability criterion for this scenario. For full-scale magnets (i.e. shaped field profile, $\ell > \ell_X$) the stability criterion is: $t_{ramp} < t_\star$, where $t_\star$ is the time at which I_1 first equals I_c. Since $t_\star$ can be calculated analytically, the stability criterion for long cables is an analytic calculation.

5.5 Summary

When the strand current, I, is greater than the critical current, I_c, at any point along the length of the cable, the resistance of the strands is no longer negligible. To analyze current distribution and stability in this so-called Resistive Domain requires numer-

---

[5] Admittedly, many of the important parameters which determine the current distribution in the cable are difficult to measure or are a priori unknown (θ, for example). Philosophically, however, a known parameter with an unknown value is quite different than an unknown source term.

ical methods to solve the coupled, second-order, non-linear set of partial differential equations which comprise the electrical and thermal descriptions of the model.

The Resistive Domain model was developed in Section 5.2 and was summarized in Eqs. (5.31)–(5.44). The details of the numerical procedure used to solve this model were discussed in Section 5.3. The numerical solution was used to study a hypothetical cable and the results were presented graphically in Figs. 5-5 through 5-11. The chosen scenario featured a full-scale magnet, $\ell \sim 75$ m. The decision was made to delay the discussion of lab-scale cables until the next chapter.

Through extensive numerical studies, a decisive conclusion was reached. Cables which are longer than their characteristic transfer length, $\ell_X = (\sigma_\perp \mathcal{R}_m)^{-1/2}$, were found to be unconditionally unstable in the Resistive Domain. This result allowed the definition of a simple stability criterion for such cables: $t_{ramp} < t_\star$, where $t_\star$ is the earliest time at which $I = I_c$ if the field is continuously ramped. The time $t_\star$ can be found by solving the analytic relation:

$$\min[I_c(x,t_\star) - I_{1_{SCdomain}}(x,t_\star)] = 0$$

where min is the minimization operator over the range $0 \leq x \leq \ell$. Since I_c and $I_{1_{SCdomain}}$ are both analytical functions, the results of the previous chapter are sufficient to analyze stability with respect to current distribution for any given full-scale magnet.

The analytic formulae in Chapter 4, however, are sufficiently complex as to make it difficult to derive a "Universal" stability law applicable to all cable designs. In other words, it is difficult to reduce the many critical parameters (ℓ, ℓ_p, ℓ_D, ℓ_J, ℓ_X, field profile, etc.) into a reduced set of non-dimensional groups. As an example of using the results of this chapter to analyze the stability of a specific cable, however, the results of the US-DPC experiment are compared to theoretical predictions in Chapter 7.

This chapter did not look at the behavior of lab-scale magnets, cables with $\ell < \ell_X$. The interesting behavior of these shorter cables is the subject of Chapter 6. The fact that the differences between lab-scale and full-scale cables are sufficient to warrant placing them in different chapters gives a hint of the difficulties in simulating larger cables in the laboratory.

Chapter 6

Current Distribution and Stability in the Resistive Domain for Lab-Scale Cables

After an unexplained ramp-rate limitation was first identified in the US-DPC experiment, [1, 38], several investigators tried to study the phenomenon using scaled-down versions of the US-DPC conductor [3, 5]. The results of these lab-scale experiments verified the existence of ramp-rate limitation but it proved difficult to correlate the behavior of the small-scale cables to the behavior of the full US-DPC.

The goal of this chapter is to theoretically study current distribution and stability in lab-scale conductors and to compare the results to the findings of the previous chapter, which addressed full-scale conductors. Unfortunately for experimenters, it is found that the cable lengths typically used in lab-scale studies are too short to properly simulate the actual behavior of full-scale magnets.

This chapter starts by carefully defining what is actually meant by the term "lab-scale" cable. In doing so, the 1-D Resistive Domain model developed in Chapter 5 is reduced to a 0-D model which, by definition, is appropriate for lab-scale magnets. Since the resulting model is still non-linear, numerical solutions are again needed to study the stability behavior in this regime.

The results of the numerical analysis point to the fact that the stability criterion developed for longer cables (i.e. $t_{ramp} < t_*$) does not accurately describe the stability behavior of lab-scale magnets (it is sufficient, but not necessary). Section 6.2 shows how the "stability events" which occur when $I = I_c$ can lead to either quench or recovery, depending on several different factors. The concept of marginal stability is defined in Section 6.2.4 and the remainder of the chapter is devoted to deriving the marginal stability conditions for a given lab-scale cable.

In Section 6.3, the non-linear set of 0-D equations for lab-scale magnets in the Resistive Domain are linearized to allow an analytical study of stability. Although several simplifying assumptions are necessary, analytic solutions for the marginal stability criterion are derived and presented graphically. The implications for ramp-rate limitation qualitatively agree with experimental evidence.

6.1 Derivation of Lab-Scale Cable Regime

Lab-scale cables are characterized by their relatively short length and their inability to generate large magnetic fields. In order to simulate the high field conditions encountered by full-scale magnets, lab-scale magnets are usually placed within the bore of a background field magnet. For the purposes of this chapter, then, the magnetic field is considered to be spatially uniform and indpendent of the transport current.

The short lengths of lab-scale cables mean the influence of joint effects can span the entire cable. The results of Chapter 5 showed that the joints did not play an important role in the Resistive Domain for large-scale cables. For lab-scale cables, on the other hand, we will see that the proximity of low-resistance joints to the normal zone region will allow rapid current-transfer out of the resistive strand. Unlike full-scale magnets, lab-scale cables are not necessarily doomed to eventual quench even if they do enter the Resistive Domain.

The complete Resistive Domain model derived in Chapter 5 for full-scale magnets can be reduced to a simpler model for the case of lab-scale cables which satisfy certain cable length criteria. The reduced model results in coupled, non-linear ODE's which are in general easier to analyze than the PDE's of Chapter 5. The 0-D model for lab-scale cables and the associtated validity criteria are now derived.

6.1.1 Zero-D Model for Lab-Scale Cables

We have already stipulated that the magnetic field profile is uniform for the case of lab-scale cables. If the current and temperature profiles are also uniform, then the 1-D Resistive Domain model developed in Chapter 6 reduces to a 0-D model. To derive the conditions for when the 0-D model is valid, we start with the 1-D equations, given in Section 5.2.3, and then use perturbation analysis (similar to the procedure used for the Short Cable Regime in the Superconducting Domain, Section 4.3.2). The current equation and the temperature equations will be discussed separately.

Zero-D Current Equation

The 1-D current equation and its boundary conditions were given in Eqs. (5.31)–(5.44) and are repeated here for convenience:

$$\alpha^2 \frac{\partial^2 \langle I \rangle}{\partial x^2} - \frac{\partial \langle I \rangle}{\partial t} - \frac{1}{2\mathcal{L}} (\mathcal{R}_1 + \mathcal{R}_2) \langle I \rangle = -\frac{1}{\mathcal{L}} \mathcal{R}_2 I_{T/2} - \frac{\partial I_{T/2}}{\partial t} \tag{6.1}$$

$$x = 0; \qquad \langle I \rangle - \ell_J \frac{\partial \langle I \rangle}{\partial x} = -\ell_J \frac{\dot{B}_\perp w \ell_p \sigma_\perp}{2\pi} \sin\theta_0 + I_{T/2} \tag{6.2}$$

$$x = \ell; \qquad \langle I \rangle + \ell_J \frac{\partial \langle I \rangle}{\partial x} = \ell_J \frac{\dot{B}_\perp w \ell_p \sigma_\perp}{2\pi} \sin\theta_1 + I_{T/2} \tag{6.3}$$

where $\langle I \rangle$ is the total current in strand *one* locally averaged over the twist-pitch length and $I_{T/2}$ represents one-half the transport current.[1]

The two necessary criteria which define the lab-scale regime will now be defined:

i. $\ell < \ell_J$

ii. $\ell < \ell_X$.

---

[1] While the shorthand notation I was used in Chapter 5, we return to the notation $\langle I \rangle$ to avoid confusion when $\langle I \rangle$ is expanded in a perturbation series later on.

where ℓ_J is the boundary length scale, $\ell_J = (\sigma_\perp \Re_J)^{-1}$, introduced in Section 4.2.3, and ℓ_X is the characteristic transfer length, $\ell_X = (\sigma_\perp \mathcal{R}_m)^{-\frac{1}{2}}$, introduced in Section 5.4.1. For typical parameter values, the second criterion is more restrictive than the first and corresponds to cables with $\ell < 5 - 10$ m. To simplify the scaling arguments which will be used shortly, we thus assume the following ordering: $\ell < \ell_X < \ell_J$.

If we define the small number $\epsilon \equiv \ell/\ell_X$, we can expand $\langle I \rangle$ in a perturbation series with the first two terms equal to:

$$\langle I \rangle (x,t) = \langle I \rangle_0 (x,t) + \langle I \rangle_2 (x,t) + \dots$$

where $\langle I \rangle_2 / \langle I \rangle_0 \sim \epsilon^2$. Substituting this expansion into Eq. (6.1) and keeping only the terms of order ϵ^0 produces the result:

$$\frac{\partial^2 \langle I \rangle_0}{\partial x^2} = 0 \tag{6.4}$$

Substituting the perturbation series into the boundary conditions and keeping terms of order $\ell_J/\ell > 1/\epsilon^2$ produces the boundary conditions on the $\langle I \rangle_0$ component of the series:

$$x = 0; \qquad \frac{\partial \langle I \rangle_0}{\partial x} = 0 \tag{6.5}$$

$$x = \ell; \qquad \frac{\partial \langle I \rangle_0}{\partial x} = 0 \tag{6.6}$$

The solution to Eq. (6.4) in consideration of these boundary conditions is $\langle I \rangle_0 (x,t) = \langle I \rangle_0 (t)$, an unknown function of time which is independent of x.

To determine the time-dependence of $\langle I \rangle_0$, it is necessary to look at the ϵ^2 order terms from Eq. (6.1):

$$\alpha^2 \frac{\partial^2 \langle I \rangle_2}{\partial x^2} - \frac{\partial \langle I \rangle_0}{\partial t} - \frac{1}{2\mathcal{L}} (\mathcal{R}_1 + \mathcal{R}_2) \langle I \rangle_0 = -\frac{1}{\mathcal{L}} \mathcal{R}_2 I_{T/2} - \frac{\partial I_{T/2}}{\partial t} \tag{6.7}$$

Integrating this equation over the length of the cable produces the result

$$\alpha^2 \frac{1}{\ell}\left(\left.\frac{\partial \langle I\rangle_2}{\partial x}\right|_{x=\ell} - \left.\frac{\partial \langle I\rangle_2}{\partial x}\right|_{x=0}\right) - \frac{\partial \langle I\rangle_0}{\partial t} - \frac{1}{2\mathcal{L}}\left(\mathcal{R}_1 + \mathcal{R}_2\right)\langle I\rangle_0 = -\frac{1}{\mathcal{L}}\mathcal{R}_2 I_{T/2} - \frac{\partial I_{T/2}}{\partial t} \tag{6.8}$$

The ϵ^0 order terms in boundary conditions can be used to solve for the $\frac{\partial}{\partial x}\langle I\rangle_2$ terms in Eq. (6.8) and thus provide closure:

$$x = 0; \qquad \ell_J \frac{\partial \langle I\rangle_2}{\partial x} = \langle I\rangle_0 + \ell_J \frac{\dot{B}_\perp w \ell_p \sigma_\perp}{2\pi}\sin\theta_0 - I_{T/2} \tag{6.9}$$

$$x = \ell; \qquad \ell_J \frac{\partial \langle I\rangle_2}{\partial x} = -\langle I\rangle_0 + \ell_J \frac{\dot{B}_\perp w \ell_p \sigma_\perp}{2\pi}\sin\theta_1 + I_{T/2} \tag{6.10}$$

Using Eqs. (6.9) and (6.10) to substitute into Eq. (6.8) provides the desired equation for $\langle I\rangle_0$:

$$\alpha^2 \frac{1}{\ell\ell_J}\left(-2\langle I\rangle_0 + \ell_J \frac{w\ell_p\sigma_\perp}{2\pi}(\sin\theta_1 - \sin\theta_0) + 2I_{T/2}\right) \\ - \frac{\partial \langle I\rangle_0}{\partial t} - \frac{1}{2\mathcal{L}}\left(\mathcal{R}_1 + \mathcal{R}_2\right)\langle I\rangle_0 = -\frac{1}{\mathcal{L}}\mathcal{R}_2 I_{T/2} - \frac{\partial I_{T/2}}{\partial t} \tag{6.11}$$

which when rearranged gives:

$$\frac{\partial \langle I\rangle_0}{\partial t} + \left(\frac{1}{\tau_J} + \frac{\mathcal{R}_1 + \mathcal{R}_2}{2\mathcal{L}}\right)\langle I\rangle_0 = \frac{\partial I_{T/2}}{\partial t} + \left(\frac{1}{\tau_J} + \frac{\mathcal{R}_2}{\mathcal{L}}\right) I_{T/2} + \Psi \tag{6.12}$$

where $\Psi \equiv \frac{\dot{B}_\perp w \ell_p}{4\pi\ell\mathcal{L}}(\sin\theta_1 - \sin\theta_0)$, $\tau_J = \mathcal{L}\ell/\Re_J$, and θ_0 and θ_1 correspond to the alignment of the joints with respect the magnetic field at $x = 0$ and $x = \ell$, respectively.

Equation (6.12) is the desired current equation for lab-scale cables. Because of the functional dependencies of $\mathcal{R}_1$ and $\mathcal{R}_2$ (refer to Section 5.2.1), Eq. (6.12) is still coupled to the temperature equations when the cable is in the Resistive Domain, i.e. $\langle I\rangle_0 > I_c$. Importantly, though, the current equation is now 0-D in space, thus greatly simplifying analysis for cables which meet the criteria: $\ell < \ell_J$ and $\ell < \ell_X$.

Zero-D Temperature Equations

Once we have determined that the current equation for lab-scale magnets is 0-D, it is relatively easy to derive the 0-D temperature equations. We start by reiterating the 1-D thermal equations developed in Chapter 5, Eqs. (5.32)–(5.34)

$$\begin{aligned}
\rho_s C_s A_s \frac{\partial T_1}{\partial t} &= A_s \frac{\partial}{\partial x} \kappa_s \frac{\partial T_1}{\partial x} - \kappa_\perp (T_1 - T_2) - hp(T_1 - T_h) \\
&\quad + \mathcal{R}_1 I^2 + \frac{1}{2} \frac{1}{\sigma_\perp} (\frac{\partial I_1}{\partial x})^2 \qquad (6.13) \\
\rho_s C_s A_s \frac{\partial T_2}{\partial t} &= A_s \frac{\partial}{\partial x} \kappa_s \frac{\partial T_2}{\partial x} - \kappa_\perp (T_2 - T_1) - hp(T_2 - T_h) \\
&\quad + \mathcal{R}_2 (I_T - I)^2 + \frac{1}{2} \frac{1}{\sigma_\perp} (\frac{\partial I_1}{\partial x})^2 \qquad (6.14) \\
\rho_h C_h A_h \frac{\partial T_h}{\partial t} &= hp(T_1 - T_h) + hp(T_2 - T_h) \qquad (6.15)
\end{aligned}$$

The first thing to notice is that the source terms (Joule heating) are spatially uniform in lab-scale magnets due to the uniformity of the current, $\frac{\partial I}{\partial x} = 0$. Since the intial condition is also uniform and the end conditions are adiabatic (refer to Eqs. (5.39)–(5.44)), no axial temperature gradients are produced. Thus the conduction terms are identically zero, $\frac{\partial}{\partial x} \kappa_s \frac{\partial}{\partial x} T_1 = \frac{\partial}{\partial x} \kappa_s \frac{\partial}{\partial x} T_2 = 0$.

Without the conduction terms, the 1-D thermal model reduces directly to the desired 0-D model:

$$\begin{aligned}
\rho_s C_s A_s \frac{\partial T_1}{\partial t} &= \mathcal{R}_1 \langle I \rangle_0^2 - \kappa_\perp (T_1 - T_2) - hp(T_1 - T_h) \qquad (6.16) \\
\rho_s C_s A_s \frac{\partial T_2}{\partial t} &= \mathcal{R}_2 (I_T - \langle I \rangle_0)^2 - \kappa_\perp (T_2 - T_1) - hp(T_2 - T_h) \qquad (6.17) \\
\rho_h C_h A_h \frac{\partial T_h}{\partial t} &= hp(T_1 - T_h) + hp(T_2 - T_h) \qquad (6.18)
\end{aligned}$$

These 0-D equations, appropriate for lab-scale magnets, are still non-linear (due to the Joule heating terms) but are much easier to solve numerically than their corresponding 1-D counterparts. If properly linearized, the equations can also be studied analytically, as will be done in Section 6.3.

6.1.2 Summary of Lab-Scale Model Equations

For cables in uniform magnetic fields that meet the length criteria $\ell < \ell_J$ and $\ell < \ell_X$, the 0-D lab-scale model equations, derived above, descirbe the coupled thermal and electrical behavior in the Resistive Domain, when $\langle I \rangle_0 > I_c$. For convenience, the model equations are summarized here. The substitution $I \approx \langle I \rangle_0$ has been used to simplify the notation.

Model Equations:

$$\frac{\partial I}{\partial t} = -\left(\frac{1}{\tau_J} + \frac{\mathcal{R}_1 + \mathcal{R}_2}{2\mathcal{L}}\right) I + \frac{\partial I_{T/2}}{\partial t} + \left(\frac{1}{\tau_J} + \frac{\mathcal{R}_2}{\mathcal{L}}\right) I_{T/2} + \Psi \tag{6.19}$$

$$\rho_s C_s A_s \frac{\partial T_1}{\partial t} = \mathcal{R}_1 I^2 - \kappa_\perp (T_1 - T_2) - hp(T_1 - T_h) \tag{6.20}$$

$$\rho_s C_s A_s \frac{\partial T_2}{\partial t} = \mathcal{R}_2 (I_T - I)^2 - \kappa_\perp (T_2 - T_1) - hp(T_2 - T_h) \tag{6.21}$$

$$\rho_h C_h A_h \frac{\partial T_h}{\partial t} = hp(T_1 - T_h) + hp(T_2 - T_h) \tag{6.22}$$

Auxiliary Equations:

$$\mathcal{R}_1 = \begin{cases} 0 & I \leq I_c(B, T_1) \\ \mathcal{R}_m\left(1 - \frac{I_c(B,T_1)}{I}\right) & I > I_c(B, T_1) \end{cases} \tag{6.23}$$

$$\mathcal{R}_2 = \begin{cases} 0 & I_T - I \leq I_c(B, T_2) \\ \mathcal{R}_m\left(1 - \frac{I_c(B,T_2)}{I_T - I}\right) & I_T - I > I_c(B, T_2) \end{cases} \tag{6.24}$$

$$I_c(B, T) = \begin{cases} \frac{\xi}{B}\left(1 - \frac{T - T_b}{T_c - T_b}\right) & T < T_c(B) \\ 0 & T \geq T_c(B) \end{cases} \tag{6.25}$$

$$T_c(B) = \begin{cases} T_b + (T_{c0} - T_b)\left(1 - \frac{B}{B_{c0}}\right) & B < B_{c0} \\ T_b & B \geq B_{c0} \end{cases} \tag{6.26}$$

The initial condition for the current equation is found from the analytic results of the Short Cable Length Regime of the Superconducting Domain (see Section 4.3.2), evaluated at $t = t_\star$, the time when strand *one* first becomes resistive. At $t = t_\star$, the temperature of the strands equals the background helium temperature, T_b. Thus, all together, the initial conditions which are needed to solve the model equations

Eqs. (6.19)–(6.22) are:

Initial Conditions:

$$t = t_\star \; ; \qquad I = I_{SCdomain}(t_\star) \tag{6.27}$$

$$T_1 = T_2 = T_h = T_b \tag{6.28}$$

where the notation $I_{SCdomain}$ is used to refer to the analytic solution for the current in strand *one* obtained from the results of the Superconducting Domain analysis in Section 4.3.2.

The model equations, Eqs. (6.19)–(6.22), form a set of non-linear first order ordinary differential equations. Because of the non-linear terms, a numerical solution is needed to solve the system. The numerics will be presented in the next section.

The model equations can be linearized in order to obtain approximate analytic solutions which provide insight into the behavior of lab-scale cables in the Resistive Domain. This approximate analytic method is the subject of Section 6.3.

6.1.3 Numerical Solution Technique

Since the lab-scale model equations have been reduced to a set of first order ordinary differential equations, there are several numerical techniques appropriate for solving the model. The chosen method uses a variable-order, variable-step method implementing Backward Difference Formulae as provided by the NAG Fortran Library Routine D02EAF, [39]. Details of this method are given in [40].

The model equations as given above with their auxiliary equations and initial conditions, Eqs. (6.19)–(6.28), are structured in a format which complies with a fortran code that has been written to calculate the solutions. The code acts as a driver for the D02EAF routine [39], which does the actual work of solving the time-evolution of current and temperatures. The resulting code was used to generate the numerical results which are presented in the following sections.

6.2 Numerical Results for Stability of Lab-scale Cables

After running just a few cases, it was apparent that the behavior of lab-scale cables is dramatically different than the behavior of full-scale cables. The primary difference is the ability of lab-scale cables to enter the Resistive Domain without fully quenching. In other words, even if the current in strand *one* reaches its critical current (due to induced circulating currents), a quick redistribution of current to strand *two* can allow the cable to recover to a superconducting state. This process has also been observed experimentally using magnetic pick-up coils which register the rapid redistribution of current as a voltage "blip" [5].

While the explanation of the occurence of "blips" is an important result in itself, the main goal of the theoretical model being developed here is to explain the overall stability behavior of lab-scale cables. In this section, we will present representative cases which exhibit the difference between stable and unstable operating scenarios for lab-scale cables. We will then introduce the concept of marginal stability, the operating scenario for which a given cable is on the stable/unstable cusp. The numerical model can be run in an iterative fashion to map out the marginal stability line for varying magnetic field ramp rates, $\dot{B}_\perp$. In other words, the model will be used to study Ramp-Rate Limitation for small-scale cables.

6.2.1 Hypothetical Lab-Scale Cable

To demonstrate the behavior of lab-scale cables in ramping magnetic fields, numerical results are presented graphically for the case of a hypothetical cable design. The hypothetical design is similar to the actual cable design of small-scale experiments conducted at MIT [2, 3]. The theoretical results presented here will be developed further in Chapter 7 to allow a direct comparison to the experimental results. For now, the hypothetical cable is used to communicate the main features observed in lab-scale cables.

cable length	ℓ	1 m
twist-pitch length	ℓ_p	15 cm
cable width	w	0.5 cm
effective inductance per length	$\mathcal{L}$	0.7 μH
transverse electrical conductivity	$\sigma_\perp$	100 Ω^{-1}m^{-1}
transverse joint resistance	$\Re_J$	1 $\mu\Omega$
joint orientation at $x = 0$	θ_0	$-\pi/4$
joint orientation at $x = \ell$	θ_1	$\pi/4$
helium background temperature	T_b	4.5 K
helium pressure	P_h	5 atm.
helium cross-sectional area	A_h	0.64 mm^2
strand (one) cross-sectional area	A_s	0.48 mm^2
volume fraction superconductor	λ	0.45
matrix resistance per length	$\mathcal{R}_m$	1 mΩ-m^{-1}
heat transfer coefficient	h	1000 W/m^2-K
transverse thermal conductivity	$\kappa_\perp$	∞ W/m-K

Table 6.1: The Hypothetical Lab-Scale Cable Properties.

The parameters of the hypothetical cable design are presented in Table 6.1. Since the lab-scale cables are tested in the bore of larger background field magnets, the transport current is independent of the magnetic field. In the cases studied here, the transport current is constant while the spatially uniform magnetic field is ramped linearly in time. For a given cable, then, the operating scenario is defined by two independent quantities: the transport current, I_T, and the ramp-rate, $\dot{B}_\perp$.

Since the hypothetical cable falls under the Short Cable Length/Short-Circuit Joint regime of the Superconducting Domain, Eq. (4.70) describes the circulating current in strand *one* up until the point $\langle I \rangle = I_c$. Adding half the transport current (a constant) to the circulating current gives the total current in strand *one* in the Superconducting Domain:

$$\begin{aligned} I(t) &= I_{T/2} + \langle I_B \rangle (t) \\ &= I_{T/2} + \Psi \tau_J \left(1 - e^{-t/\tau_J}\right) \end{aligned} \tag{6.29}$$

where $\dot{B}_\perp$ is the uniform ramp-rate of the magnetic field; $\tau_J \equiv \mathcal{L}\ell/\Re_J$ is the characteristic time constant of an insulated two strand cable; and $\Psi \equiv \frac{\dot{B}_\perp w \ell_p}{4\pi\ell\mathcal{L}}(\sin\theta_1 - \sin\theta_0)$ is the inductive source term.

At time $t = t_\star$, the current in strand one reaches the critical current and the cable enters the Resistive Domain. In the Resistive Domain, the time-evolution of the current becomes coupled to the time-evolution of the temperatures and the full model, Eqs. (6.19)–(6.22), becomes necessary, starting from the initial condition $I_\star \equiv I(t_\star) = I_c(B(t_\star), T_b)$.

For a given cable and given cooling conditions (i.e., specified heat transfer coefficient, h) the cable can either quench or recover after entering the Resistive Domain, depending on the value of the initial condition, $I_\star$. In turn $I_\star$ is dependent on the transport current, I_T, and the ramp-rate, $\dot{B}_\perp$. To demonstrate the different possible outcomes, two examples are given using the hypothetical cable described in Table 6.1.

6.2.2 Example of Instability

In the first example, the total tansport current is $I_T = 135$ Amps and the ramp-rate is $\dot{B}_\perp = 1$ T/s. Using Eq. (6.29) to calculate the total current in strand *one*, I(t), and Eq. (6.25) to calculate the critical current, I_c(t), for times $t \leq t_\star$, the onset of the Resistive Domain is calculated to begin at $t = t_\star = 5.40$ s and $I = I_\star = 385$ Amps. The time-evolution of I and I_c is plotted in Fig. 6-1 for $0 < t < t_\star$.

Once the cable enters the Resistive Domain the time-evolution of the currents and temperatures occurs on a much faster time-scale. Figure 6-2 shows the current in strands *one* and *two*, I_1 and I_2, as well as the critical current, I_c, for the first 5 ms after $t = t_\star$.[2] The strand temperature, $T \equiv T_1 = T_2$, and the helium temperature, T_h, are plotted over the same range of time in Fig. 6-3. As the plots indicate, under these operating conditions ($I_T = 135$ Amps, $\dot{B}_\perp = 1.0$) the cable quenches quickly after it reaches the Resistive Domain.

---

[2] Since $\kappa_\perp = \infty$ for this hypothetical case, $T_1 = T_2$ and thus $I_{c_1} = I_{c_2} = I_c$.

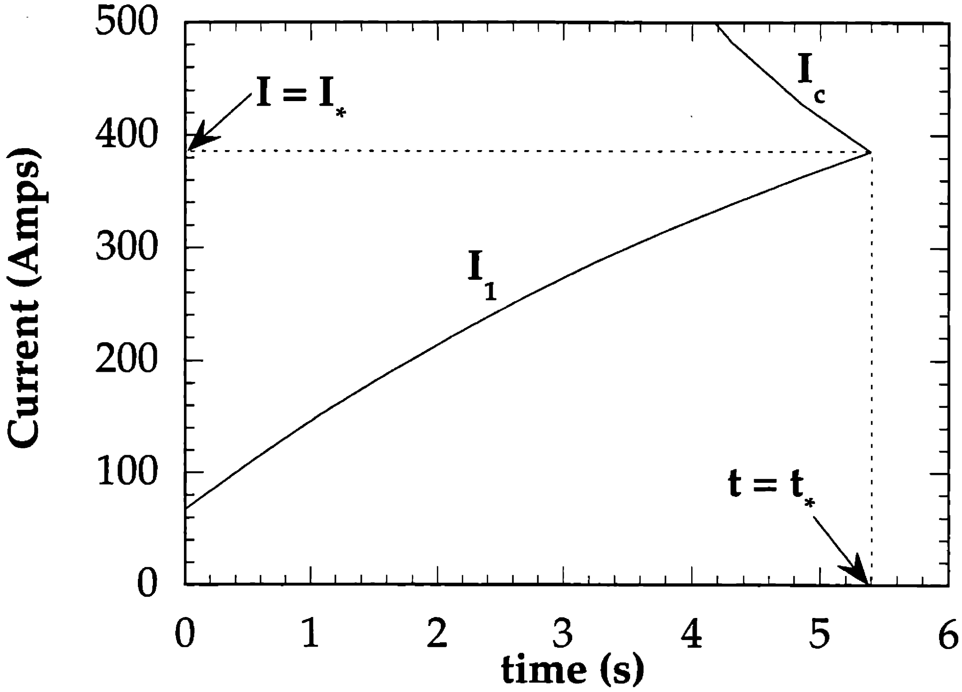

Figure 6-1: The strand *one* current and critical current for the hypothetical cable in the Superconducting Domain: $I_T = 135$ Amps, $\dot{B}_\perp = 1.0$ T/s, $t_\star = 5.40$ s, $I_\star = 385$ Amps.

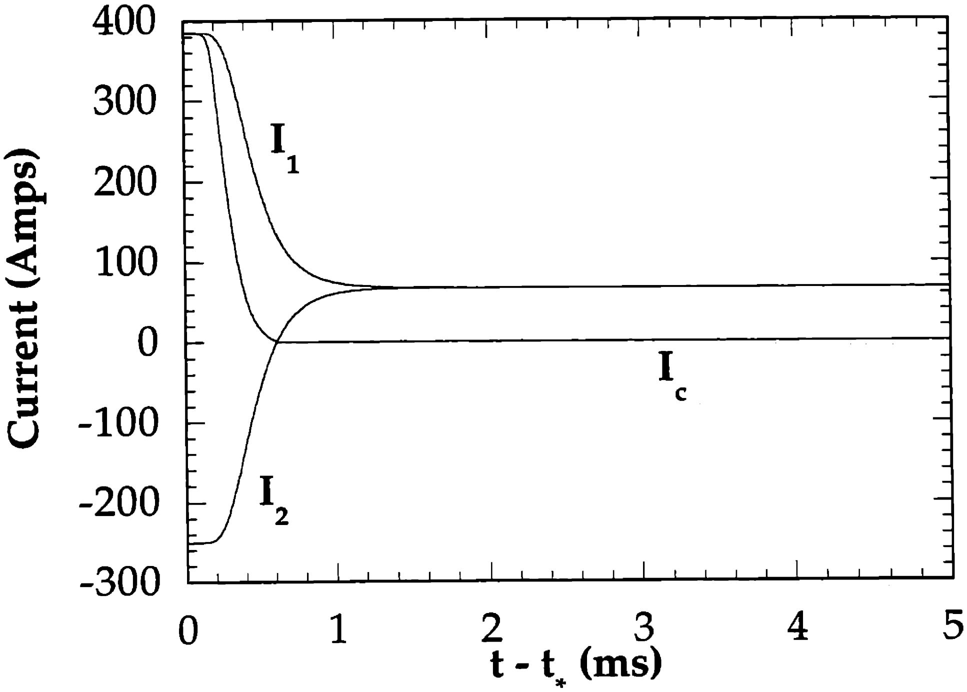

Figure 6-2: The strand currents and the critical current for the hypothetical cable in the Resistive Domain. Unstable case: $I_T = 135$ Amps, $\dot{B}_\perp = 1.0$ T/s.

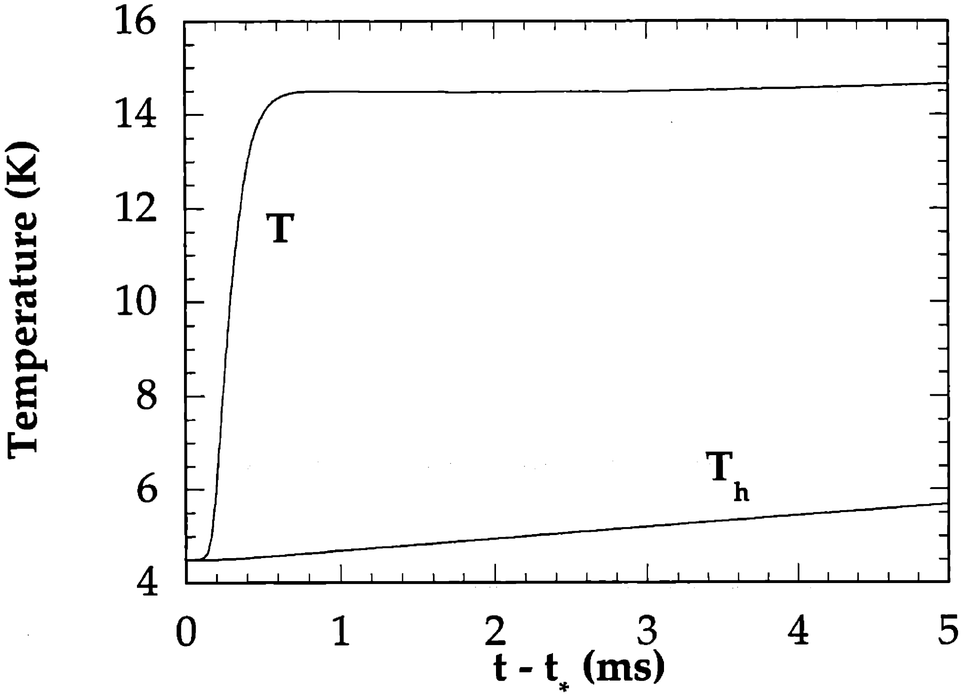

Figure 6-3: The strand and helium temperatures for the hypothetical cable in the Resistive Domain. Unstable case: $I_T = 135$ Amps, $\dot{B}_\perp = 1.0$ T/s.

6.2.3 Example of Stability

Let's see what happens if the operating condition is changed only slightly. In the second example, the transport current is decreased by 5 Amps to $I_T = 130$ Amps while the ramp-rate remains the same, $\dot{B}_\perp = 1$ T/s. As before, the time evolution of I and I_c is plotted for $0 < t < t_\star$ in Fig. 6-4. For this case, $t_\star = 5.42$ s and $I_\star = 384$ Amps, almost the same as in the previous example.

What happens after the cable enters the Resistive Domain, however, is substantially different than what happened in the previous example. Figure 6-5 shows the current in strands *one* and *two* I_1 and I_2, as well as the critical current, I_c, for the first 5 ms after $t = t_\star$. The strand temperature, $T \equiv T_1 = T_2$, and the helium temperature, T_h, are plotted over the same range of time in Fig. 6-6. As the plots indicate, under these operating conditions (I_T= 130 Amps, $\dot{B}_\perp$= 1.0 T/s) the cable is able to return to the Superconducting Domain (i.e. $I < I_c$) even after it enters the Resistive Domain. This ability to "recover" under certain operating conditions

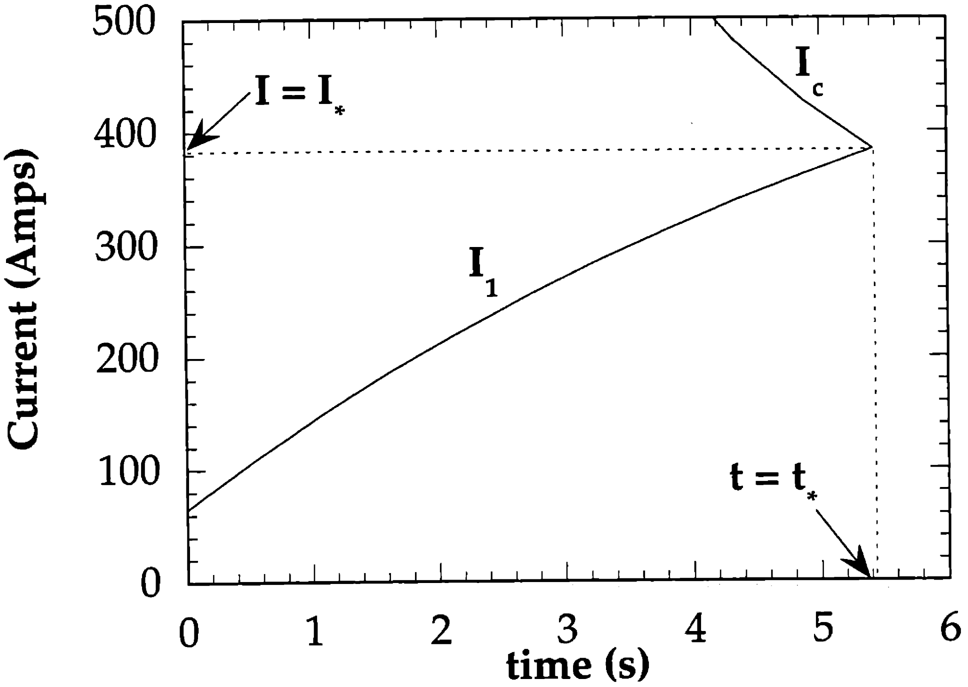

Figure 6-4: The strand *one* current and critical current for the hypothetical cable in the Superconducting Domain. Stable Case: $I_T = 130$ Amps, $\dot{B}_\perp = 1.0$ T/s, $t_\star = 5.42$ s, $I_\star = 384$ Amps.

is only observed in lab-scale cables—longer cables always fully quench after entering the Resistive Domain.

In Fig. 6-7, the time-evolution of the currents is allowed to continue beyond the first occurence of the Resistive Domain. As seen in the plot, each time I reaches the ever-decreasing I_c, due to currents induced while the cable is in the Superconducting Domain, a "blip" occurs. During the blip, the cable is in the Resistive Domain and the current is quickly redistributed among the strands until the cable re-enters the Superconducting Domain. The time-evolution of the temperatures during this cyclic behavior is shown in Fig. 6-8. If ramped long enough, the cable will eventually quench, but only when the transport current itself (without the circulating current) reaches the critical current.

Since the cable in this example is able to survive the series of blips, it can be operated at close to the DC limit.[3] The cable is thus said to be "stable" with regard

---

[3] The rise in the background helium temperature due to the repeated quench/recovery blips

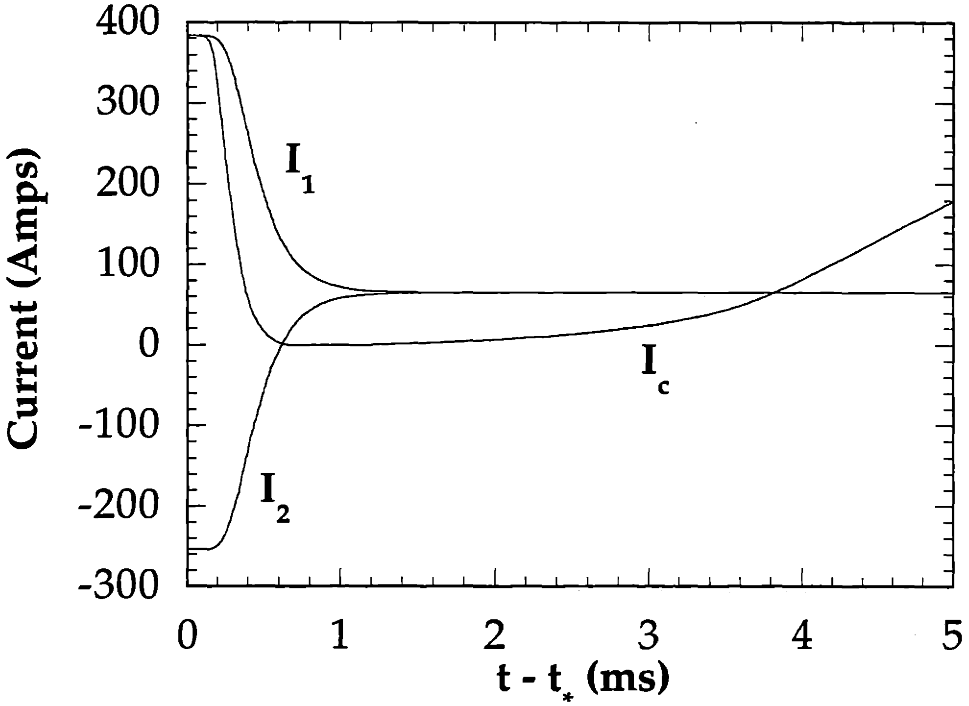

Figure 6-5: The strand currents and the critical current for the hypothetical cable in the Resistive Domain. Stable Case: $I_T = 130$ Amps, $\dot{B}_\perp = 1.0$ T/s.

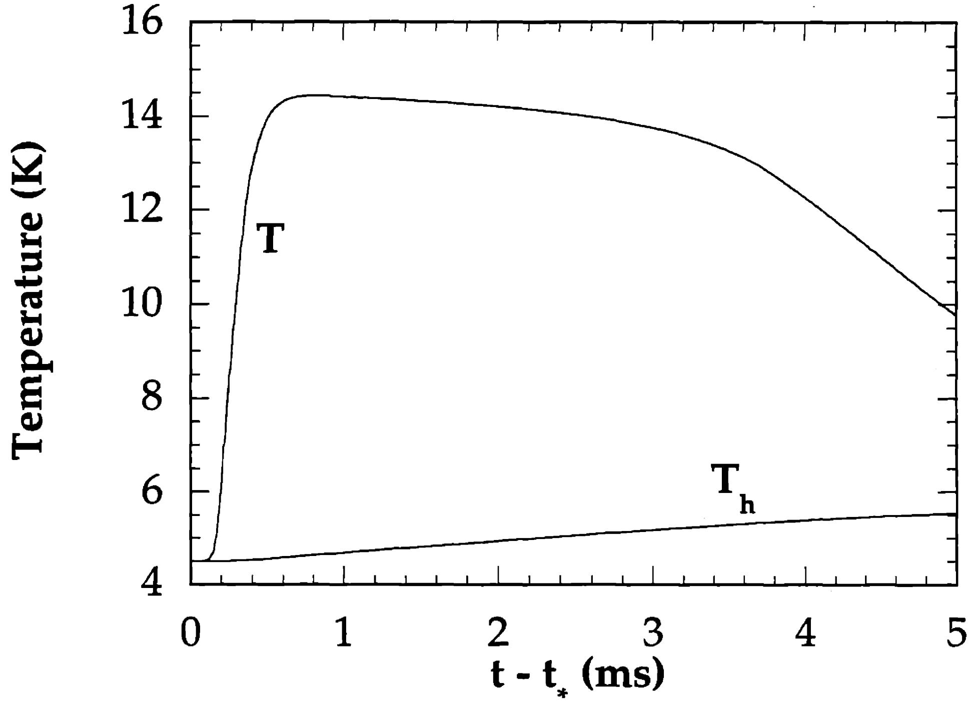

Figure 6-6: The strand and helium temperatures for the hypothetical cable in the Resistive Domain. Stable Case: $I_T = 130$ Amps, $\dot{B}_\perp = 1.0$ T/s.

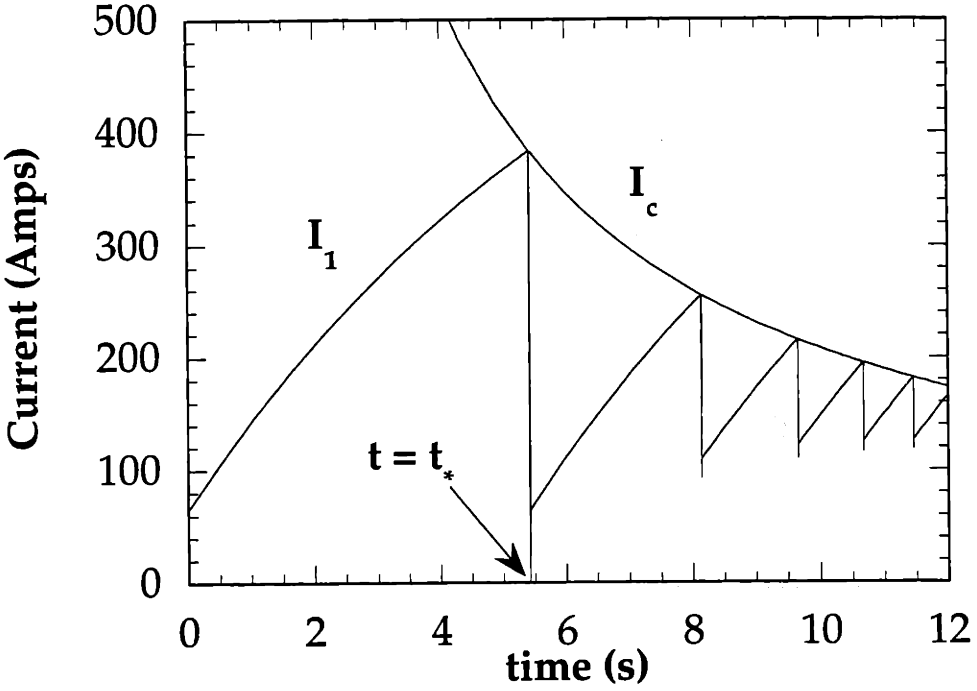

Figure 6-7: The strand *one* current and the critical current for the hypothetical cable as it cycles between the Superconducting Domain and the Resistive Domain. Stable Case: $I_T = 130$ Amps, $\dot{B}_\perp = 1.0$ T/s.

to ramp-rate limitation for this operating condition. Numerous factors (in fact every factor listed in Table 6.1) affect whether a two-strand cable is stable or unstable but for a given design the stability is determined solely by I_T and $\dot{B}_\perp$.

In determining whether a cable is stable or unstable for a given operating scenario (i.e. given I_T and $\dot{B}_\perp$), it is the first blip which is critical. If the cable can survive the first blip without quenching, it will be stable to all further blips (until $I_T = I_c$, the DC limit). This behavior is explained by the fact that $I_\star$ is greatest for the first blip (due the monotonically decreasing I_c). Since the intial Joule heating generated when the cable enters the Resistive Domain is proportional to $I_\star^2$, the power balance between heating and cooling is most heavily weighted toward heating during the first blip. If the cooling is sufficient to bring the cable back into the Superconducting Domain for the first blip, it will be more than sufficient for the subsequent blips.

Strong evidence supporting the ability of lab-scale cables to survive multiple en-

---

reduces the effective critical current from the DC value, but this is a relatively minor effect.

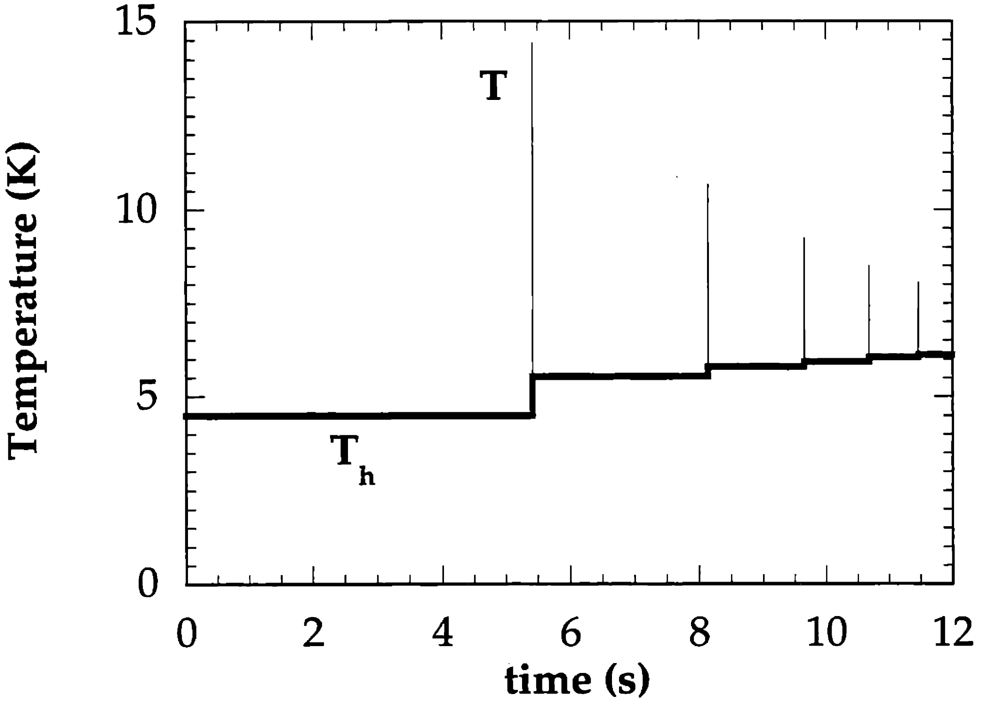

Figure 6-8: The strand and helium temperatures for the hypothetical cable as it cycles between the Superconducting Domain and the Resistive Domain. Stable Case: $I_T = 130$ Amps, $\dot{B}_\perp = 1.0$ T/s.

counters with the Resistive Domain has been gathered experimentally [4, 5]. Using voltage taps, pick-up coils, and hall probes, researchers have detected short-lived voltage spikes as well as rapid redistribution of current in 1–3 m samples exposed to ramping magnetic fields. Previous attempts [4, 9] to explain these phenomena have also looked at the effects circulating currents and reached the same conclusion proposed in this thesis. In those efforts, however, the current distribution was not coupled to the thermal behavior so as to allow an overall explanation of stability in lab-scale cables, as will be covered in the next section.

6.2.4 Marginal Stability in Lab-Scale Cables

By focusing on the behavior of the cable during the first blip, we can define what we mean by "marginal stability". If the cable is on the borderline between recovering or quenching during the first blip, it is marginally stable. This concept is presented graphically in Fig. 6-9. In the figure, the strand temperature is plotted versus time

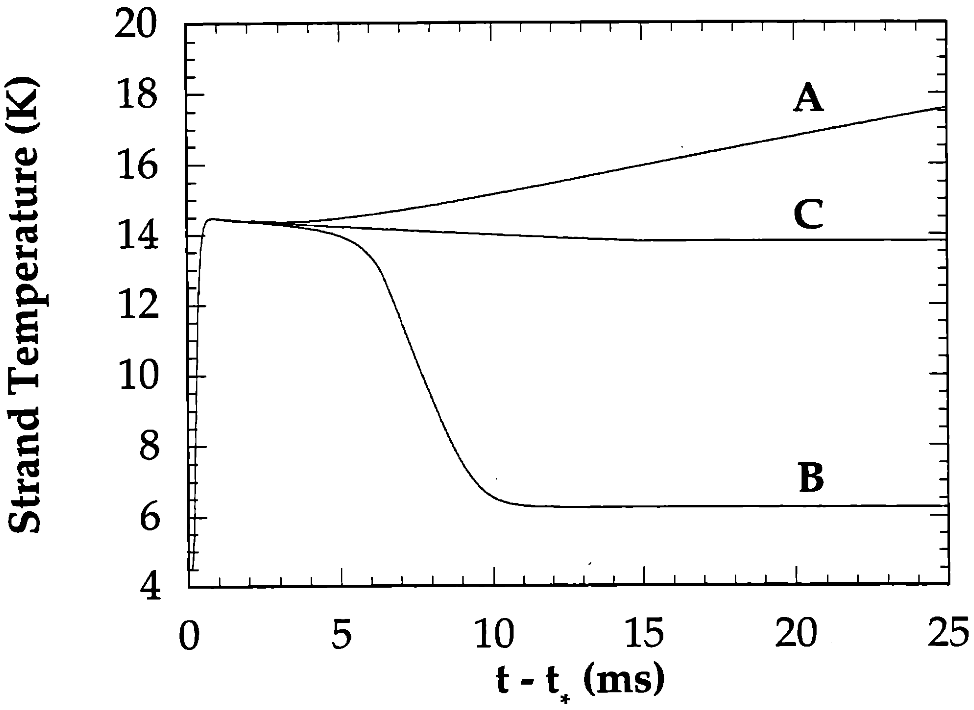

Figure 6-9: Strand temperatures for the hypothetical cable during the first blip for three cases: A, unstable; B, stable; and C, marginally stable.

for the first 5 ms after the onset of the first blip. In case A, the cable is in an unstable operating scenario and quenches—the temperature begins to increase monotonically before the strands cool enough to re-enter the Superconducting Domain. In case B, the cable is stable since the cooling is sufficient to reduce the strand temperature enough to allow the cable to recover. In case C, however, the strand temperature neither rises monotonically, indicating quench, nor cools back down to within the Superconducting Domain, indicating recovery. Case C is exactly the "marginal stability case".

Mathematically, the marginal stability case can be defined as the operating scenario which leads to the condition $\frac{\partial}{\partial t}T = \frac{\partial^2}{\partial t^2}T = 0$ as $t \to \infty$. If this condition is met, the cable reaches a steady-state equilibrium where the Joule heating is exactly balanced by the cooling; the cable is neither quenching nor recovering.

The numerical procedure used to solve the current and temperature evolution in the Resistive Domain can be run iteratively to determine the operating scenario which produces the marginal stability case. For a given ramp-rate, $\dot{B}_{\perp}$, the transport current, I_T, is varied until the result of the first blip is the stady state equilibrium

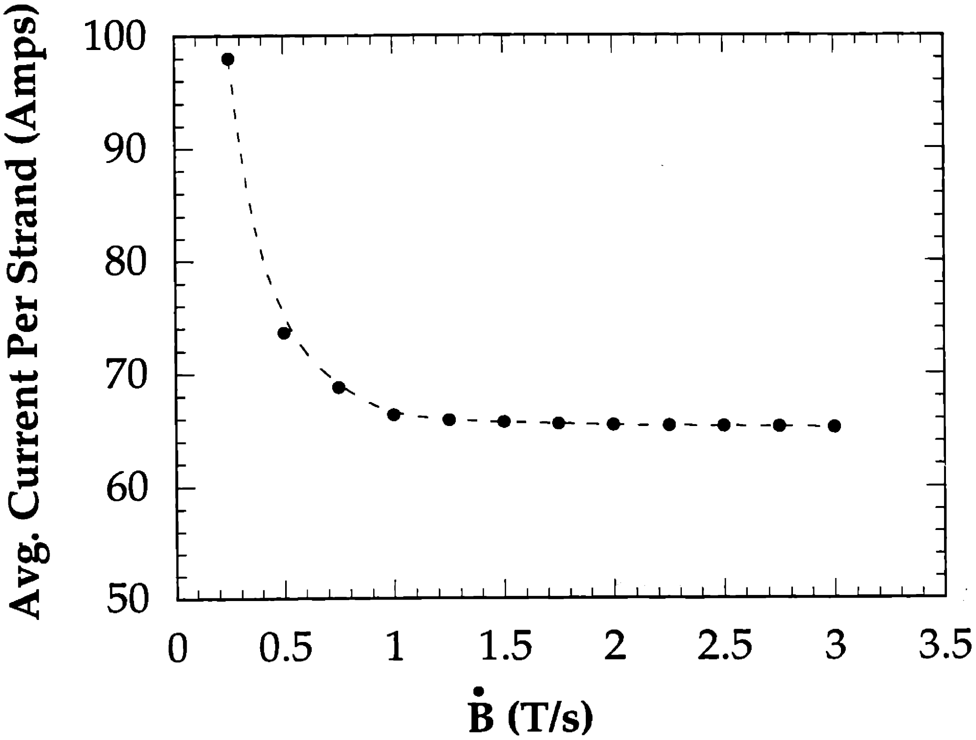

Figure 6-10: The marginal stability line for the hypothetical cable. • numerical results; - - - curve fit.

$\frac{\partial}{\partial t}T = \frac{\partial^2}{\partial t^2}T = 0$. Using this numerical procedure, the marginal stability line is plotted in Fig. 6-10 for the hypothetical cable described in Table 6.1. For operating scenarios below the marginal stability line in the I_T–$\dot{B}_\perp$ phase domain, the cable is stable and can reach peak fields near the DC design limit after surviving numerous blips. For operating scenarios above the marginal stability line, the cable is unstable and will quench on the first blip, much below the DC design limit.

It is difficult to extensively test the implications of the existence of a marginal stabiliy criteria for lab-scale cables using the iterative numerical procedure just described. For this reason, it was decided to linearize the non-linear equations in order to study the problem analytically. The linearized equations lack the accuracy of the numerical results but the important qualitative features are maintained. Using the analytic solutions to the linearized equations, the current distribution and stability behavior of lab-scale cables can be studied in greater detail.

6.3 Linearized Resistive Domain

Even though the current and temperature equations for lab-scale cables reduce to a set of equations which are 0-D in space, the resulting model is still non-linear. In the previous section, the model equations were solved numerically and iteration was used to find the marginal stability line for a given cable design. In general, this procedure is not adequate for doing parametric studies of cable design since it is computationally inefficient. We would like to find a way to solve the model equations analytically to improve efficiency and, more importantly, gain insight into how the different cable parameters affect the stability.

In this section, we will linearize the current and temperature equations in order to allow an analytic study of current distribution and stability in lab-scale cables. The numerical results of the previous section will be used to help scale the linearized parameters. The end goal is to calculate the "marginal" case for a specified cable, i.e. to determine at which I_T and $\dot{B}_\perp$ the cable reaches an unstable equilibrium between quenching and recovering.

In the following discussion, we will limit ourselves to the scenario of constant transport current and linearly ramping magnetic field. Also, the cables which will be studied will fall into the Short Cable Length/Short-Circuit Joint Regime identified in Chapter 4. This regime is appropriate for almost any lab-scale cable design.

Two a priori assumptions will be made as well. First, the two strands will be considered to be in near-perfect thermal contact, $T_2 \approx T_1 \equiv T$. This assumption will be valid for strands in good thermal contact and is needed in order to reduce the linear analysis from a third order ODE to a tractable second order ODE. The second assumption is that the helium temperature remains approximately constant over the timeframe of the stability event, i.e. $T_h \approx T_b$. This latter assumption is generally valid and was born out through numerous numerical examples. With these restrictions in mind, the scenario which will be considered in the linearized analysis is summarized in Table 6.2.

Short Length Regime	$\ell < \ell_D$
Short-Circuit Joints	$\ell < \ell_J$
good thermal contact	$T \equiv T_1 \approx T_2$
constant helium temp.	$T_h \approx T_b$

Table 6.2: Restrictions in effect for the linearized stability analysis.

6.3.1 Linearized Resistive Domain Equations

The current equation for lab-scale cables in the Resistive Domain was given in Eq. (6.19):

$$\frac{\partial I}{\partial t} + \left(\frac{1}{\tau_J} + \frac{\mathcal{R}_1 + \mathcal{R}_2}{2\mathcal{L}}\right) I = \frac{\partial I_{T/2}}{\partial t} + \left(\frac{1}{\tau_J} + \frac{\mathcal{R}_2}{\mathcal{L}}\right) I_{T/2} + \Psi \tag{6.30}$$

where Ψ was defined in Eq. (6.12). Using Eq. (6.23) to substitute for the $\mathcal{R}_1$ and $\mathcal{R}_2$ coefficients reveals the coupling to the temperature dependent critical current, I_c. For example, if $I > I_c$ but $I_2 = I_T - I < I_c$ we have:

$$\frac{\partial I}{\partial t} + \frac{1}{\tau_J} I + \frac{\mathcal{R}_m}{2\mathcal{L}}(I - I_c(B,T)) = \frac{\partial I_{T/2}}{\partial t} + \frac{1}{\tau_J} I_{T/2} + \Psi \tag{6.31}$$

To see the coupling to the temperature equation directly, we need to substitute for the critical current, I_c(B,T). If the magnetic field at the onset of the Resistive Domain is defined to be $B(t_\star) \equiv B_\star$, the approximation $B(t) \approx B_\star$ can be used (even for rapid $\dot{B}_\perp$) for the extent of the Resistive Domain since it lasts for only a very brief time. In this case, the critical current simplifies to:

$$I_c(B,T) = I_c(T) = I_\star \left(1 - \frac{\vartheta}{\vartheta_{c\star}}\right) \tag{6.32}$$

where $I_\star \equiv \xi / B_\star$ and ϑ is a simple transformation of the temperature, $\vartheta \equiv T - T_b$. The scale factor $\vartheta_{c\star}$ is constant for the duration of the stability event; from Eq. (6.26), $\vartheta_{c\star} \equiv (T_{c0} - T_b)(1 - B_\star / B_{c0})$.

Substituting Eq. (6.32) into Eq. (6.31) yields the final result:

$$\frac{\partial I}{\partial t} + \left(\frac{1}{\tau_J} + \frac{\mathcal{R}_m}{2\mathcal{L}}\right) I = \frac{\mathcal{R}_m}{2\mathcal{L}} I_\star \left(1 - \frac{\vartheta}{\vartheta_{c\star}}\right) + \frac{\partial I_{T/2}}{\partial t} + \frac{1}{\tau_J} I_{T/2} + \Psi \qquad (6.33)$$

where the temperature dependence is finally explicit. Equation (6.33) is a linear equation which is coupled, however, to the temperature equation which is non-linear.

The temperature equations were given in Eqs. (6.20)–(6.22). Using the restrictions listed in Table 6.2, the temperature equations for the two strands and the helium are reduced to a single equation since $T_2 \approx T_1 \equiv T$ and $T_h \approx T_b$. Again, using the notation, $\vartheta \equiv T - T_b$, the remaining equation becomes:

$$\rho_s \bar{C}_s A_s \frac{\partial \vartheta}{\partial t} + 2hp\vartheta = \mathcal{R}_1 I^2 + \mathcal{R}_2 (I_T - I)^2 \qquad (6.34)$$

where the constant $\bar{C}_s$ replaces the temperature dependent C_s. The decision of which value to use for $\bar{C}_s$ is determined by fitting the linear model to the results of the non-linear model. For a wide range of cases, the value $\bar{C}_s = 0.3$ J/m-K provided the optimal fit.[4]

The non-linear Joule heating terms on the RHS of Eq. (6.34) need to be linearized. Looking for the moment at the case when $\mathcal{R}_1 > 0$ but $\mathcal{R}_2 = 0$, substituting Eq. (6.23) for $\mathcal{R}_1$ in Eq. (6.34) produces the result:

$$\rho_s \bar{C}_s A_s \frac{\partial \vartheta}{\partial t} + 2hp\vartheta = \mathcal{R}_m I (I - I_c) \qquad (6.35)$$

Using the numerical results as a guide, it was found that the behavior of the cable was most sensitive to the difference $(I - I_c)$ while the factor which multiplies this difference, I, was much less critical. For this reason it was decided to approximate the non-linear Joule heating term with the following linear equivalent: $\mathcal{R}_m I (I - I_c) \mapsto \mathcal{R}_m \bar{I} (I - I_c)$.

The value of the linearizing approximation, $\bar{I}$, can be chosen in a way to most closely match the numerical results for a number of cases. In general, $\bar{I}$ falls between the initial current at the onset of the Resistive Domain, $I_\star$, and the average current

---

[4] For comparison, $C_s(T = 5K) \approx 0.15$ J/(kg-K) and $C_s(T = 10K) \approx 0.85$ J/(kg-K).

per strand, $I_{T/2}$:

$$\bar{I} = zI_\star + (1-z)I_{T/2} \tag{6.36}$$

where $0 < z < 1$. After running many trials, the value $z = 0.4$ was chosen to optimize the match between the analytic linear and numerical non-linear models.

Substituting the temperature dependent equation for I_c, Eq. (6.32), and the linearized Joule heating term into Eq. (6.35) results in the desired linearized temperature equation:

$$\rho_s \bar{C}_s A_s \frac{\partial \vartheta}{\partial t} + 2hp\vartheta = \mathcal{R}_m \bar{I}[I - I_\star(1 - \vartheta/\vartheta_{c\star})] \tag{6.37}$$

The coupled current and temperature equations, Eqs. (6.33) and (6.37), are both first order, linear ordinary differential equations. The two equations can be solved simultaneously using standard solution techniques. The most direct method is substitution, which results in a single second order differential equation.

6.3.2 Solving the Linearized Equations

Combining Eqs. (6.33) and (6.37) results in a second order differential equation for the current, I. To study the marginal stability problem, it is useful to divide the time-evolution into three segments to take advantage of the piecewise continuous nature of $\mathcal{R}_1$ and $\mathcal{R}_2$:

I. $0 < t < t_\star$ Both strands are superconducting, $\mathcal{R}_1 = \mathcal{R}_2 = 0$.

II. $t_\star < t < t_x$ Strand *one* is resistive but strand *two* is superconducting, $\mathcal{R}_1 > 0, \mathcal{R}_2 = 0$.

III. $t > t_x$ Both strands are resistive. $\mathcal{R}_1 > 0, \mathcal{R}_2 > 0$.

At the transition times ($t = t_\star$ and $t = t_x$), the current and temperature must be continuous. Also, the initial conditions at $t = 0$ are specified: $I = I_{T/2}$ and $\vartheta = 0$. Thus, for a given I_T and $\dot{B}_\perp$, the problem becomes a straightforward series of three initial value problems with suitable initial conditions found from the solution of the previous region.

To calculate the marginal stability case, however, we want to start at the end and work backwards—this is not so straightforward. Since the mathematics (mostly algebra) becomes quite intense, the details are left for Appendix C. In the next paragraphs, however, the procedure used to develop an analytic stability criterion will be described using figures in lieu of equations wherever possible. To do so, we will first consider the problem in the "forward" sense (starting with a given I_T and $\dot{B}_\perp$) before considering how to begin at the desired end condition ($\frac{\partial}{\partial t}\vartheta = \frac{\partial^2}{\partial t^2}\vartheta = 0$ as $t \to \infty$) and working backward.

Overview of Linear Model Solution Techniques

For $0 < t < t_\star$, the cable is in the Superconducting Domain and the current distribution can be calculated using the results of Chapter 4. The value of $t_\star$ can be calculated analytically by setting the current in strand *one* equal to the critical current. This procedure is shown graphically in Fig. 6-11. The interface conditions which are needed at the transition time $t = t_\star$ are: $\vartheta = 0$ and $I(t_\star) = I_\star$, as indicated in the figure.

For times $t > t_\star$, strand *one* becomes resistive while strand *two* remains superconducting. The coupled current and temperature equations for this region of the Resistive Domain were given in Eqs. (6.33) and (6.37). While the mathematical details of the solution for the period of time $t_\star < t < t_x$ are given in Appendix C, the results can be described in general using representative figures.

Depending on the cable design (geometry, cooling conditions, joint resistance, etc.) and the operating scenario (I_T and $\dot{B}_\perp$), the system can be in one of three "mathematical states" after $t = t_\star$: overdamped, critically damped or underdamped.[5] The behavior of the solution varies depending on which state the cable is in. Examples for each of the three possibilities are given in Fig. 6-12 where the strand *one* current and the critical current are plotted vs. time in the left column and temperature vs.

---

[5] Overdamped corresponds to a characteristic equation for the second order system with two distinct real roots; critically damped implies a single, repeated real root; and underdamped means the two roots are complex conjugates.

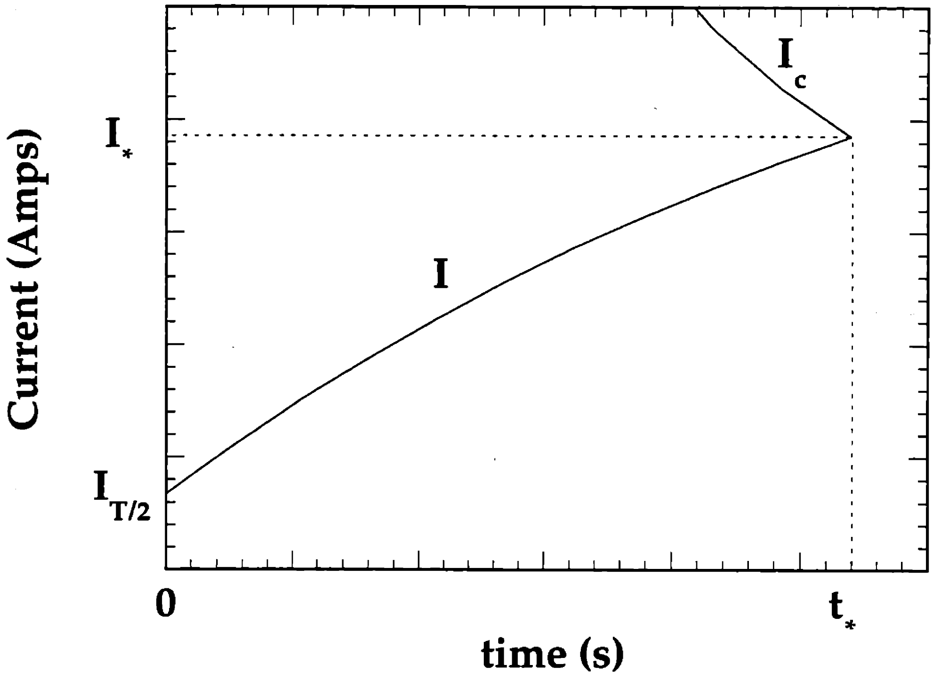

Figure 6-11: Analytical results for time $0 < t < t_\star$. The solutions from Chapter 4 can be used to calculate $t_\star$, $I_\star$, and $B_\star = \dot{B}_\perp t_\star$.

time is plotted in the right column. For now, the strand *two* current is being ignored even though it plays a critical role in the stability process, as will be discussed shortly. In the underdamped case, the solution is truncated at $t = t_{\text{rec}}$, the time at which strand *one* again becomes superconducting, $I < I_c$.

For the critically damped and overdamped cases, the temperature increases monotonically and the critical current goes to zero. In these cases, the quenching of the second strand, at some time $t = t_x$ is inevitable. Of course, from a stability point of view, this event only makes matters worse as the Joule heating in strand *two* increases the rate at which the strand temperature increases. Thus for the critically damped and overdamped conditions, the cable cannot recover and is therefore "unstable".

For different initial conditions, however, the cable will be in the underdamped state when it enters the Resistive Domain. For this case, the cable can behave in several different ways. The first possibility is that strand *one* will recover before strand *two* becomes resistive. This scenario is depicted in Fig. 6-13a and corresponds to the stable operating regime for the cable. A second possibility is that the second strand becomes

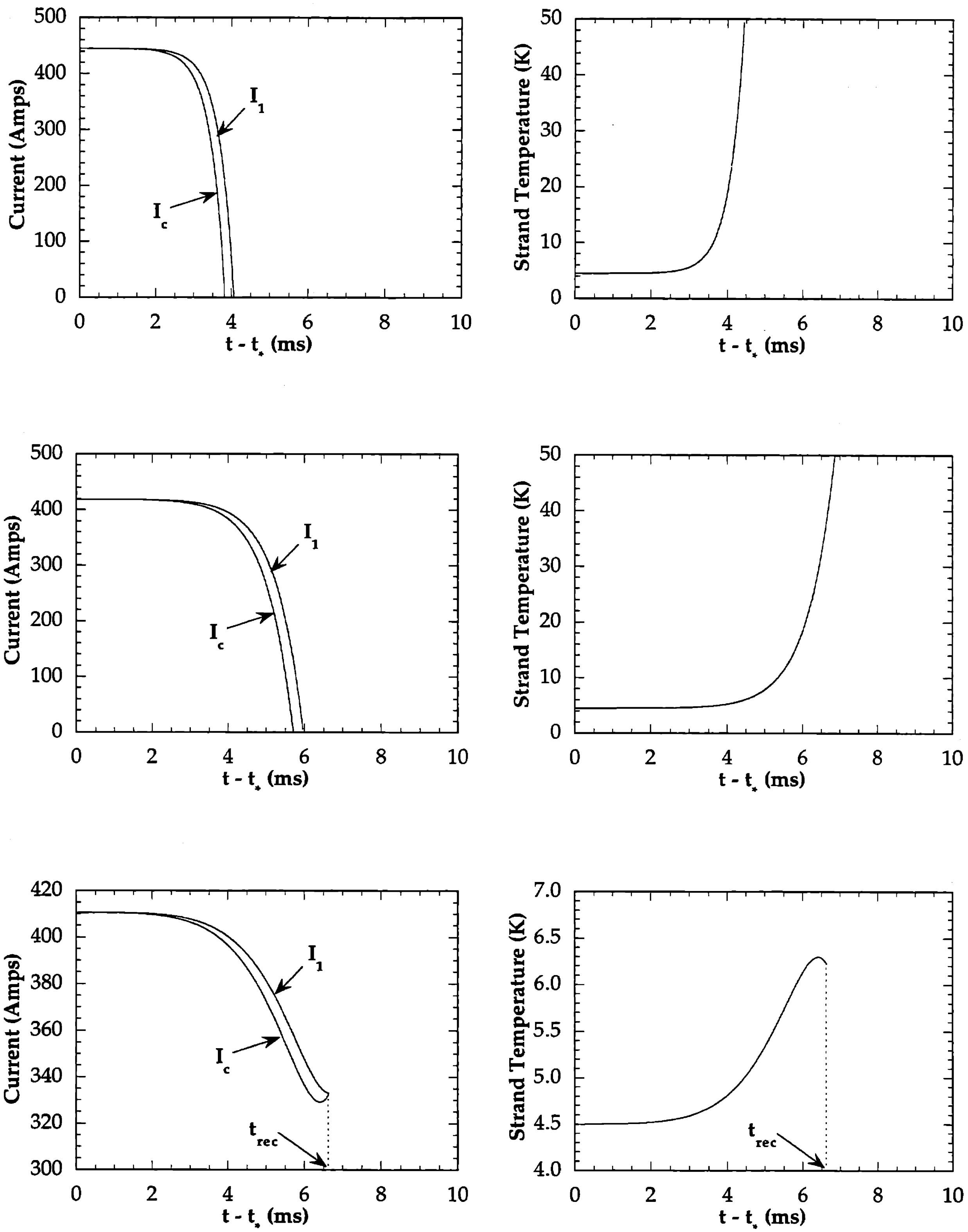

Figure 6-12: Examples of overdamped (top), critically damped (middle), and underdamped (bottom) behavior after the onset of the Resistive Domain.

resistive while the critical current is still declining (i.e. the strand temperature is still increasing). Like the overdamped case just described, the added Joule heating from strand *two* causes the temperature rise to accelerate thus preventing the possibility of recovery, as depicted in Fig. 6-13b.

It is within the third subset of the underdamped state that we must look for the marginal stability case. As shown in Fig. 6-13c, the critical current can be increasing (i.e. the strand temperature is decreasing) when the second strand becomes resistive at some time $t = t_x$. This means that if the second strand did not contribute to the Joule heating, the cable would recover. And even with the added Joule heat from strand *two*, there is still a *chance* the cable may recover. In the marginal stability case, the additional Joule heat from strand *two* exactly balances the excess cooling which was contributing to the declining strand temperature before strand two can became resistive. The net result is both strands remain resistive, but there is an exact balance between the Joule heating and the cooling provided by the helium.

In summary, for a given cable, the onset of the Resistive Domain occurs at $t = t_\star$ and $I = I_\star$, which both depend on the operating conditions I_T and $\dot{B}_\perp$. Depending on $I_\star$ the cable is in one of three states during the Resistive Domain: under-, over- or critically damped. The underdamped case provides the only possibility of recovery but non-recovery is possible for this case, as well. To find the $I_\star$ which leads to the marginal stability case, it is necessary to find the boundary within the underdamped case between quench and recovery. Unfortunately, because of the exponential nature of the solutions and the complication of having to solve interface conditions at $t = t_x$ and $t = t_\star$, finding the marginal $I_\star$ requires the solution of four simultaneous transcendental equations. The mathematics of this process are included in Appendix C. Having found the $I_\star$ which generates the marginal stability solution, it is a simple matter to solve for the transport current, I_T, which results in that $I_\star$ for a given $\dot{B}_\perp$ using the analytic results of Chapter 4.

Although the marginal stability case resides within the underdamped regime, in practice it was found to lie very near the border between the underdamped and critically damped states. Since it is much easier to solve the single value of $I_\star$ which

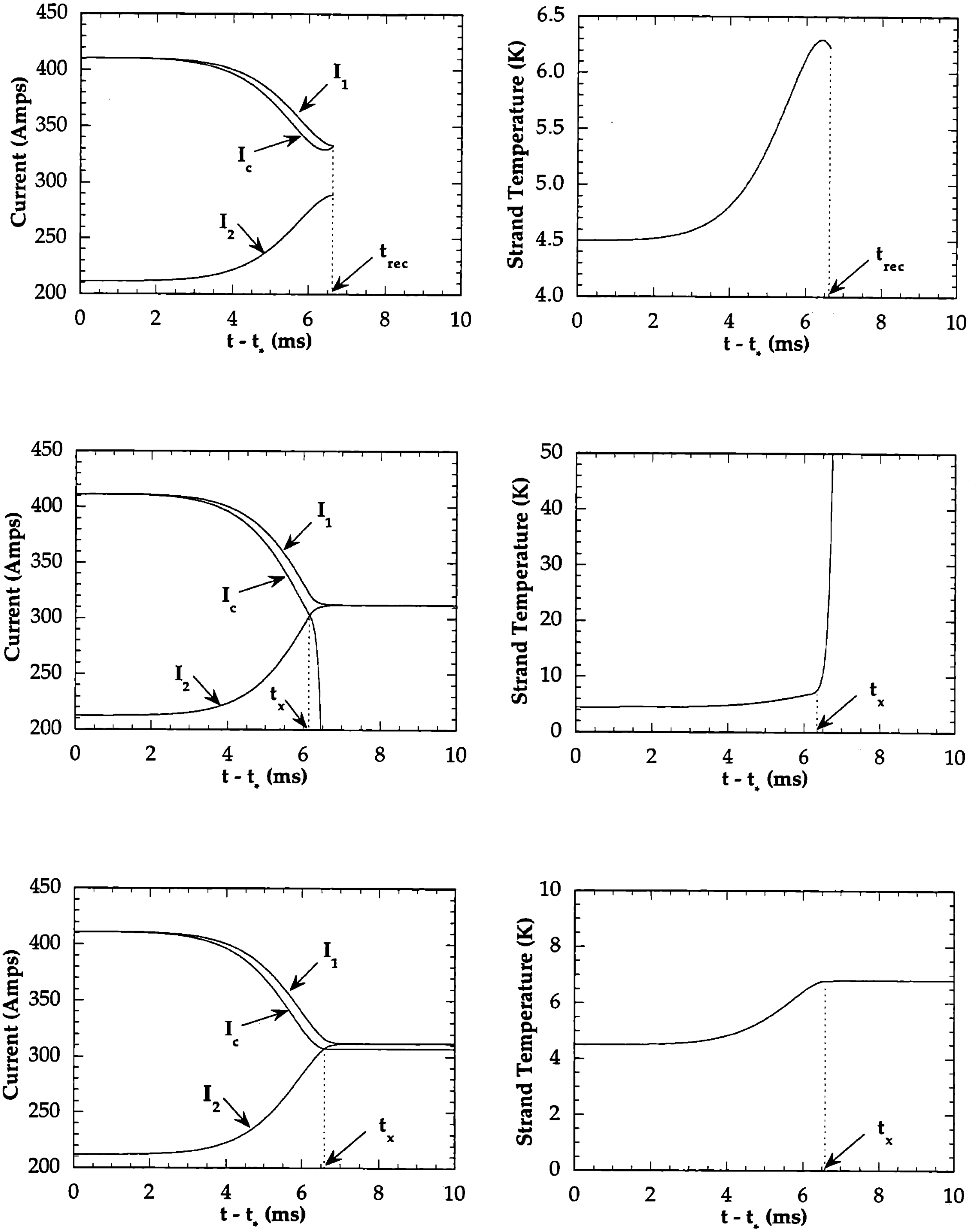

Figure 6-13: Examples of: (a) recovery (top); (b) quench (middle); and (c) the marginal stability limit (bottom) for the case of underdamped behavior.

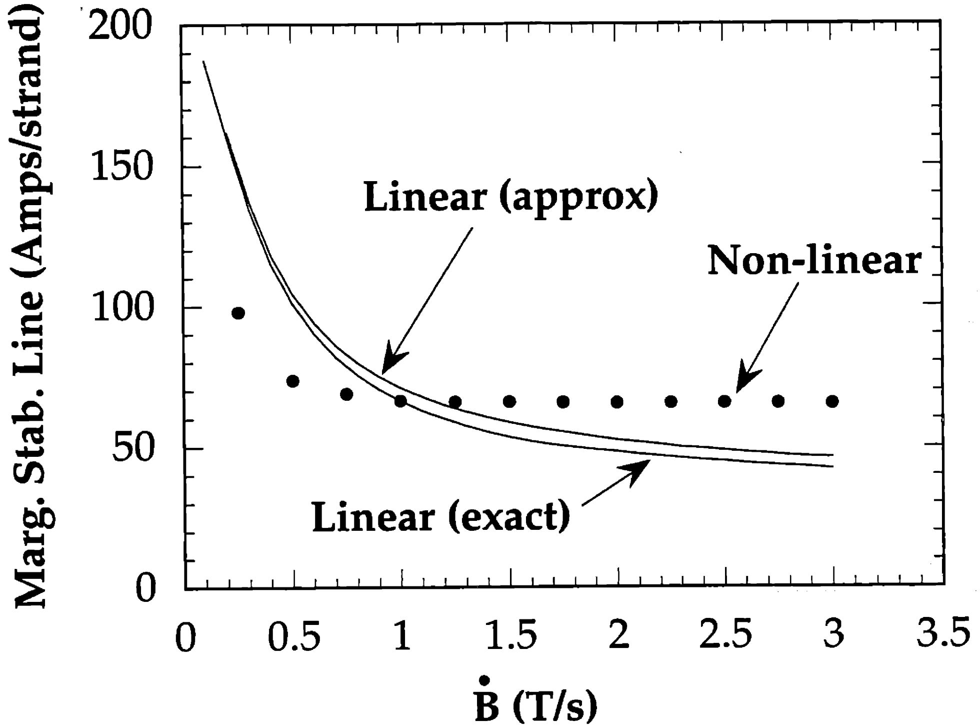

Figure 6-14: Comparison of the Marginal Stability Line as calculated using the full non-linear model, the linear model, and the approximation to the linear model.

corresponds to the critically damped case than it is to solve the transcendental system of equations needed for the more precise solution, this discovery provides a simple approximate solution to the marginal stability line for a given cable. The full details of this approximate method are also described in Appendix C.

The results of the linearized marginal stablity analysis are compared to the non-linear results in Fig. 6-14 for the cable previously studied in Section 6.2.4. The figure shows the exact and approximate solutions to the linearized marginal stability line, as discussed above, along with the previously presented numerical results to the non-linear equations. The two linear methods agree well with each other and agree qualitatively with the non-linear results. While some accuracy has been lost by linearizing the equations, the benefit of speedier calculation allows parametric studies which would be more difficult if the non-linear equations had to be used.

The linearized equations can also be studied to isolate dimensionless parameters which characterize the stability behavior of the cable. Although more work can be done in this area, an interesting balance of dimensionless variables which leads to the

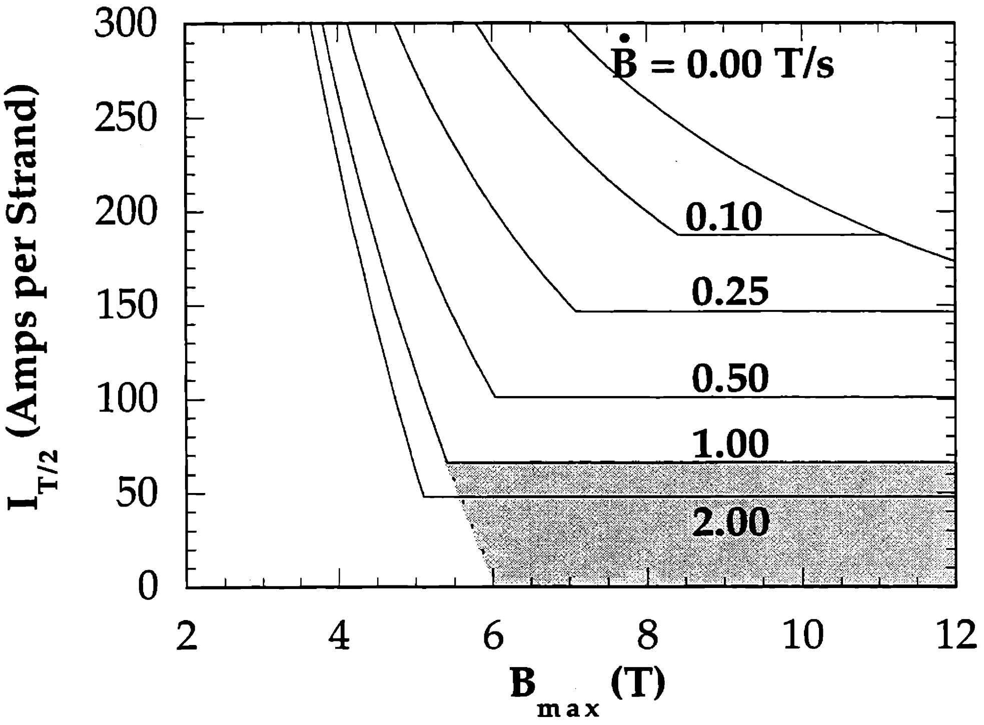

Figure 6-15: Marginal stability plot for hypothetical lab-scale cable using linearized model equations. View I.

marginal stability case is discussed in Appendix C, Section C.4.

6.3.3 Results of the Linearized Resistive Domain Model

Using the analytical results of the linearized model described in Section 6.3.1 and derived in detail in Appendix C, the stability behavior of lab-scale cables in ramping magnetic fields can now be explored. Using the hypothetical cable outlined in Table 6.1, the complete range of operating scenarios (i.e., I_T and $\dot{B}_\perp$) can be mapped out. Again, we will consider linear field ramps, $\dot{B}_\perp$, and constant transport current, I_T.

In Fig. 6-15, the stability regimes for the hypothetical cable are shown as the transport current per strand, $I_{T/2}$, vs. maximum background field, B_{max} for several values of field ramp-rate, $\dot{B}_\perp$. The cable will quench if the operating point determined by the combination of B_{max} and $I_{T/2}$ is above the limitation delineated for the desired $\dot{B}_\perp$ and will not quench if the operating point is below the limit.

For each value of $\dot{B}_\perp$, there is a discontinuity in the stability limitation which corresponds to the transition between quenching and recovering after the first "blip". For example, for $\dot{B}_\perp = 1$ T/s in Fig. 6-15, the discontinuity occurs at $I_{T/2} = 65$ Amps and $B_{\max} = 5.4$ T. For values of transport current per strand $I_{T/2} > 65$ Amps, the cable quenches the first time it enters the Resistive Domain, corresponding to the stability limitation line to the left of $B_{\max} = 5.4$ T. For $I_T < 65$, however, the cable can survive the first and subsequent trespasses into the Resistive Domain until the point where $I_{T/2} \approx I_c$, the DC operating limit (which occurs at $B > 12$ T for this example). This explains the discontinuity in the stability line and opens up a much greater region of stable operating scenarios which would not be available if the cable always quenched on the first blip. This additional region is shaded in Fig. 6-15 for the $\dot{B}_\perp = 1$ T/s case.

Another way to view the same information is presented in Fig. 6-16 where the stability limitation for various value of $\dot{B}_\perp$ are plotted as fraction of critical current, $I_{T/2}/I_c$, vs. $B_{\max}$. Further, in Figs. 6-17 and 6-18, the stability limitation for the same hypothetical cable is plotted with $\dot{B}_\perp$ as the dependent variable for several values of $B_{\max}$. These extra views of the same data are presented since the experimental literature has not settled on a single standard.

In general, these theoretical results agree with the findings of recent experiments. A direct comparison of theory to an actual lab-scale experiment will be presented in the next chapter.

6.4 Conclusions

In this chapter we derived the 0-D model equations which are appropriate for lab-scale cables in uniform background magnetic fields. The coupled electrical and thermal equations were still non-linear, however, requiring numerical techniques to find exact solutions. The numerical results revealed that lab-scale cables behave much differently than the full-scale cables discussed in Chapter 5. In particular, unlike full-scale cables, lab-scale cables exhibited the ability in some cases to survive an excursion into the Resistive Domain without experiencing a non-recovering quench.

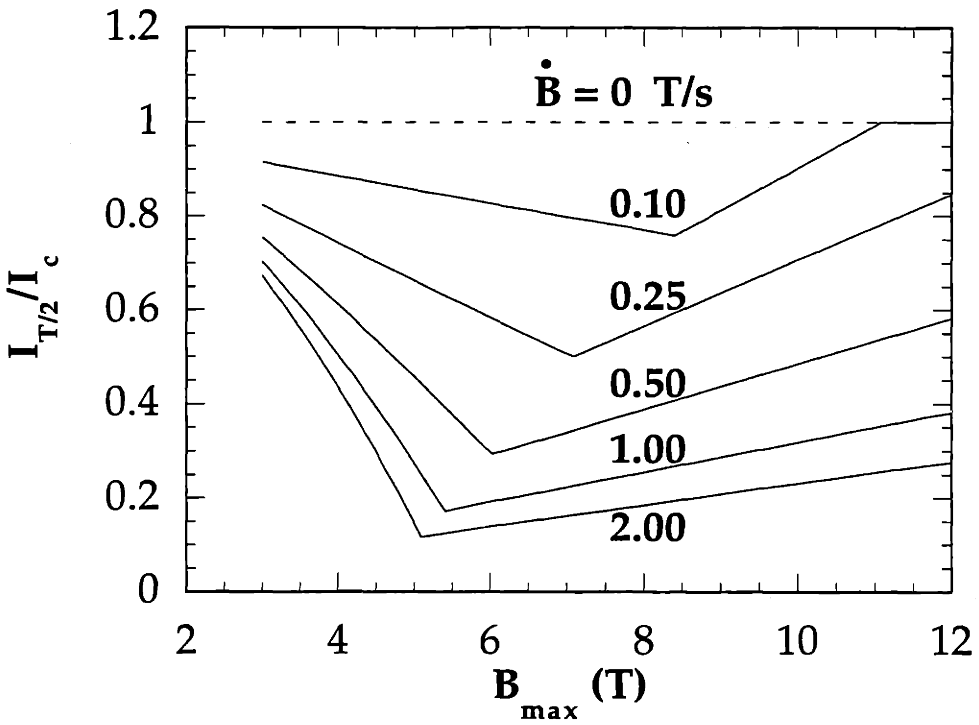

Figure 6-16: Marginal stability plot for hypothetical lab-scale cable using linearized model equations. View II.

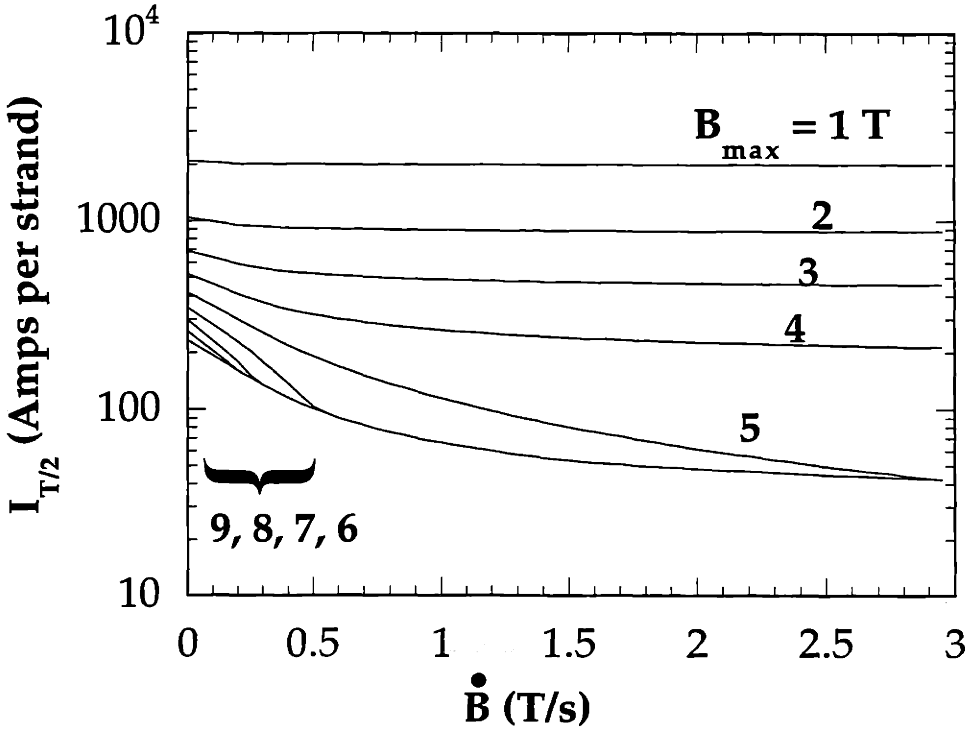

Figure 6-17: Marginal stability plot for hypothetical lab-scale cable using linearized model equations. View III.

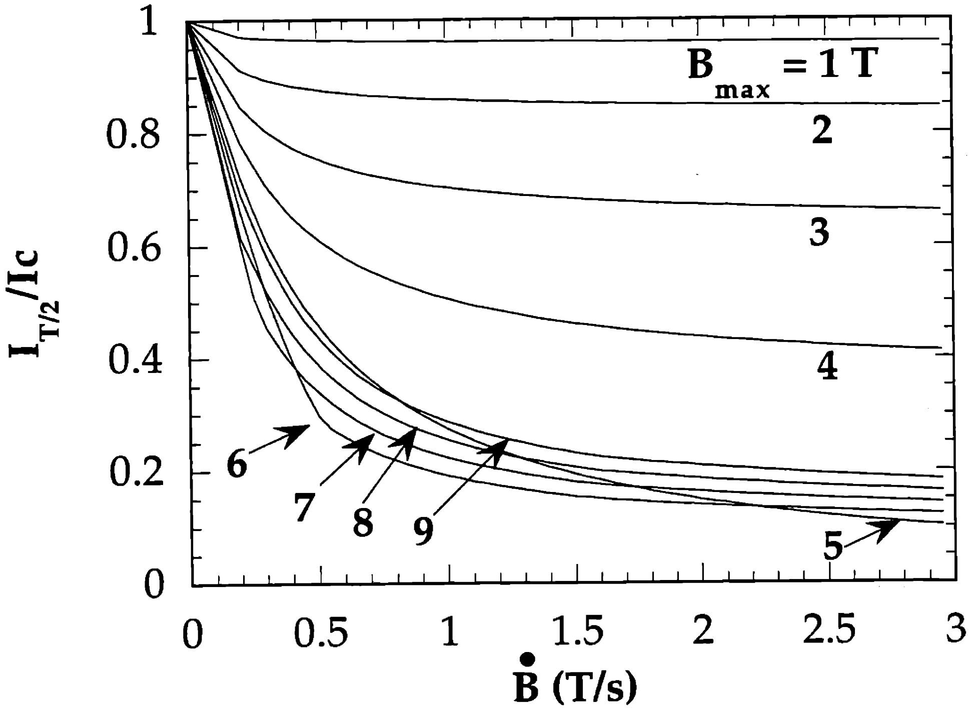

Figure 6-18: Marginal stability plot for hypothetical lab-scale cable using linearized model equations. View IV.

Motivated by the desire to study the criteria which determine whether a lab-scale cable is stable (i.e. recovers) or unstable when it first enters the Resistive Domain, the non-linear lab-scale model was linearized to allow an analytical treatment of the problem. Although the linearization yielded the desired solution, the necessary math was cumbersome enough to be presented separately in Appendix C. The general procedure, however, is described in Section 6.3.2.

The final result of the linearized model was an analytic relation which provided the stability limit for a given cable as a function of the transport current, I_T, the field ramp-rate, $\dot{B}_\perp$, and the maximum magnetic field achieved, $B_{\max}$. The results were presented graphically in Section 6.3.3 for a hypothetical cable design with DC transport current.

In Chapter 5 it was stated that to avoid quench in a full-scale cable, the current in strand *one*, I, cannot be allowed to reach the critical current, I_c. Using the same criterion for lab-scale cables would be too simplistic (and pessimistic). For low enough transport currents, the cable can actually survive several episodes in which I

is temporarily greater than I_c but then recovers back to $I < I_c$. Such a cable is said to be operating in a stable mode since, despite episodic Joule heating, the cable can be ramped to near its DC limit without fully quenching.

In a real cable, diagnostics designed to measure current redistribution and resistive voltage register repeated "blips" (i.e. spikes) while the backround field is being ramped. The term "blips" has thus been used in this thesis to refer to the repeated, rapid redistribution of current which occurs each time one of the strands reaches the critical current. The correspondence of these theoretically predicted blips with the experimentally measurd blips is strong evidence that the two-strand model is adequate to explain the most important features of the behavior of multi-strand cables.

The theory developed in this chapter will be compared to experimental results for a 27-strand cable in Chapter 7.

Chapter 7

Application of the Two-Strand Model to Multi-Strand Cables

In Chapters 3 through 6, the two-strand model was used to demonstrate the importance of circulating currents for cables operated in ramping magnetic fields. In this chapter, we will try to extend this analysis to more complicated cable geometries in order to compare the theoretical findings to experimental results. The limitations of the two-strand framework limit the accuracy to which real experiments can be simulated, but the theoretical results nonetheless qualitatively match several important features found experimentally.

Two experiments have been chosen for analysis and each will be presented separately. First, however, some general concerns about how to best model multi-strand cables are discussed.

7.1 The Two Sub-Cable Model

To accurately calculate the circulating currents in a multi-strand cable is a difficult proposition. The direct approach of tracking the current in each strand individually clearly gets out of hand very quickly when considering cables with upwards of a thousand strands. One alternative is to use a continuum model which carefully translates the twisting strands into a continuous non-isotropic medium. This approach was used successfully in calculating AC Losses for multi-strand cables [24], but proved to be too cumbersome for the purposes of this thesis.

Thus, instead of generating a new and more difficult model from scratch, it was decided to modify the two-strand model in such a way that it could be used to study multi-strand cables. It is important to realize that the work presented in this section represents a "conceptual" approach to current distribution and stability issues in multi-strand cables rather than an exact physical model. The simplifying assumption which allows the use of the two-strand model for the study of multi-strand cables will now be discussed.

As described in Chapter 2, a cable-in-condut conductor (CICC) is composed of many composite superconducting strands. The full cable is formed in stages with each stage formed by twisting together the results of the previous stage (see Section 1.2.2). For example, the US-DPC cable [1] was formed as follows: sets of three strands were twisted into "triplets;" sets of three triplets were twisted into "ninelets;" sets of five ninelets were twisted into "sub-cables;" and, finally, five sub-cables were twisted together to form the full cable. A schematic cross-section of the final cable is shown in Fig. 7-1.

Since each successive stage of the cable winding has a longer twist–pitch length than the previous one, the major portion of the flux imbalance which causes circulating currents is contributed by the final stage. For this reason, it is appropriate to approximate the magnitude of the circulating currents by focusing on the last stage flux linkage between the sub-cables while ignoring the finer scale structure. In order to take advantage of the two-strand model developed in this thesis, two of the five subcables are isolated for study, as indicated by the shaded regions in Fig. 7-1. Each of the two shaded sub-cables is treated as a "pseudo-strand" for the purpose of calculating an estimate of the current distribution.

The biggest modification needed, then, in order to analyze the multi-strand cable using the two-strand model is to account for the number of strands of which each sub-cable is composed. Also the spacing between centers, w, and the twist-pitch length, ℓ_p, are now associated with the final winding stage. Using these modifications, the

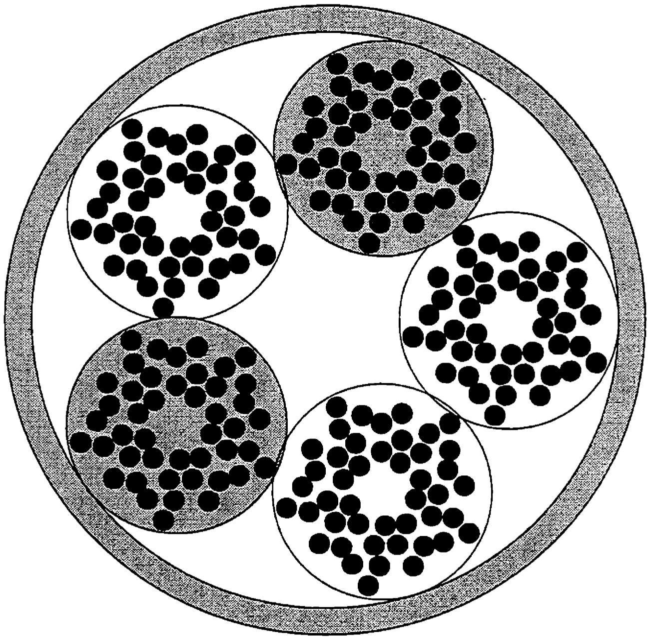

Figure 7-1: Schematic cross-section of the 225 strand US-DPC cable highlighting two of the five final stage "sub-cables".

two-strand model can be used to study the qualitative effects of current distribution in multi-strand cables. Two examples of this procedure are given in Sections 7.2 and 7.5 below.

Before getting to the examples, however, two other aspects of multi-strand cables should be discussed. In Chapter 3, the two-strand model was developed using a simplified model of the terminations which connect the superconducting cable to the power supply. In this chapter, we will consider a somewhat more sophisticated model of these "joints." Also, up until now, the orientation of the cable with respect to the direction of the magnetic field at the joints has been considered an arbitrary parameter. In this chapter, a statistical procedure will be used to calculate the expected value of this important variable in order to better match the theoretical model to an actual cable design.

Rather than developing these added concepts independently, the improved joint model and statistical study of the end conditions will be derived in the context of the US-DPC cable, which will be presented as the first example in the next section.

total number of strands	N_{tot}	225
number of strands per subcable	N	45
cable length	ℓ	150 m
twist-pitch length	ℓ_p	30 cm
length of joint	ℓ_T	100 cm
cable width	w	1.5 cm
effective inductance per length	$\mathcal{L}$	1 μH
transverse electrical conductivity	$\sigma_\perp$	$<100\ \Omega^{-1}\mathrm{m}^{-1}$
transverse joint resistance	$\Re_J$	3 $\mu\Omega$
peak field ramp-rate	$\dot{B}_{\max}$	1 T/s
field ramp-rate at joints	$\dot{B}_{\min}$	0.5 T/s
load-line (at peak field)	Λ	24 A/strand/T
load-line (at joints)	Λ_J	12 A/strand/T

Table 7.1: Selected US-DPC Cable Properties.

The specific results from this first example are easily generalized and can be applied directly to a second example, which is discussed in Section 7.5.

7.2 Theoretical Model of US-DPC Experiment

As mentioned in Chapter 2, the United States Demonstration Poloidal Coil (US-DPC) tests were the first to identify the phenomenon now known as Ramp Rate Limitation. The US-DPC experiment is described in detail in [1] and the pertinent US-DPC cable parameters are summarized in Table 7.1. In this section, we will use the two-strand cable model developed in Chapters 3, 4 and 5 to study the effects of circulating currents in the US-DPC and make comparisons to the experimental results.

Using the two sub-cable analogy defined in Section 7.1, two of the five US-DPC sub-cables are isolated to approximate the dominant contribution to the circulating currents. Since each sub-cable has 45 strands, the value of the circulating current in the Superconducting Domain calculated using the results of Chapter 4 need to be divided by $N = 45$ to determine the "per-strand" result. Similarly, since the full cable consists of 225 strands, the transport current needs to be divided by $N_{tot} = 225$

to determine the "per-strand" basis.

In the US-DPC experiment, the magnetic field was produced by the coil itself and thus the magnetic field is proportional to the transport current.[1] The details of the winding geometry and the spatial distribution of the magnetic field intensity are contained in [1]. As mentioned in Chapter 5, only the values of the field intensity at the joints and the center of the cable are needed to determine current distribution and stability. The constants of proportionality relating the magnetic field to the transport current at these three locations are given in Table 7.1.

For the purposes of this chapter, only the experimental runs which utilized a linear ramping of the transport current (and thus magnetic field) are considered. The linear ramp starts at $t = 0$, $I_T = 0$, and $B = 0$ and continues until a "flat-top" threshold is reached at $t = t_{ramp}$, $I_T = I_{max}$, and $B = B_{\text{max}}$. This scenario corresponds to a considerable database of experimental results.

7.2.1 Characterizing the US-DPC Cable

The transconductance, $\sigma_\perp$, is not known for the US-DPC cable. However, the cable was especially designed to minimize $\sigma_\perp$ by coating each strand with a thin layer of chrome oxide [1]. For this reason, it is reasonable to assume that the transconductance is low, specifically $\sigma_\perp < 100\ \Omega^{-1}\text{m}^{-1}$ as indicated in Table 7.1. For this range of $\sigma_\perp$, the US-DPC cable falls into the short cable regime as defined for the Superconducting Domain in Section 4.3.2.[2] Rather than using the results of Section 4.3.2, though, the governing equation for current distribution in the US-DPC model will be rederived in this chapter to better account for the actual joint design used to terminate the cable. We will, however, make use of one key finding developed for the short cable regime without rederiving it from scratch: the current in each strand is spatially uniform over the length of the cable.

---

[1] Some runs were conducted in the presence of additional background field magnets, but they will not be discussed in this thesis.

[2] Although the US-DPC can be considered a "short cable" for the purposes of current distribution in the Superconducting Domain, it is still a "full-scale" cable from the purposes of stability analysis in the Resistive Domain, as will be discussed shortly.

Another finding from a previous chapter will also be used here without further discussing the details. Although, the value of $\sigma_\perp$ is not known precisely, conservative estimates of the transfer length, ℓ_X, range from 5 to 20 m. Since the cable length, ℓ, is much longer than ℓ_X, the cable is classified as a "full-scale" cable as defined in Section 5.4.1. The implications of this classification are that the cable will quench if it enters the Resistive Domain—the current cannot redistribute fast enough to allow the cable to recover. Thus, if $I = I_c$ anywhere along the cable (i.e. at the center, where I_c is lowest), the cable quenches.

The time at which $I = I_c$ for a linear ramp has previously been defined as $t = t_\star$. If, however, the ramp is terminated before $t = t_\star$, the current never reaches the critical current limt. In the experiment, the transport current (and thus the magnetic field) was ramped at a linear rate up until $t = t_{ramp}$, at which time the current and field were held constant. Thus, the criterion for stabiliy in the US-DPC experiment can be summarized as $t_{ramp} < t_\star$. On the other hand, if the ramp time is such that $t_{ramp} > t_\star$, the cable will quench at time $t = t_\star$, before it reaches flat-top.

With this criterion in mind, we now derive the governing equation for the current distribution in the US-DPC cable taking into consideration further details of the joint design.

7.2.2 Model of Joints for US-DPC Cable

When developing the two-strand model equations in Chapter 3, the joints were treated as idealized resistors at either end of the cable. While that approach was appropriate for explaining the physics associated with circulating currents and current distribution in general, the unique joint design of the US-DPC cable requires special treatment.

A schematic of the US-DPC cable is shown in Fig. 7-2 where the finite joint length, ℓ_T, is emphasized. In this case, $\ell_T = 1$ m (the figure is not drawn to scale). The two "strands" in the figure now represent two sub-cables, as discussed in Section 7.1. The full cable geometry is discussed in full detail in [1].

A cross-section of one of the two low-resistance joints is shown in Fig. 7-3. The figure shows the connection between two of the three double-pancake windings which

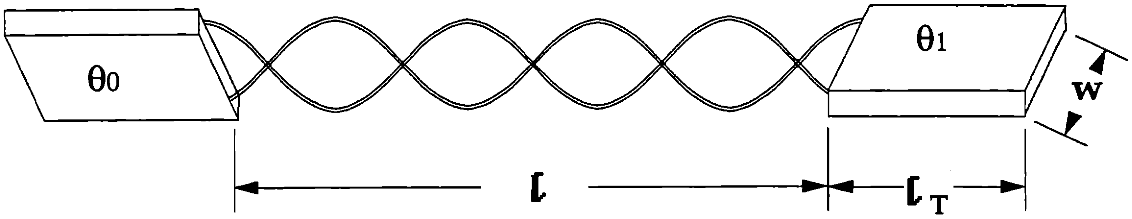

Figure 7-2: Schematic of one section of the US-DPC cable with terminations.

comprise the full US-DPC coil. At the joints, the five sub-cables are untwisted and encased in a solder-filled, flattened copper tube, as shown in the figure. The two flattened ends of the adjacent pancakes are then overlapped and bonded. Again, the full details are given in [1].

The two sub-cables which have been isolated for study are shaded in Fig. 7-3. The five short vertical arrows in the figure represent the path of the transport current as it travels through the joint. The resistance of the this current path was found by measurement to be $\Re_{||} \approx 1$ nΩ. The long horizontal arrow is indicative of the current path of the circulating currents as they close through the joints. The resistance of this path is what we have defined as $\Re_J$, the transverse resistance of the joint (refer to Section 3.3.3).

To make an initial estimate of $\Re_J$ from the measured value $\Re_{||}$, we can use simple ratios derived from the geometry of the joint design. If the resistivity of the copper tubing, η_{tube}, is considered to be the dominant resistive term, the ratio $\Re_J/\Re_{||}$ can

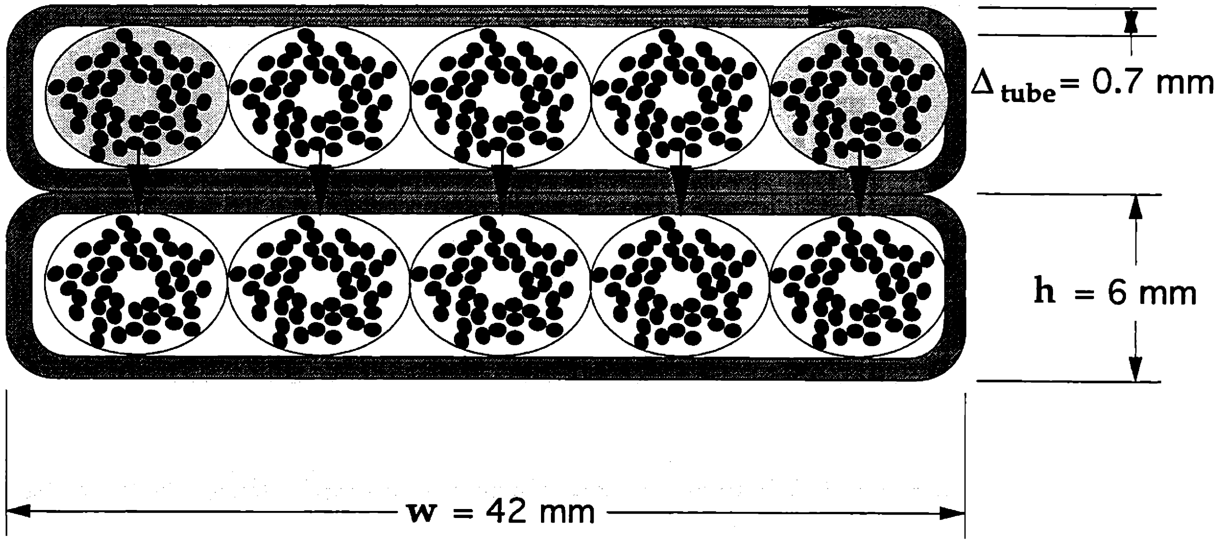

Figure 7-3: Cross-ssection of the "lap" joint configuration used to join sections of the US-DPC cable.

be found from the following relations:

$$\Re \equiv \eta \ell / A$$

$$\Re_{\|} \sim \frac{\eta_{tube} \Delta_{tube}}{w \ell_T} \tag{7.1}$$

$$\Re_J \sim \frac{\eta_{tube} w}{\Delta_{tube} \ell_T} \tag{7.2}$$

where the dimensions w and Δ_{tube} are defined in Fig. 7-3. Equations (7.1) and (7.2) can be re-arranged to give $\Re_J/\Re_{\|} = w^2/\Delta_{tube}^2$. Using the dimensions of the joint given in the figure and the measured value of $\Re_{\|}$, the transverse joint resistance is estimated to be $\Re_J \approx 3\mu\Omega$.

7.2.3 Governing Equation for Current Distribution in US-DPC Model

Due to the design of the joints used in the US-DPC cable, the governing equation for current distribution needs to be modified from the one given in Chapter 4. The source of the difference is the fact that the sub-cables are not twisted within the joint region. The ramping magnetic field therefore produces an appreciable flux linkage between sub-cables in the joint region which has not been included in the original analysis. In this section, we will include the effects of this added source term for the case of the US-DPC cable.

Because the flux through the joints is now being included, the cable must be divided into three regions, as diagrammed in Fig. 7-4. The two joints are each characterized by a transconductance σ_J which can be derived from the overall transverse joint resistance, $\Re_J$, and the physical length of the joint, ℓ_T (where subscript T stands for "termination" since the notation ℓ_J has already been used):

$$\sigma_J \equiv \frac{1}{\Re_J \ell_T}$$

The two-subcables being studied (see Fig. 7-3) are straight and parallel in each joint, separated by the distance w. The additional reference frames, x_1 and x_2 (shown in Fig. 7-4), will be used to simplify the math later on.

As mentioned in Section 7.1, the cable itself can be considered insulated over its length, ℓ, since it falls into the short-cable length regime as defined in Section 4.3.2. Thus, the current in each sub-cable cannot vary over the length—the current which enters the one sub-cable at the joint does not transfer to the other sub-cable. Therefore, to determine the current distribution in the cable, it is only necessary to focus on the joints.

To develop the governing equation for the current distribution, the procedure is exactly analagous to the development presented in Chapter 3. In this chapter, the derivation will use the concepts presented in Chapter 3 without directly commenting on many of the steps. The reader should refer to Section 3.4 for a review of the full

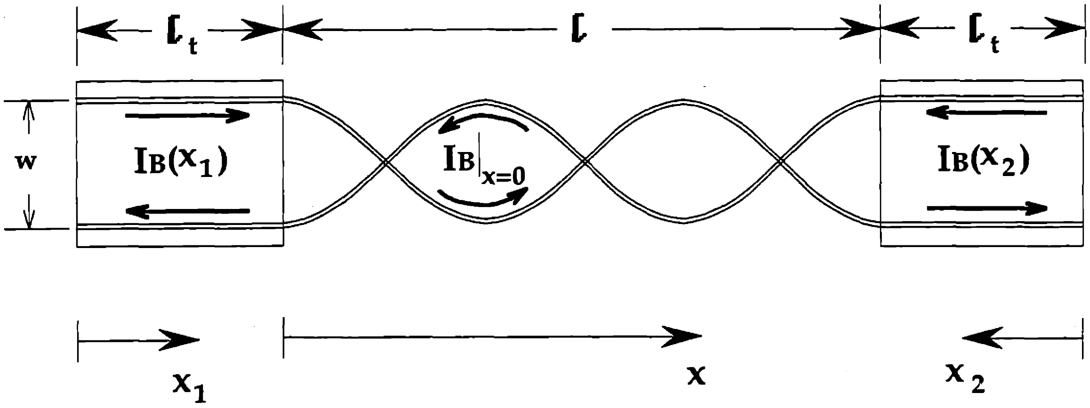

Figure 7-4: The three regions of the US-DPC cable model: 2 joints and the cable itself. (Note, the figure is not drawn to scale: $\ell \gg \ell_T$.)

details.

The magnetic field is approximately uniform over the relatively short length of the joints. At the leftmost joint, the perpendicular component of the magnetic field is $B|_{x=0} \cos\theta_0$ where θ_0 is the orientation of the joint with respect to the direction of the magnetic field. Similarly, $B|_{x=\ell} \cos\theta_1$ applies at the other joint. If we assume the magnetic field profile is symmetric about the center of the cable, the simplification $B_J \equiv B|_{x=0} = B|_{x=\ell}$ can be used, where B_J stands for the magnetic field at the joints.

Within the first joint, $0 < x_1 < \ell_T$, Faraday's law can be used to determine the induced current (see Section 3.4 for more details):

$$\frac{1}{\sigma_J}\frac{\partial^2 I_B}{\partial x_1^2} - 2\mathcal{L}\frac{\partial I_B}{\partial t} = w\frac{\partial B_J}{\partial t}\cos\theta_0$$

or

$$\alpha_J^2 \frac{\partial^2 I_B}{\partial x_1^2} - \frac{\partial I_B}{\partial t} = \frac{w}{2\mathcal{L}}\frac{\partial B_J}{\partial t}\cos\theta_0 \tag{7.3}$$

where $\alpha_J^2 = 1/(2\sigma_J\mathcal{L})$ and w is the width of the joint. The reference frame x_1 is

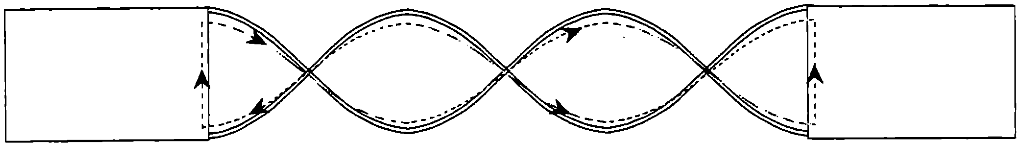

Figure 7-5: The contour of integration necessary to determine the second interface condition, see Eq. (7.6).

defined in Fig. 7-4. Similarly, in the second joint, $0 < x_2 < \ell_T$, we get:

$$\alpha_J^2 \frac{\partial^2 I_B}{\partial x_2^2} - \frac{\partial I_B}{\partial t} = \frac{w}{2\mathcal{L}} \frac{\partial B_J}{\partial t} \cos\theta_1 \tag{7.4}$$

where the reference frame x_2 is defined as shown in Fig. 7-4.

Because the current over the cable length is constant, the first interface condition is simply:

$$x_1 = x_2 = \ell_T; \qquad I_B \text{ continuous} \tag{7.5}$$

The second interface condition is more involved. Using Faraday's law around the closed path indicated in Fig. 7-5 produces the following equation:

$$\frac{1}{\sigma_J} \frac{\partial I_B}{\partial x}\bigg|_{x=0^-} + 2\mathcal{L}\ell \frac{\partial I_B}{\partial t}\bigg|_{x=0} - \frac{1}{\sigma_J} \frac{\partial I_B}{\partial x}\bigg|_{x=\ell+} = -\int_0^\ell w \frac{\partial B_\perp(x)}{\partial t} \cos\left(\frac{2\pi x}{\ell_p} + \theta\right) dx$$

Doing the calculus and transforming to the auxiliary reference frames x_1 and x_2, this equation reduces to the second necessary interface condition:

$$x_1 = x_2 = \ell_T \ ; \qquad \frac{\partial I_B}{\partial t} + \frac{\alpha_J^2}{\ell}\left(\frac{\partial I_B}{\partial x_1} + \frac{\partial I_B}{\partial x_2}\right) = -\frac{w \dot{B}_J \ell_p}{4\pi\mathcal{L}\ell} (\sin\theta_1 - \sin\theta_0) \tag{7.6}$$

where $\dot{B}_J \equiv \frac{\partial}{\partial t} B_J$ and the presumption is made that the magnetic field is approximately constant over the distance of one twist-pitch length, see Section 4.2.2.

In addition to the two interface conditions, two other boundary conditions are required. In each joint, the induced current must be zero at the end of the joint not connected to the cable. In other words:

$$x_1 = 0 \quad ; \quad I_B = 0 \tag{7.7}$$

$$x_2 = 0 \quad ; \quad I_B = 0 \tag{7.8}$$

Together, Eqs. (7.5)–(7.8) provide the four necessary boundary conditions to solve for the induced current, I_B, in each of the three regions—joint, cable, joint—of the US-DPC model. Within the joints, I_B is a function of x_1 over the range $0 < x_1 < \ell_T$ and a function of x_2 over the range $0 < x_2 < \ell_T$. Along the length of the cable, however, I_B does not depend on x but is determined solely from the interface conditions where the cable meets the joints.

With the boundary and interface conditions now specified, we can turn to solving the induced current equations for the US-DPC model. Using separation of variables to find the homogenous solution, I_{B_h}, to Eqs. (7.3) and (7.4) produces :

$$I_{B_h} = \sum_{n=1}^{\infty} a_n e^{-k_n^2 \alpha_J^2 t} \begin{cases} \sin(k_n x_1) \; ; & 0 < x_1 < \ell_T \\ \sin(k_n \ell_T) \; ; & 0 < x < \ell \\ \sin(k_n x_2) \; ; & 0 < x_2 < \ell_T \end{cases} \tag{7.9}$$

where Eqs. (7.7) and (7.8) have already been used to eliminate "cos" terms and Eq. (7.5) has been used to to determine the coefficients, a_n, are the same in each of the three regions. The parameters k_n need to be determined using the remaining interface condition, Eq. (7.6).

Plugging Eq. (7.9) into Eq. (7.6) provides the transcendental equation necessary to generate the values of k_n:

$$k_n \ell \tan(k_n \ell_T) = 2 \tag{7.10}$$

for $n = 1, 2, 3, \ldots, \infty$. Inspecting Eq. (7.9), however, we see that the solutions for I_{B_h} exponentially decay in time as k_n increases. Since we are typically interested in ramp times on the order of 1 s or greater, we can limit the infinite series to a finite number of terms while still maintaining any desired accuracy. The cut-off criterion can be expressed as $k_n^2 \alpha_J^2 t_{ramp} \gg 1$, at which point further terms become negligible.

For the US-DPC cable, the $n = 1$ term is dominant for time-scales of interest and all higher terms are negligible. Thus, dropping the subscript n, the results above simplify:

$$I_{B_h} = a e^{-k^2 \alpha_J^2 t} \begin{cases} \sin(k x_1) \ ; & 0 < x_1 < \ell_T \\ \sin(k \ell_T) \ ; & 0 < x < \ell \\ \sin(k x_2) \ ; & 0 < x_2 < \ell_T \end{cases} \tag{7.11}$$

where k is determined from the transcendental equation:

$$k\ell \tan(k\ell_T) = 2 \tag{7.12}$$

and $0 < k < \pi/(2\ell_T)$.

Having solved for the homogenous solutions (except for the scaling constant a which will be found from the initial conditions), it is next necessary to find the particular solutions which complete the model. Since Eqs. (7.3) and (7.4) are second order, the particular solutions in each of the joint regions have the form:

$$I_{B_p} = \begin{cases} b_1 x_1^2 + c_1 x_1 & ;0 < x_1 < \ell_T \\ b_2 x_1^2 + c_2 x_2 & ;0 < x_2 < \ell_T \end{cases} \tag{7.13}$$

where the constant coefficients can be solved using substitution into the original equations,Eqs. (7.3) and (7.4), along with the interface conditions, Eqs. (7.5) and (7.8). The results are:

$$\begin{aligned} b_1 &= -\frac{w \dot{B}_J \cos\theta_0}{4\mathcal{L}\alpha_J^2} && (7.14) \\ b_2 &= -\frac{w \dot{B}_J \cos\theta_1}{4\mathcal{L}\alpha_J^2} && (7.15) \\ c_1 &= -\frac{w \dot{B}_J \ell_T}{8\mathcal{L}\alpha_J^2} \left[\frac{\ell_p}{\pi \ell_T} (\sin\theta_1 - \sin\theta_0) - (\cos\theta_1 + 3\cos\theta_0) \right] && (7.16) \\ c_2 &= c_1 + (b_1 - b_2)\ell_T && (7.17) \end{aligned}$$

The final unknown, a, can now be determined from the initial conditions. The initial condition $I_B(x, t=0) = 0$ can only be specified for the region $0 \leq x \leq \ell$ (i.e. the length of the cable, but not the joint regions) because the rapidly decaying terms in Eq. (7.9) have been truncated. Since we are not interested in the fast time-scale response in the joints, however, we do not need accurate initial conditions in those regions anyway.

Combining Eqs. (7.11) and (7.13) to generate the complete solution for the induced current in strand *one*, $I_B = I_{B_h} + I_{B_p}$, along with the coefficients derived in Eqs. (7.14) and (7.17) and the initial condition $I_B(x=0, t=0) = 0$ gives the final answer:

$$I_B = \begin{cases} b_1 x_1^2 + c_1 x_1 - \left(b_1 \ell_T^2 + c_1 \ell_T\right)\left(\sin kx_1 / \sin k\ell_T\right) e^{-k^2 \alpha_J^2 t} & ;0 < x_1 < \ell_T \\ \left(b_1 \ell_T^2 + c_1 \ell_T\right)\left(1 - e^{-k^2 \alpha_J^2 t}\right) & ;0 < x < \ell \\ b_1 x_2^2 + c_1 x_2 - \left(b_1 \ell_T^2 + c_1 \ell_T\right)\left(\sin kx_2 / \sin k\ell_T\right) e^{-k^2 \alpha_J^2 t} & ;0 < x_2 < \ell_T \end{cases} \tag{7.18}$$

where b_1 and c_1 are known from Eqs. (7.14)–(7.17).

To demonstrate the behavior of this solution, an example is shown in Fig. 7-6 for arbitrary values of θ_0 and θ_1. Profiles of the induced current per strand are shown at several times for $\dot{B}_{\text{max}} = 1$ T/s. Note that the figure is not drawn to scale as in actuality the cable length, ℓ, is much longer than the length of either joint, ℓ_T. Do to its orientation (i.e. θ_0), in the first joint the induced current tends to be negative. In the second joint, however, the induced current tends to be positive and of a larger magnitude. The net result is a positive induced current which is constant over the length of the cable due to the relatively low transconductance, $\sigma_\perp$.

Since we are most interested in the current distribution in the cable (as opposed to the current distribution in the joints), it is useful to isolate the middle branch of Eq. (7.18) and introduce simplifying notation:

$$I_B = \dot{B}_J \frac{w\ell_T}{4N\Re_J}\left[(\cos\theta_1 + \cos\theta_0) - \epsilon\,(\sin\theta_1 - \sin\theta_0)\right]\left(1 - e^{-t/\tau}\right) \;;0 < x < \ell \tag{7.19}$$

where $\tau \equiv (k\alpha_J)^{-2}$ and $\epsilon \equiv \ell_p/(\pi\ell_T)$. The factor N has been introduced to convert the total induced current (given in Eq. (7.18)) to the desired induced current per strand. Equation (7.19) will be used to determine the stability behavior of the US-

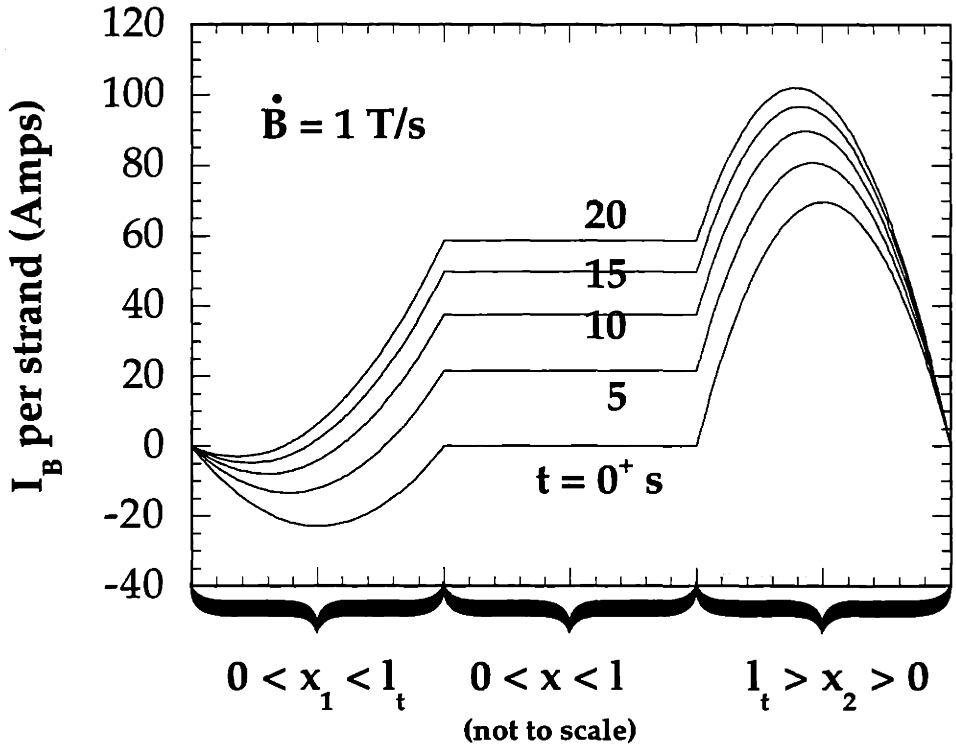

Figure 7-6: An example of the induced current per strand in the three regions of the US-DPC model cable. The end regions represent the finite length joints ($\ell_T = 1$ m) while the center region represents the actual cable length ($\ell = 150$ m).

DPC model cable.

7.2.4 Statistical Expectation of Flux Imbalance

In the example depicted in Fig. 7-6, the orientations of the joints were chosen arbitrarily. Since θ_0 and θ_1 are such important parameters, though, it makes sense to use a more rigorous approach in assigning their values. In this section, a statistical approach will be taken to find the "expected" contribution of θ_0 and θ_1.

The orientation of the joints contribute to the induced current through the scaling factor:

$$\varsigma \equiv \left[(\cos\theta_1 + \cos\theta_0) - \epsilon\,(\sin\theta_1 - \sin\theta_0)\right] \tag{7.20}$$

which appears in Eq. (7.19). To determine the expected value, Exp[ς], we first need to split ς into one component that depends only on θ_0 and one component that depends only on θ_1:

$$\begin{aligned} \varsigma &= \varsigma_0 + \varsigma_1 \\ \varsigma_0 &\equiv \cos\theta_0 + \epsilon\sin\theta_0 \qquad (7.21) \\ \varsigma_1 &\equiv \cos\theta_1 - \epsilon\sin\theta_1 \qquad (7.22) \end{aligned}$$

We can derive the partial distribution function, PDF, of both ς_0 and ς_1 using a graphical procedure. The next step is to build the PDF of the combination of ς_0 and ς_1. Then the expected value, Exp[ς], can be found by integrating the weighted PDF of ς. The whole procedure is detailed in Appendix B and the final result for the US-DPC model is:

$$\mathrm{Exp}\left[\varsigma\right] = 0.95$$

Using this result in Eq. (7.19) removes all arbitrariness in the model. The final result becomes:

$$I_B = \dot{B}_J \frac{w\ell_T}{4N\Re_J} \mathrm{Exp}\left[\varsigma\right]\left(1 - e^{-t/\tau}\right) \tag{7.23}$$

With this expectation for the induced current per strand, the final step needed before comparing theoretical predictions to the experimental results is a description of the critical current relations for the US-DPC conductor.

7.2.5 Field Profile and I_c relation for US-DPC

For the US-DPC magnet, the peak field occurs at the center of the cable, $x = \ell/2$, and is directly proportional to the transport current: $B_{\max} = I_T/(N_{tot}\Lambda)$. At the joints, the magnetic field is significantly less than the peak field but is still proportional to I_T: $B_J = I_T/(N_{tot}\Lambda_J)$. Both Λ and $\Lambda_J$were given previously in Table 7.1 for the US-DPC experiment.

The ramp-rate of the field at the joints, $\dot{B}_J$, determines the magnitude of the induced current, I_B. The magnitude of the field at the center of the cable, $B_{\max}$, determines the limiting critical current, I_c, which in turn determines the onset of the Resistive Domain. The magnetic field at intermediate locations along the cable varies slowly between B_J and $B_{\max}$ but the exact profile is not necessary for this analysis (due to reasons discussed in Section 4.2.2).

Instead of the generalized Kim model for the critical current used in previous chapters, we now turn to a more sophisticated model which has been specifically tuned to match the properties of the actual US-DPC strands. The desired I_c relation was originally developed in references [41, 42] and was benchmarked against experimental measurements in [1]. The resulting I_c (on a per-strand basis) is plotted against magnetic field for a fixed temperature, $T = 4.5$ K, in Fig. 7-7. The full relation is included for ease of reference in Appendix D, Eq. (D.1).

7.3 Comparing the Theoretical Model to Experimental Results for US-DPC Experiment

Having solved for the induced currents,Eq. (7.23), and with an accurate model of the critical current, Eq. (D.1), it is now possible to predict the stability behavior of the US-DPC experiment. As mentioned in Section 7.2.1, the US-DPC is a full-scale

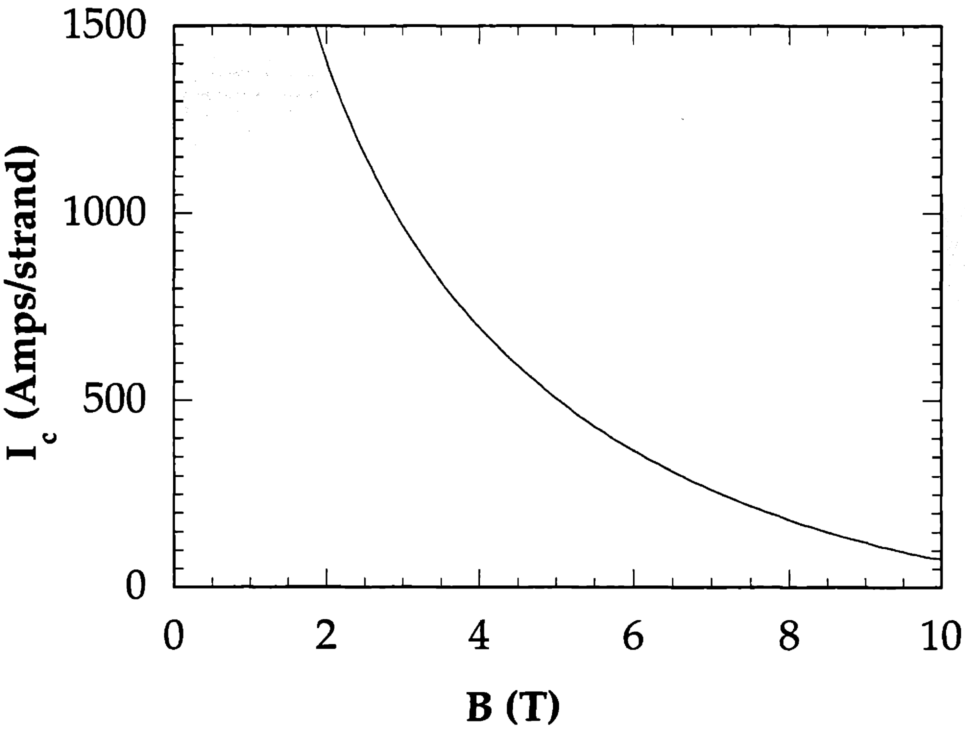

Figure 7-7: Critical current per strand, I_c, for the US-DPC vs. magnetic field at the temperature $T = 4.5$ K.

magnet which will quench if it enters the Resistive Domain. The stability criterion can thus be stated as $t_{ramp} < t_\star$ where t_{ramp} is the time at which the linear ramp is ended and the transport current is held constant (i.e., "flat–top") and $t_\star$ is the time at which the current per strand in the first sub-cable equals the critical curent for a linear ramp. The value of $t_\star$ is dependent on the ramp-rate, $\dot{B}_\perp$.

Figure 7-8 shows the average transport current at quench, I_q, vs. the time at which quench occurs, t_q, according to both experimental and theoretical results. Also shown in the figure is the critical current per strand, I_c, in the peak-field region at the time of quench. The theory can be seen to correctly predict the originally unexpected result that the cable quenches at a transport current significantly lower than the critical current.

According to the theory, the cable quenches when the transport current is less than the critical current because one sub-cable is carrying much more than its fair share of current due to the induced circulating currents, I_B. The model of current

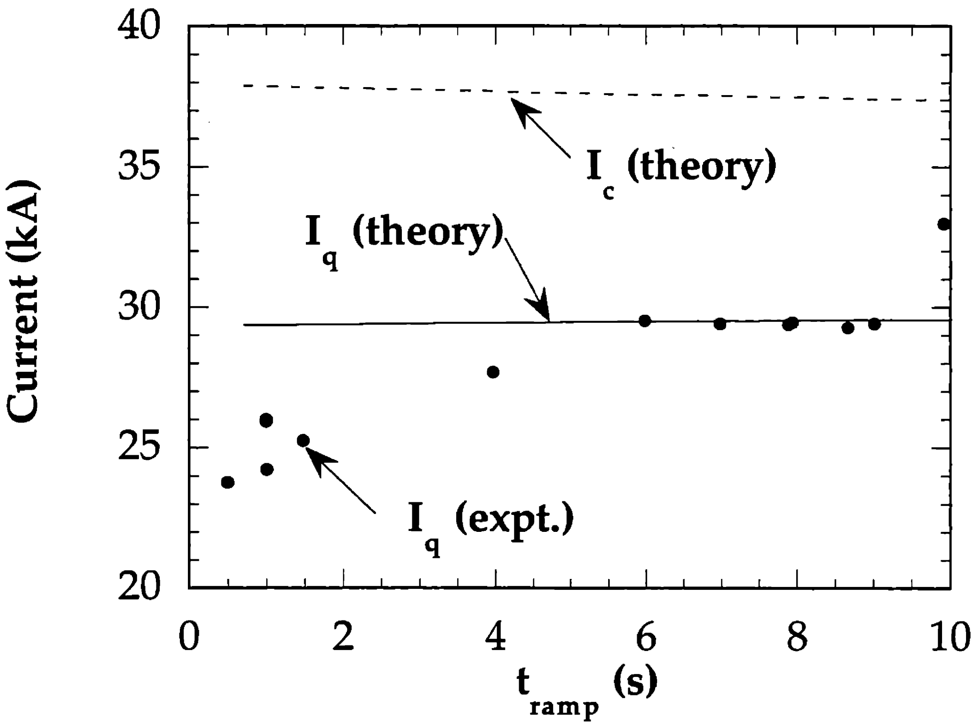

Figure 7-8: Quench current per strand, I_q, vs. ramp time, t_{ramp}, for the US-DPC single coil test, [1]. Experimental (•) and theoretical (—) results.

distribution developed in this thesis thus provides an explanation for much of the performance degradation experienced by the US-DPC.

While the theoretical results explain most of the significant discrepancies between the expected quench current, I_c, and the actual quench current, I_q, the theory does not match the shape of the experimental results at lower ramp times, t_{ramp}. While the theoretical curve does tend to decrease as it approaches the origin, the slope is too slight to match the observed data. This qualitative difference can be attributed to the limitations of the two sub-cable model. It is expected that the concept of circulating currents can better explain the shape of the data if a more sophisticated (i.e. multi-strand or continuum) model were used to better estimate the induced currents.

7.4 Conclusions from the US-DPC Example

The results of the US-DPC model can be interpreted to reveal several conclusions. Of primary interest is the fact that the calculated circulating currents can account for the premature quenches which were experienced experimentally. The two sub-cable model has sufficient explanatory power to predict the approximately 25% discrepanccy between expected and actual results. A more sophisticated model would be needed, however, to explain the "finer detail" of the results, namely the slight dependence of quench current on ramp time.

A more specific conclusion concerns the joint design used to connect sections of the US-DPC cable. Since the last stage sub-cables are untwisted over the length of the joint region, there is a significant increase in the magnetic flux linkage which drives the circulating currents for this type of design. If the twisting of the sub-cables could be maintained throughout the joint region, the induced currents could be substantially reduced and performance would improve correspondingly.

One further point to mention is that the US-DPC cable fell into the "short cable length" regime, $\ell << \ell_D$ as defined in Section 4.3.2, because the strands were relatively well insulated due to the chrome coating. While the chrome coating reduces AC losses by minimizing interstrand coupling current, it also allows the circulating currents to diffuse more quickly into the high-field region of the cable. This second consideration may take precedence (or at least must be considered) in future cable designs. The analytic results of Chapter 4 provide helpful tools in studying these effects of the trans-conductance, $\sigma_\perp$.

7.5 Theoretical Model of Lab-Scale Experiment

After the surprising results of the US-DPC, researchers at MIT designed a series of lab-scale tests to further study ramp-rate limitation and the general performance degradation of superconducting cables in ramping magnetic fields. One of these lab-scale experiments will now be used as a second example of the application of the theoretical results from previous chapters to actual cables. Unlike the US-DPC example, for this case the general theoretical model of Chapters 4, 5 and 6 does not have to be much tailored to match the experimental cable geometry. Accordingly, the desired theoretical model of the lab-scale experiment will be developed rather quickly making reference to relevant sections of this thesis without going into added detail.

The theoretical constructs which will be used to analyze the results of these experiments were developed for a two-strand cable in Chapter 6. We will again use the two sub-cable approach (see Section 7.1) to adapt the two-strand results to a multi-strand cable. In the experiment discussed here, the transport current, I_T, was held constant while the spatially uniform background magnetic field was increased from zero to B_{max} at a linear rate, $\dot{B}_{\perp}$.

The details of a series of MIT lab-scale experiments are given in several published accounts, [2, 3, 4, 5]. Pertinent aspects of the 27 strand cable design for one set of experiments [2, 43] are recounted in Table 7.2. Some of the parameters listed in Table 7.2 are "engineering" estimates rather than measured values. Notably, the transverse joint resistance, $\Re_J$, and the heat transfer coefficient, h, have been chosen to be consistent with generally accepted estimates but these values can not be corroborated at this time. For the purpose of demonstrating the utility of the theory, however, they are deemed to be sufficient.[3]

For the parameters listed in Table 7.2, the cable falls into the Short-cable length/-short-circuit joint regime when in the Superconducting Domain and the lab-scale cable regime when in the Resistive Domain. Thus, the two-strand model results of Section 4.3.2 can be used with only minor modifications to study the behavior of the 27 strand experimental lab-scale cable.[4]

The first modification involves a simple accounting for the number of strands. To reduce all quantities to a "per-strand" basis, the transport current has to be

---

[3] In fairness, a few other values of $\Re_J$ and h were tried but did not match experimental results as well as the values listed in Table 7.2.

[4] Since the sub-cables remain twisted within the joint region, we can dispense with the more difficult joint model developed for the US-DPC cable in Section 4.3.2 above and return to the simpler geometry diagrammed in Fig. 3-1.

cable length	ℓ	1 m
twist-pitch length	ℓ_p	15 cm
cable width	w	0.5 cm
effective inductance per length	$\mathcal{L}$	0.34 μH
transverse electrical conductivity	$\sigma_\perp$	$< 100\ \Omega^{-1}\text{m}^{-1}$
transverse joint resistance	$\Re_J$	1 $\mu\Omega$
helium background temperature	T_b	4.5 K
helium pressure	P_h	5 atm.
helium cross-sectional area	A_h	0.64 mm^2
strand (one) cross-sectional area	A_s	0.48 mm^2
volume fraction superconductor	λ	0.45
matrix resistance per length	$\mathcal{R}_m$	1 mΩ-m^{-1}
heat transfer coefficient	h	1000 W/m^2-K

Table 7.2: Selected Properties of the MIT Lab-Scale Cable.

divided by $N_{tot} = 27$ while the circulating current calculated between two sub-cables needs to be divided by $N = 9$, the number of strands per sub-cable. The second modification concerns the trigonometric factor $\sin\theta_1 - \sin\theta_0$ in the source term Ψ, which first appears in Eq. (6.12). This factor can be studied statistically using the same methods derived in Appendix B to eliminate the need to arbitrarily select θ_0 and θ_1. The result is:

$$\text{Exp}\left[\sin\theta_1 - \sin\theta_0\right] = 0.85$$

7.6 Comparing Theoretical Model to Experimental Results of the Lab-Scale Experiment

At this point it is possible to use the results of Chapter 6 to compare theoretical predictions to experimental results. Figure 7-9 shows the experimentally determined stability behavior of the lab-scale cable as reported in [43] at two different ramp rates, $\dot{B}_\perp = 0.72$ and 1.64 T/s. The results were obtained by keeping the transport current (y-axis) constant and noting at what magnetic field (x-axis) the cable quenched for each value of $\dot{B}_\perp$.

The figure also shows the correponding theoretical predictions for each $\dot{B}_\perp$ us-

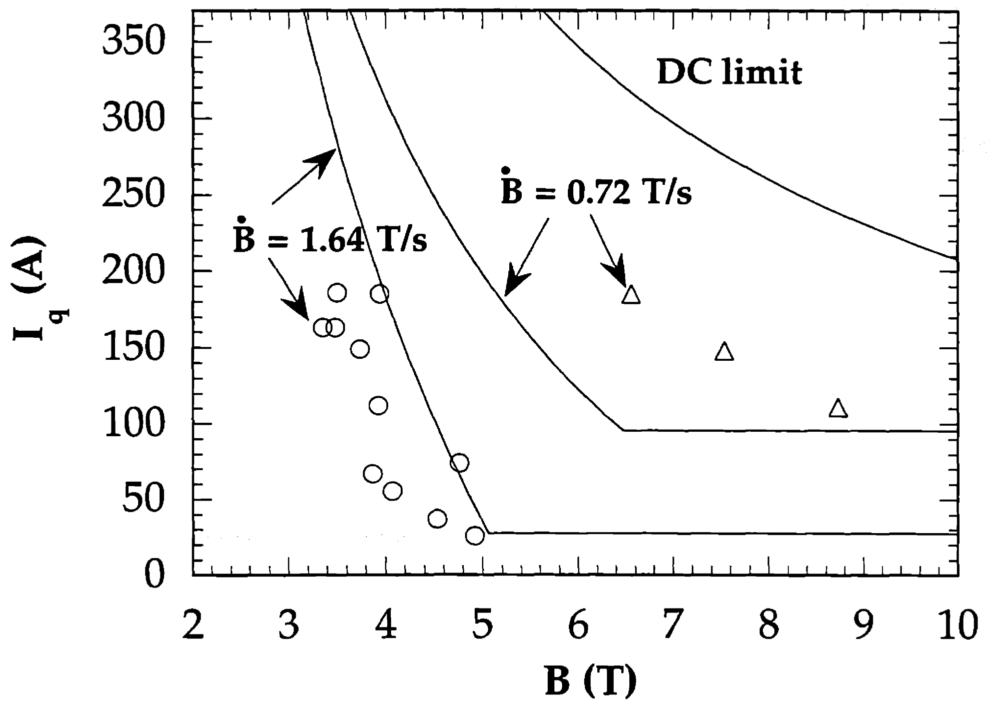

Figure 7-9: DC quench current per strand, I_q, vs. quench field, B_{max}, for the lab-scale cable test, [2, 43]. Experimental ($\circ, \triangle$) and theoretical (—) results for two ramp rates, $\dot{B}_{\perp}$.

ing the linearized stability model developed in Section 6.3. While the results do not match the experimental data perfectly, the theory qualitatively accounts for the adverse effects of increased $\dot{B}_{\perp}$ on the performance of the cable. If circulating currents were not considered, for instance, the cable would be expected to operate at nearly the DC limit, indicated in Fig. 7-9. The theory not only accounts for the general degradation of performance in ramping magnetic fields but also qualitatively predicts the dependence on $\dot{B}_{\perp}$.

7.7 Conclusions from Lab-Scale Cable Model

The comparison of theoretical predictions to measured results for the lab-scale cable experiments is convincing evidence that circulating currents play an important role in stability for superconducting cables. Further investigation is needed, however, to better estimate important parameters such as $\Re_J$ and h, before these results can be considered conclusive. Also, a more detailed theoretical model (i.e. multi-strand or continuum instead of two-strand) may be needed to fully explain the experimental data.

Chapter 8

Conclusions

The problem of uneven current distribution in superconducting cables is of considerable importance to designers of superconducting magnets which will be operated in transient conditions. This thesis provides a theoretical foundation for the study of induced circulating currents which can be a major source of current imbalance in CICC magnets. While the limited scope of the thesis prevented a comprehensive investigation of all aspects of the current distribution problem, several significant contributions were realized.

The theoretical model used throughout the thesis is based on a two-strand, twisted cable terminated in idealized joints. Compared to actual CICC windings with 100's or 1000's of strands, the geometrical simplicity of the two-strand model has the dual advantage of being mathematically tractable and physically intuitive. Nonetheless, the two-strand model captures all of the relevant physics and provides a compelling analogy for the behavior of current distribution in larger cables.

Most importantly, the results of the two-strand model provide important scaling parameters which can be used to characterize CICC magnets into distinct regimes determined by cable length and joint design. Since current distribution and stability criteria differ for each regime, the theory has important implications for the modelling of large-scale cables with sub-sized experiments. The scaling parameters also identify the important design parameters which most effect current distribution in superconducting cables.

8.1 Current Distribution

The analysis of Chapter 4 resulted in two derived length scales which can be used to characterize superconducting cables operated in ramping magnetic fields. The diffusion length, $\ell_D = \sqrt{t_{ramp}}/\sqrt{2\sigma_\perp \mathcal{L}}$, provides a benchmark in determining whether the cable length, ℓ, should be considered short, finite, or infiinite for the specified ramp time, t_{ramp}. The induced circulating currents for each of these length classifications possess different qualitative behaviors. In general, short cables experience proportionately larger imbalances than do finite or infinite cables.

The boundary scale length, $\ell_J = (\sigma_\perp \Re_J)^{-1}$, is a second independent characteristic of the cable. The boundary scale determines the distance from the ends of the cable at which the joint effects begin to saturate. The relative ordering of the cable length, ℓ, and the boundary scale, ℓ_J, determines the appropriate regime—open-circuit, resistive, or short-circuit—for a given cable. For each of these joint regimes, the induced circulating currents exhibit different patterns of behavior, resulting in a total of nine distinct solution regimes (e.g., "short length/resistive joint," "finite length/short-circuit joint," etc.). Figure 4-11 provides a handy summary of the nine regimes and a reference to the pertinent solutions for each.

Since both the diffusion length scale and the boundary length scale depend on the the transverse conductance, $\sigma_\perp$, this one parameter has great influence on the current distribution within a cable. Unfortunately, $\sigma_\perp$ is very difficult to measure and is practically unknown for most cables. This concern is mentioned again in Section 8.4, suggestions for future work.

One interesting discovery from the theoretical analysis was that the magnitude of the induced currents was only dependent on the field ramp-rate at the joints, $\dot{B}_\perp(x=0)$ and $\dot{B}_\perp(x=\ell)$. This result is important when comparing lab-scale experiments with uniform background field distributions to full-scale experiments in which the field at the joints is typically much lower ($\sim 50\%$) than the peak field. The result also suggests extra care should be taken to place joints in low field regions or provide magnetic shielding (if possible) to reduce the destabilizing effects of circulating currents.

8.2 Stability Criteria

The current distribution model needs to be coupled to a thermal model in order to predict the time-evolution of the current and temperature once the strand current reaches the critical current. In Chapter 5, the necessary model was derived and used to study the behavior of cables once they enter this so-called Resistive Domain. Unfortunately, the resulting system of equations is non-linear and needs to be solved numerically using advanced algorithms designed to solve higher order boundary value problems.

The numerical results quickly yielded an important discovery, however: the stability behavior of cables which enter the Resistive Domain depends primarily on the overall length of the cable, ℓ, and the transfer length, $\ell_X = (\sigma_\perp \mathcal{R})^{-1/2}$. For cable lengths longer than the transfer length, the cable invariably quenched soon after entering the Resistive Domain. For cables shorter than the transfer length, though, either quench or a rapid recovery were possible, depending on the cable design.

For practical design parameters, cables with $\ell > \ell_X$ are "full-scale" magnets ($\ell \gtrsim 50$ m) which generate their own magnetic field. For such magnets, the stability criterion can be calculated using the analytic results of the current distribution calculations of Chapter 4 to determine the total current (transport current + circulating current) in strand *one*. This current, I, must be less than the critical current, I_c, at time $t = t_{ramp}$. Thus, the stability criterion is:

$$t = t_{ramp} \; ; \quad I = I_{T/2} + I_B < I_c$$

where $I_{T/2}$ is the average transport current per strand and I_B is the analytically calculated circulating current.

For "lab-scale" cables, the length is typically $\ell < \ell_X$ and the stability criterion is much more involved. In this case, however, several approximations are valid which allow the non-linear, coupled partial differential equations of the stability model to be linearized and studied analytically. The linearized equations can be solved to yield a marginal stability line which provides a boundary between stable and unstable regimes in the phase plane defined by the operating conditions I_T and $\dot{B}_\perp$. This result was shown graphically in Fig. 6-14.

The theoretical study of lab-scale cables provided a convincing explanation for many experimentally observed phenomena. Most interestingly, the theory predicts that lab-scale cables which are operated within the stable regime may experience a rapid redistribution of current when strand *one* reaches the critical current. Such redistribution of current has been measured experimentally as a voltage "blip" using specially designed diagnostics [4, 5].

The ability of lab-scale cables to recover from the Resistive Domain in certain conditions must be carefully considered when using lab-scale experiments to predict the behavior of full-scale magnets. Lab-scale results which exhibit the tell-tale "blips" of rapid current redistribution cannot be directly compared to full-scale results since full-scale magnets do not have a similar recovery mechanism.

8.3 Comparisons to Experiments

Although the main contribution of the two-strand model is its ability to explain important scaling relations and not its quantitative accuracy, the results of the model were nonetheless compared to the results of two different experiments. As expected, agreement between experiment and theory left a little to be desired, but the theory did explain some of the more confounding results of the two experimental campaigns.

The modified two-strand model provided a convincing argument that circulating currents accounted for the approximately 25% degradation in the expected performance of the United States Demonstration Poloidal Coil (US-DPC). Although the US-DPC results exhibited a stronger dependence on ramp-rate, $\dot{B}_\perp$, than the theory predicted, it is believed that further refinements of the two-strand model could eventually account for this discrepancy as well.

The comparison of the theory to lab-scale results did better in matching the ramp-rate dependency observed experimentally. Again, the theory proved to be a better "qualitative" match than a "quantitative" one, but that was the original goal of the model anyway. The results offer enough encouragement to merit further investigation using a more sophisticated approach, as will be discussed in the next section.

8.4 Future Directions

The two-strand model was a necessary first step in the treatment of current distribution and the related stability criteria for cabled superconductors. The model demonstrated the importance of circulating currents and provided a foundation on which future work can be built. The following areas warrant further investigation:

- The two-strand model highlights the importance of various cable parameters which are usually not measured. Specifically, the transverse cable conductance, $\sigma_\perp$, and the transverse joint resistance, $\Re_J$, strongly influence the behavior of circulating currents in superconducting cables but neither is a well known value for a given cable design. An experimental program to develop a reliable method of testing these parameters would be quite valuable in this regard.

- While the two-strand model provides a useful analogy for more complicated cables, a more sophisticated approach would be needed to develop an accurate predictive tool. During the course of researching this topic, some success was achieved in developing a continuum model which incorporated the multiple twisting stages of a fully transposed cable. This effort should be renewed if it is determined that a more accurate picture of current distribution is necessary.

- This thesis emphasizes the importance of joint design in determining the magnitude and effects of current distribution in CICC magnets. A joint designed to offer the lowest possible DC resistance is not necessarily the best choice for a magnet operating in transient fields; lowering the transverse joint resistance, $\Re_J$, tends to increase the magnitude of induced circulating currents. Although purposefully *increasing* $\Re_J$ leads to higher cooling costs, it would help to reduce uneven current distributions. Alternatively, it may be worth investigating the possibility of magnetically shielding the joint region since only $\dot{B}_\perp$ at the joints contributes to circulating currents.

- In the future, small-scale experiments designed to simulate full-scale magnets will have to be designed more carefully. As mentioned many times previously, the relative length of the cable compared to the length scales ℓ_J, ℓ_D, and ℓ_X determines the current distribution and stability behavior. Without careful attention to joint design and transconductance, the ordering of ℓ, ℓ_J, ℓ_D, and ℓ_X for a small-scale simulation will not match the ordering for the original full-scale design.

With further work, it seems probable that the harmful effects of non-uniform current distribution can be completely understood and successfully controlled in future magnets.

Appendix A

Inverse Laplace Transforms

While most of the Laplace transforms encountered in Chapter 4 could be inverted directly using tables [30], there was one instance which required special treatment. Equation (4.97) represented the solution in the transform domain for the induced currents in a cable of "finite" length and "resistive" joints. In this appendix, the inverse transform of this solution will be found using contour integration and residue theory.

A.1 Residue Calculus

In general, the transform pair $f(t) \Leftrightarrow g(p)$ can be related through the following definition:

$$f(t) = \sum_n \mathrm{Res}\{e^{pt} g(p); \quad a_n\} \tag{A.1}$$

where the points a_n are the complex poles of $g(p)$ and the notation $\mathrm{Res}\{g(p); \quad a\}$ is used to indicate the residue of $g(p)$ at $p = a$. The residue is defined as:

$$\mathrm{Res}\{g(p); \quad a\} = \frac{1}{(m-1)!} \left[\frac{d^{m-1}}{dp^{m-1}} \{(p-a)^m g(p)\} \right]_{p=a} \tag{A.2}$$

wher m is the order of the pole (i.e., singularity) which exists at $p = a$, (note that p is in general complex).

If the function $g(p)$ can be expressed as a ratio

$$g(p) = \frac{N(p)}{D(p)} \tag{A.3}$$

where $N(p)$ is finite and non-zero at $p = a$ (i.e. a is a simple pole, $m = 1$), then L'hospital's rule can be used to evaluate Eq. (A.2)

$$\text{Res}\{g(p); \quad a\} = \frac{N(a)}{D'(a)} \tag{A.4}$$

Further details of this procedure can be found in [44].

A.2 Solving the Finite Length, Resistive Joints Case

Equation (4.97) can now be solved using the techniques just described. To start, the equation is repeated here:

$$\begin{aligned} Z &= Z_1 + Z_2 \\ &= \frac{\ell_J}{2}(b_0' - b_1') \frac{\cosh\left(\frac{\sqrt{p}x}{\alpha}\right)}{p\left[\cosh\left(\frac{\sqrt{p}\ell}{2\alpha}\right) + \frac{\sqrt{p}\ell_J}{\alpha}\sinh\left(\frac{\sqrt{p}\ell}{2\alpha}\right)\right]} \\ &\quad - \frac{\ell_J}{2}(b_0' + b_1') \frac{\sinh\left(\frac{\sqrt{p}x}{\alpha}\right)}{p\left[\sinh\left(\frac{\sqrt{p}\ell}{2\alpha}\right) + \frac{\sqrt{p}\ell_J}{\alpha}\cosh\left(\frac{\sqrt{p}\ell}{2\alpha}\right)\right]} \end{aligned} \tag{A.5}$$

The first term on the RHS can be rewritten:

$$Z_1(p) = \frac{\ell_J}{2}(b_0' - b_1')\frac{\ell^2}{4\alpha^2} g_1(\frac{p\ell^2}{4\alpha^2}) \tag{A.6}$$

where:

$$g_1(s) = \frac{\cosh(\frac{2x}{\ell}\sqrt{s})}{s\left(\cosh(\sqrt{s}) + \frac{2\ell_J}{\ell}\sqrt{s}\sinh(\sqrt{s})\right)} \tag{A.7}$$

To find the inverse Laplace transform of g_1 it is necessary to identify the poles of the equation. Using the notation $g_1(s) = N(s)/D(s)$, the poles are identified as the zeroes of the function $D(s)$:

$$D(s) = 0 = s\left(\cosh(\sqrt{s}) + \frac{2\ell_J}{\ell}\sqrt{s}\sinh\sqrt{s})\right) \tag{A.8}$$

The first zero is easily identified as $s = a_0 = 0$. The remaining zeroes are more easily identified when the mapping $s_n = -\hat{k}_n^2$ is employed for $n = 1, 2, 3 \ldots \infty$. Using standard identities for $\sinh(i\hat{k}_n)$ and $\cosh(i\hat{k}_n)$, $D(s) = 0$ when:

$$2\frac{\ell_J}{\ell}\hat{k}_n \tan(\hat{k}_n) = 1\ ; \quad n > 0 \tag{A.9}$$

where the values of $\hat{k}_n > 0$ produce the poles $a_n = -\hat{k}_n^2$, all of order $m = 1$. Identifying the correct poles, as we have just done, is the most critical part of process.

The next step is to use L'hospital's rule as described above to evaluate the desired residue at each of the poles:

$$\begin{aligned} f_1(t) &= \sum_n \mathrm{Res}\{e^{pt}g_1(p);\quad a_n\} \\ &= \sum_n e^{a_n t}\frac{N(a_n)}{D'(a_n)} \\ &= \sum_n \frac{e^{-\hat{k}_n^2 t}\cos(\frac{2x}{\ell}\hat{k}_n)}{\cos\left(\hat{k}_n\right) - \left(\frac{1}{2} + 3\frac{\ell_J}{\ell}\right)\hat{k}_n \sin\left(\hat{k}_n\right) - \frac{\ell_J}{\ell}\hat{k}_n^2\cos\left(\hat{k}_n\right)} \end{aligned} \tag{A.10}$$

where $\hat{k}_0 = 0$ and $\hat{k}_n$ are evaluated using Eq. (A.9). Having determined the transform pair $g_1(s) \Leftrightarrow f_1(t)$ it is possible to evaluate the needed inverse using the chain-rule:

$$\begin{aligned} g_1(s) &\Leftrightarrow f_1(t) \\ g_1(\frac{p\ell^2}{4\alpha^2}) &\Leftrightarrow \frac{4\alpha^2}{\ell^2}f_1(\frac{4\alpha^2 t}{\ell^2}) \end{aligned}$$

Plugging this result and Eq. (A.10) back into Eq. (A.6) produces the result:

$$\mathcal{L}^{-1}\{Z_1\} = \\ \frac{\ell_J}{2}\left(b_0' - b_1'\right)\left[1 + \sum_{n=1}^{\infty}\left(\frac{e^{-4\hat{k}_n^2\alpha^2 t/\ell^2}\cos\left(\hat{k}_n\frac{x}{\ell}\right)}{\cos\left(\hat{k}_n\right) - \left(\frac{1}{2} + 3\frac{\ell_J}{\ell}\right)\hat{k}_n\sin\left(\hat{k}_n\right) - \frac{\ell_J}{\ell}\hat{k}_n^2\cos\left(\hat{k}_n\right)}\right)\right] \tag{A.11}$$

The solution for the inverse of the second term on the RHS of Eq. (A.5), Z_2, can be found in the same manner. The a_0 pole is again $a_0 = 0$ and the equation which generates the poles for $n > 0$ is $a_n = -\check{k}_n^2$ where:

$$2\frac{\ell_J}{\ell}\check{k}_n\cot\left(\check{k}_n\right) = -1 \ ; \qquad n > 0 \tag{A.12}$$

For the $n > 0$ poles, finding the residue is again easiest using L'hospital's rule. The pole at $a_0 = 0$, however, is of second order, $m = 2$, and thus it is necessary to use the formal definition of the residue, Eq. (A.2).

The solution for the inverse of the Z_2 component of the transform turns out to be:

$$\mathcal{L}^{-1}\{Z_2\} = \\ -\frac{\ell_J}{2}\left(b_0' + b_1'\right)\left[\frac{x}{\ell_J + \frac{\ell}{2}} + \sum_{n=1}^{\infty}\left(\frac{e^{-4\check{k}_n^2\alpha^2 t/\ell^2}\sin\left(\check{k}_n\frac{x}{\ell}\right)}{\sin\left(\check{k}_n\right) + \left(\frac{1}{2} + 3\frac{\ell_J}{\ell}\right)\check{k}_n\cos\left(\check{k}_n\right) - \frac{\ell_J}{\ell}\check{k}_n^2\sin\left(\check{k}_n\right)}\right)\right] \tag{A.13}$$

where $\check{k}_0 = 0$ and $\check{k}_n$ are evaluated using Eq. (A.12).

Combining Eqs. (A.11) and (A.13) produces the desired solution for the induced currents in a finite cable with resistive joints as given in Eq. (4.98).

Appendix B

Statistical Expectation of Flux Imbalance

The purpose of this appendix is to describe the procedure used to determine the statisical expectation of the flux imbalance term, ς, which first appeared in Eq. (7.19). For ease of reference, that term is repeated here:

$$\varsigma \equiv [(\cos\theta_1 + \cos\theta_0) - \epsilon\,(\sin\theta_1 - \sin\theta_0)] \tag{B.1}$$

where θ_0 and θ_1 represent the unknown orientation of the joint with respect to the direction of the magnetic field at $x = 0$ and $x = \ell$, respectively. The coefficient ϵ is defined as $\epsilon \equiv \ell_p/(\pi\ell_T)$. For the US-DPC cable described in Table 7.1, $\epsilon = 0.1$.

To determine Exp[ς], the statistical expectation of ς, it is necessary to split ς into two components:

$$\begin{aligned} \varsigma &= \varsigma_0 + \varsigma_1 \\ \varsigma_0 &\equiv \cos\theta_0 + \epsilon\sin\theta_0 && \text{(B.2)} \\ \varsigma_1 &\equiv \cos\theta_1 - \epsilon\sin\theta_1 && \text{(B.3)} \end{aligned}$$

Since θ_0 and θ_1 are both random variables with identical, uniform probability distribution functions (PDF's), ς_0 and ς_1 are also random variables with identical PDF's.[1] This similarity property simplifies the analysis since only one PDF has to be derived to characterize both ς_0 and ς_1. To generalize, then, the variable χ has been chosen to represent either ς_0 or ς_1 and the variable Θ has been chose to represent either θ_0 or θ_1. Thus:

$$\chi = \cos\Theta + \epsilon\sin\Theta \Longleftrightarrow \begin{cases} \varsigma_0 = \cos\theta_0 + \epsilon\sin\theta_0 \\ \varsigma_1 = \cos\theta_1 - \epsilon\sin\theta_1 \end{cases}$$

The variable Θ is a uniformly distributed random variable: $-\infty < \Theta < \infty$. Due to the periodicity of the "sin" and "cos" operators, however, we can equivalently define Θ to be a uniformly distributed random variable over a finite domain: $\Theta_{\text{min}} \leq \Theta < \Theta + 2\pi$, where the choice of Θ_{min} is arbitrary.

To simplify the construction of the PDF of χ, it is easiest to choose Θ_{min} to correspond with a local minimum of χ, as shown graphically in Fig. B-1. For the range chosen in the figure, the specific value of Θ_{min} is:

$$\Theta_{\text{min}} = \tan^{-1}(\epsilon) - \pi \tag{B.4}$$

and the value of Θ which maximizes χ is :

$$\Theta_{\text{max}} = \tan^{-1}(\epsilon) \tag{B.5}$$

The corresponding minimum and maximum of χ are:

$$\chi_{\text{min}} = \cos\Theta_{\text{min}} + \epsilon\sin\Theta_{\text{min}} \tag{B.6}$$

$$\chi_{\text{max}} = \cos\Theta_{\text{max}} + \epsilon\sin\Theta_{\text{max}} \tag{B.7}$$

We will use the definition $F_\chi(\chi_0) \equiv \mathrm{P}\left[\chi \leq \chi_0\right]$ to mean the probability that the random variable χ is less than the designated value, χ_0. $F_\chi(\chi_0)$ is also known as the cumulative distribution function (CDF) of χ. From Fig. B-1 it is immediately evident

---

[1] While the second terms in Eqs. (B.2) and (B.3) have different signs, this only accounts for a phase shift. Thus ς_0 and ς_1 have the same PDF.

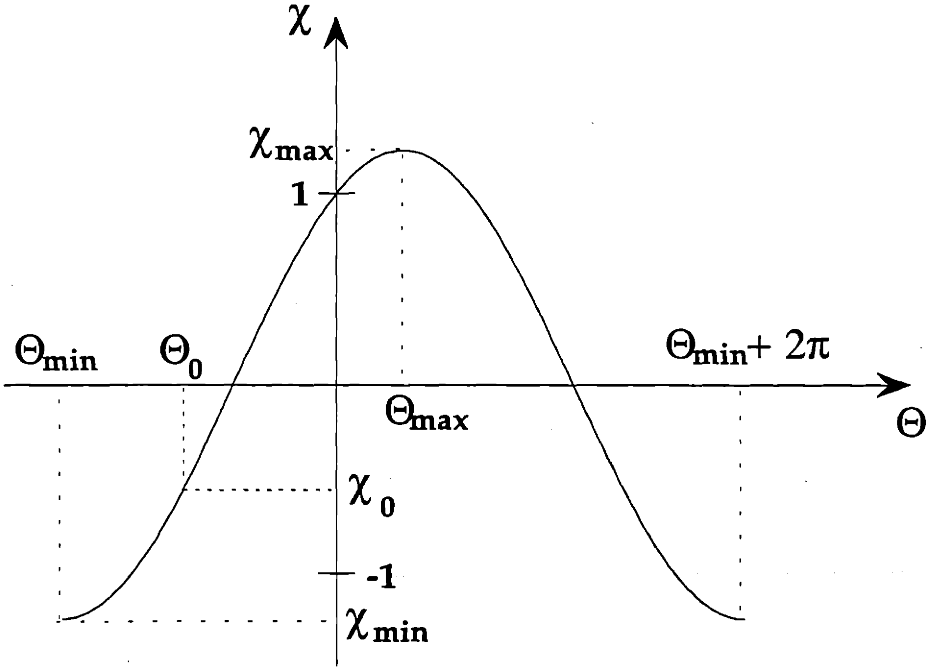

Figure B-1: The random variable χ vs. Θ where Θ is a uniformly distributed random variable such that $\Theta_{\text{min}} \leq \Theta < \Theta_{\text{min}} + 2\pi$.

that:

$$F_\chi(\chi_0) = \begin{cases} 1 & ; \ \chi_0 \geq \chi_{\text{max}} \\ 0 & ; \ \chi_0 \leq \chi_{\text{min}} \end{cases} \tag{B.8}$$

For values of χ_0 such that $\chi_{\text{min}} < \chi_0 < \chi_{\text{max}}$, the CDF is more difficult to calculate. The critical step in the process is calculating the value of Θ_0 such that $\Theta_{\text{min}} < \Theta_0 < \Theta_{\text{max}}$ and $\chi_0 = \cos\Theta_0 + \epsilon\sin\Theta_0$. An example is included in Fig. B-1. The desired relation between Θ_0 and χ_0 was found to be:

$$\Theta_0 = 2\tan^{-1}\left(\frac{\epsilon - \sqrt{1+\epsilon^2-\chi_0^2}}{1+\chi_0}\right) \tag{B.9}$$

With Θ_0 solved in terms of χ_0, the calculation of $F_\chi(\chi_0)$ for $\chi_{\text{min}} < \chi_0 < \chi_{\text{max}}$ can be determined geometrically with the assistance of Fig. B-1. For the example in the figure, χ is less than χ_0 over the following subset of the Θ domain:

$$[\Theta_{\text{min}} < \Theta < \Theta_0] \cup [\Theta_{\text{min}} + 2\pi - (\Theta_0 - \Theta_{\text{min}}) < \Theta < \Theta_{\text{min}} + 2\pi] \tag{B.10}$$

where the second piece of the range is found from symmetry conditions. Since Θ is uniformly distributed over the full range $\Theta_{\min} < \Theta < \Theta_{\min} + 2\pi$, the ratio of the subset, Eq. (B.10) to the full range defines $F_\chi(\chi_0)$. The final result (including the parts calculated in Eq. (B.8)) is:

$$F_\chi(\chi_0) = \begin{cases} 1 & ; \ \chi_0 \geq \chi_{\max} \\ (\Theta_0 - \Theta_{\min})/\pi & ; \ \chi_{\min} < \chi_0 < \chi_{\max} \\ 0 & ; \ \chi_0 \leq \chi_{\min} \end{cases} \tag{B.11}$$

where Θ_0 is defined in Eq. (B.9), $\Theta_{\min}$ is defined in Eq. (B.4), and $\chi_{\min}$ and $\chi_{\max}$ are defined in Eqs. (B.6) and (B.7).

Having found the CDF, $F_\chi(\chi_0)$, it is now necessary to calculate the partial distribution function (PDF) which is defined as $f_\chi(\chi_0) \equiv \frac{\partial}{\partial\chi} F_\chi(\chi_0)$. Thus differentiating Eq. (B.11) produces:

$$f_\chi(\chi_0) = \begin{cases} 0 & ; \ \chi_0 \geq \chi_{\max} \\ [\pi(\epsilon \cos\Theta_0 - \sin\Theta_0)]^{-1} & ; \ \chi_{\min} < \chi_0 < \chi_{\max} \\ 0 & ; \ \chi_0 \leq \chi_{\min} \end{cases} \tag{B.12}$$

We have already ascertained that $f_{\varsigma_0} = f_{\varsigma_1} = f_\chi$. In technical terms, ς_0 and ς_1 are "indepentally and identically distributed." In this special case, the combined distribution for $\varsigma = \varsigma_0 + \varsigma_1$ can be calculated using the convolution integral [45]:

$$f_\varsigma(z_0) = f_{\varsigma_0+\varsigma_1}(z_0) = \int_{-\infty}^{\infty} f_\chi(\chi_0) f_\chi(z_0 - \chi_0) d\chi_0 \tag{B.13}$$

where $f_\chi(\chi_0)$ is given in Eq. (B.12).

There is one additional subtlety which must be included in the analysis. By definition, the induced current in strand *one* is positive;[2] thus, instead of finding the PDF for ς, we truly want the PDF for $|\varsigma|$, the absolute value. Exploiting the

---

[2] Instead of allowing the induced current in strand *one* to be negative, we would first re-label the strands. Thus the induced current in the strand labeled *one* is always nonnegative.

symmetry of the problem, we find that:

$$f_{|\varsigma|}(z_0) = 2\int_{-\infty}^{\infty} f_\chi(\chi_0) f_\chi(z_0 - \chi_0) d\chi_0 \tag{B.14}$$

where $z_0 > 0$.

The final step is to calculate the expected value of $|\varsigma|$. By definition:

$$\text{Exp}\left[|\varsigma|\right] = \int_0^{\infty} z_0 f_{|\varsigma|}(z_0) dz_0 \tag{B.15}$$

where $f_{|\varsigma|}(z_0)$ is itself an integral as defined in Eq. (B.14). Equation (B.15) is thus a double integral equation which must be calculated using numerical means. The indices of integration, however, can be set to finite values by determining the finite, non-trivial domain of the integrands (i.e. the domain over which the integrands are not equal to zero). This step has been omitted here, but is straightforward.

For the purposes of this thesis, a fortran routine was written to evaluate Eq. (B.15) for differing cable designs. For the example presented in Section 7.2, the result was found to be $\text{Exp}\left[|\varsigma|\right] = 0.95$. In the main body of the thesis, this result is written using the simplified (although slightly misleading) notation $\text{Exp}\left[\varsigma\right] = 0.95$.

Appendix C

Analytic Solution to Linearized Stability Equations

The coupled linearized current and temperature equations derived in Chapter 6 can be solved using standard solution techniques. Unfortunately, the algebra becomes quite involved and thus the details have been saved for this appendix.

C.1 Solving Current and Temperature Evolution from Given Initial Conditions

Following the structure proposed in Section 6.3.2, the derivation is divided into three segments:

I. $0 < t < t_\star$ Both strands are superconducting, $\mathcal{R}_1 = \mathcal{R}_2 = 0$.

II. $t_\star < t < t_x$ Strand *one* is resistive but strand *two* is superconducting, $\mathcal{R}_1 > 0, \mathcal{R}_2 = 0$.

III. $t > t_x$ Both strands are resistive. $\mathcal{R}_1 > 0, \mathcal{R}_2 > 0$.

C.1.1 $0 < t < t_\star$

Before the current in strand *one* reaches the critical current, the current distribution is described by the Superconducting Domain solutions developed in Section 4.3.2. For the Short Length/Short-Circuit Joint Regime appropriate for lab-scale cables, Eq. (4.70) gives the current in strand *one* in the Superconducting Domain, $0 < t < t_\star$:

$$I_1 = I_{T/2} + \Psi\tau_J\left(1 - e^{-t/\tau_J}\right) \tag{C.1}$$

where $\tau_J = \mathcal{L}\ell/\Re_J$ and

$$\Psi \equiv \frac{\dot{B}_\perp w \ell_p}{4\pi\ell\mathcal{L}}\left(\sin\theta_1 - \sin\theta_0\right) \tag{C.2}$$

The angles θ_0 and θ_1 represent the orientation of the joints with respect to the direction of the transverse magnetic field.

At the time $t = t_\star$, the current in strand *one*, from Eq. (C.1), equals the critical current. The values of $t_\star$ can be found using by setting Eq. (C.1) equal to Eq. (6.25), the equation for the critical current. The value of the strand *one* current and the magnetic field at $t = t_\star$ are defined to be $I_\star$ and $B_\star$, respectively.

The hunt for the marginal stability case actually begins at $t = t_\star$, $I = I_\star$ and $B = B_\star$ when the first blip occurs in the cable. The transport current can be deduced from these three variables using Eq. (6.25) and Eq. (C.1):

$$I_{T/2} = \frac{\xi}{B_\star} - \Psi\tau_J\left(1 - e^{-t_\star/\tau_J}\right) \tag{C.3}$$

Once the cable enters the Resistive Domain, the duration of the stability event is short enough ($\sim$ 10 ms) that the magnetic field is approximately constant, i.e. $B(t) \approx B_\star$. Thus, the critical current, $I_c(B,T)$ becomes:

$$\begin{aligned} I_c(B,T) \approx I_c(B_\star,\vartheta) &= \frac{\xi}{B_\star}\left(1 - \frac{\vartheta}{\vartheta_{c\star}}\right) \\ &= I_\star\left(1 - \frac{\vartheta}{\vartheta_{c\star}}\right) \end{aligned} \tag{C.4}$$

where ϑ is a simple transformation of the temperature, $\vartheta \equiv T - T_b$. The scale factor $\vartheta_{c\star}$ is constant for the duration of the stability event; it depends on the superconductor properties and the magnetic field at the time of the blip, $t_\star$: $\vartheta_{c\star} \equiv (T_{c0} - T_b)\,(1 - B_\star/B_{c0})$.

C.1.2 $t_\star < t < t_x$

For times $t > t_\star$, the cable becomes resistive and the current equation is coupled to the temperature equations. The current equation for lab-scale cables in the Resistive Domain was given in Eq. (6.19) and is rewritten here:

$$\frac{\partial I}{\partial t} + \left(\frac{1}{\tau_J} + \frac{\mathcal{R}_1 + \mathcal{R}_2}{2\mathcal{L}}\right) I = \frac{\partial I_{T/2}}{\partial t} + \left(\frac{1}{\tau_J} + \frac{\mathcal{R}_2}{\mathcal{L}}\right) I_{T/2} + \Psi \tag{C.5}$$

where Ψ is defined in Eq. (C.2).

The temperature equations were given in Eqs. (6.20)–(6.22). Using the restrictions listed at the outset of Section 6.3, the temperature equations for the two strands and the helium are reduced to a single equation since $T_2 \approx T_1 \equiv T$ and $T_h \approx T_b$. Using the notation, $\vartheta \equiv T - T_b$, these relations become: $\vartheta_2 = \vartheta_1 = \vartheta$ and $\vartheta_h = 0$. The remaining equation becomes:

$$\rho_s \bar{C}_s A_s \frac{\partial \vartheta}{\partial t} + 2hp\vartheta = \mathcal{R}_1 I^2 + \mathcal{R}_2 (I_T - I)^2 \tag{C.6}$$

where the constant $\bar{C}_s$ replaces the temperature dependent $C_s(\vartheta)$. The decision of which value to use for $\bar{C}_s$ is determined by fitting the linear model to the results of the non-linear model, as discussed in Section 6.3.1.

Looking ahead, Section C.1.3 will deal with the equations for cases when both strands are resistive. For now, $\mathcal{R}_2 = 0$ and Eqs. (C.5) and (C.6) simplify. Using Eq. (6.23) to substitute for $\mathcal{R}_1$, the results are:

$$\frac{\partial I}{\partial t} + \left(\frac{1}{\tau_J} + \frac{1}{2}\frac{1}{\tau_m}\right) I = \frac{\partial I_{T/2}}{\partial t} + \frac{1}{\tau_J} I_{T/2} + \frac{1}{\tau_m} I_c + \Psi \tag{C.7}$$

$$\rho_s \bar{C}_s A_s \frac{\partial \vartheta}{\partial t} + 2hp\vartheta = \mathcal{R}_m \bar{I}(I - I_c) \tag{C.8}$$

where $\tau_m = \mathcal{L}/\mathcal{R}_m$ and the introduction of the variable $\bar{I}$ is discussed in Section 6.3.1 (refer to Eq. (6.36)). Although $\tau_m^{-1} \gg \tau_J^{-1}$, the τ_J terms cannot be dropped since the τ_m term on the RHS of Eq. (C.8) cancels the τ_m term on the LHS at $t \approx t_\star$.

Substituting the temperature dependent equation for I_c, Eq. (C.4), into Eq. (C.8) results in the desired linearized temperature equation:

$$\rho_s \bar{C}_s A_s \frac{\partial \vartheta}{\partial t} + 2hp\vartheta = \mathcal{R}_m \bar{I}[I - I_\star(1 - \vartheta/\vartheta_{c\star})] \tag{C.9}$$

Rearranging this result produces:

$$\bar{\alpha}\tau_m \frac{\dot{\vartheta}}{\vartheta_{c\star}} + \bar{\beta}\frac{\vartheta}{\vartheta_{c\star}} = -\left(1 - \frac{I}{I_\star}\right) \tag{C.10}$$

where the dimensionless coefficients have been defined as follows:

$$\begin{aligned} \bar{\alpha}(I_\star) &= \frac{\rho_s \bar{C}_s A_s \vartheta_{c\star}(I_\star)}{\mathcal{R}_m \bar{I}(I_\star) I_\star \tau_m} && \text{(C.11)} \\ \bar{\beta}(I_\star) &= \frac{2ph\vartheta_{c\star}(I_\star)}{\mathcal{R}_m \bar{I}(I_\star) I_\star} - 1 && \text{(C.12)} \end{aligned}$$

and $\dot{\vartheta} \equiv \frac{\partial}{\partial t}\vartheta$. Since the value of $I_\star$, the strand current when it first becomes resistive, depends only on the operating conditions (I_T, $\dot{B}_\perp$), the coefficients are constants for a given scenario.

The next step is to use the current equation to find a second relation for ϑ which can be substituted into Eq. (C.10). Substituting the temperature dependent equation for I_c, Eq. (C.4), into the current equation, Eq. (C.7), and rearranging gives:

$$\frac{\vartheta}{\vartheta_{c\star}} = 1 - 2\tau_m \frac{\dot{I}}{I_\star} - \left(1 + \frac{2\tau_m}{\tau_J}\right)\frac{I}{I_\star} + \frac{2\tau_m \Psi}{I_\star} - \frac{\tau_m}{\tau_J}\frac{I_T}{I_\star} \tag{C.13}$$

Plugging this last result into Eq. (C.10) produces a second-order linear Initial Value

Problem (IVP) with the initial conditions $I = I_\star$ and $\dot{I} = \Psi + (I_{T/2} - I_\star)/\tau_J$ at $t = t_\star$:

$$\ddot{I} + \dot{I}/\tau_R + \omega_R^2 I = K_R I_\star/\tau_m^2 \tag{C.14}$$

where the constant coefficients are defined as follows:

$$\begin{aligned}
\tau_R^{-1} &= \left(\frac{1}{2\tau_m} + \frac{1}{\tau_J} + \frac{\bar{\beta}}{\tau_m \bar{\alpha}}\right) && \text{(C.15)} \\
\omega_R^2 &= \frac{\bar{\beta}}{\tau_m \bar{\alpha}}\left(\frac{1}{2\tau_m} + \frac{1}{\tau_J}\right) + \frac{1}{2\bar{\alpha}\tau_m^2} && \text{(C.16)} \\
K_R &= \frac{1+\bar{\beta}}{2\bar{\alpha}} + \frac{\bar{\beta}\tau_m}{\bar{\alpha} I_\star}\left(\Psi + \frac{I_{T/2}}{\tau_J}\right) && \text{(C.17)}
\end{aligned}$$

and $\bar{\alpha}$ and $\bar{\beta}$ are defined in Eqs. (C.11) and (C.12). Each of these constant coefficients depends on the operating conditions since they are implicit functions of $I_\star$.

As discussed in Section 6.3.2, Eq. (C.14) can be characterized as over-damped, critically damped, or under-damped. The under-damped case is of immediate interest since it corresponds to the operating scenario which produces the marginal stability condition.[1] The characteristic equation for the second order ODE, Eq. (C.14), has complex roots, $p \pm qi$, in the under-damped case and the solution is of the form:

$$I = I_\star \left[e^{p(t-t_\star)/\tau_m}\left(c_1 \cos\left[q(t-t_\star)/\tau_m\right] + c_2 \sin\left[q(t-t_\star)/\tau_m\right]\right) + K_R(\omega_R \tau_m)^{-2}\right] \tag{C.18}$$

where:

$$\begin{aligned}
p &= \tau_m/(2\tau_R) \\
q &= (1/2)\left[4(\omega_R\tau_m)^2 - (\tau_m/\tau_R)^2\right]^{1/2}
\end{aligned}$$

and the constants c_1 and c_2 can be found from the initial conditions:

$$c_1 = 1 - K_R(\omega_R\tau_m)^{-2}$$

---

[1] See Section 6.2.4 for a discussion concerning marginal stability in the linearized model.

$$c_2 = \frac{1}{q}\left[\frac{\tau_m\Psi}{I_\star} + \frac{\tau_m}{\tau_J}\left(\frac{I_{T/2}}{I_\star} - 1\right)\right] - \frac{p}{q}c_1$$

Using Eq. (C.13), the temperature can be extracted from the current equation just derived, Eq. (C.18), yielding:

$$\frac{\vartheta}{\vartheta_{c\star}} = 1 - e^{p(t-t_\star)/\tau_m}\left[\begin{array}{l} [2pc_1 + 2qc_2 + (1+2\tau_m/\tau_J)c_1]\cos\left[q(t-t_\star)/\tau_m\right] \\ \quad + [2pc_2 - 2qc_1 + (1+2\tau_m/\tau_J)c_2]\sin\left[q(t-t_\star)/\tau_m\right] \end{array}\right]$$
$$- (1+2\tau_m/\tau_J)K_R(\omega_R\tau_m)^{-2} + \frac{2\tau_m}{I_\star}\left(\Psi + I_{T/2}/\tau_J\right) \qquad \text{(C.19)}$$

Knowing both I and ϑ for times $t_\star < t < t_x$, it is possible to calculate the occurrence of t_x, the time at which the current in strand two equals the critical current, $I_c(B_\star, \vartheta)$, or t_{rec}, the time at which the first strand recovers. Due to the complexity of Eqs. (C.18) and (C.19), however, this calculation requires iteration; there is no closed form solution.

C.1.3 $t > t_x$

For cases in which the second strand quenches, we need to continue with the evolution. For times $t > t_x$, both strands are resistive, $\mathcal{R}_1 > 0, \mathcal{R}_2 > 0$, and Eq. (C.5) can be rewritten:

$$\dot{I} + \frac{1}{\tau_q}I = \Psi + \frac{1}{\tau_q}I_{T/2} + \frac{\partial I_{T/2}}{\partial t} \qquad \text{(C.20)}$$

where $1/\tau_q \equiv (1/\tau_J + 1/\tau_m)$. Notice that this equation is no longer coupled to the temperature equation. The initial condition is $I = I_x \equiv I(t = t_x)$ and the solution is thus:

$$I = (I_x - I_f)e^{-(t-t_x)/\tau_q} + I_f \qquad \text{(C.21)}$$

where $I_f \equiv \tau_q\Psi + I_{T/2}$.

The temperature equation, Eq. (C.6), for $t > t_x$ can be rewritten

$$\alpha_0\tau_m\frac{\dot{\vartheta}}{\vartheta_{c\star}} + \beta_0\frac{\vartheta}{\vartheta_{c\star}} = \left(\frac{2\bar{I}}{I_T} - 1\right)\frac{I}{I_\star} + \left(\frac{I_T - \bar{I}}{I_\star} - 1\right) \qquad \text{(C.22)}$$

where the dimensionless coefficients have been defined as follows:

$$\alpha_0(I_\star) = \frac{\rho_s \bar{C}_s A_s \vartheta_{c\star}(I_\star)}{\mathcal{R}_m I_{T/2} I_\star \tau_m} \tag{C.23}$$

$$\beta_0(I_\star) = \frac{2ph\vartheta_{c\star}(I_\star)}{\mathcal{R}_m I_T I_\star} - 1 \tag{C.24}$$

For practical operating scenarios, it is important to note that $\alpha_0 > 0$ while $\beta_0 < 0$.

Using equation Eq. (C.21) and the initial condition $\vartheta = \vartheta_x \equiv \vartheta(t = t_x)$ (found previously from iteration), the solution to Eq. (C.22) is:

$$\frac{\vartheta}{\vartheta_{c\star}} = a_0 + a_1 e^{-(t-t_x)/\tau_q} + a_2 e^{-\beta_0(t-t_x)/(\alpha_0\tau_q)} \tag{C.25}$$

where

$$\begin{aligned} a_0 &= \left(\frac{I_T - \bar{I}}{I_\star} - 1\right) / \beta_0 \\ a_1 &= \left(\frac{2\bar{I}}{I_T} - 1\right)\left(\frac{I_x - I_f}{I_\star}\right) / \left(\beta_0 - \alpha_0\tau_m/\tau_q\right) \\ a_2 &= \frac{\vartheta_x}{\vartheta_{c\star}} - a_1 - a_0 \end{aligned}$$

Having solved the current and temperature equation in all three regions, we can track the evolution of I and ϑ for all time $t_\star < t < \infty$ for any given operating scenario.

C.2 Solving for Initial Conditions from Specified End Result

To determine the operating scenario which corresponds to the marginal stability case, it is necessary to start with the final result of the current and temperature evolution and work backwards. In Section 6.2.4 it was determined that the marginal stability case corresponded with the limit $\dot{\vartheta} = \ddot{\vartheta} = 0$ as $t \to \infty$. Investigating Eq. (C.25), we see that this condition is equivalent with the specification $a_2 = 0$ since the factor

β_0/α_0 is negative. In mathematical terms, the stability criterion for a "lab-scale" two strand cable can thus be stated:

$$a_2(I_\star) = 0$$

where a_2 is a complicated function of the initial condition, $I_\star$.

The difficulty arises when we try to invert the functional dependence $a_2(I_\star)$ to achieve a stability criterion in terms of $I_\star(a_2)$, an expression which can be directly related to the operating scenario. Unfortunately there is no closed form solution for the value of $I_\star$ which corresponds to $a_2 = 0$. To obtain the exact answer, an iterative routine was used to solve the transcendental equations derived in Section C.1 to provide the results presented in Chapter 6.

While the numerical solution of a system of equations is much speedier than iteratively evolving the full equations from varying initial conditions, it is still less satisfying than an analytic result. It was discovered, however, that while the exact solution to the linearized model still requires a numerical solution (albeit a much simpler one) an approximate solution can be found using purely analytical calculations.

C.3 Approximate Solution to the Linearized Stability Model

After working extensively with the linearized two-strand model, it was discovered that for typical cable designs the marginal stability condition nearly coincided with the resonance condition for the second order system. Although we proved the cable actually needs to be under-damped to be in the marginal stability case (see Section 6.3.2), the critically damped case is in fact an excellent predictor of marginal stability (see Fig. 6-14 for a comparison).

Since it is much simpler to solve for the operating condition which corresponds to critical damping than it is to solve for the condition which leads to $a_2 = 0$, this approximate method was found to be much more useful (and nearly as accurate) as the method described in Section C.2. Referring to Eq. (C.14), the resonance condition is seen to be:

$$4\tau_R^2\omega_R^2 = 1 \tag{C.26}$$

For cables of interest, $\tau_m << \tau_J$ and the following approximations are valid (refer to Eqs. (C.15) and (C.16)):

$$\begin{aligned}\tau_R &\approx \frac{\tau_m}{1/2+\bar{\beta}/\beta_0}\\ \omega_R &\approx \frac{\bar{\beta}+1}{2\bar{\alpha}\tau_m^2}\end{aligned}$$

Substituting these values into Eq. (C.26) reveals the approximate stability criterion for the linearized equations:

$$1+\bar{\beta}/2-\bar{\alpha}/8-\bar{\beta}^2/(2\bar{\alpha}) = 0 \tag{C.27}$$

where $\bar{\alpha}$ and $\bar{\beta}$ are defined in Eqs. (C.11) and (C.12). Using only algebra (finding the root of a cubic polynomial is the most difficult step [46]), Eq. (C.27) can be solved to give the value of $I_\star$ which corresponds with the marginal stability case. The operating conditions, I_T and $\dot{B}_\perp$ can be derived from $I_\star$ using Eq. (C.3). The final results are demonstrated in Section 6.3.3.

C.4 Scaling Considerations

The dimensionless variables in the simplified stability criteria, Eq. (C.27), can be thought of as the following ratios (refer to Eqs. (C.11) and (C.12)):

$$\begin{aligned}\bar{\alpha} &\sim \frac{\text{Change in Enthalpy}}{\text{Joule Energy}}\\ \bar{\beta} &\sim \frac{\text{Net Cooling Power}}{\text{Joule Power}}\end{aligned}$$

Substituting these "conceptual equivalences" into Eq. (C.27) provides the following:

$$\text{Joule Energy} = \\ +\frac{1}{8}\text{Change in Enthalpy} + \frac{1}{2}\text{Net Cooling Energy}\left(\frac{\text{Net Cooling Energy}}{\text{Enthalpy}} - 1\right) \tag{C.28}$$

It was hoped that the energy balance represented by Eq. (C.28) would lead to new insights into scaling relations for the stability criterion for lab-scale cables. No significant insights were discovered, however, and thus this avenue of inquiry was not pursued further.

Appendix D

Critical Current Model for the US-DPC Experiment

The critical current properties of the Nb_3Sn wires which were used in the US-DPC experiment are well modeled by the critical current equation developed by Summers et. al. [41]. For ease of reference, the relevant details are briefly repeated here.

The heuristic equation is:

$$I_c(B,T,\varepsilon) = C(\varepsilon)\,[B_{c2}(T,\varepsilon)]^{-1/2}\,(1-t^2)^2 b^{-1/2}(1-b)^2 \tag{D.1}$$

where

$$\begin{aligned}
C(\varepsilon) &= C_0(1-a\,|\varepsilon|^u)^{1/2} \\
B_{c2} &= B_{c20}(\varepsilon)(1-t^2)^2\left[1-0.31t^2(1-1.77\ln(t))\right] \\
B_{c20} &= B_{c20m}(1-a\,|\varepsilon|^u) \\
t &= T/T_{c0}(\varepsilon) \\
b &= B/B_{c2}(T,\varepsilon) \\
T_{c0}(\varepsilon) &= T_{c0m}(1-a\,|\varepsilon|^u)^{1/w} \\
a &= 900 \text{ for} \varepsilon < 0, a = 1200 \text{ for} \varepsilon > 0 \\
u &= 1.7
\end{aligned}$$

$$\begin{aligned} w &= 3 \\ B_{c20m} &= \text{Maximum (strain-free) upper critical field} \\ T_{c0m} &= \text{Maximum zero-field critical temperature} \\ C_0 &= \text{Coefficient independent of } T, B, \varepsilon \\ \varepsilon &= \text{Uniaxial strain} \end{aligned}$$

The three parameters—B_{c20m}, T_{c0m}, and C_0—are related to the material properties of the superconductor. The strain, ε, depends on manufacturing processes as well as operating conditions. For the US-DPC coil, the values of these parameters were found to be: [1]

$$\begin{aligned} B_{c20m} &= 27.5 \text{ T} \\ T_{c0m} &= 16 \text{ K} \\ C_0 &= 8800 \text{ AT}^{-1/2} \\ \varepsilon &= -0.1\% \end{aligned}$$

Using these parameters, Eq. (D.1) has been used in Section 7.2.5 to produce Fig. 7-7.

Bibliography

[1] T. A. Painter, M.M. Steeves, M. Takayasu, et al. Test data from the US-demostration poloidal coil experiment. Technical report, Massachusetts Institute of Technology Plasma Fusion Center, 1992.

[2] Sangkwon Jeong et al. Ramp-rate limitation experiments in support of the TPX magnets. In *Symposium on Fusion Engineering*, page 1331, September 1995.

[3] Makoto Takayasu, Matthew Ferri, et al. Measurements of ramp-rate limitation of cable-in-conduit conductors. In *Proc. Applied Superconductivity Conference*, 1992.

[4] M. Takayasu, V. S. Vysotsky, et al. Spike voltages seen during "quick charge" ramp limitation tests on Nb3Sn cable-in-conduit conductors. In *Proc. Applied Superconductivity Conference*, October 1996.

[5] V. S. Vysotsky et al. New method of current distribution studies for ramp-rate stability of multistrand superconducting cables. In *Proc. Applied Superconductivity Conference*, October 1994.

[6] V. S. Vysotsky, M. Takayasu, et al. Current distribution in a 12 strand Nb3Sn CICC and its influence on ramp rate limitation. In *Proc. Applied Superconductivity Conference*, October 1996.

[7] A. P. Verwejj and H. H. J. ten Kate. Super coupling currents in rutherford type of cables due to longitudinal non-homogeneities of dB/dt. In *Proc. Applied Superconductivity Conference*, October 1994.

[8] L. Krempasky and C. Schmidt. Ramp-rate limitation in large superconducting magnets due to supercurrents. *Cryogenics*, 36:471, 1996.

[9] Mamoru Shimada. Non-uniform current effects. Talk at MIT Plasma Fusion Center, Conductor Analysis Meeting, October 1995.

[10] M. O. Hoenig. Internally cooled cabled superconductors, parts I and II. *Cryogenics*, July and August 1980.

[11] T. P. Orlando. *Foundations of Applied Superconductivity.* Addison-Wesley, 1991.

[12] Martin N. Wilson. *Superconducting Magnets.* Oxford University Press, 1983.

[13] L. Bottura and J. V. Minervini. *FORTRAN Code: HESTAB.* Garching, Germany, 1987.

[14] B. Turck. Transverse resistance in cable-in-conduit conductors. In *Applied Superconductivity Conference*, Chicago, IL, 1992.

[15] H. A. Haus and J. R. Melcher. *Electromagnetic Fields and Energy.* Prentice-Hall, 1989.

[16] M. O. Hoenig, Y. Iwasa, and D. B. Montgomery. Internally cooled cabled superconductors. In N. Sacchetti, M. Spadoni, and S. Stipcich, editors, *Proc. 5th Int. Conf. Magnet Technology*, page 20, Frascati Italy, 1975.

[17] Luca Bottura, Neil Mitchell, and Joseph Minervini. Design criteria for stability in cable-in-conduit conductors. *Cryogenics*, 31:510, July 1991.

[18] J. V. Minervini M. M. Steeves. Status of US-DPC ramp rate limitation analysis. In *Proc. of the ITER Magnet R&D Workshop*, pages 137–152, Naka-machi, Ibaraki, Japan, Sept 1991.

[19] Matthew A. Ferri. Current distribution in cable-in-conduit superconductors. Master's thesis, MIT, 1994.

[20] W. J. Carr. *AC Loss and Macroscopic Theory of Superconductors.* Gordon and Breach, 1983.

[21] Ed Niessen. *Continuum Electromagnetics of Composite Superconductors.* PhD thesis, Universiteit Twente, 1993.

[22] Arjan P. Verwejj. *Electrodynamics of Superconducting Cables in Accelerator Magnets.* PhD thesis, Universiteit Twente, 1995.

[23] C. Y. Gung, M.M. Steeves, and J. V. Minervini. Energy dissipation in CS model coil joint during normal operation. In *Symposium on Fusion Engineering*, page 1331, September 1995.

[24] Yu Ju Chen. *A Comprehensive Electromagnetic Analysis of AC Losses in Large Superconducting Cables.* PhD thesis, Massachusetts Institute of Technology, 1996.

[25] Luca Bottura and Joseph Minervini. Modelling of dual stability in a cable-in-conduit conductor. In *Proc. Applied Superconductivity Conference*, September 1990.

[26] Y. B. Kim, C. F. Hempstead, and A.R. Strnad. Magnetization and critical supercurrents. *Phys. Rev.*, 129:528, 1963.

[27] F. W. Grover. *Inductance Calculations.* Dover Press, 1946.

[28] M. D. Sumption, E. W. Collings, et al. Contact resistance and cable loss measurements of coated strands and cables wound from them. In *Applied Superconductivity Conference*, page 1331, October 1994.

[29] S. A. Egorov et al. Interstrand coupling AC-losses in multistage cable-in-conduit superconductors. *Cryogenics*, 32:439, 1992.

[30] Harry Bateman. *Tables of Integral Transforms*, volume 1. McGraw-Hill Book Company, Inc., 1954.

[31] Harry Bateman. *Higher Transcendental Functions*, volume 2. McGraw-Hill Book Company, Inc., 1953.

[32] Y. B. Kim, C. F. Hempstead, and A.R. Strnad. Flux-flow resistance in type-II superconductors. *Phys. Rev.*, 139:A1163, 1965.

[33] Ali Shajii. *Theory and Modelling of Quench in Cable-In-Conduit Superconducting Magnets.* PhD thesis, Massachusetts Institute of Technology, 1994.

[34] Luca Bottura and O.C. Zienkiewicz. Quench analysis of large superconducting magnets, parts I and II. *Cryogenics*, 32:659, 1992.

[35] R. Byron Bird, Warren E. Stewart, and Edwin N. Lightfoot. *Transport phenomena.* Wiley, 1960.

[36] U. M. Ascher, R. M. M. Mattheij, and R. D. Russell. *Numerical Solution of Boundary Value Problems for Ordinary Differential Equations.* Prentice Hall, 1988.

[37] U. M. Ascher, J. Christiansen, and R. D. Russell. Collocation software for boundary-value ODEs. *ACM Trans. Math. Software*, 7:209–222, 1981.

[38] MIT Plasma Fusion Center. *U.S.-DPC Test Results Workshop*, Cambridge, MA, 1991.

[39] Oxford UK The Numerical Algorithms Group Ltd. Nag fortran library, 1996.

[40] G. Hall and J. M. Watt. *Modern Numerical Methods for Ordinary Differential Equations.* Clarendon Press, 1976.

[41] L.T. Summers et al. A model for prediction of Nb3Sn critical current as a function of field, temperature, strain, and radiation damage. *IEEE Trans. on Magnetics*, MAG-27(2):2041+, 1991.

[42] Makoto Takayasu et al. Critical currents of Nb3Sn wires of the US-DPC coil. In *Proc. CEC-ICMC Conference*, Huntsville, AL, June 1991.

[43] Vytaly Vysotsky. Experiments with bifillar sample (sample of Sangkwon Jeong). Compiled data from experimental campaigns of July 5, 15, and 29, 1994, Nov 1994.

[44] Francis B. Hildebrand. *Advanced Calculus for Applications*. Prentice-Hall, 1976.

[45] Jack R. Benjamin and C. Allin Cornell. *Probability, Statistics and Design for Civil Engineers*. McGraw-Hill, 1970.

[46] Murray R. Spiegel. *Mathematical Handbook of Formulas and Tables*. Schaum's Outline Series. McGraw-Hill Book Company, 1968.